NASA/TM–2020-5006765/Volume II
NESC-RP-16-01183

Composite Overwrapped Pressure Vessel (COPV) Damage Tolerance Life Analysis Methodology and Test Best Practices

Appendices

Heather K. Hickman/NESC, and Richard W. Russell/NESC
Langley Research Center, Hampton, Virginia

David S. Dawicke
Analytical Services and Materials, Hampton, Virginia

William Leser, Patrick E. Leser, and Russell A. Wincheski
Langley Research Center, Hampton, Virginia

Jacob D. Hochhalter
University of Utah, Salt Lake City, Utah

Lorie R. Grimes Ledesma
Jet Propulsion Laboratory, Pasadena, California

Kauser S. Imtiaz
Johnson Space Center, Houston, Texas

August 2020

NASA STI Program . . . in Profile

Since its founding, NASA has been dedicated to the advancement of aeronautics and space science. The NASA scientific and technical information (STI) program plays a key part in helping NASA maintain this important role.

The NASA STI program operates under the auspices of the Agency Chief Information Officer. It collects, organizes, provides for archiving, and disseminates NASA's STI. The NASA STI program provides access to the NTRS Registered and its public interface, the NASA Technical Reports Server, thus providing one of the largest collections of aeronautical and space science STI in the world. Results are published in both non-NASA channels and by NASA in the NASA STI Report Series, which includes the following report types:

- TECHNICAL PUBLICATION. Reports of completed research or a major significant phase of research that present the results of NASA Programs and include extensive data or theoretical analysis. Includes compilations of significant scientific and technical data and information deemed to be of continuing reference value. NASA counter-part of peer-reviewed formal professional papers but has less stringent limitations on manuscript length and extent of graphic presentations.

- TECHNICAL MEMORANDUM. Scientific and technical findings that are preliminary or of specialized interest, e.g., quick release reports, working papers, and bibliographies that contain minimal annotation. Does not contain extensive analysis.

- CONTRACTOR REPORT. Scientific and technical findings by NASA-sponsored contractors and grantees.

- CONFERENCE PUBLICATION. Collected papers from scientific and technical conferences, symposia, seminars, or other meetings sponsored or co-sponsored by NASA.

- SPECIAL PUBLICATION. Scientific, technical, or historical information from NASA programs, projects, and missions, often concerned with subjects having substantial public interest.

- TECHNICAL TRANSLATION. English-language translations of foreign scientific and technical material pertinent to NASA's mission.

Specialized services also include organizing and publishing research results, distributing specialized research announcements and feeds, providing information desk and personal search support, and enabling data exchange services.

For more information about the NASA STI program, see the following:

- Access the NASA STI program home page at *http://www.sti.nasa.gov*

- E-mail your question to help@sti.nasa.gov

- Phone the NASA STI Information Desk at 757-864-9658

- Write to:
  NASA STI Information Desk
  Mail Stop 148
  NASA Langley Research Center
  Hampton, VA 23681-2199

NASA/TM–2020-5006765/Volume II
NESC-RP-16-01183

Composite Overwrapped Pressure Vessel (COPV) Damage Tolerance Life Analysis Methodology and Test Best Practices

Appendices

Heather K. Hickman/NESC, and Richard W. Russell/NESC
Langley Research Center, Hampton, Virginia

David S. Dawicke
Analytical Services and Materials, Hampton, Virginia

William Leser, Patrick E. Leser, and Russell A. Wincheski
Langley Research Center, Hampton, Virginia

Jacob D. Hochhalter
University of Utah, Salt Lake City, Utah

Lorie R. Grimes Ledesma
Jet Propulsion Laboratory, Pasadena, California

Kauser S. Imtiaz
Johnson Space Center, Houston, Texas

National Aeronautics and
Space Administration

Langley Research Center
Hampton, Virginia 23681-2199

August 2020

Available from:

NASA STI Program / Mail Stop 148
NASA Langley Research Center
Hampton, VA 23681-2199
Fax: 757-864-6500

NASA Engineering and Safety Center
Technical Assessment Report

Volume II

Composite Overwrapped Pressure Vessel (COPV) Damage Tolerance Life Analysis Methodology and Test Best Practices

June 4, 2020

Table of Contents

Appendix A. Excerpts from AIAA S-081B on Damage Tolerance

This appendix includes excerpts from the standard ANSI/AIAA S-081B, Space Systems – Composite Overwrapped Pressure Vessels, for the reader's reference.

Section 4.2 Terms and Definitions

Damage Tolerance Life

The required period of time and number of cycles that the metallic liner of a COPV, containing the largest undetected crack, flaw, or discontinuity, must survive without leak or burst in the expected service environment

Linear Elastic Fracture Mechanics

An approach to analyzing the propagation of flaws in materials. The material is assumed to be isotropic and linear elastic and the stress field near the crack tip is calculated using the theory of elasticity. When the stress intensity at the crack tip exceeds the material fracture toughness, the crack will grow in an unstable manner.

Precrack

A fatigue crack of regular configuration (i.e., a half-ellipse or a segment of a circle) produced at a prescribed location, whose depth and length are equal to or greater than predetermined target values, and whose subsequent fracture behavior will not be influenced by any detail of the preparation process.

Service Life

The period of time and/or number of cycles for all relevant load events that occur over the entire COPV lifetime. The service life includes all manufacturing (including autofrettage, if one is performed), operational cycles, testing, loading, handling, storage, transportation, and launch. The service life also includes, if applicable, reentry or recover from orbit, post-landing events, refurbishment, retesting, and reuse.

Note 1: For damage tolerance assessment, the portion of the service life prior to screening (NDT) for pre-existing flaws may be excluded.

Note 2: For reliability assessment, service life includes only the operational portion of the service life or a specified period, such as a per-flight basis.

Stable Crack Extension

A displacement-controlled crack extension beyond the stretch-zone width that stops when the applied displacement is held constant

Stress Intensity Factor

A parameter that characterizes the stress-strain behavior at the tip of a crack contained in a linear elastic, homogenous, and isotropic body.

Stretch-zone Width

The length of crack extension that occurs during crack-tip blinting, for examples, prior to the onset of unstable brittle crack extension, pop-in, or slow stable crack extension. The stretch-zone width is in the same plane as the original (unloaded) fatigue precrack and refers to an extension beyond the original crack size.

Worst-case Location

An identified location in the liner (includes the boss and associated shear region) where a flaw would lead to the most unfavorable LBB or damage tolerance life conditions

Note: the analyses to determine the worst-case location for LBB and damage tolerance life are different.

Section 5.2.13.1 Damage Tolerance Life Design

The region(s) of the COPV to which damage tolerance is applied shall be designed such that the COPV liner possesses a minimum damage tolerance life of four (4) times the service life without sustained load crack growth, detrimental deformation, leakage, or rupture. The portion of the service life prior to screening (NDT) for pre-existing flaws may be excluded from the damage tolerance life. The damage tolerance life may be different for different regions of the COPV depending on the point at which NDT is conducted for each region.

NOTE: A minimum of 13 full MEOP cycles is specified for the service life in accordance with Section 5.1.6.

The initial flaw (crack) size for assessment shall be greater than or equal to the minimum NDT capability associated with the inspection technique (Section 10.4.2) for screening of initial flaws. The initial flaw (crack) size and orientation shall be determined from the sensitivity limit of the 90% probability of detection (POD) at 95% confidence level for this inspection technique.

Proof test logic shall not be used to determine the initial flaw size.

Worst-case location(s) in the liner shall be determined based on an assessment that establishes the greatest potential for a flaw to grow to leakage or rupture.

The worst-case location assessment shall include all regions of the liner (including the boss). The assessment shall incorporate, at each location, the stress, strain, thickness, initial flaw (crack) size, and material properties of the liner. The assessment may involve multiple candidate worst-case locations, including the boss region. If this damage tolerance life requirement applies to a portion of the COPV, sufficient analysis or assessment shall be performed to fully characterize the applicable region and transitional zones to other regions. The rationale for the determination of this worst-case location(s) shall be documented.

In determining the damage tolerance life, the combination of the following criteria shall be evaluated:

- The initial flaw (crack) at the worst-case location(s) and in the worst-case orientation.
- Aspect ratios of the flaw (crack) of 0.1 and 0.5 and those within that range. The range of potential aspect ratios shall be determined based on the manufacturing process or NDT. If the potential range (worst case) is shown to be broader than the range of 0.1 to 0.5, then the larger range shall be used.
- The worst-case combination of conditions that support flaw (crack) extension including external load combinations/resident pressure, composite stiffness, liner yield response, and work hardening.

- The effects of residual stresses from manufacturing processes.
- The effects of all stress conditions (cyclic and sustained), vibration loads, environments, and their combinations.
- The assessment of both elliptical embedded and semi-elliptical surface flaws (cracks), and their proximity to free surfaces.
- In assessment of flaw growth in the service life, it is permissible to delete cycles in the service life provided that those cycles are conservatively shown to develop stress intensity below ΔKth.

NOTE Autofrettage, if one is performed, is included in the service life for damage tolerance assessment, provided the autofrettage cycle occurs after NDT.

Section 6.2.1 Damage Tolerance Life Verification

The damage tolerance life requirement identified in Section 5.2.13.1 shall be verified either by analysis, in accordance with Section 7.5.1, or test, in accordance with Section 10.1, according to the following criterion:

The damage tolerance life requirement may be verified by analysis only if both of the following conditions are met:

1) The liner (or region of the liner) is shown to be elastically responding and characterized by linear elastic fracture mechanics (LEFM) throughout proof testing and the operational portion of the service life.
2) The fracture properties of the liner materials are determined in accordance with Section 7.1.

Otherwise, the damage tolerance life requirement will be verified by test.

NOTE Verification by test may be chosen for all circumstances.

Section 7.1 Metallic Material Properties

Two approaches are used for determining metallic material properties.

1) A-basis design allowables shall be used for:

   - Tensile yield strength, Fty
   - Tensile ultimate strength, Ftu
   - Shear ultimate strength, Fsu
   - Elongation

   A-basis design allowables shall be calculated per the procedures in Metallic Materials Properties Development Standardization (DOT/FAA/AR-MMPDS-10). The mechanical properties and the fatigue and fracture properties of all metallic materials shall be established for the expected operating environment. Properties shall be established from reliable sources such as Metallic Materials Properties Development Standardization, Aerospace Structural Metals Handbook, and Damage Tolerance Design Handbook. When material properties are not available, they shall be determined by test.

2) Either A-basis or nominal values based on standards such as those developed by ASTM may be used for:

   - Plane strain fracture toughness, KIC; surface-crack fracture toughness, KIE; and stress intensity factor threshold for plane strain environmentally assisted cracking, KIEAC
   - Fatigue crack growth rates, da/dN, dc/dN and corrosion fatigue growth rates
   - Fatigue, stress, and strain with respect to number of cycles, S-N, or ε-N data

   Sufficient data shall be obtained either from conducting tests or other available sources so that meaningful nominal values can be established. The test program shall establish these properties for the parent metal, weld joints, and heat-affected zones, all taking into account the fluid contents, service life, and expected operating and test environments, as appropriate. The test program shall include the effects of all plastic deformation throughout the service life, for example, during autofrettage (if one is performed) and any other plastic cycles. The values shall address alloy system, temper, product form, and thermal and chemical environments appropriate for the established service life.

For materials that exhibit high scatter (e.g., those produced by certain additive manufacturing processes) this may require either high sampling rates or reductions in material properties to provide suitable confidence bounds.

Section 7.5.1 Damage Tolerance Life Analysis

The analysis shall show that the COPV liner meets the damage tolerance life. The analysis may be performed using a crack growth software package.

Principal stresses shall be used in damage tolerance analysis if the worst-case material orientation is perpendicular to the principal stress. If the worst-case material orientation is not perpendicular to the principal stress, either principal stresses or directional stresses (perpendicular to the crack plane) shall be used in damage tolerance analysis.

For the cycles in the service life during which the liner remains elastic, the analysis shall use nominal or conservative values of fracture properties (fracture toughness, stable crack extension resistance, KIEAC, and fatigue crack growth rate data) (Section 7.1) associated with each alloy, heat-treat condition, thickness, and product form in the applicable thermal and chemical environments.

For analysis of the autofrettage cycle (if one is performed), the factor of four may be waived provided conservative crack growth properties and methodology are used in the determination of crack growth for autofrettage. Autofrettage may be assessed using EPFM. The data used for the EPFM analysis shall conservatively represent the material alloy, condition, thickness, and autofrettage cycle as validated through testing.

A separate analysis shall be conducted for each region. If mechanical properties are not known for the materials used in the COPV, then those properties will be determined from a characterization test program, as specified in Section 7.1.

> EXAMPLE The autofrettage cycle might be approached through analysis of a single event predicting the potential extension in a conservative manner using a lower bound crack extension resistance curve or equivalent technique, rather than a nominal resistance

curve. This extended defect size thus derived might then be used as the starting defect size in the damage tolerance life analysis.

At all times in the service life, the applied stress intensity factor shall be less than the surface or embedded crack fracture toughness (see ASTM E2899) and KIEAC for the applicable environment (such as embrittlement).

The stress in the uncracked ligament (the remaining cross-sectional area at the crack plane) shall remain below the flow stress throughout the analysis of the damage tolerance life.

The analysis shall account for changes in the flaw (crack) aspect ratio and the effects of all environment(s) on the crack growth rate. An assessment shall be performed to determine the range of potential aspect ratios based on the manufacturing process or NDT. If the potential range (worst case) is determined to be broader than the range of 0.1 to 0.5, then the larger range shall be used. Beneficial retardation effects on crack growth rates from variable amplitude loading shall not be used in the analysis. The strain rate (or test frequency) of the da/dN data used for the analyses should be assessed for applicability.

The damage tolerance life analysis shall be documented with the following:

- Fracture mechanics data including surface crack fracture toughness (KIE), crack extension resistance (KR), plane strain fracture toughness (KIC), stress intensity factor threshold for plane strain environmentally assisted cracking (KIEAC) in both reactive and inert fluids (if applicable), and fatigue crack growth rates (da/dN)
- Service life and environments
- NDT method(s) and corresponding initial liner flaw sizes
- Analysis assumptions and rationale including substantiation of worst-case location, orientation, and aspect ratio ANSI/AIAA S-081B-2018 28
- Calculation methodology
- Summary of significant results
- References.

This documentation shall reflect the final design iteration.

The damage tolerance life requirement is identified in Section 5.2.13.1.

Section 10.1 Damage Tolerance Life Test

The damage tolerance life requirement shall be verified by test using either coupon specimens or COPV specimens (flight or flight-representative).

The effects of service environment (e.g., temperature, humidity, fluids) shall be accounted for either by representative testing or by analytical rationale.

The damage tolerance life requirement is identified in Section 5.2.13.1.

10.1.1 Damage Tolerance Life Test—Coupon Specimens

If coupon testing is used, then verification by test shall be performed on coupons that are representative of the liner material at the worst case or relevant location(s) based on material, weld procedure, weld thickness, geometry and/or product form. Consideration should be given to the different properties and thicknesses in the parent material, weld nugget, and heat affected zones.

Rationale that the coupons are representative of the flight COPV shall be documented.

At least two coupons shall be tested for each condition (location and flaw configuration, including aspect ratio). Uniaxial coupons may be used. Each coupon shall contain a surface crack. The coupons shall meet the specimen configuration and size requirements of ASTM E740. Each coupon shall be precracked. The size of each precrack shall be greater than or equal to the minimum flaw size associated with the NDT inspection technique(s). The coupon set shall envelope plausible crack aspect ratios.

After precracking, all strains in the damage tolerance life shall be applied in sequence to each coupon.

NOTE The required damage tolerance life is four (4) times the service life. The portion of the service life prior to screening (NDT) for pre-existing flaws may be excluded from the damage tolerance life. A minimum of 13 full MEOP cycles is specified for the service life in accordance with Section 5.1.6.

Strains equal to or greater than those associated with each load cycle, including the compressive liner strains at zero pressure, shall be tested.

Test strains and strain rate shall be verified by measurement.

After completion of cyclic strain testing, the following procedures and measurements on the coupons shall be performed.

1) The crack faces will be separated in a way that will allow examination of the fracture surfaces produced during testing.

2) The fracture surface will be examined to verify that the crack has not grown to become a through-crack.

3) The initial and final crack sizes will be measured.

4) The fracture surfaces will be inspected to identify whether sustained load crack growth occurred during testing.

NOTE. Useful guidance may be found in ASTM E2899-15.

The following three criteria shall be met for verification of damage tolerance life:

1) The cracks have not grown to through-cracks in test.

2) The precrack size has been verified for conformance to liner NDT thresholds.

3) The testing confirms that no sustained load crack growth has occurred during the test.

NOTE For some materials, it is difficult to differentiate between stable crack extension and sustained load crack growth.

The damage tolerance life requirement is identified in Section 5.2.13.1.

10.1.2 Damage Tolerance Life Test—COPV Specimens

If COPV specimen testing is used, then verification by test shall be performed on test specimens that are representative of the flight COPV. The test specimens shall represent liner and overwrap configuration and properties. The test specimens shall operate with the same stress/strain hysteresis response as the flight article.

Rationale that the test specimen COPVs are representative of the flight COPV shall be documented.

At least two liner cracks shall be tested for each condition (location and aspect ratio). Each location shall contain a surface crack. Each location shall be precracked. The size of each precrack shall be greater than or equal to the minimum flaw size associated with the NDT inspection technique(s). After precracking, all load cycles in the damage tolerance life shall be applied in sequence to each test specimen.

NOTE: The required damage tolerance life is four (4) times the service life. The portion of the service life, prior to screening (NDT) for pre-existing flaws, may be excluded from the damage tolerance life. A minimum of 13 full MEOP cycles is specified for the service life in accordance with Section 5.1.6.

After completion of cyclic strain testing, the following procedures and measurements on the test specimens shall be performed.

1) The crack faces will be separated in a way that will allow examination of the fracture surfaces produced during testing.

2) The fracture surface will be examined to verify that the crack has not grown to become a through-crack.

3) The initial and final crack sizes will be measured.

4) The fracture surfaces will be inspected to identify if any sustained load crack growth has occurred during testing.

NOTE Useful guidance may be found in ASTM E2899-15.

The following three criteria shall be met for verification of damage tolerance life:

1) The cracks have not grown to through-cracks in test.

2) The precrack size has been verified for conformance to liner NDT thresholds.

3) The testing confirms that no sustained load crack growth has occurred during the test.

NOTE For some materials, it is difficult to differentiate between stable crack extension and sustained load crack growth.

The damage tolerance life requirement is identified in Section 5.2.13.1.

Appendix B. Surface Crack Testing

B.1 Overview

Surface cracks in rolled sheet material were tested in fatigue to provide data for:

- Empirical evidence of the breakdown of the assumptions of LEFM in thin walled COPV liner materials (Section 7.1.1.1)
- Comparison to NASGRO [ref. 1] predictions to demonstrate the effect of using an LEFM tool when the underlying assumptions no longer hold on crack growth predictions (Section 7.1.1.2)
- Validation of an elastic-plastic FEM used to compute J-integral values for computing new limits to be used with NASGRO when LEFM assumptions have broken down (Appendix C.4)
- Comparison to small-scale specimens extracted from tank material as well as rolled sheet in order to assess the validity of using sheet material for damage tolerance testing (Section 7.2)

B.2 Experimental Procedure

B.2.1 Testing Apparatus and Specimen Preparation

Test specimens were cut from rolled sheet material in three thicknesses (0.032, 0.048, and 0.090 inch) with dimension as shown in Figure B.1. The coupons were dog bone shaped with a 2-inch wide gage section. Crack starter notches, with dimensions 0.02-inch wide x 0.01-inch deep, were cut in each coupon via electrical discharge machining (EDM). Testing was conducted on a servo-hydraulic load frame with a load capacity of 20 kips. Two sets of stereo digital image correlation (DIC) cameras were positioned on either side of the load frame to monitor full-field strain on both surfaces of the specimen as shown in Figure B.2.

Before testing, coupons were fatigue precracked to provide a sharp crack outside of the influence of the EDM notch. Precracks were grown to a size of approximately $2c$ = 0.04” and a = 0.02”. The precracked surface was marked with Sharpie® pen to allow for a post-test measurement. This was done by holding the crack open at 90%-95% of maximum load and pressing the tip of a Sharpie® pen against the crack mouth. The Sharpie® pen was held against the specimen for 30 seconds to a minute to allow the ink to wick into the crack. The coupon was then left under load for 30 minutes to allow the ink to dry. This process was then repeated 2 to 3 times.

After precracking and marking, the coupons were prepared for DIC. DIC calculates strain fields by optically tracking the distortion of a random pattern on the specimen surface [ref. 2]. The pattern was applied to the specimen by first painting both sides of the gage section with flat white spray paint to provide contrast. Then, a fine mist of black spray paint was applied over the area of interest to create the random pattern as shown in Figure B.3.

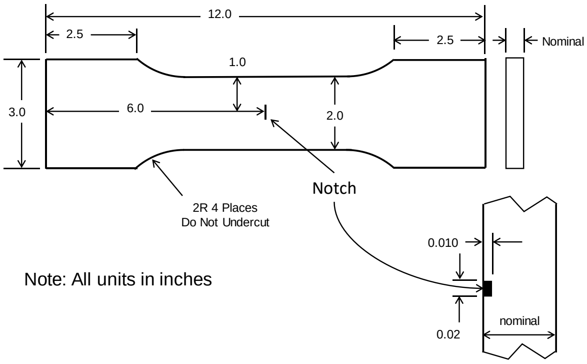

Figure B.1. Dimensions of surface crack coupons cut from rolled sheet material.

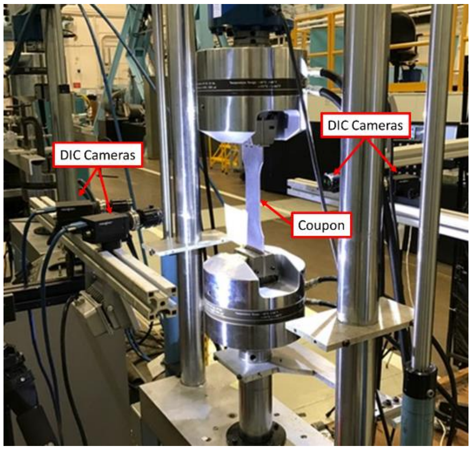

Figure B.2. Experimental setup for surface crack testing.

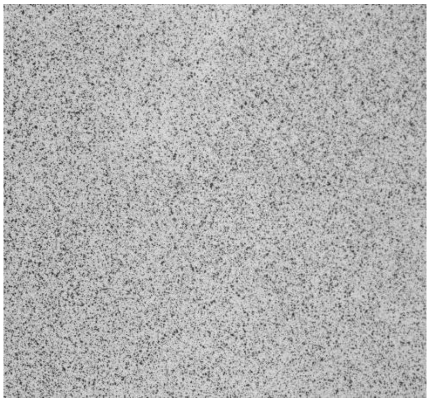

Figure B.3. An example of random speckle pattern applied to the surface of a fatigue crack coupon.

B.2.2 Testing Procedure

Fatigue testing was conducted at stress levels of 30, 35, and 40 ksi with constant amplitude loading and a stress ratio of R = 0.1. DIC was used to measure crack mouth opening displacement (CMOD) on the front face and strain on the back face. The first two cycles were run at 0.01 Hz to allow for DIC measurements.

These measurements represented CMOD and back-face strain of the precrack. The coupon was then cycled at 10 Hz in approximately 1000 cycle intervals. Between each interval, two 0.01 Hz cycles were performed for DIC measurements. Tests were stopped at various predetermined values of CMOD to ensure a variety of final crack sizes. The specimens were then fractured to expose the fatigue crack surfaces.

The crack surfaces were then measured with an optical microscope. An example of such a measurement is shown in Figure B.4. The EDM notch, Sharpie® pen-stained precrack, final fatigue crack and ductile failure region are all clearly visible. The Sharpie® pen allows the precrack to be distinguished from the final crack, allowing for the start and end points of the test to be measured.

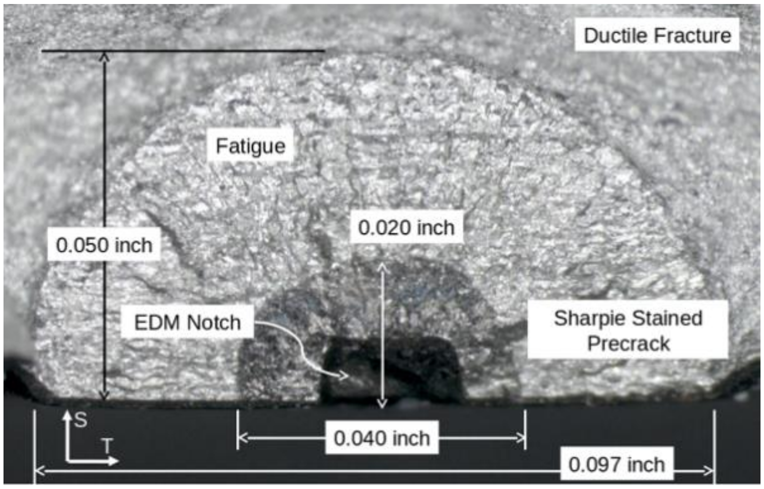

Figure B.4. An example of a post-test crack measurement showing the EDM notch, the Sharpie® pen-stained precrack, and the final fatigue crack.

B.2.3 Data Processing

The raw data collected during each test consisted of:

- Crack measurements a and $2c$ for the starting and ending crack sizes
- A series of images covering two full load cycles for the starting and ending crack sizes as well as at various points during the crack growth
- Loading values that corresponded to each image
- Cycle counts corresponding to each set of DIC images.

DIC images were processed using the commercial software VIC3D [ref. 3]. From this data, back face strains were monitored. Plastic strains developing on the back face indicated the breakdown of LEFM assumptions (See Section 7.1.1.1). CMOD was calculated by using a virtual extensometer across the center of the crack mouth, positioned 0.02 inch above and below the crack as shown in Figure B.5. Combined with the loading and cycle data, cycles of CMOD were obtained as shown in Figure B.6. This allowed for the extraction of maximum and minimum values of CMOD. Due to sampling rate mismatch with the load frame, maximum and minimum CMODs, which should correspond with the maximum and minimum applied stress, were obtained through a post-processing step. A linear fit in the CMOD vs. far-field applied stress space was applied to the loading and unloading segments of each fatigue cycle, and then the max and min were extrapolated along this line. This process is illustrated in Figure B.7.

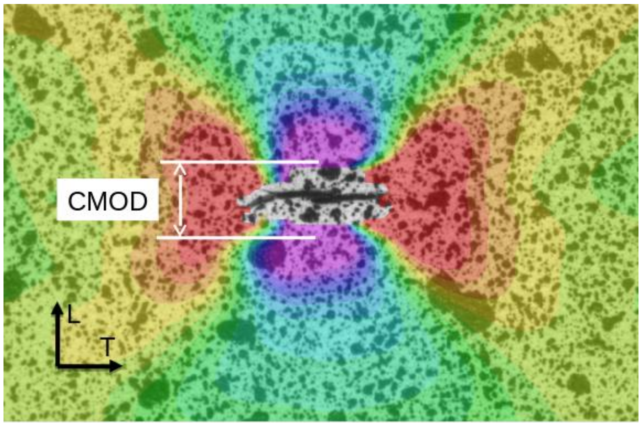

Figure B.5. An example of virtual extensometer positioning for calculation of CMOD.

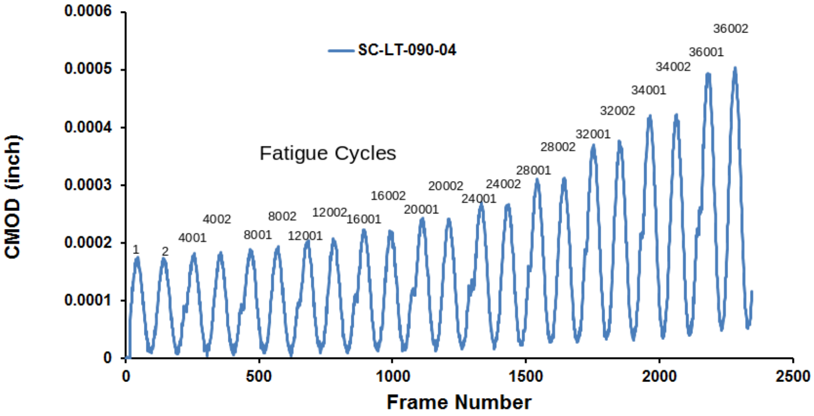

Figure B.6. Cycles of CMOD labeled by test cycle.

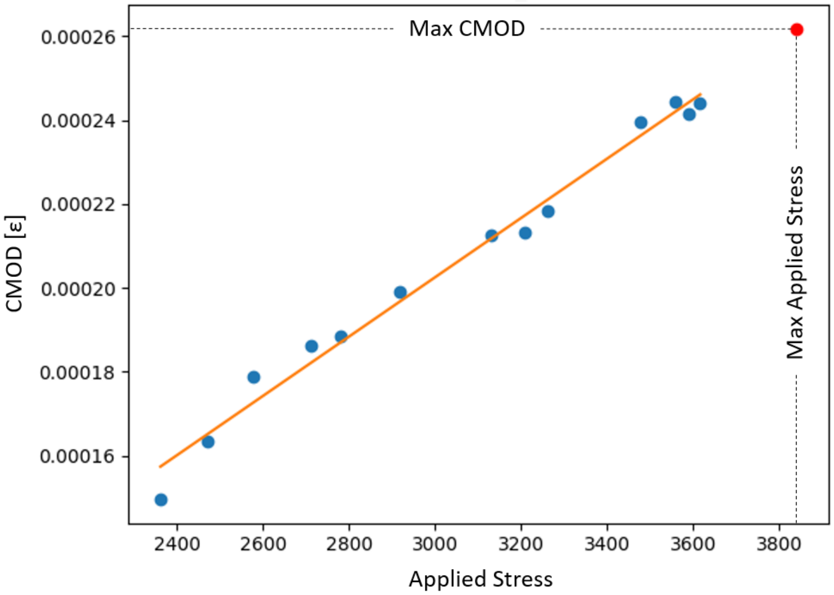

Figure B.7. Post-processing step to acquire $CMOD_{max}$ for a given fatigue cycle. Procedure for $CMOD_{min}$ was similar, but used the unloading portion of the CMOD vs. stress data.

Delta CMOD defined as $\Delta CMOD = CMOD_{max} - CMOD_{min}$ was then used to estimate crack depths (a) in between the measured starting and ending as. Assuming that $\Delta CMOD = 0$ when $a = 0$, a quadratic fit was made using the two end points of the test and 0 as shown in the top panel of Figure B.8. This relationship between a and $\Delta CMOD$ was then used to estimate values of a for each cycle where CMOD measurements were made. This allowed for estimates of $a\ vs\ N$ curves to be made for each test that could then be compared to predictions made by NASGRO (see the bottom panel of Figure B.8 for an example and Section 7.1.1.2 for details). These estimates were also used to calculate $\frac{da}{dn} vs\ \Delta K$ to be compared to data from small-scale testing (see Section 7.2 for details on this comparison).

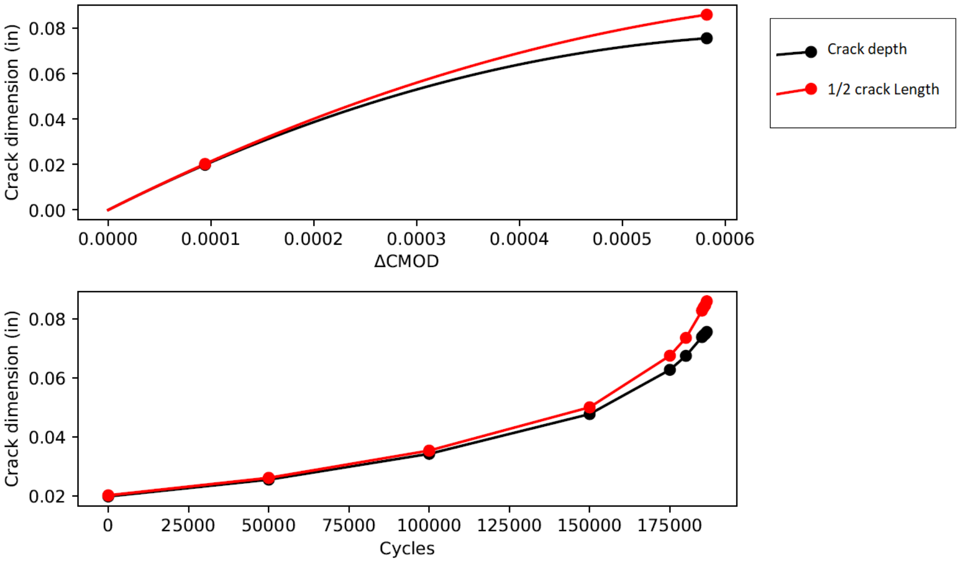

Figure B.8. Example of quadratic fit between test data end points to estimate relationship between CMOD and crack depth (top) and resulting a vs N relationship after converting measured CMOD to crack depth (bottom).

B.3 Results

This section documents all of the results obtained from the testing of surface cracks in rolled sheet material. Table B.1 lists the data for all tests conducted on AA6061-T6. The table includes the test identifier, the thickness of the coupon, the maximum load used for fatigue cycling, the measured lengths of the precrack (a_0 and c_0) and final crack (a_f and c_f), the ratio of a/c for each crack, and the total number of cycles applied. Figures B.9 through B.11 show the observed relationship between a and $\Delta CMOD$ for t = 0.032 inch, 0.048 inch, and 0.090 inch, respectively. Figure B.12 shows the observed crack growth rate for the AA6061-T6 surface crack tests vs ΔK. NASGRO predictions of a vs N and c vs N are compared to the observed crack growth in Figures B.13 through B.30.

Table B.1. Test Results for Surface Cracks in AA6061-T6 Rolled Sheet

Test ID	t (in)	σ (ksi)	a_0 (in)	c_0 (in)	a_0/c_0	a_f (in)	c_f (in)	a_f/c_f	cycles
FL-LT-032-11	0.032	35	0.0195	0.0213	0.9155	0.0264	0.0303	0.8713	3502
FL-LT-032-13	0.032	40	0.0202	0.0200	1.0110	0.0270	0.0299	0.9030	2502
FL-LT-032-18	0.032	35	0.0200	0.0209	0.9569	through	0.0372	--	5302
FL-LT-032-20	0.032	40	0.0208	0.0233	0.8927	0.0278	0.0327	0.8494	1752
FL-LT-050-02	0.048	30	0.0335	0.0345	0.9705	0.0458	0.0494	0.9278	3002
FL-LT-050-03	0.048	30	0.0205	0.0216	0.946	0.0405	0.0442	0.9154	24002
FL-LT-050-04	0.048	40	0.0203	0.0209	0.9713	0.037	0.0370	1.0000	3502
FL-LT-050-07	0.048	40	0.0267	0.0283	0.9435	0.0427	0.0472	0.9047	1702
FL-LT-050-12	0.048	35	0.0318	0.0292	1.0905	0.0423	0.0451	0.9390	2502
FL-LT-050-13	0.048	35	0.0192	0.0201	0.9576	0.0359	0.0383	0.9373	8202
FL-LT-050-16	0.048	35	0.0251	0.0270	0.9314	0.0461	0.0494	0.9332	6002
FL-TL-032-01	0.032	30	0.0195	0.0201	0.9701	through	0.0372	--	12002
FL-TL-032-06	0.032	30	0.0167	0.0195	0.8564	0.0183	0.0210	0.8714	4002
FL-TL-032-08	0.032	30	0.0192	0.0205	0.9366	0.0261	0.0291	0.8969	8514
FL-TL-032-09	0.032	30	0.0176	0.0203	0.8670	0.0187	0.0218	0.8578	3000
FL-TL-032-10	0.032	30	0.0191	0.0205	0.9317	0.0299	0.0347	0.8617	10002
FL-TL-032-15	0.032	30	0.0184	0.0197	0.9340	0.0249	0.0284	0.8768	10002
FL-TL-032-17	0.032	35	0.0195	0.0209	0.9330	0.0280	0.0316	0.8861	5202
FL-TL-032-19	0.032	40	0.0181	0.0201	0.9005	through	0.0422	--	4202
FL-TL-050-01	0.048	40	0.0311	0.0305	1.0197	0.0447	0.0490	0.9122	1602
FL-TL-050-03	0.048	30	0.0265	0.0267	0.9895	0.0444	0.0489	0.9091	8002
FL-TL-050-10	0.048	30	0.0198	0.0205	0.9657	0.0374	0.0376	0.9925	17002
FL-TL-050-12	0.048	40	0.0236	0.0221	1.0679	0.0368	0.0392	0.9388	2502
FL-TL-050-17	0.048	35	0.0250	0.0240	1.0438	0.0444	0.0446	0.9955	5502
FL-TL-090-19	0.090	20	0.0199	0.0203	0.9803	0.0757	0.0861	0.8792	186502
SC-LT-032-01	0.032	30	0.0195	0.0195	1.0000	0.0250	0.0260	0.9615	8000
SC-LT-032-02	0.032	30	0.0220	0.0215	1.0233	0.0280	0.0305	0.9180	8000
SC-LT-032-04	0.032	30	0.0218	0.0218	1.0000	0.0300	0.0357	0.8389	12000
SC-LT-090-04	0.090	30	0.0200	0.0200	1.0000	0.0500	0.0485	1.0309	36000
SC-LT-090-06	0.090	30	0.0190	0.0200	0.9500	0.0430	0.0425	1.0118	32000
SC-LT-090-08	0.090	30	0.0200	0.0205	0.9756	0.0564	0.0560	1.0071	36000
SC-LT-090-09	0.090	30	0.0200	0.0200	1.0000	0.0310	0.0300	1.0333	16000
SC-LT-090-10	0.090	30	0.0210	0.0205	1.0244	0.0650	0.0665	0.9774	27500
SC-LT-090-12	0.090	30	0.0223	0.0200	1.1155	0.0758	0.0755	1.0038	26000
SC-LT-090-13	0.090	35	0.0210	0.0190	1.1082	0.0376	0.0336	1.1190	9000
SC-LT-090-14	0.090	35	0.0210	0.0218	0.9642	0.0607	0.0614	0.9894	12000
SC-LT-090-15	0.090	35	0.0230	0.0243	0.9453	0.0570	0.0564	1.0115	7000
SC-LT-090-16	0.090	35	0.0250	0.0231	1.0823	0.0602	0.0563	1.0702	11000
SC-LT-090-18	0.090	35	0.0302	0.0264	1.1461	0.0760	0.0789	0.9632	10000
SC-LT-090-19	0.090	35	0.0252	0.0229	1.0992	0.0628	0.0606	1.0355	11000

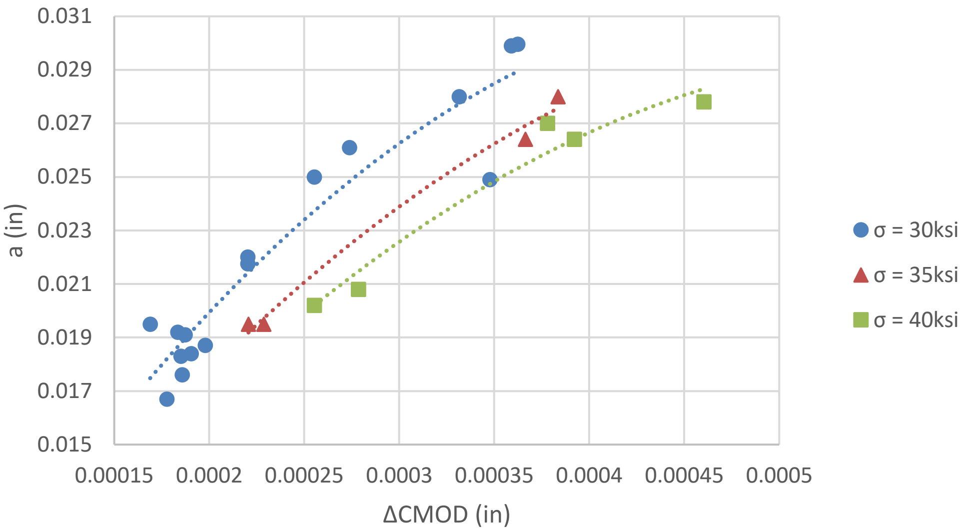

Figure B.9. a vs ΔCMOD for surface cracks in AA6061-T6 rolled sheet with thickness = 0.032 inch at different stress levels.

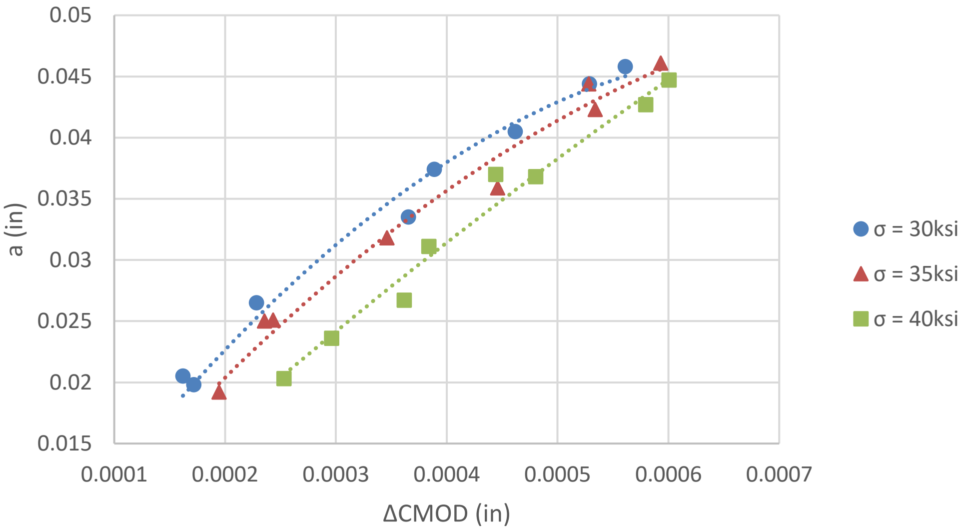

Figure B.10. a vs ΔCMOD for surface cracks in AA6061-T6 rolled sheet with thickness = 0.048 inch at different stress levels.

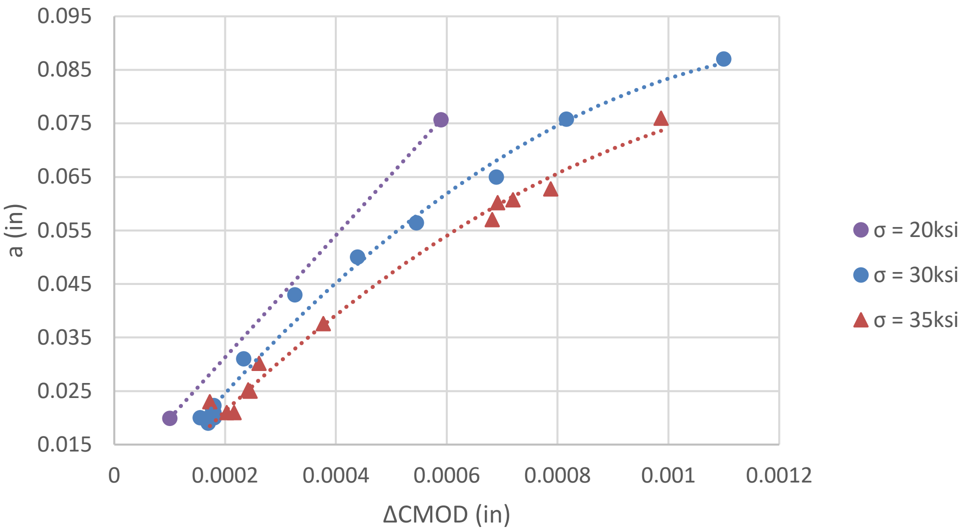

Figure B.11. a vs ΔCMOD for surface cracks in AA6061-T6 rolled sheet with thickness = 0.090 inch at different stress levels.

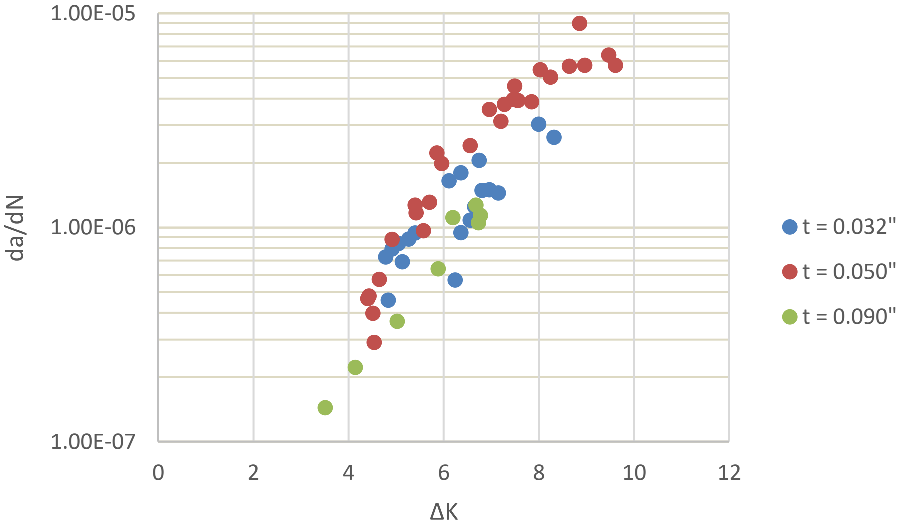

Figure B.12. da/dN vs ΔK for surface cracks in AA6061-T6 rolled sheet of thickness 0.032 inch, 0.048 inch, and 0.090 inch.

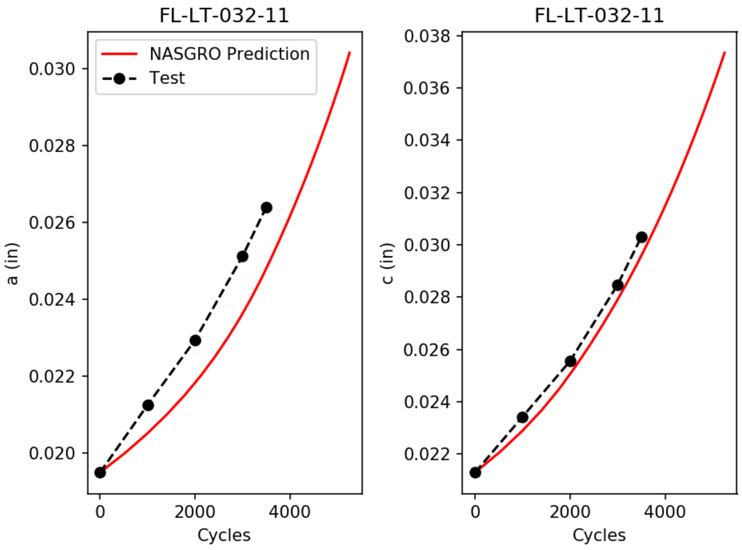

Figure B.13. a vs N and c vs N as observed during test compared to NASGRO prediction.

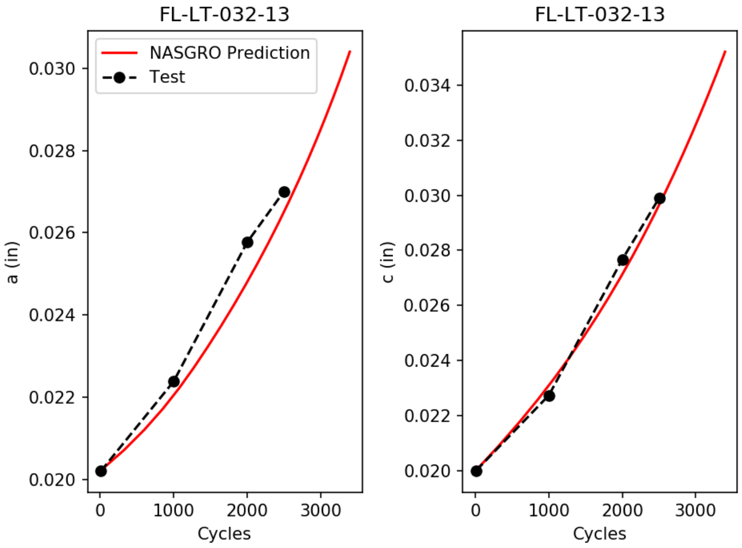

Figure B.14. a vs N and c vs N as observed during test compared to NASGRO prediction.

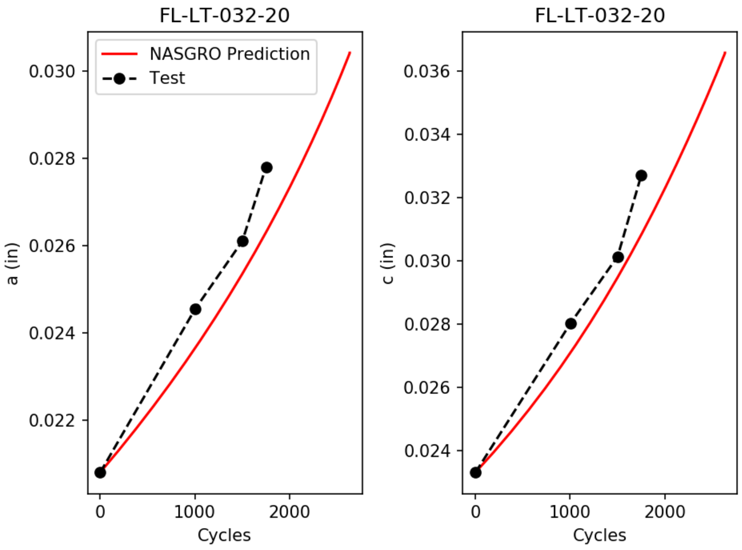

Figure B.15. a vs N and c vs N as observed during test compared to NASGRO prediction.

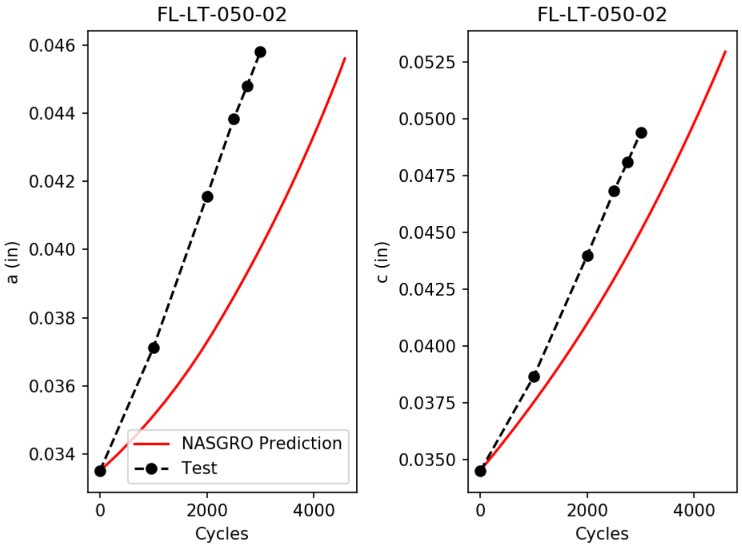

Figure B.16. a vs N and c vs N as observed during test compared to NASGRO prediction.

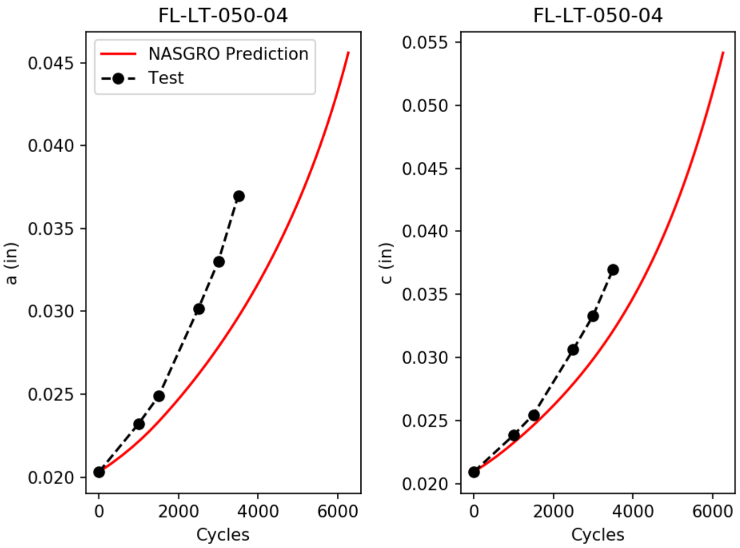

Figure B.17. a vs N and c vs N as observed during test compared to NASGRO prediction.

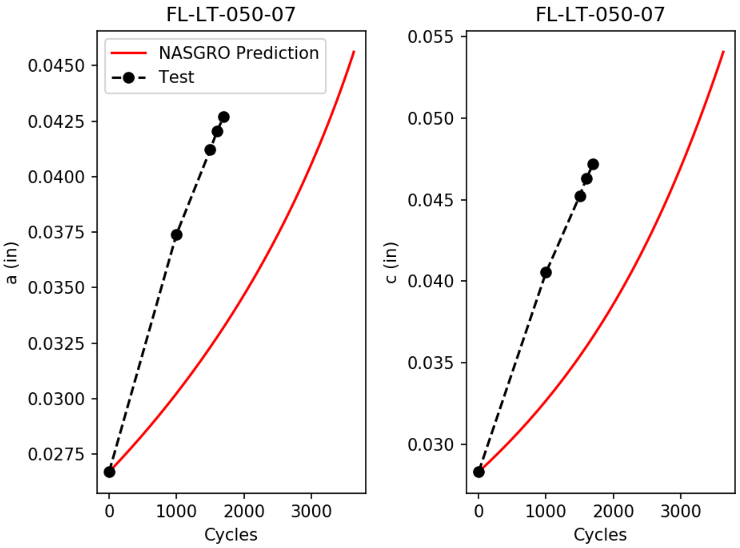

Figure B.18. a vs N and c vs N as observed during test compared to NASGRO prediction.

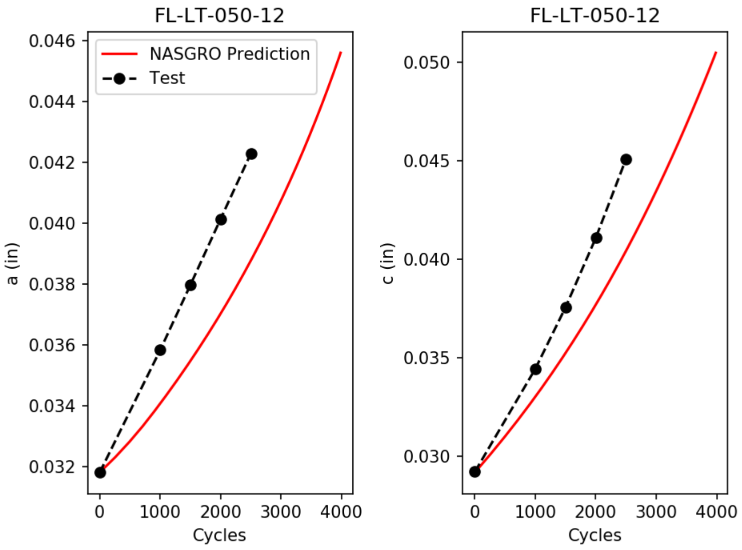

Figure B.19. a vs N and c vs N as observed during test compared to NASGRO prediction.

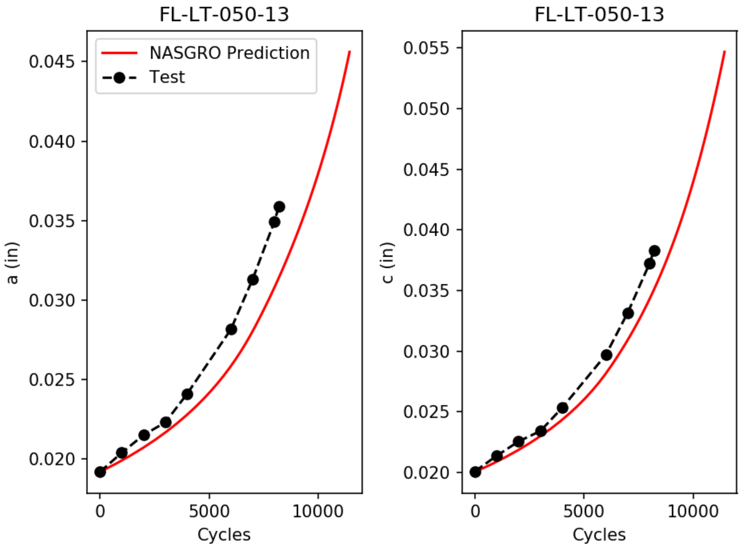

Figure B.20. a vs N and c vs N as observed during test compared to NASGRO prediction.

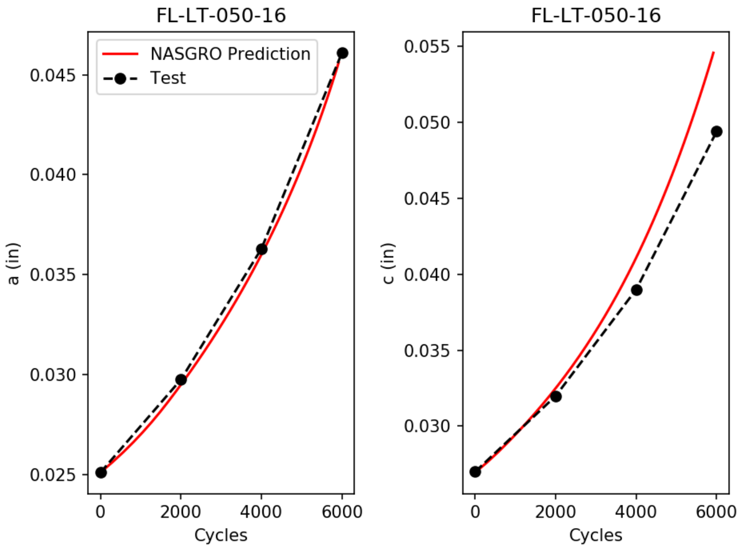

Figure B.21. a vs N and c vs N as observed during test compared to NASGRO prediction.

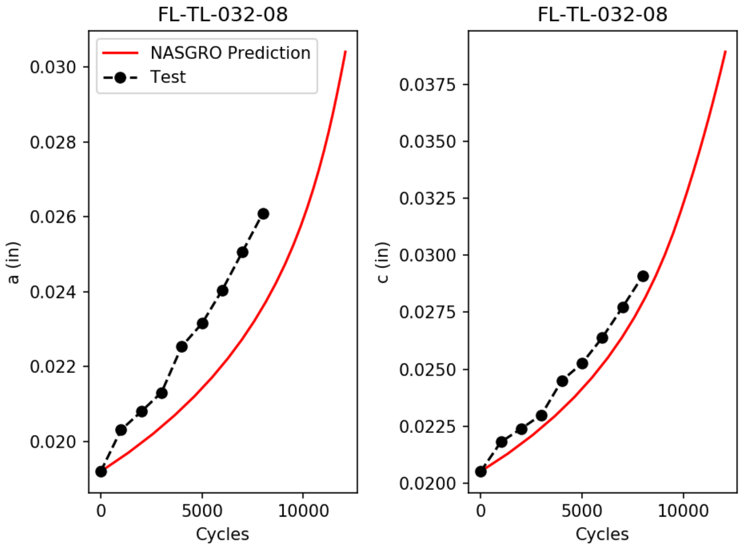

Figure B.22. a vs N and c vs N as observed during test compared to NASGRO prediction.

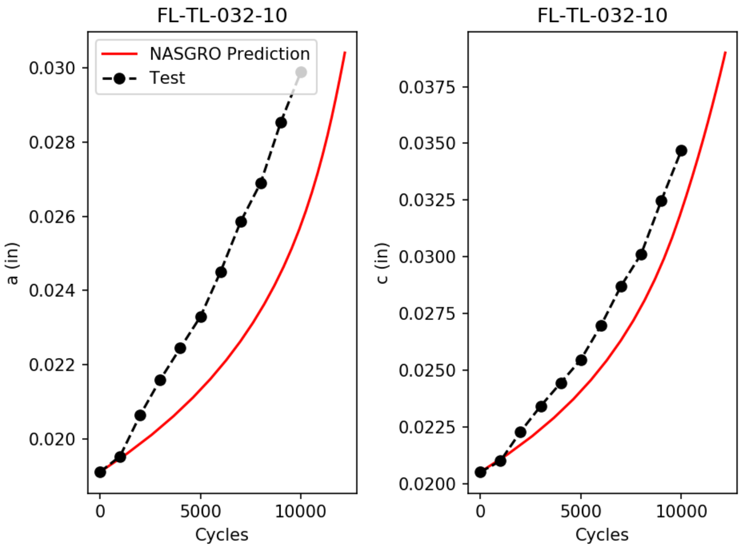

Figure B.23. a vs N and c vs N as observed during test compared to NASGRO prediction.

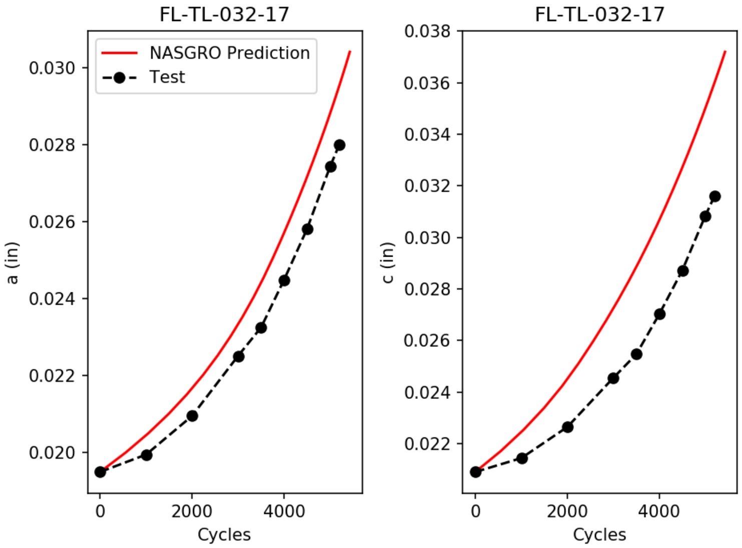

Figure B.24. a vs N and c vs N as observed during test compared to NASGRO prediction.

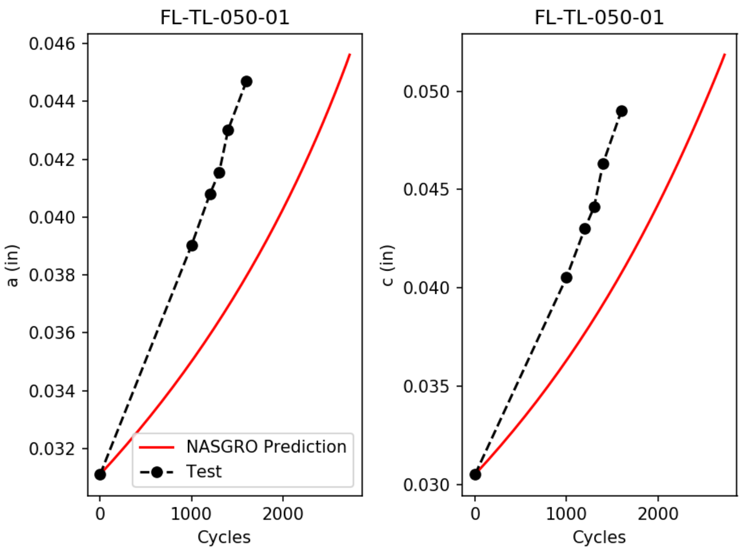

Figure B.25. a vs N and c vs N as observed during test compared to NASGRO prediction.

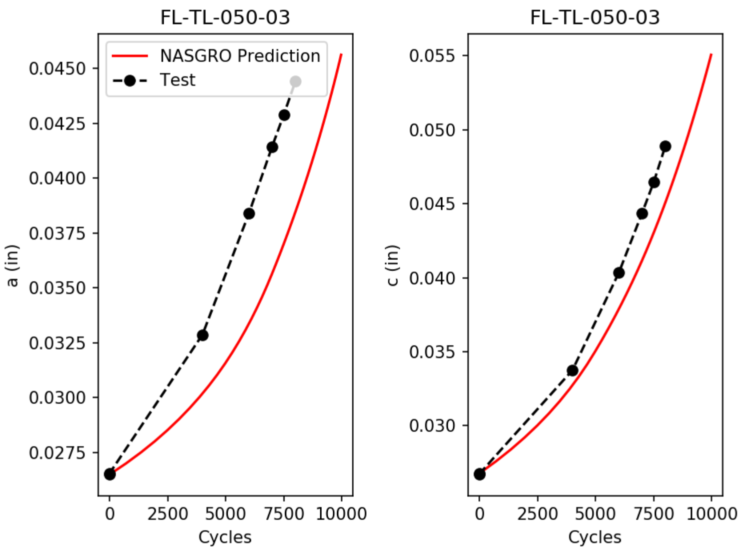

Figure B.26. a vs N and c vs N as observed during test compared to NASGRO prediction.

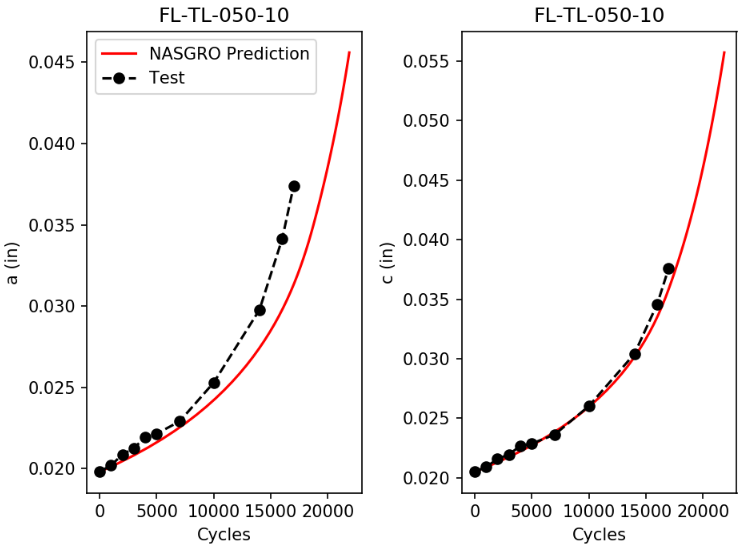

Figure B.27. a vs N and c vs N as observed during test compared to NASGRO prediction.

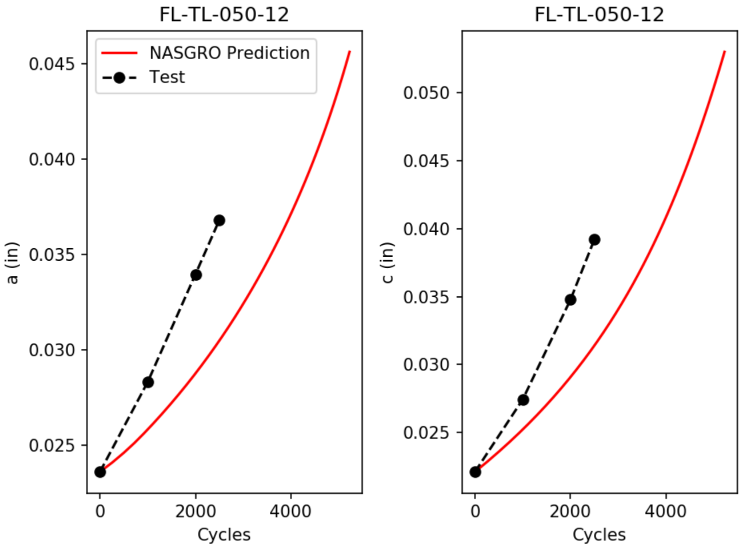

Figure B.28. a vs N and c vs N as observed during test compared to NASGRO prediction.

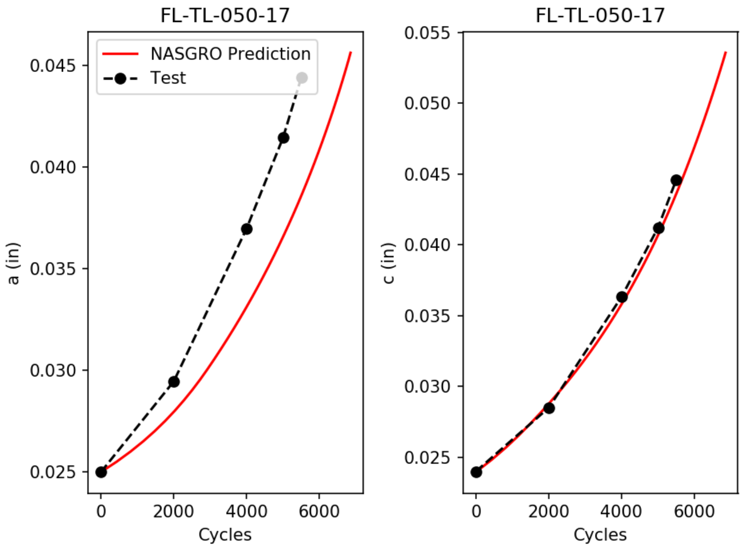

Figure B.29. a vs N and c vs N as observed during test compared to NASGRO prediction.

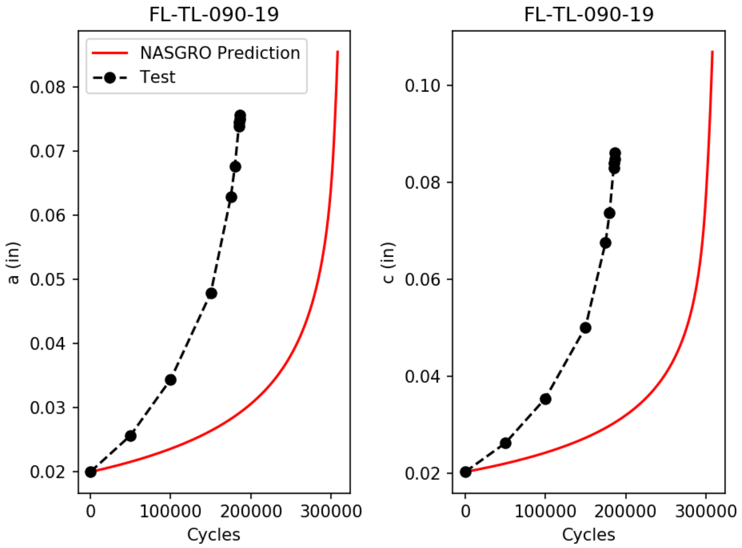

Figure B.30. a vs N and c vs N as observed during test compared to NASGRO prediction.

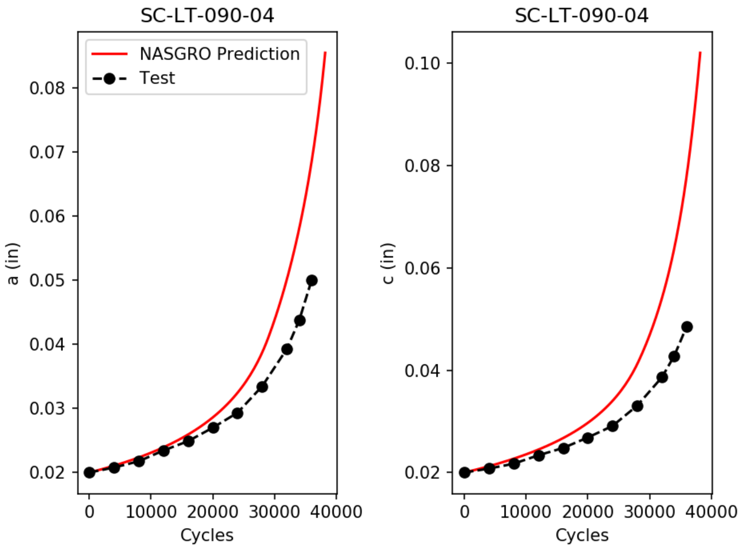

Figure B.31. a vs N and c vs N as observed during test compared to NASGRO prediction.

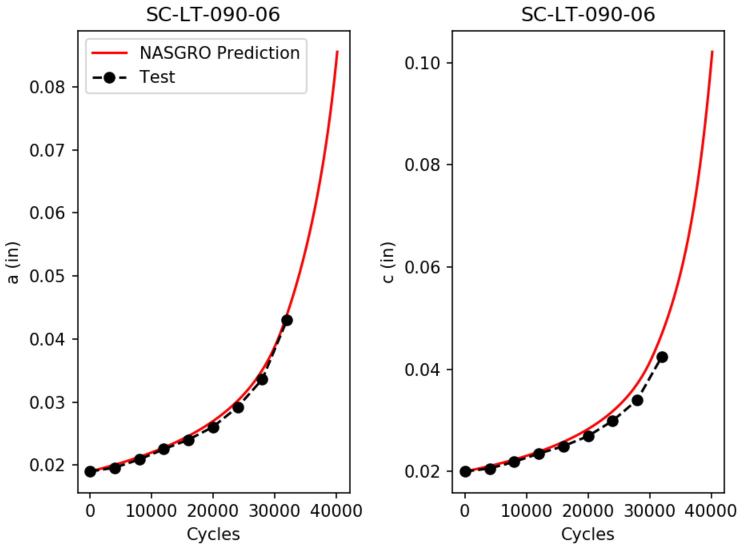

Figure B.32. a vs N and c vs N as observed during test compared to NASGRO prediction.

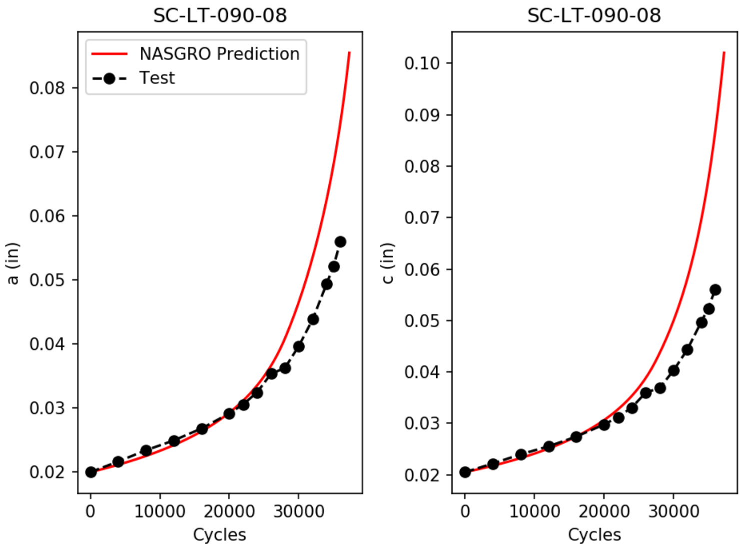

Figure B.33. a vs N and c vs N as observed during test compared to NASGRO prediction.

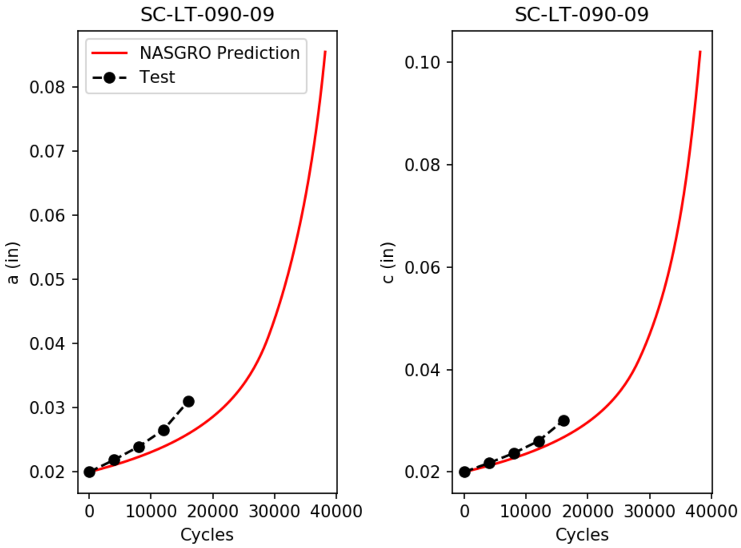

Figure B.34. a vs N and c vs N as observed during test compared to NASGRO prediction.

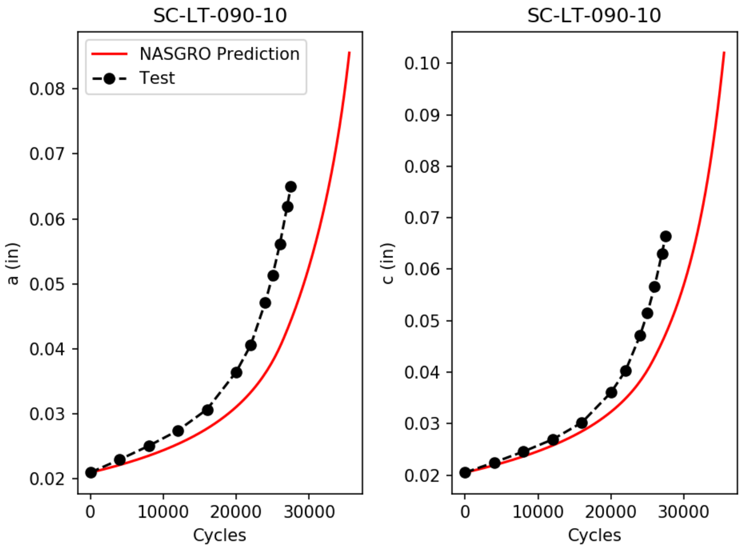

Figure B.35. a vs N and c vs N as observed during test compared to NASGRO prediction.

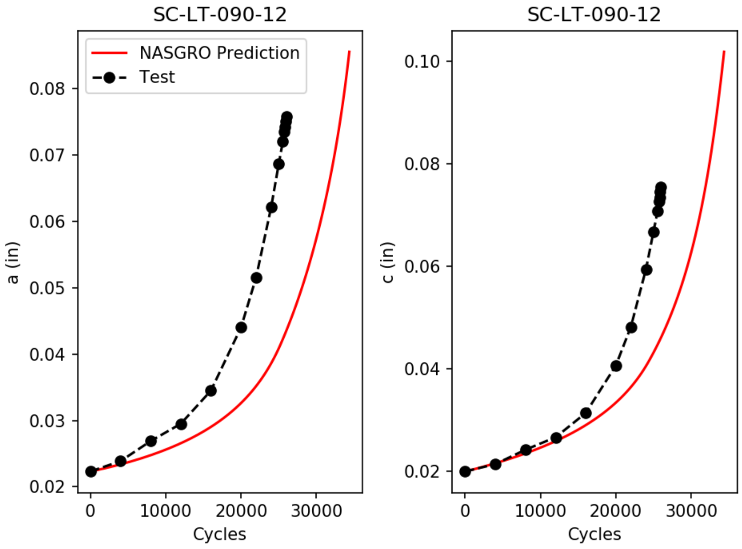

Figure B.36. a vs N and c vs N as observed during test compared to NASGRO prediction.

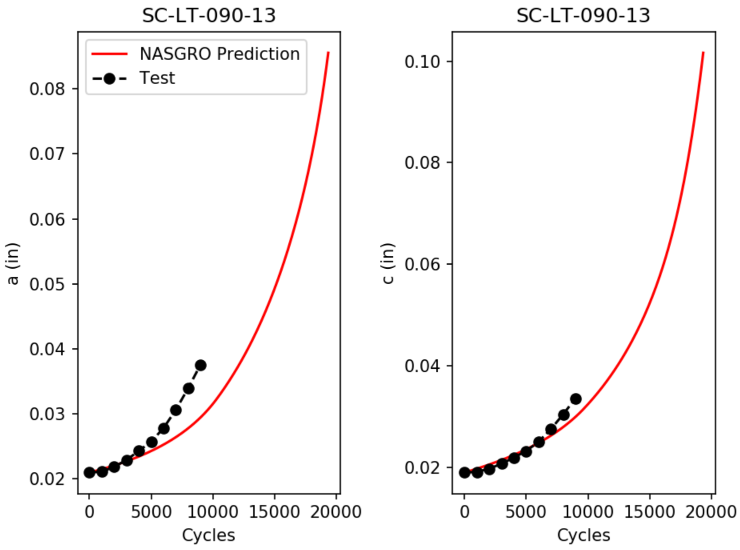

Figure B.37. a vs N and c vs N as observed during test compared to NASGRO prediction.

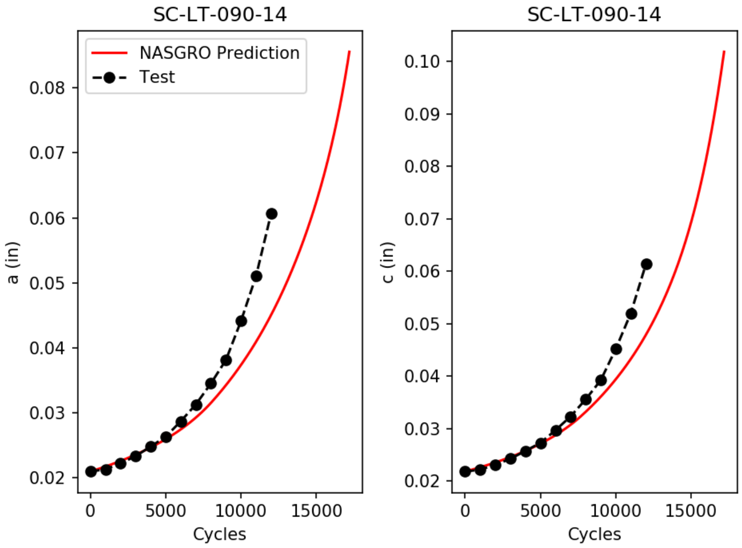

Figure B.38. a vs N and c vs N as observed during test compared to NASGRO prediction.

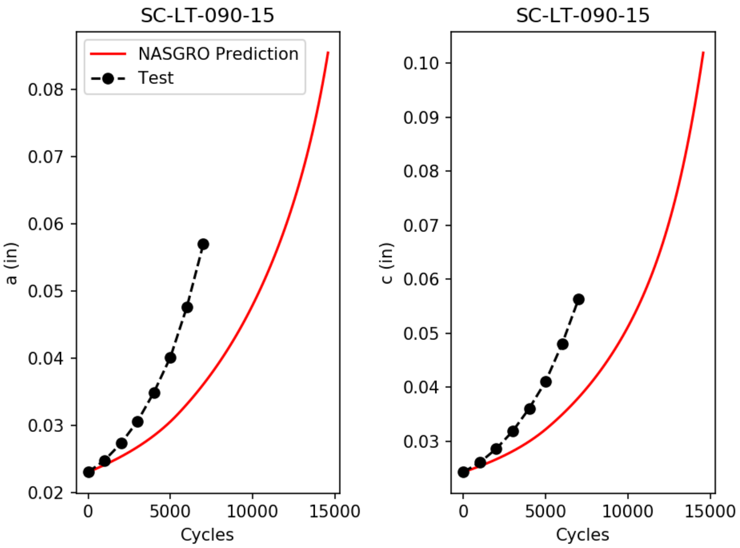

Figure B.39. a vs N and c vs N as observed during test compared to NASGRO prediction.

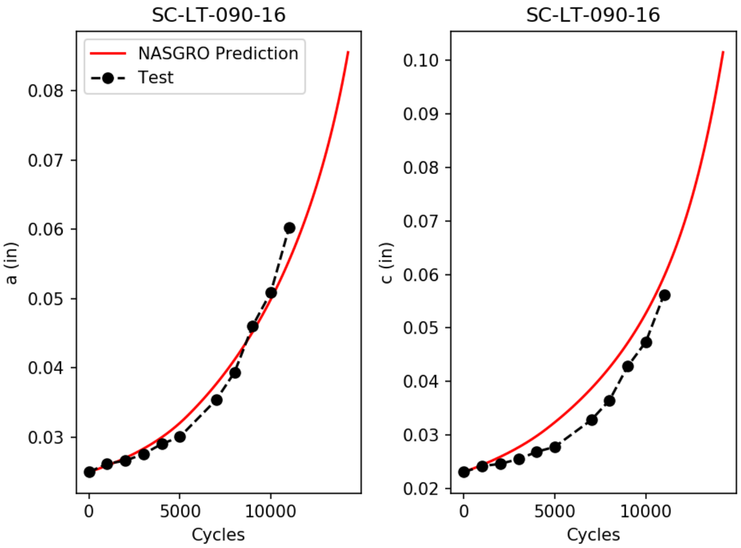

Figure B.40. a vs N and c vs N as observed during test compared to NASGRO prediction.

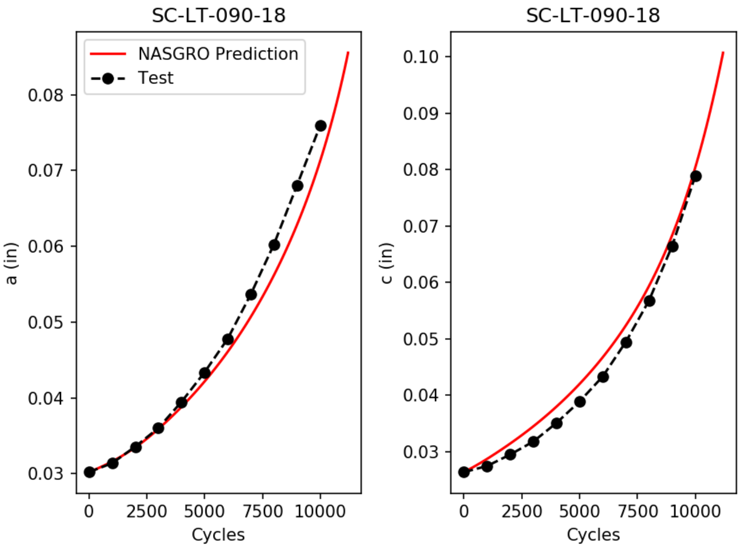

Figure B.41. a vs N and c vs N as observed during test compared to NASGRO prediction.

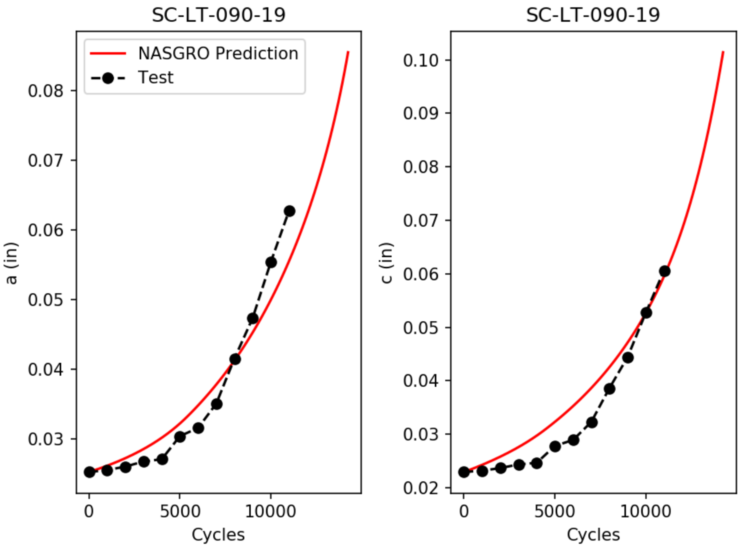

Figure B.42. a vs N and c vs N as observed during test compared to NASGRO prediction.

B.4 References

1. NASGRO, Fracture Mechanics and Fatigue Crack Growth Analysis Software, Reference Manual, v8.2, October 2017.
2. M. A. Sutton, J. J. Orteu, H. Schreier, “Image Correlation for Shape, Motion and Deformation Measurements: Basic Concepts, Theory and Applications,” Springer, 2009.
3. VIC3D, https://www.correlatedsolutions.com/vic-3d/

Appendix C. Surface Crack Finite Element Model Verification and Validation

C.1 Introduction

For COPV liners, a surface crack that breaks through the back wall of the structure represents failure of the component. These cracks will frequently exceed the limits of linear elastic fracture mechanics (LEFM) due to the combination of their thin wall thicknesses and high loads. A schematic of a typical elliptical surface crack and the dimensions of interest are shown in Figure C.1. The crack is defined as a half ellipse with dimensions *a*, the maximum depth, and *2c*, the total length on the surface. The angle describing positions along the crack front is ϕ. As the crack opens under load (σ for an applied stress or δ for an applied displacement), crack mouth opening displacement (CMOD) is measured as the distance between the upper and lower surface of the crack mouth. B is the wall thickness, W is the width of the plate, and L is the length of the plate. In practice, a COPV liner is equivalent to an infinite domain, but validation test coupons and the associated finite element models (FEM) have finite L and W dimensions.

To evaluate whether a surface crack has exceeded the limits of LEFM and calculate the adjusted failure threshold as outlined in Appendix F, a J-integral calculation must be completed that includes the effects of plasticity at all points along the crack front. Existing analytical solutions [1-4] for J vs ϕ have numerous shortcomings when it comes to the analysis of surface cracks as discussed in detail in [5]. Therefore, an EPFM analysis using a 3D FEM is used to obtain the necessary J vs ϕ results. This appendix is laid out as follows: first, a description of the FEM and associated analysis software is provided. This is followed by sections outlining the verification and validation of the modeling approach.

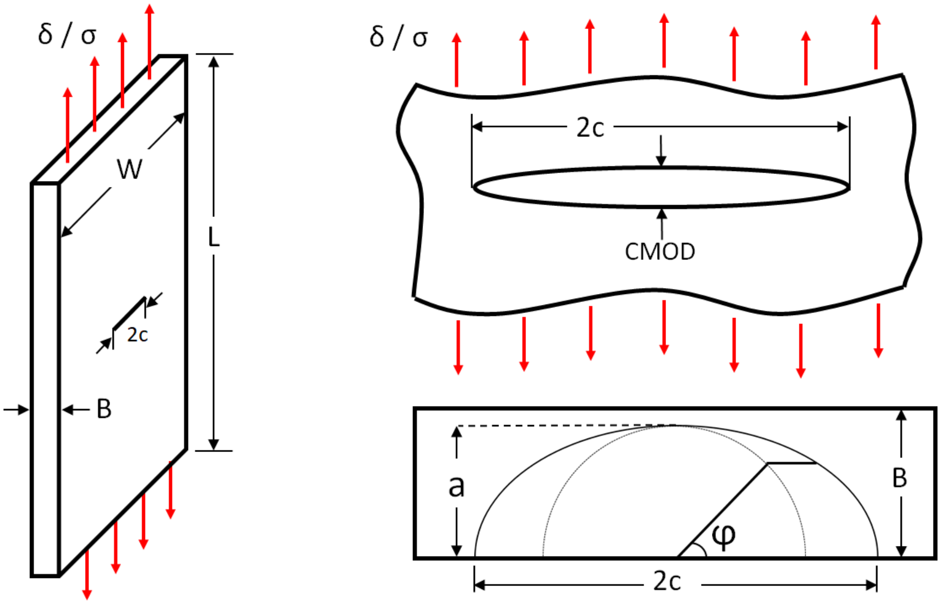

Figure C.1. Schematic of a surface crack in a flat plate and the associated dimensions to be used in the FEM.

C.2 Surface Crack FEM

C.2.1 Statement of Intended Usage

The surface crack FEM described here is used to calculate J-integrals along the crack front for surface cracks in elastically-responding thin-walled structures. It is intended to be used in conjunction with a LEFM crack growth analysis tool (e.g., NASGRO) to identify when the analysis has violated the underlying assumptions of LEFM and to provide a more conservative crack growth limit, based on EPFM, for the analysis in such a case, as compared to current practice. At this time, the model has been experimentally validated for AA6061-T6 in wall thickness ranging from 0.032 in to 0.090 inch.

C.2.2 Model Description

C.2.2.1 Software

The commercially-available software FEACrack [ref. 7] is used for mesh generation and post-processing while the finite element analysis (FEA) is performed by WARP3D [ref. 6]. Custom scripts were written in Python [ref. 8] to automate tasks including the generation of meshes, management of WARP3D simulations on NASA Langley Research Center's K3 midrange cluster, and post-processing of simulation data.

C.2.2.2 FEM

The surface crack FEM is a three-dimensional quarter-symmetry representation of a surface crack in a flat plate using 20-node reduced integration hex elements (WARP3D element type q3disop) [ref. 6]. An example mesh generated by FEACrack is shown in Figure C.2. The crack surface is highlighted in blue and crack dimensions a and c are labeled. CMOD is calculated by tracking the displacement, δ_z, of the corner of the crack face where the outer face of the plate meets the through-thickness symmetry plane and $CMOD = 2\delta_z$ to account for model symmetry. The J-integral is calculated numerically using the domain integral method implementation in WARP3D along each contour in the crack tube as shown in Figure C.3 [ref. 6]. Ten contours are used in this model and the convergence of J in the outer contours is show below in Section C.3.2. The size of the mesh around the crack front can be controlled by holding the size of the crack tube constant and changing the number of elements that it contains. Convergence of CMOD values based on number of elements in the crack tube is shown in Section C.3.2The inputs to the model are the crack depth, a, the crack half length, c, the wall thickness B, and the material properties representing the material of interest. The material properties required include elastic parameters Young's modulus, E, and Poisson's ratio, v, and a piecewise linear function describing the yield behavior of the material beginning at the yield stress, σ_{ys}. The material properties used to represent AA6061-T6 are shown in Table 1 and were obtained from tensile test data. The model is loaded by applying a displacement to the top surface until the far-field stress in the model is $\sigma = 0.95\sigma_{ys}$.

The model outputs consist of CMOD, which is primarily used for experimental validation, far-field stress, and J vs ϕ which is described in Section 7.1 and Appendix F.

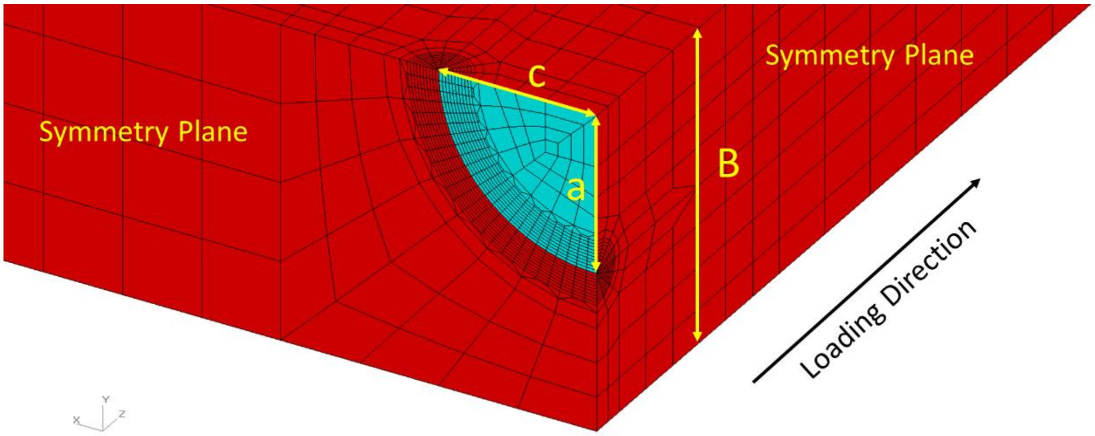

Figure C.2. Example surface crack mesh.

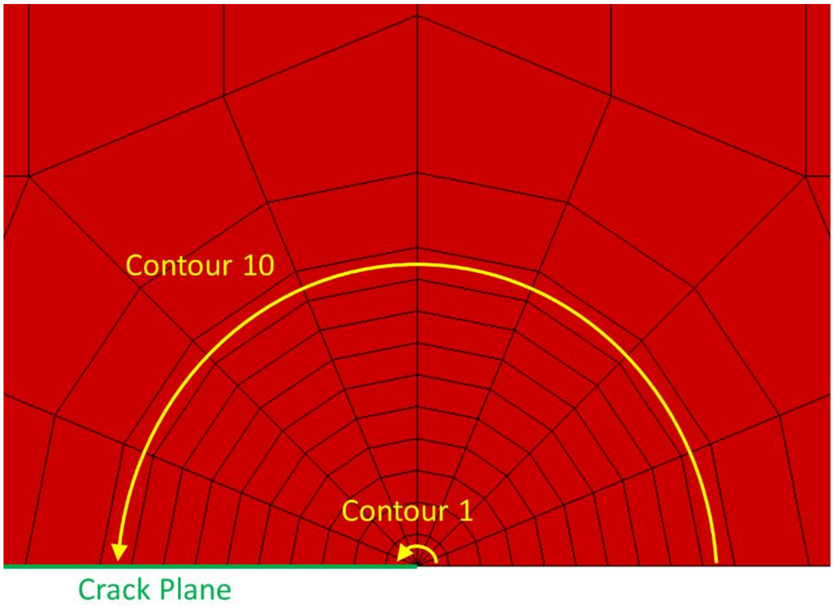

Figure C.3. Example crack tube with 10 contours for calculation of domain integrals.

Table C.1. Material Properties for AA6061

Property	Value
Young's Modulus, E (psi)	**10.103E+6**
Poisson's Ratio, ν	**0.3**
Total Strain	**Stress (psi)**
0.00439473	**44400.0**
0.0162079	**46500.0**
0.0283960	**48400.0**
0.0486533	**51000.0**
0.0738513	**53000.0**
0.0989997	**54500.0**
0.149197	**56500.0**
0.199346	**58000.0**

C.3 Verification

C.3.1 Code Verification

The finite element solver used in this study was WARP3D [ref. 6]. Pre-compiled binaries were used and simulations were run on two machines:

1. Laptop running Red Hat Linux 7.6 with an Intel Xeon(R) CPU E3-1535M v6 @ 3.10 GHz with 8 cores.
2. K3 Midrange Cluster at NASA Langley Research Center. Simulations were run on 1 Haswell node

To ensure that the code was operating properly, a suite of verification tests included with the WARP3D distribution were run. These tests consist of a set of analyses designed to exercise various parts of the code to calculate J-integrals under various loading conditions in varying cracked geometry configurations. Table C.2 shows the results of the verification tests for both the laptop and K3.

Table C.2. WARP3D Verification Test Results

Test ID	Reference Solution	Laptop Solution	Laptop Error	K3 Solution	K3 Error
A_1	0.025740	0.025740	0.00%	0.025740	0.00%
A_2	0.025740	0.025740	0.00%	0.025740	0.00%
A_3	0.026300	0.026300	0.00%	0.026300	0.00%
A_4	0.025740	0.025740	0.00%	0.025740	0.00%
B_1	0.025660	0.025660	0.00%	0.025660	0.00%
B_2	0.025450	0.025450	0.00%	0.025450	0.00%
B_3	0.026160	0.026160	0.00%	0.026160	0.00%
C_1	0.308100	0.308100	0.00%	0.308100	0.00%
C_2	0.306800	0.306800	0.00%	0.306800	0.00%
D_1	0.305500	0.305500	0.00%	0.305500	0.00%
D_2	0.296200	0.296200	0.00%	0.296200	0.00%
D_3	0.328400	0.328400	0.00%	0.328400	0.00%
F_1	0.021590	0.021590	0.00%	0.021590	0.00%
F_2	0.021590	0.021590	0.00%	0.021590	0.00%
F_3	0.021370	0.021370	0.00%	0.021370	0.00%
F_4	0.021590	0.021590	0.00%	0.021590	0.00%
G_1	0.427400	0.427400	0.00%	0.427400	0.00%
G_2	0.440100	0.440100	0.00%	0.440100	0.00%
H_1	0.106600	0.106600	0.00%	0.106600	0.00%
H_2	0.109200	0.109200	0.00%	0.109200	0.00%
H_3	0.099140	0.099140	0.00%	0.099140	0.00%
H_4	0.093520	0.093520	0.00%	0.093520	0.00%
I_1	0.001147	0.001147	0.00%	0.001147	0.00%
I_2	0.001133	0.001133	0.00%	0.001133	0.00%
I_3	0.083700	0.083700	0.00%	0.083700	0.00%
I_4	0.083670	0.083670	0.00%	0.083670	0.00%
I_5	0.081730	0.081730	0.00%	0.081730	0.00%
I_6	0.081700	0.081700	0.00%	0.081700	0.00%
J_1	0.439700	0.439700	0.00%	0.439700	0.00%
J_2	0.431500	0.431500	0.00%	0.431500	0.00%
J_3	0.429900	0.429900	0.00%	0.429900	0.00%
J_4	0.206800	0.196100	5.17%	0.196300	5.08%
K_1	0.516700	0.516700	0.00%	0.516700	0.00%
K_2	0.515500	0.515500	0.00%	0.515500	0.00%

Test ID	Reference Solution	Laptop Solution	Laptop Error	K3 Solution	K3 Error
K_3	0.513200	0.513200	0.00%	0.513200	0.00%
K_4	0.240400	0.240400	0.00%	0.236900	1.46%
L_1	0.642000	0.642000	0.00%	0.642000	0.00%
L_2	0.592500	0.592500	0.00%	0.592500	0.00%
L_3	0.667200	0.667200	0.00%	0.667200	0.00%
L_4	0.242700	0.242700	0.00%	0.242700	0.00%
M_1	0.504500	0.504500	0.00%	0.504500	0.00%
M_2	0.484000	0.484000	0.00%	0.484000	0.00%
M_3	0.507700	0.507700	0.00%	0.507700	0.00%
M_4	0.289600	0.289600	0.00%	0.289600	0.00%
N_1	0.458300	0.458300	0.00%	0.458300	0.00%
N_1	0.520900	0.520900	0.00%	0.520900	0.00%
N_1	0.505400	0.505400	0.00%	0.505400	0.00%
N_2	0.448900	0.448900	0.00%	0.448900	0.00%
N_2	0.463100	0.463100	0.00%	0.463100	0.00%
N_2	0.486900	0.486900	0.00%	0.486900	0.00%
N_3	0.461500	0.461500	0.00%	0.461500	0.00%
N_3	0.534900	0.534900	0.00%	0.534900	0.00%
N_3	0.522700	0.522700	0.00%	0.522700	0.00%
N_4	0.194300	0.194300	0.00%	0.194300	0.00%
N_4	0.229600	0.229600	0.00%	0.229600	0.00%
N_4	0.204000	0.204000	0.00%	0.204000	0.00%
O_1	0.005478	0.005478	0.00%	0.005478	0.00%
O_2	0.005093	0.005093	0.00%	0.005093	0.00%
O_3	0.431200	0.431200	0.00%	0.431200	0.00%
O_4	0.003038	0.003038	0.00%	0.003038	0.00%
P_1	0.003363	0.003363	0.00%	0.003363	0.00%
P_2	0.003353	0.003353	0.00%	0.003353	0.00%
P_3	0.000842	0.000842	0.00%	0.000842	0.00%
P_4	0.001270	0.001270	0.00%	0.001270	0.00%
P_5	0.000842	0.000842	0.00%	0.000842	0.00%
P_5a	0.001270	0.001270	0.00%	0.001270	0.00%
P_6	0.000840	0.000840	0.00%	0.000840	0.00%
P_6a	0.001268	0.001268	0.00%	0.001268	0.00%
P_7	0.000843	0.000843	0.00%	0.000843	0.00%
Q_1	0.015100	0.015100	0.00%	0.015100	0.00%
Q_1	1.104000	1.104000	0.00%	1.104000	0.00%
R_1	0.113300	0.113300	0.00%	0.113300	0.00%

Test suite E was omitted because it was designed to test a WARP3D run script using MPI that was not used during this study. The two tests that produced differences from the reference solutions are highlighted in Table C.1. Both tests involved the calculation of J-integrals in functionally graded materials, which is a capability not used in the current study. All other tests showed identical results between the reference solutions and solutions obtained on both the laptop and K3.

C.3.2 Model Verification

C.3.2.1 Model Dimensions

The critical dimensions to be incorporated in the model are the wall thickness, B, the crack depth, a, and the crack length on the surface, 2c, as shown in Figure C.1. The goal of this modeling work is to generate a lookup table or surrogate model that can be used in conjunction with a NASGRO analysis to provide insight to when the underlying assumptions of LEFM have been violated and to provide a conservative limit to the analysis. To that end, large numbers of FEM will be required. To facilitate this, Python scripts have been created to automate the creation, running, and post-processing of the FEA. The Python code employs unit tests to ensure that they operate properly (e.g., read the right values from WARP3D output files). Additionally, intermediate files generated by the process can be inspected to ensure the correct models are being generated. Figure C.4 shows an example of the workflow for model generation starting with a user generated model dimensions file in Figure C.4(a). The desired crack depth is highlighted by the red box, the crack length by the green box, and the wall thickness by the blue boC. Figure C.4(b) shows an example of a windows batch file that is generated with python from the model dimensions file. This batch script will automate the generation of a surface crack mesh and WARP3D input file in FEACrack. The relevant dimensions are highlighted again to demonstrate that they have been successfully transferred. In Figure C.4(c), the final WARP3D input file is inspected to demonstrate that the dimensions in the model match the user input. The “Crack Node Data” section show the values for a and c (the model is symmetric so only half of the crack is modeled, so the 2c dimension has been reduced to c). In the model coordinate system, the cracked surface is on the y = 0 plane and the back-surface falls on the y = -B plane where B is the wall thickness. The wall thickness can therefore be verified by inspection of the nodal coordinates in the ligament. The final node in the ligament falls on the back surface and is shown to be at coordinate (0.0, -0.032, 0.0) which corresponds to the desired wall thickness of 0.032 inch.

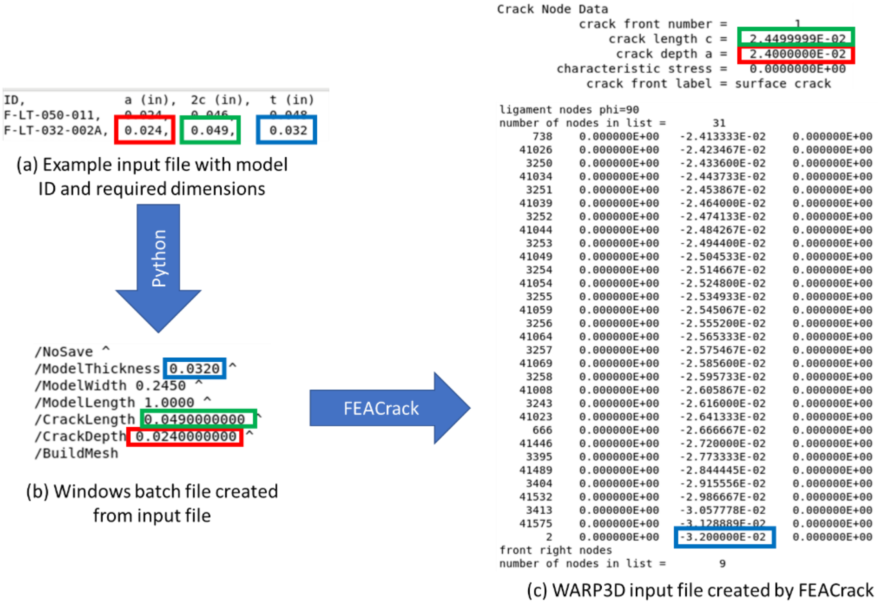

```
ID,               a (in),  2c (in),   t (in)
F-LT-050-011,     0.024,   0.046,     0.048
F-LT-032-002A,    0.024,   0.049,     0.032
```

(a) Example input file with model ID and required dimensions

```
/NoSave ^
/ModelThickness 0.0320 ^
/ModelWidth 0.2450 ^
/ModelLength 1.0000 ^
/CrackLength 0.0490000000 ^
/CrackDepth 0.0240000000 ^
/BuildMesh
```

(b) Windows batch file created from input file

```
Crack Node Data
           crack front number =          1
               crack length c =  2.4499999E-02
                crack depth a =  2.4000000E-02
        characteristic stress =  0.0000000E+00
            crack front label = surface crack

ligament nodes phi=90
number of nodes in list =       31
     738    0.000000E+00   -2.413333E-02    0.000000E+00
   41026    0.000000E+00   -2.423467E-02    0.000000E+00
    3250    0.000000E+00   -2.433600E-02    0.000000E+00
   41034    0.000000E+00   -2.443733E-02    0.000000E+00
    3251    0.000000E+00   -2.453867E-02    0.000000E+00
   41039    0.000000E+00   -2.464000E-02    0.000000E+00
    3252    0.000000E+00   -2.474133E-02    0.000000E+00
   41044    0.000000E+00   -2.484267E-02    0.000000E+00
    3253    0.000000E+00   -2.494400E-02    0.000000E+00
   41049    0.000000E+00   -2.504533E-02    0.000000E+00
    3254    0.000000E+00   -2.514667E-02    0.000000E+00
   41054    0.000000E+00   -2.524800E-02    0.000000E+00
    3255    0.000000E+00   -2.534933E-02    0.000000E+00
   41059    0.000000E+00   -2.545067E-02    0.000000E+00
    3256    0.000000E+00   -2.555200E-02    0.000000E+00
   41064    0.000000E+00   -2.565333E-02    0.000000E+00
    3257    0.000000E+00   -2.575467E-02    0.000000E+00
   41069    0.000000E+00   -2.585600E-02    0.000000E+00
    3258    0.000000E+00   -2.595733E-02    0.000000E+00
   41008    0.000000E+00   -2.605867E-02    0.000000E+00
    3243    0.000000E+00   -2.616000E-02    0.000000E+00
   41023    0.000000E+00   -2.641333E-02    0.000000E+00
     666    0.000000E+00   -2.666667E-02    0.000000E+00
   41446    0.000000E+00   -2.720000E-02    0.000000E+00
    3395    0.000000E+00   -2.773333E-02    0.000000E+00
   41489    0.000000E+00   -2.844445E-02    0.000000E+00
    3404    0.000000E+00   -2.915556E-02    0.000000E+00
   41532    0.000000E+00   -2.986667E-02    0.000000E+00
    3413    0.000000E+00   -3.057778E-02    0.000000E+00
   41575    0.000000E+00   -3.128889E-02    0.000000E+00
       2    0.000000E+00   -3.200000E-02    0.000000E+00
front right nodes
number of nodes in list =        9
```

(c) WARP3D input file created by FEACrack

Figure C.4. (a) Example of model dimensions file, (b) Example windows batch file created by python scripts that process model dimension file, and (c) Example WARP3D input file created by FEA crack.

C.3.2.2 Mesh Convergence

The model outputs of interest are the crack mouth opening displacement (CMOD) and J vs ϕ. CMOD will be used for experimental validation of the model while J vs ϕ is required for the calculation of the LEFM limits as described in Section 7.1 and Appendix F. The mesh around the crack front can be refined by holding the size of the crack tube (as shown in Figures C.2 and C.3) constant while increasing the number of contour rings. Figure C.5 shows CMOD results vs number of contour rings for a surface crack model with a/B = 0.5 and a/c = 1.0. The model was run with varying numbers of contours ranging from 1 to 20. Each model was loaded with a displacement boundary condition until the far-field stress reached 95% of yield. CMOD measurements were made at 25 equally spaced stress intervals and are normalized by the value obtained from the simulation with 20 contours such that all load steps can be compared. With only 1 contour ring the CMOD values for all load steps fall within 2% of the value with 20 contour rings. At 10 contour intervals, the CMOD values have converged to < 1%.

Similarly, J vs ϕ can be compared across the models with differing numbers of contours. Figure C.6 shows J vs ϕ for all models at the most severe loading condition of $\sigma/\sigma_{ys} = 0.95$. Values of J converge to < 1% with 4 contour rings and to < 0.2% with 10 contour rings. In addition to checking for convergence of J across models with differing numbers of contour rings, J must also converge across contours. To check this convergence, FEACrack calculates a path dependence index at each ϕ for every load step in an analysis,

$$d_p = \frac{J_{max} - J_{min}}{2 * J_{avg}}$$

Where d_p is the path dependence index, and J_{max}, J_{min} and J_{avg} are the maximum, minimum, and average values, respectively, of J calculated across all contours, excluding the first one. J values with a path dependence < 0.05 are considered to be converged [ref. 7]. Figure C.7 shows the maximum path dependence taken along the crack front for a series of surface cracks, modeled with 10 contour rings, with crack depths ranging from a/B = 0.6 to a/B = 0.9, across a variety of loading conditions up to $\sigma/\sigma_{ys} = 0.95$. All of the J calculations show convergence over 10 contour rings.

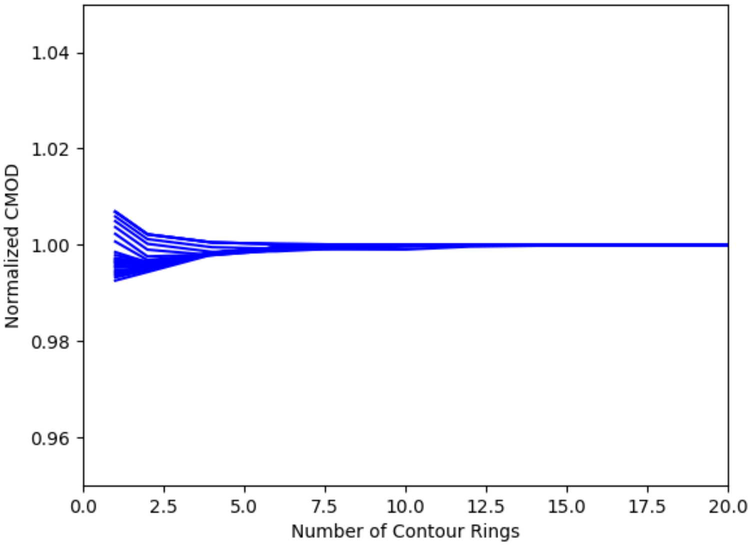

Figure C.5. Convergence of CMOD as a function of the number of contour rings around the crack front.

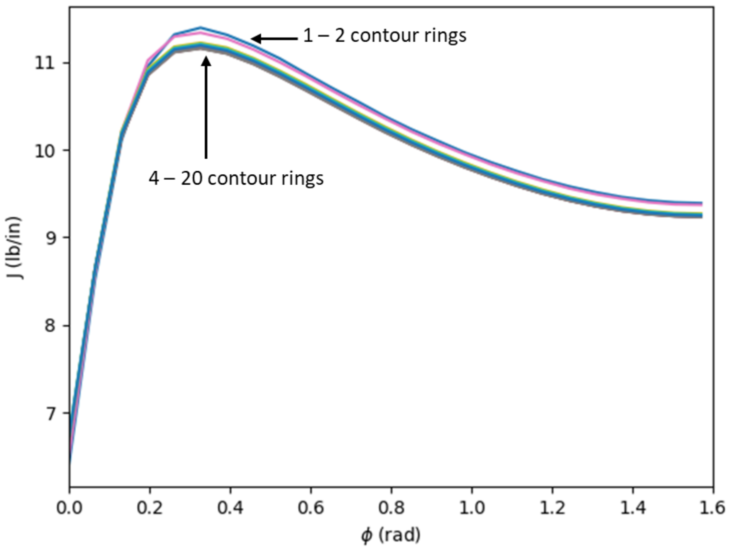

Figure C.6. J vs ϕ for $\sigma/\sigma_{ys} = 0.95$ for models with 1-20 contour rings.

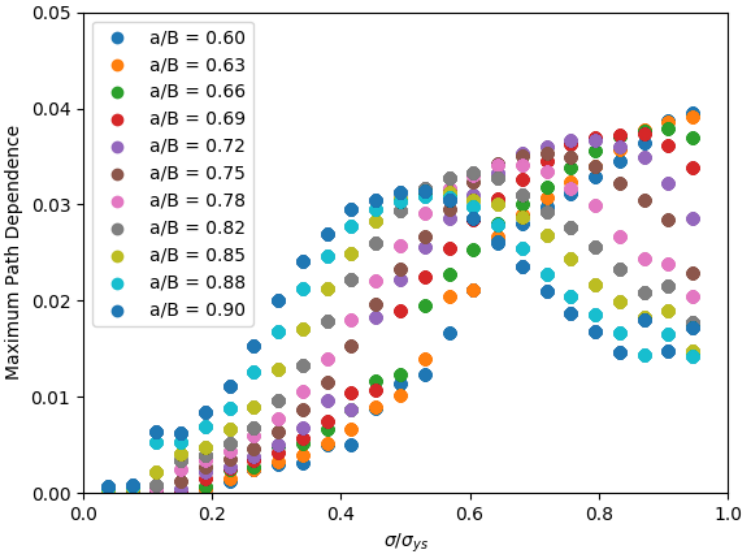

Figure C.7. Maximum path dependence of the J-integral calculation for various crack depths and loading conditions.

C.3.2.3 Effect of Finite Width

To study the effect of a finite width in the surface crack FEM, a surface crack simulated with a series of models with widths varying from 2 to 10 times the value of 2c. A reference solution was generated with a width of 1 inch to match the width of the specimens used in the experimental validation study (see Section C.4). Figure C.8 shows CMOD for a series of load levels up to $\sigma/\sigma_{ys} = 0.95$. At each load, the CMOD is normalized by the reference solution. CMOD converged to <1% at a width of 9 times 2c for all load levels. Figure C.9 shows the convergence of J vs ϕ at the most severe loading case where the far-field stress, $\sigma/\sigma_{ys} = 0.95$. Similarly to CMOD, J converges to <1% when N = 9.

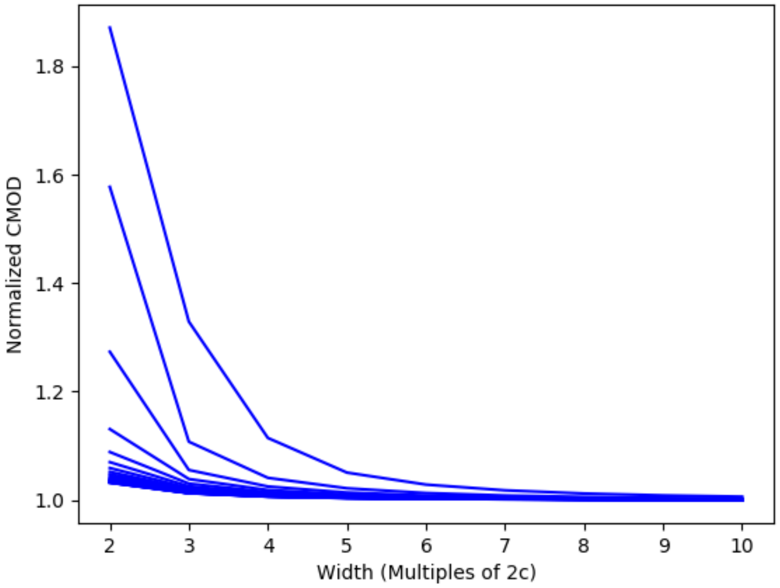

Figure C.8. CMOD for varying loads normalized by a reference solution with W = 1 in vs model width of $W = N * 2c\ for\ N = 2..10$.

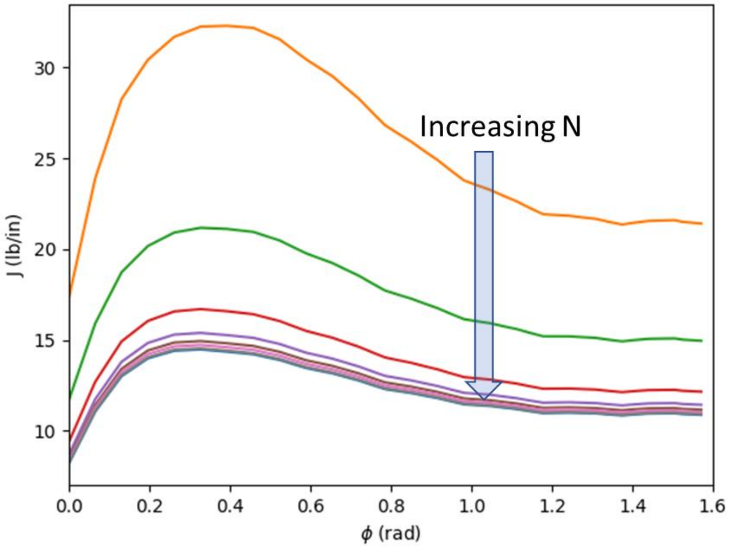

Figure C.9. J vs ϕ with far field stress $\sigma/\sigma_{ys} = 0.95$ for models with varying widths defined by $W = N * 2c\ for\ N = 2..10$.

C.4 Model Validation

C.4.1 Validation of J-integral Calculations

To validate the J-integral calculations, J values for ϕ = 90° with a far-field stress of approximately 15 ksi were compared to NASGRO K_a calculations for all of the cracks in the experimental validation set. At this low load, the effects of plasticity are low and the conversion of elastic-plastic J to mode I elastic K should hold.

$$K_I = \sqrt{\frac{JE}{(1-\nu^2)}}$$

The NASGRO values of $K_a = K_{I_{\phi=90°}}$ were calculated using crack case SC30 [ref. 9]. The results of the comparison are shown in Table C-3. The majority of cases had errors of <1% as compared to NASGRO calculations. A few cases with deep cracks where crack-tip plasticity is more severe even at a relatively low load had errors <3%. Overall, these results show excellent agreement between LEFM values of K_I and the elastic-plastic J to K_I conversion.

Table C.3. Comparison Between KI Calculated from Elastic-plastic J and NASGRO SC30

Test ID	**FEM J (lb/in)**	**J to K_I $(psi\sqrt{in})$**	**$K_a(psi\sqrt{in})$**	**% Error**
FL-LT-032-11L	1.022919	3369.963	3422.561	1.54%
FL-LT-032-11S	0.708791	2805.198	2804.883	-0.01%
FL-LT-032-20L	1.143395	3562.892	3602.822	1.11%
FL-LT-032-20S	0.78281	2948.034	2941.007	-0.24%
FL-LT-050-02S	1.132027	3545.136	3529.955	-0.43%
FL-LT-050-03L	1.468659	4037.987	4097.828	1.46%
FL-LT-050-03S	0.689944	2767.651	2760.936	-0.24%
FL-LT-050-04L	1.20106	3651.631	3648.397	-0.09%
FL-LT-050-04S	0.661962	2710.947	2700.084	-0.40%
FL-LT-050-07L	1.565742	4169.314	4291.761	2.85%
FL-LT-050-07S	0.925682	3205.793	3199.993	-0.18%
FL-LT-050-12L	1.488548	4065.237	4156.82	2.20%
FL-LT-050-12S	0.92377	3202.48	3166.83	-1.13%
FL-LT-050-13L	1.267231	3750.873	3755.076	0.11%
FL-LT-050-13S	0.633281	2651.568	2639.415	-0.46%
FL-LT-050-16S	0.878782	3123.525	3124.597	0.03%
FL-TL-032-06L	0.702463	2792.647	2790.221	-0.09%
FL-TL-032-06S	0.647092	2680.326	2684.355	0.15%
FL-TL-032-08S	0.677548	2742.676	2728.983	-0.50%
FL-TL-032-09L	0.733114	2852.925	2850.889	-0.07%
FL-TL-032-09S	0.676677	2740.913	2744.885	0.14%
FL-TL-032-10S	0.678153	2743.9	2744.206	0.01%
FL-TL-032-15S	0.649178	2684.642	2683.666	-0.04%
FL-TL-032-17L	1.061322	3432.638	3527.147	2.68%
FL-TL-032-17S	0.692332	2772.436	2759.227	-0.48%
FL-TL-050-01S	0.986103	3308.762	3288.792	-0.61%
FL-TL-050-03S	0.865778	3100.33	3093.436	-0.22%
FL-TL-050-10L	1.22415	3686.564	3678.132	-0.23%
FL-TL-050-10S	0.648653	2683.556	2684.575	0.04%
FL-TL-050-12L	1.295808	3792.93	3799.691	0.18%

Test ID	FEM J (lb/in)	J to $K_I\ (psi\sqrt{in})$	$K_a(psi\sqrt{in})$	% Error
FL-TL-050-12S	0.695127	2778.027	2760.073	-0.65%
FL-TL-050-17S	0.760714	2906.131	2896.49	-0.33%
FL-TL-090-19L	2.826297	5601.617	5734.885	2.32%
FL-TL-090-19S	0.603172	2587.766	2595.161	0.28%
SC-LT-032-01L	0.856204	3083.138	3090.291	0.23%
SC-LT-032-01S	0.634197	2653.484	2637.534	-0.60%
SC-LT-032-02L	1.017067	3360.309	3436.41	2.21%
SC-LT-032-02S	0.696113	2779.998	2758.147	-0.79%
SC-LT-090-04L	1.542579	4138.359	4121.563	-0.41%
SC-LT-090-04S	0.593402	2566.723	2564.62	-0.08%
SC-LT-090-06S	0.593585	2567.119	2564.746	-0.09%
SC-LT-090-08L	1.800273	4470.681	4449.986	-0.47%
SC-LT-090-08S	0.609588	2601.492	2610.393	0.34%
SC-LT-090-09L	0.91782	3192.15	3187.49	-0.15%
SC-LT-090-09S	0.593402	2566.723	2564.62	-0.08%
SC-LT-090-10L	2.148864	4884.374	4879.614	-0.10%
SC-LT-090-10S	0.608154	2598.432	2594.999	-0.13%
SC-LT-090-12L	2.410464	5173.147	5243.123	1.33%
SC-LT-090-12S	0.586366	2551.46	2549.075	-0.09%
SC-LT-090-13L	1.029188	3380.273	3368.191	-0.36%
SC-LT-090-13S	0.55393	2479.887	2488.236	0.34%
SC-LT-090-14L	1.980653	4689.307	4672.828	-0.35%
SC-LT-090-14S	0.650642	2687.668	2686.517	-0.04%
SC-LT-090-18S	0.78666	2955.276	2944.025	-0.38%

C.4.2 Experimental Validation of CMOD

CMOD calculated from the elastic-plastic FEM was validated experimentally by comparing to CMOD calculated using digital image correlation (DIC) during testing of surface-cracked specimens under tension. A full description of the test procedures can be found in Appendix B. Two types of tests were conducted. In the first, AA6061-T6 specimens with dimensions W = 2.0 inch, L = 4.0 inch, B = 0.032 inch, 0.050 inch, and 0.09 inch were fatigue precracked to an approximate crack size of a = 0.02 in and 2c = 0.04 in and then tested under cyclic loading. CMOD measurements were made at peak load as the crack grew. The precrack was marked with Sharpie® pen for post-test analysis. The cracks were grown to varying depths and then fractured. The cracks defined by the marked precrack and the final fatigue crack surface were modeled to compare simulated CMOD with experimentally measured CMOD.

The second set of tests were designed to mimic the autofrettage process. After precracking, these specimens were then loaded in displacement control until the far-field strain matched the prescribed autofrettage strain. CMOD was measured with DIC continuously. The CMOD results during the portion of the test where the far-field strain remained elastic was compared to FEM results.

Figure C.10 shows a typical result from a crack growth test under cyclic loading. The observed CMOD is offset from the model due to the build-up of plastic strain around the crack tip. This shift can be seen in the experimental data when looking at CMOD for all loading cycles as shown in Figure C.11. The test is stopped every 4000 cycles to take DIC measurements over 2 cycles. The corresponding cycle count is shown over DIC cycle. The DIC data shown in Figure

C.10 corresponds to the last ramp from minimum to load to maximum load as highlighted in green in Figure C.11. Introducing a test-equivalent load cycle into the FEA reproduces this effect as shown in Figure C.12. The load/unload/load sequence is marked by numbered arrows. After 1 cycle, the CMOD in the model is in excellent agreement with the test data on the subsequent loading. Similar results are observed for the elastic portion of the autofrettage tests as shown in Figure C.13. In this case, there is no cyclic loading after the DIC reference image is taken, so there is no offset in the data vs model results. Again, the FEA CMOD results are in close agreement with the measured CMOD during test.

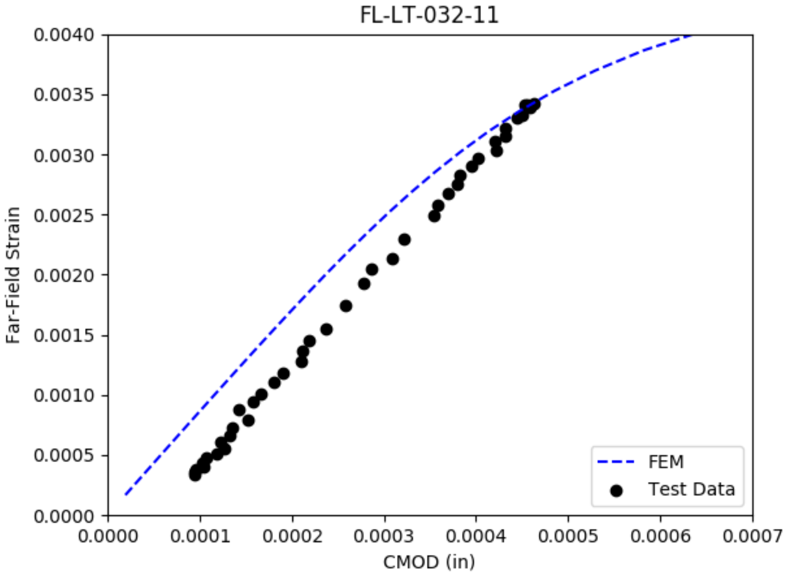

Figure C.10. Typical results for far-field strain vs CMOD comparing DIC measurements to elastic-plastic FEM results.

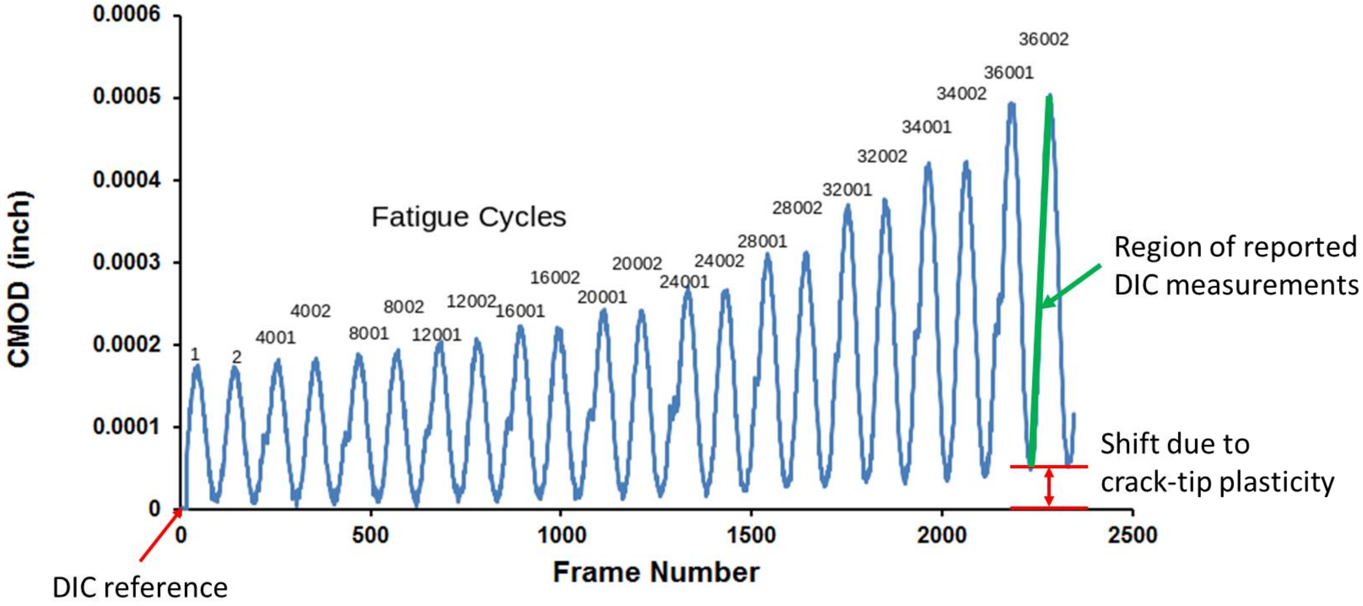

Figure C.11. CMOD vs DIC frame number showing the shift in CMOD as plastic strain accumulates around the crack-tip.

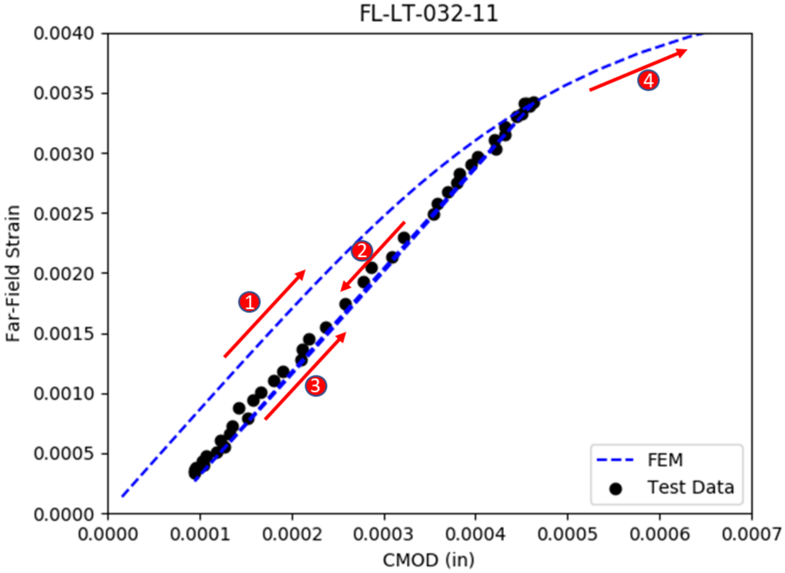

Figure C.12. Far-field strain vs CMOD comparing DIC measurements to elastic-plastic FEM results including the effects of cyclic loading.

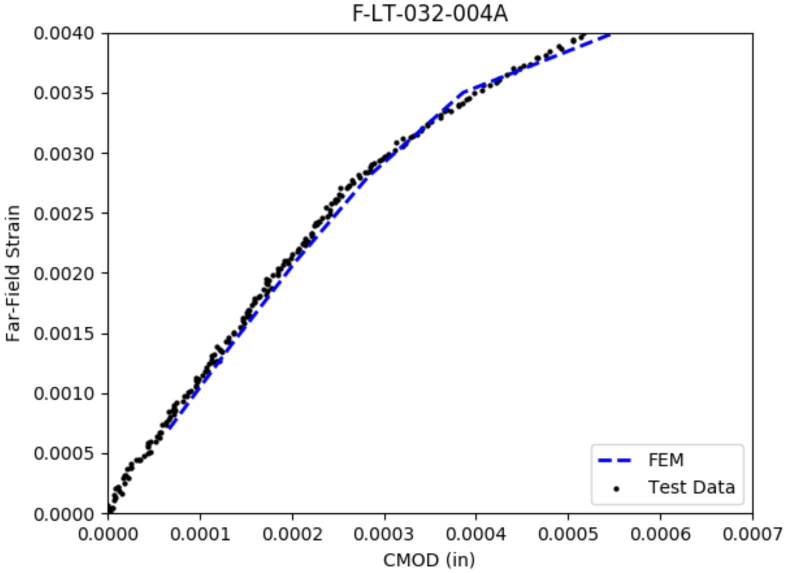

Figure C.13. Example far-field strain vs CMOD comparison between elastic portion of autofrettage test and FEM.

The ultimate purpose of the FEM is to calculate the J-integral at the angle of growth initiation ϕ_{init} as outlined in Section 7.1.2 and Appendix F. Therefore, it is important to understand how errors in CMOD affect J. A set of models were created with a/B = 0.3, 0.5, and 0.8 and a nominal a/c = 1.0. Then, to simulate errors, each nominal crack size was perturbed by ±0.001, ±0.002, and ±0.005 inch. This was done by changing a while holding c constant, changing c while holding a constant, and changing a and c together. It was found that both J and CMOD were most sensitive to changes in crack depth, a. Therefore, all errors in CMOD are assumed to be a result of errors in the crack depth measurement, representing the worst-case errors.

From these simulations, a relationship between errors in J as a function of errors in CMOD can be found for varying crack depths as shown in Figure C.14. This relationship is then used to plot bounds for J error <5% and J error <10% as a function of CMOD error and a/B as shown in Figure C.15. The black dots represent the difference in CMOD between test data and FEM results. Most of the models fall within the J error <10% bounds and many of the models above a/B = 0.6 fall within the J error <5% bounds. One reason for the higher error in the smaller cracks was due to bleeding of the Sharpie® pen during testing. Steps were taken to ensure the Sharpie® pen used to mark the precrack was dry, but it is possible that solvent made its way into the crack while the surface of the specimen was being cleaned as preparation for DIC. As the crack advanced, the re-wetted Sharpie® pen could seep onto the newly exposed crack surfaces, causing post-test measurements to indicate a longer crack. Removal of all model runs based on measurements of Sharpie® penned cracks leads to results as shown in Figure C.16. The majority of data points now fall into the region where error in J <5% and no models would indicate an error in J >10%.

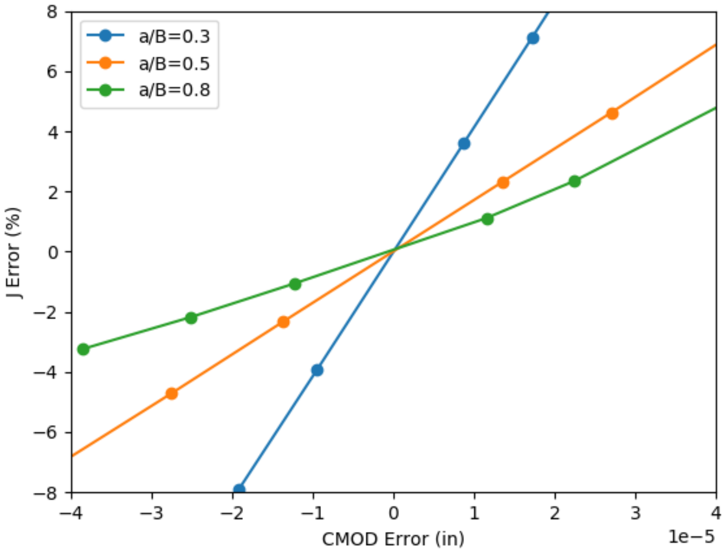

Figure C.14. % Error in J-integral as a function of absolute error caused by errors in crack depth, a.

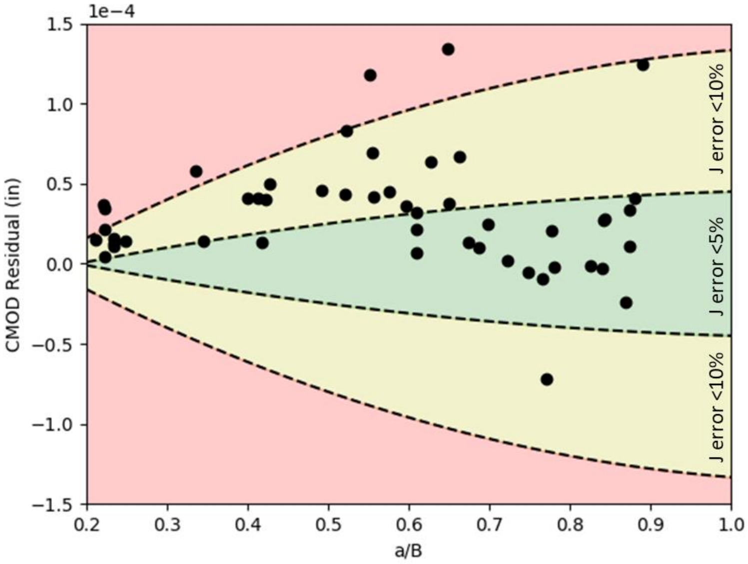

Figure C.15. Expected % error in J based as a function of errors in CMOD at varying a/B.

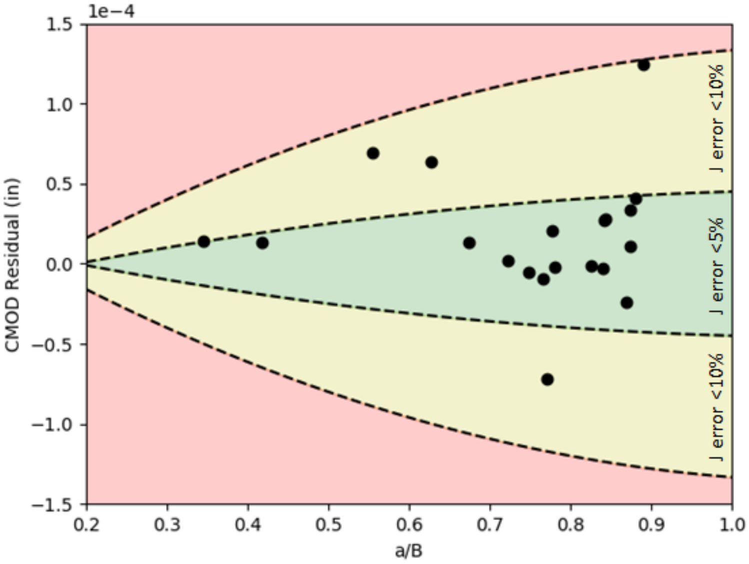

Figure C.16. Expected % error in J based as a function of errors in CMOD at varying a/B with all models based on measurements of cracks marked with Sharpie® pen ink removed.

C.5 References

1. Kumar, V.; German, M.D.; and Shih, C.F.: An Engineering Approach for Elastic-Plastic Fracture Analysis, Tech. Rep. NP-1931, Electric Power Research Institute, Schenectady, NY, July 1981.
2. Kumar, V.; German, M.D.; Wilkening, W.W.; et al.: Advances in Elastic-Plastic Fracture Analysis, Tech. Rep. NP-3607, Electric Power Research Institute, Schenectady, NY, August 1984.

3. Kumar, V.; and German, M.D.: Elastic-Plastic Fracture Analysis of Through-Wall and Surface Flaws in Cylinders, Tech. Rep. NP-5596, Electric Power Research Institute, Schenectady, NY, January 1988.
4. Ainsworth, R.A.: “The assessment of defects in structures of strain hardening material,” Engineering Fracture Mechanics, Vol. 19, No. 4, pp. 633–642, 1984.
5. Allen, P.A.; and Wells D.N.: “Elastic-Plastic J-Integral Solutions for Surface Cracks in Tension Using an Interpolation Methodology,” NASA/TP-2013-217480, Marshall Space Flight Center, Huntsville, Alabama, 2013.
6. WARP3D, Static and Dynamic Nonlinear Analysis of Fracture in Solids, Dodds, R.H., University of Illinois at Urbana-Champaign, http://www.warp3d.net/
7. FEACrack, Quest Integrity Group, https://www.questintegrity.com/software-products/feacrack
8. Python, https://www.python.org
9. NASGRO, Fracture Mechanics and Fatigue Crack Growth Analysis Software, Reference Manual, v9.0, May 2018.

Appendix D. Tensile Testing

D.1 Overview

Tensile tests were conducted on AA6061-T6, IN718, and Ti 6Al-4V sheet material of varying thickness and Ti 6Al-4V tank material. The dimensions of the typical tensile coupon are shown in Figure D-1. DIC was used to monitor strain using a virtual extensometer. Global strains used an extensometer length of 3 inches and local strains around the tensile failure were measured with an extensometer length of 0.4 inches.

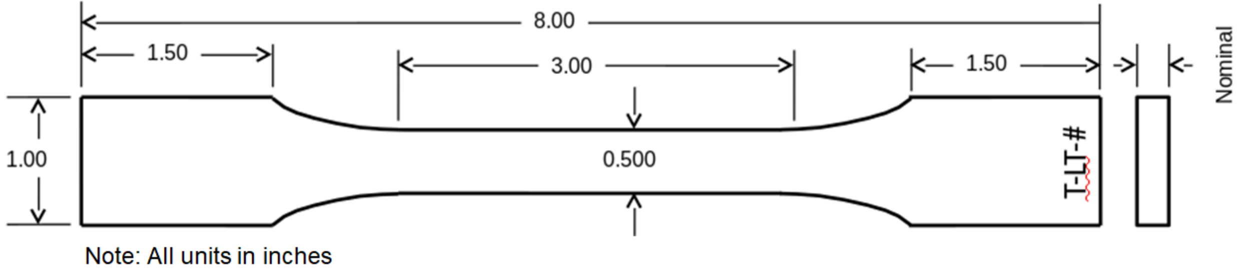

Figure D-1. Typical tensile coupon configuration.

D.2 Al6061 Tensile Data

Tensile data for Al6061 is shown in Figure D-2. Calculated elastic modulus, yield strength and ultimate tensile strength are shown in Table D-1.

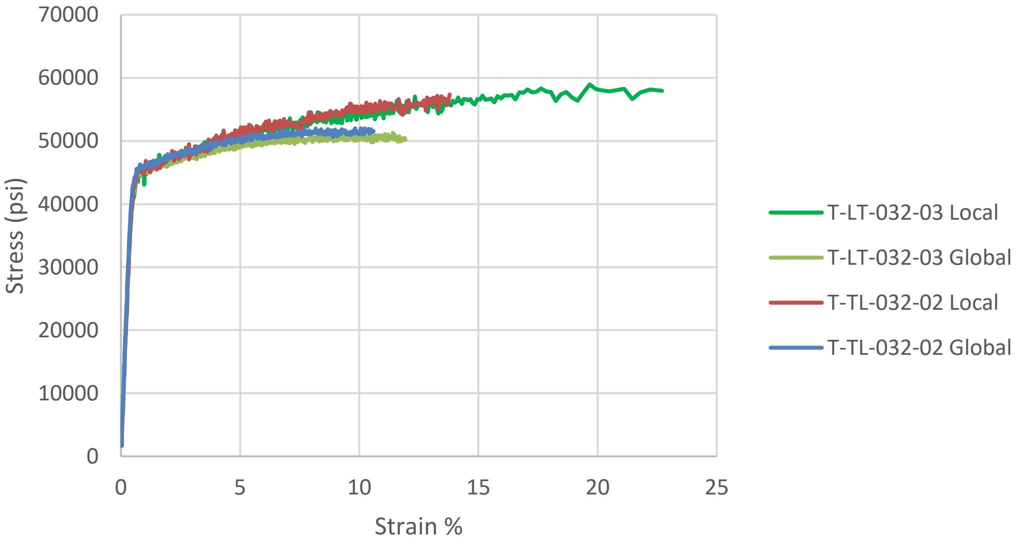

Figure D-2. AA6061-T6 sheet tensile data.

Table D.1. AA6061-T6 Tensile Data Summary

ID	Thickness (inch)	Width (inch)	E (psi)	σ_{ys} (psi)	σ_{ult} (psi)
T-TL-032-02	0.0320	0.4960	10,173,000	44,800	52,002
T-LT-032-03	0.0320	0.4970	10,033,000	44,000	51,287
Average Sheet	**0.0320**	**0.4965**	**10,103,000**	**136,848**	**51,644**

D.3 Ti 6Al-4V Tensile Data

Tensile data for Ti 6Al-4V sheet are shown in Figure D-3. The figure shows tensile results for coupons extracted from a Ti 6Al-4V dome. Calculated elastic modulus, yield strength and ultimate tensile strength are shown in Table D-2 for both sheet and tank material.

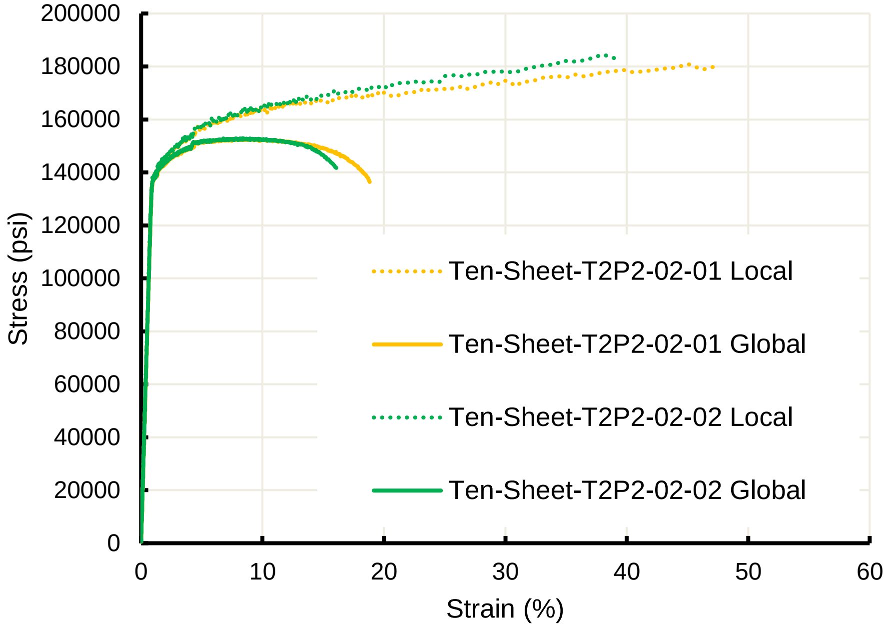

Figure D-3. Ti 6Al-4V sheet tensile data.

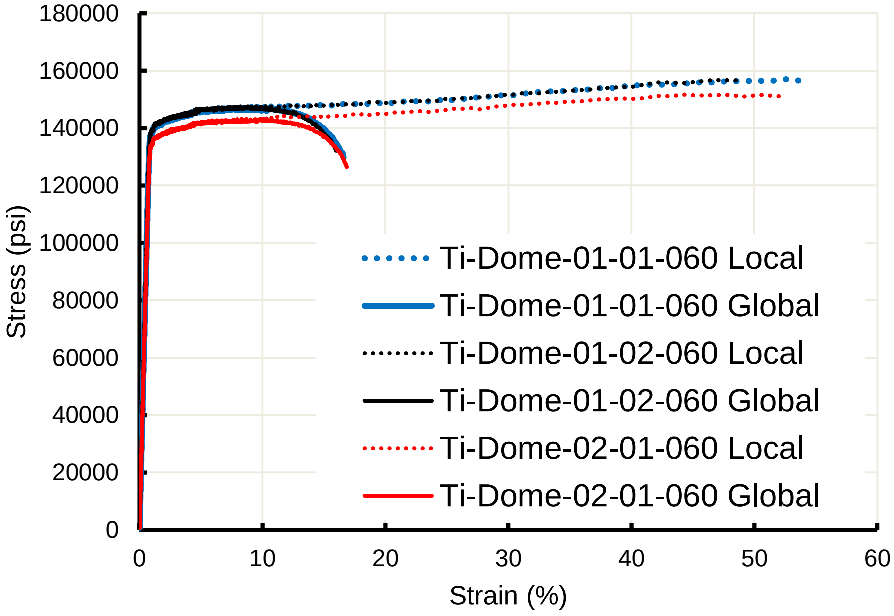

Figure D-4. Ti 6Al-4V dome tensile data.

Table D.2. Ti 6Al-4V Tensile Data Summary

ID	Thickness (inch)	Width (inch)	E (psi)	σ_{ys} (psi)	σ_{ult} (psi)
Ti-Dome-01-01-060	0.0590	0.5000	17,153,230	137,650	147,104
Ti-Dome-01-02-060	0.0595	0.5010	17,211,496	138,787	147,502
Ti-Dome-02-01-060	0.0600	0.4995	16,593,116	134,108	143,096
Average Dome	**0.0595**	**0.5002**	**16,985,947**	**136,848**	**145,900**
Ten-Sheet-T2P2-02-01	0.0835	0.5000	15,945,792	137,535	152,652
Ten-Sheet-T2P2-02-02	0.0835	0.5000	15,912,529	137,993	152,919
Average Sheet	**0.0835**	**0.5000**	**15,929,161**	**137,764**	**152,786**

D.4 IN718 Tensile Data

Figures D.5, D.6, and D.7 show tensile response for IN718 sheet of thickness 0.03”, 0.05”, and 0.09”, respectively. Calculated elastic modulus, yield strength and ultimate tensile strength for all three thicknesses are shown in Table D-3.

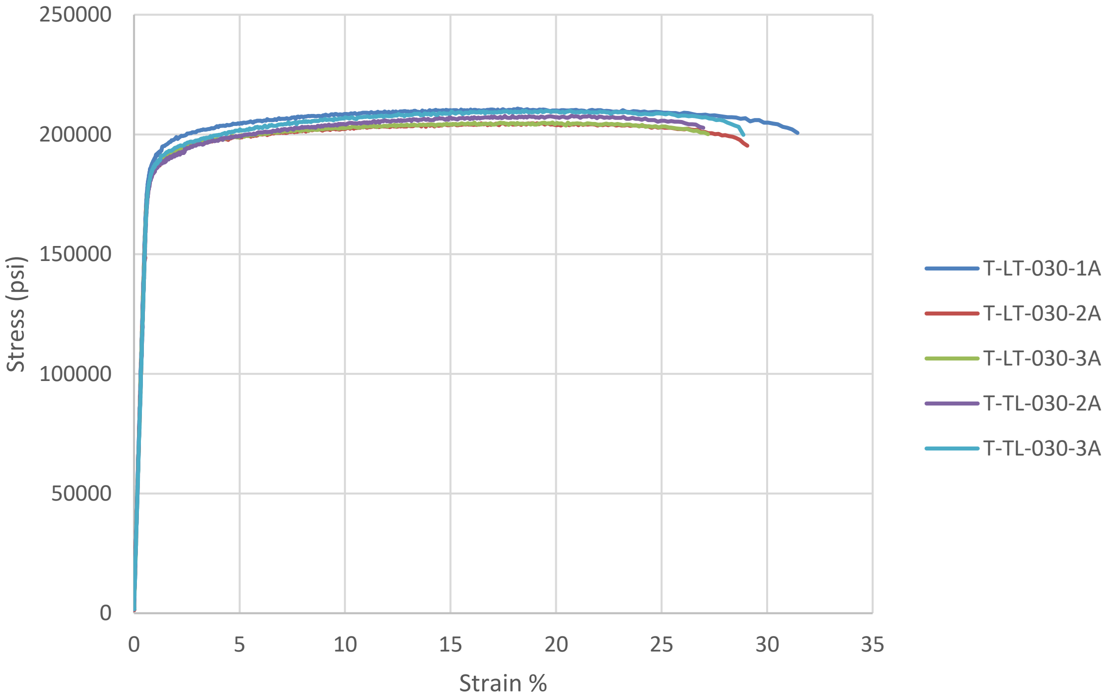

Figure D-5. IN718 tensile data (thickness = 0.030”).

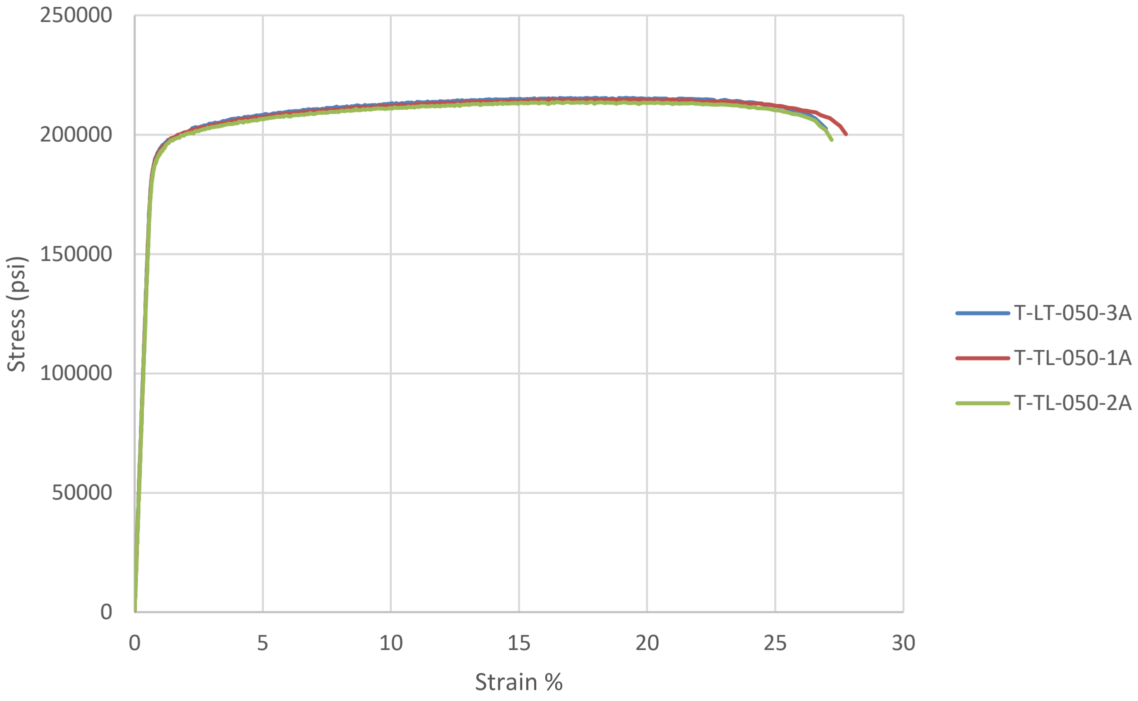

Figure D-6. IN718 tensile data (thickness = 0.050”).

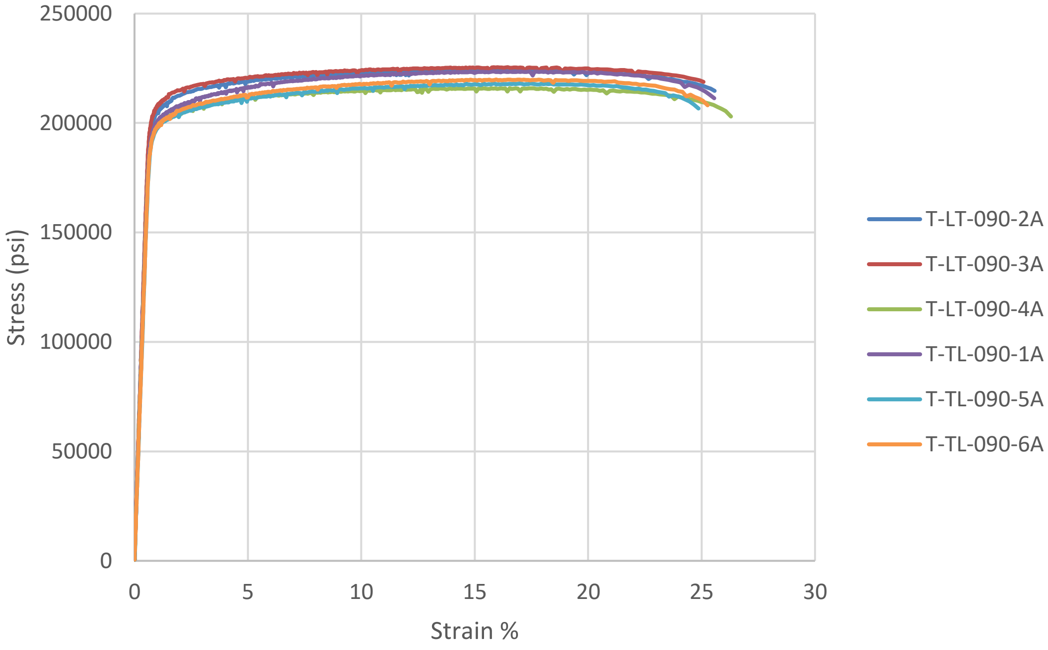

Figure D-7. IN718 tensile data (thickness = 0.090”).

Table D-3: IN718 Tensile Data Summary

ID	Thickness (inch)	Width (inch)	E (psi)	σ_{ys} (psi)	σ_{ult} (psi)
T-TL-030-3A	0.0295	0.5120	29,424,944	184,141	210,791
T-LT-030-1A	0.0300	0.5020	30,902,754	185,836	204,675
T-LT-030-2A	0.0300	0.5170	29,738,537	181,930	204,984
T-LT-030-3A	0.0300	0.5170	29,758,864	181,932	207,806
T-TL-030-2A	0.0300	0.5110	29,355,232	181,663	209,861
Average Sheet 0.03”	**0.0299**	**0.5118**	**29,836,066**	**183,100**	**207,623**
T-LT-050-3A	0.0500	0.5110	29,717,827	190,604	215,445
T-TL-050-1A	0.0500	0.5110	29,613,541	190,223	214,821
T-TL-050-2A	0.0500	0.5110	29,256,322	189,290	213,698
Average Sheet 0.05”	**0.0500**	**0.5110**	**29,529,230**	**190,039**	**214,655**
T-LT-090-2A	0.0900	0.5020	31,735,575	201,215	224,138
T-LT-090-3A	0.0900	0.5000	31,990,784	204,152	225,495
T-TL-090-1A	0.0900	0.5100	30,409,563	197,156	215,962
T-TL-090-6A	0.0915	0.5110	29,961,147	195,679	223,643
T-LT-090-4A	0.0920	0.5100	30,618,218	195,372	218,062
T-TL-090-5A	0.0920	0.5120	29,708,721	194,509	219,887
Average Sheet 0.09”	**0.0910**	**0.5075**	**30,737,335**	**198,014**	**221,197**

Appendix E. Long Crack Data

Fatigue crack growth rate tests were conducted on middle crack tension coupons following the procedures described in the ASTM E647 [ref. 1] standard. The coupons were 3 inches wide with an initial crack of length 2c = 0.5 inches. The tests were conducted at a constant cyclic stress at R = 0.1 and 0.5. The crack growth rate measurements were in good agreement with the results from the NASGRO database (M6AB13AB1) [ref. 2] for AA6061-T6. However, the crack growth rate data from the coupon tests we generated at lower ΔK values than available in the NASGRO database, as shown in Figure E.1. The limited range of ΔK data in the NASGRO database resulted in the NASGRO generated fit to the data that extrapolated the data at lower ΔK values. The extrapolated fit did not agree with the coupon measurements, as shown in Figure E.2. A bi-linear power law fit was applied to the coupon measurements to better describe the behavior in the lower ΔK region, as shown in Figure E.3. The tabular values of the bi-linear power law fit are provided in Table E.1. The bi-linear power law fit was used in the NASGRO predictions of fatigue crack growth life for this assessment.

Table E.1. Values of the AA6061-T6 Bi-linear Power Law Fit

R = 0.1	
Delta-K (ksi inch^1/2)	da/dN (inch/cycle)
1	6.38E-11
5.21	5.19E-07
7	2.60E-06
40	2.70E-04

R = 0.5	
Delta-K (ksi inch^1/2)	da/dN (inch/cycle)
1	1.03E-09
5.21	2.26E-06
7	5.17E-06
40	0.000687

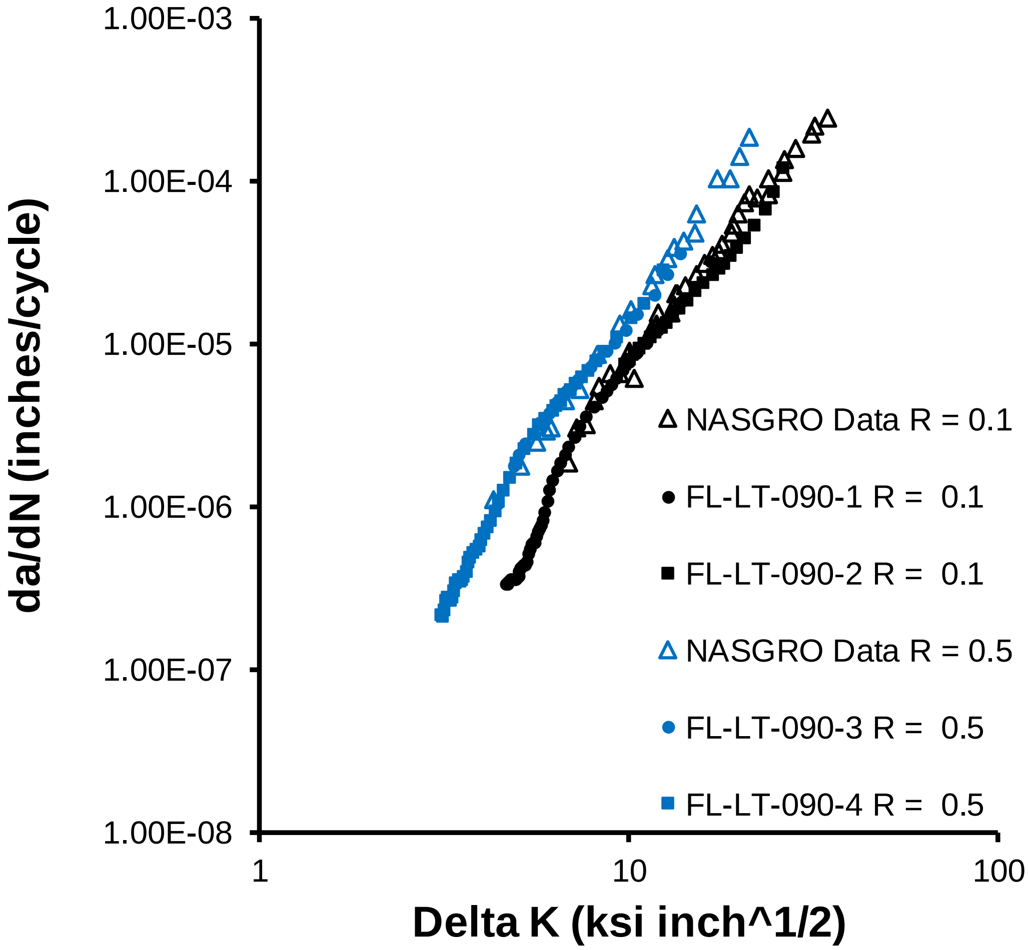

Figure E.1. Fatigue crack growth rate data for AA6061-T6.

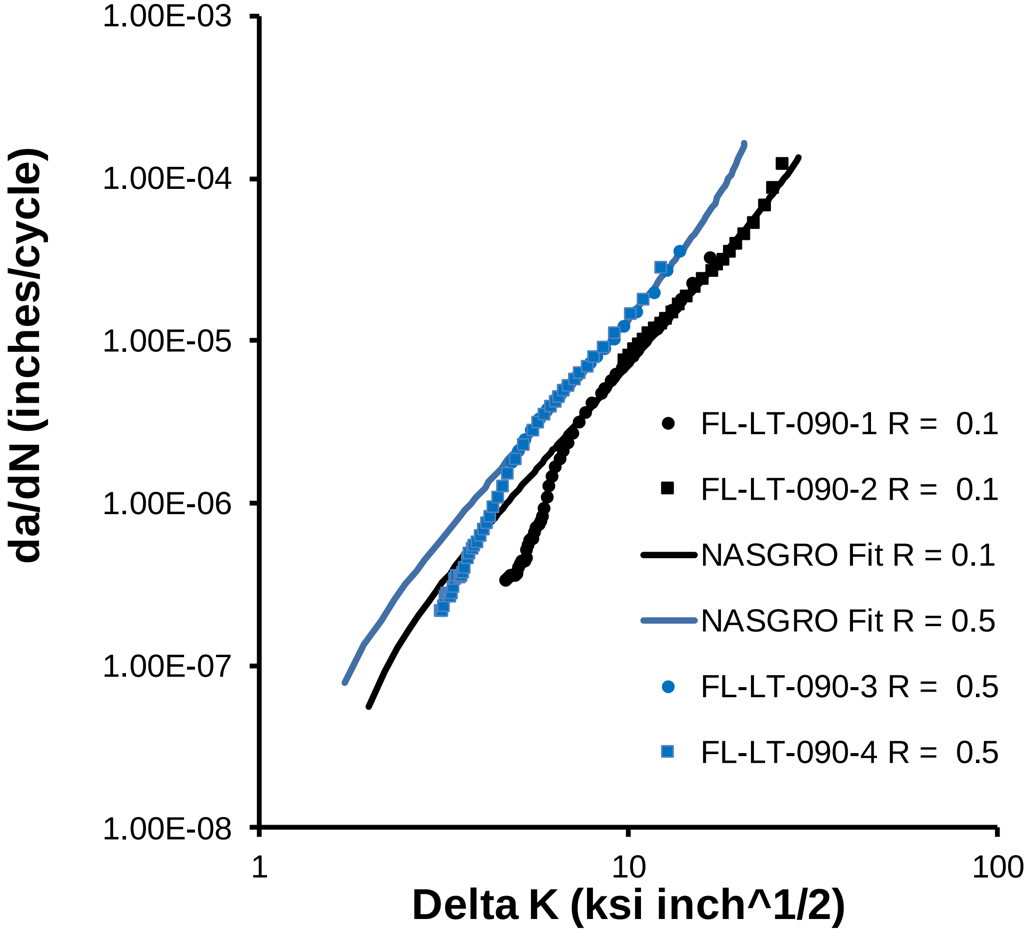

Figure E.2. Fatigue crack growth rate data for AA6061-T6 and the fit from the NASGRO database [ref. 2].

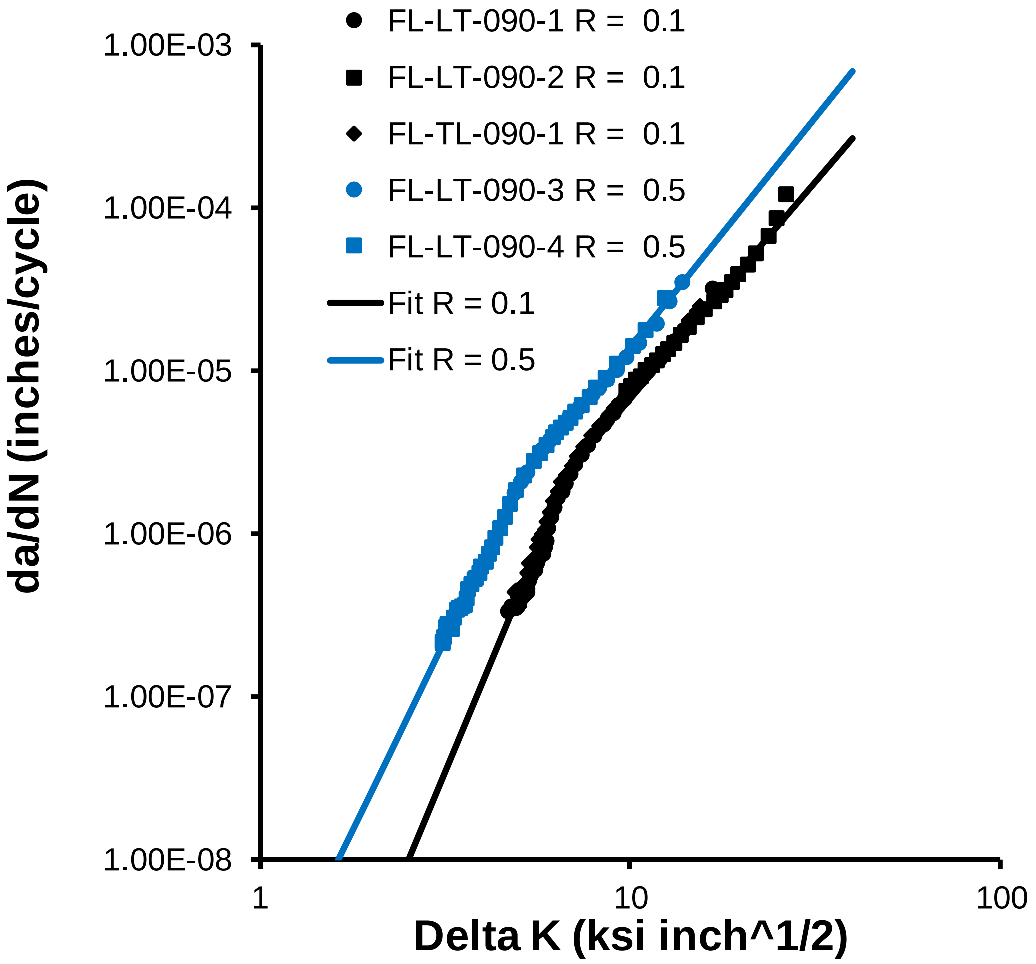

Figure E.3. Fatigue crack growth rate data for AA6061-T6 and a bi-linear power law fit.

References

1. “Standard test Method for Measurement of Fatigue Crack Growth Rates,” E647-15, 2015.
2. NASGRO, Fracture Mechanics and Fatigue Crack Growth Analysis Software, Reference Manual, v9.0, May 2018.

Appendix F. Calculation of LEFM Limit and Derivation of Modified Failure Criteria

Appendix F.1. Calculation of LEFM Limit

Approach Overview

As part of the modified approach to LEFM-based damage tolerance life analysis of thin-walled metallic COPV liners, the M-lifetime crack length, a_F, is checked against three limits: a_i, a_L, and a_i^*. The first of these is the Irwin limit and can be computed directly for a given material, liner thickness, and maximum stress intensity factor (see Section 7.1.2). The second is the LEFM limit and marks the point in the analysis after which LEFM assumptions are no longer valid. The final limit is a function of the first two as well as an elastic-plastic FEA (see Appendix C.2). The following details the calculation of the LEFM limit, a_L.

The proposed procedure is based on the definition of the single-parameter linear-elastic regime in ASTM E2899-15 [4]. This standard provides a test and analysis methodology for the measurement of initiation toughness in semi-elliptical surface cracks in flat, rectangular panels subjected to increasing monotonic tension or bending. The standard applies to metallic materials that are assumed to be homogenous and free of residual stress, and the effects of cyclic loading are not addressed. ASTM E2899-15 provides a framework for categorizing test conditions into one of three regimes: linear-elastic, elastic-plastic, or field collapse. This categorization is based on an analysis of both toughness and crack-tip constraint. Fracture in a particular regime is further characterized as either single-parameter or two-parameter fracture. For example, the two-parameter linear-elastic regime requires both the stress intensity factor K and a constraint parameter Ω to describe toughness. The single-parameter linear-elastic regime is K-dominant and, therefore, it has been extended to describe the region in which LEFM tools can be applied. All other regimes, including the two-parameter linear-elastic regime, imply conditions in which the assumptions underpinning standard LEFM tools are violated.

The procedure for identifying the point during a damage tolerance life analysis at which LEFM assumptions are no longer valid is:

1. Crack growth is simulated to failure using an approved LEFM tool (see Step 1 in Section 7.1.2).
2. Every time step[1] of the analysis is categorized into a regime according to ASTM E2899-15.
3. Scanning in sequential order, the first time step that is categorized into something other than the single-parameter linear-elastic regime is identified.
4. The LEFM limit, a_L, is defined as the crack depth associated with the time step immediately prior[2] to the time step identified in Step 3.

---

[1] Time is measured in cycles for fatigue crack growth, and the time step is dependent on user-defined settings and the LEFM tool being used. Some tools allow the user to request output at specific times or crack sizes. Each time step should have a corresponding crack size and applied stress according to a user-provided load spectrum.

[2] Note that this definition of the LEFM limit is always conservative. Since the time steps are a discretization of a continuous process, the true instantaneous LEFM limit (per the definition based on ASTM E2899-15) is greater than the identified a_L. An analyst can reduce discretization error in the a_L estimate by increasing the frequency of output (i.e., increase the number of time steps).

Calculating the LEFM Limit Based on ASTM E2899-15

According to Section 9.2.1.3 of ASTM E2899-15, the stress intensity factor K is adequate for analysis (i.e., under given conditions, crack assessment can be conducted in accordance with the single-parameter linear-elastic regime) if the following inequality holds,

$$r_a, r_b \geq \frac{J_{\phi_i} E}{\left(\sigma_{ys}\right)^2},$$

where r_a and r_b are characteristic lengths calculated at the crack initiation angle ϕ_i (see Figure F.1), σ_{ys} is the yield stress, E is the elastic modulus, and J_{ϕ_i} is the elastic *J*-integral evaluated at ϕ_i. Therefore, for the purposes of the approach outlined in this report, LEFM assumptions are assumed to be violated when either

$$r_a \text{ or } r_b < \frac{J_{\phi_i} E}{\left(\sigma_{ys}\right)^2}.$$

The characteristic crack lengths r_a and r_b are measurements taken normal to and in-plane with the crack front at the initiation angle, ϕ_i, as shown in Figure 2. The initiation angle is a parametric angle defined on a semi-circle with radius equal to the crack depth, a_0. The initiation angle corresponds to the point at which crack initiation would first occur if the cracked body were subjected to a monotonically increasing tension or bending force. Methods for calculating r_a, r_b and ϕ_i are detailed in subsequent sub-sections.

Note that the net section stress criterion discussed in Section 9.2.1.3 of ASTM E2899-15 is considered redundant. It is assumed that an approved LEFM tool used for damage tolerance life assessment will already have verified that stress in the remaining cross-sectional area at the crack plane remains below the flow stress throughout the analysis as required by Section 7.5.1 of AIAA S-081B.

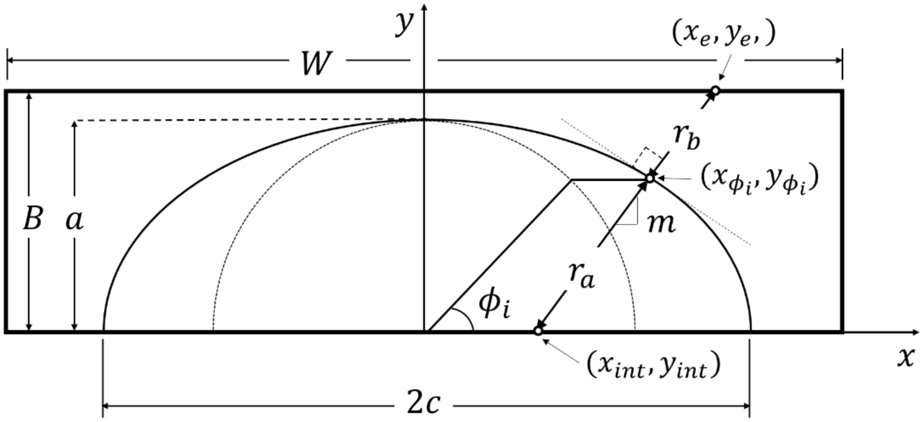

Figure F.1. Schematic of characteristic lengths for an elliptical surface crack.

Calculation of the Characteristic Lengths

As shown in Figure F.1, the point of initiation on the crack front is obtained via a projection in the x-direction of the point on the semi-circle corresponding to the initiation angle. This point is identified in the Cartesian reference frame as (x_{ϕ_i}, y_{ϕ_i}). The method for determining the initiation angle ϕ_i is outlined in the next sub-section. A vector $\vec{r}_b$ extending from this point in the outward crack front normal direction intersects the free surface of the cracked geometry at either the back surface ($y_e = B$) or the side surface ($x_e = W/2$). It is assumed here that, for a surface crack in a metallic pressure vessel liner, $x_e \ll W$, meaning the vector $\vec{r}_b$ will always intersect the back surface. If this is not the case, see Annex 3 of ASTM E2899-15 for additional guidance. A second vector $\vec{r}_a$ extending in the opposite direction intersects the cracked surface ($y_{int} = 0$). The magnitude of these two vectors are r_b and r_a, respectively. The characteristic lengths r_a and r_b can then be calculated using the following geometric relations:

$$r_a = \sqrt{\left(x_{\phi_i} - x_{int}\right)^2 + y_{\phi_i}^2}$$

$$r_b = \sqrt{\left(x_e - x_{\phi_i}\right)^2 + \left(B - y_{\phi_i}\right)^2},$$

where

$$x_{\phi_i} = c(\cos\phi_i)$$

$$y_{\phi_i} = a(\sin\phi_i)$$

$$x_{int} = x_{\phi_i} - \frac{a^2(\cos\phi_i)}{c}$$

$$x_e = x_{\phi_i} + \frac{B - y_{\phi_i}}{m}$$

$$m = \frac{y_{\phi_i}c^2}{x_{\phi_i}a^2}$$

and a and c are the crack depth and half length, respectively, and B is the liner thickness.

Calculation of the Initiation Angle

The standard method for computing the initiation angle in ASTM E2899-15 involves identification of the angle along the crack front where local crack extension first occurs under monotonically increasing tension or bending. For the adaptation used in this report, there is no physical test and thus no physical measurement can be made. However, for cases where ϕ_i cannot be identified via inspection of a fracture surface, ASTM E2899-15 Annex A5.2 provides an alternative method for estimating ϕ_i by analysis. This method was used here and is outlined below. The initiation angle is that which maximizes the following function of T-stress (an elastic parameter) and the elastic-plastic *J*-integral along the crack front,

$$\phi_i = \arg\max_{\phi} \begin{cases} \dfrac{J_\phi^*}{J_{max}^*}\left(\dfrac{T_\phi}{\sigma_{ys}} + 1\right) \; for \; \dfrac{T_\phi}{\sigma_{ys}} \leq 0 \\ \dfrac{J_\phi^*}{J_{max}^*}\left(\dfrac{T_\phi}{4\sigma_{ys}} + 1\right) \; for \; \dfrac{T_\phi}{\sigma_{ys}} > 0 \end{cases}$$

where J_ϕ^* is the elastic-plastic J-integral at the parametric angle ϕ, $J_{max}^* = \max_{\phi} J_\phi^*$, and T_ϕ is the T-stress at the parametric angle ϕ. Tabulated values of $\frac{T_\phi}{\sigma_{ys}}$ for semi-elliptical surface cracks in tension and bending can be found in Annex A2 of ASTM E2899-15. In the examples provided herein, the normalized T-stress was linearly interpolated from these tables. Crack aspect ratios $a/c > 1.0$ were not provided in ASTM E2899-15, and so an additional table for surface-cracks in tension with $a/c = 1.2$ was generated using the FEM described in Appendix C. The crack initiation angle was calculated by discretizing the continuous parametric angle defined from 0 to 90 degrees, resulting in a set $\left\{\phi_j\right\}_{j=1}^N$ where N is the total number of angles for which the elastic and elastic-plastic *J*-integral was computed by FEA for a given crack geometry. The value of N varied with crack size. Crack initiation angle was approximated as

$$\phi_i \approx \max_j \; \phi_j.$$

Appendix F.2. Derivation of Modified (Knockdown) Irwin Limit

Overview of Approach

The portion of the LEFM crack growth predicted to lie beyond the LEFM limit is penalized to add conservatism to the overall analysis while acknowledging that the error accumulation due to the violated assumptions is gradual. Penalization is provided in the form a knockdown on the Irwin limit, effectively reducing the amount of allowable crack growth from the nominal requirement. The modified limit *is not intended* to be a predictive tool for crack growth under elastic-plastic conditions. To this end, the following goals were considered when deriving the knockdown factor on the Irwin limit:

1. The methodology for applying the modified limit should be simple and should not significantly disrupt current damage tolerance life analysis procedures.
2. The magnitude of the knockdown should increase as the difference between the LEFM limit and the *M*-lifetime predicted crack depth increases.
3. Crack growth preceding the LEFM limit should not be penalized for succeeding violations of LEFM assumptions.
4. The modified Irwin limit should be bounded by the LEFM limit and the original Irwin limit.
5. The derivation of the limit should be rooted in fracture mechanics where possible (i.e., the modified limit should be intuitive).

Derivation of Modified Irwin Limit

Paris et al. [refs. 5, 6] introduced a power law relationship between the one-dimensional fatigue crack growth rate and the range of stress intensity factor, ΔK, for conditions of small-scale yielding at the crack tip in the early 1960s,

$$\frac{da}{dN} = C(\Delta K)^n$$

Under LEFM conditions, ΔK is widely accepted as an accurate measure of crack driving force. Numerous modifications of Paris' Law have been introduced since, including the NASGRO equation [refs. 3, 7]. In general, however, the driving force can be defined as $\beta = f(\boldsymbol{a}, \boldsymbol{P}, \ldots)$, where $\boldsymbol{a}$ describes the crack state and $\boldsymbol{P}$ describes the applied load. Additional parameters can be included for geometric effects, etc. This yields the general power law relation

$$\frac{da}{dN} = C\beta^n.$$

As discussed in Section 7.1.2, the use of LEFM (e.g., ΔK) outside of its applicable regime results in a gradual accumulation of error when integrating the crack growth rate equation. A crude approximation of how this error affects crack growth predictions can be derived by substituting a driving force that takes elastic-plastic material response into account. In the following, elastic-plastic functions or parameters are indicated by the superscript * notation, while their elastic counterparts do not have a superscript. The crack growth rate for the elastic-plastic condition is thus

$$\frac{da^*}{dN} = C(\beta^*)^n$$

A schematic of this idealized crack growth behavior is shown in Figure F.2.

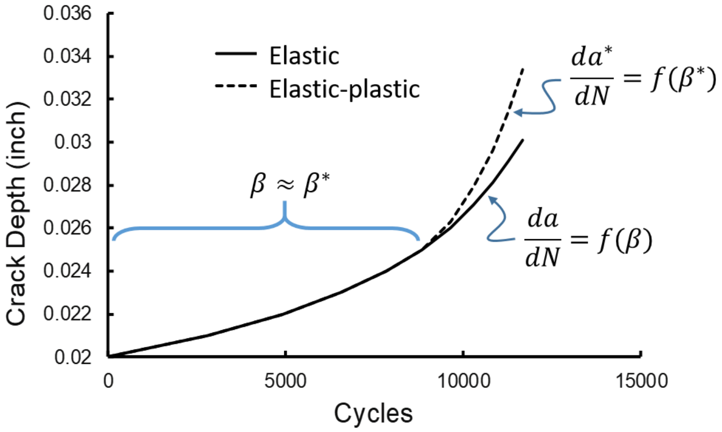

Figure F.2. Schematic of divergence of predicted crack growth due to use of elastic or elastic-plastic driving forces.

These elastic and elastic-plastic crack growth equations correspond to the elastic and elastic-plastic material response due to an identical far-field, applied load spectrum. Therefore, da and da^* are infinitesimal crack growth increments induced by the same infinitesimal cycle increment, dN. This enables the calculation of the relative rate

$$\frac{da^*/dN}{da/dN} = \frac{da^*}{da} = \frac{C(\beta^*)^n}{C(\beta)^n} = \left(\frac{\beta^*}{\beta}\right)^n.$$

It is assumed in this derivation that the driving force ratio $\frac{\beta^*}{\beta} \geq 1$ and increases as LEFM assumptions breakdown (i.e., $a_F \rightarrow a_i$ according to the definitions in Section 7.1.2). Rearranging and assuming the crack size under both elastic and elastic-plastic conditions are initially equal to a_L, or the point at which LEFM assumptions are violated,

$$\int_{a_L}^{a_F^*} da^* = \int_{a_L}^{a_F} \left(\frac{\beta^*}{\beta}\right)^n da.$$

Here, a_F and a_F^* are the elastic and elastic-plastic crack lengths after application of the *M*-lifetime load spectrum. Applying the simplifying assumption that $d\beta/da = d\beta^*/da^* = 0$ and integrating gives

$$a_F^* - a_L = \left(\frac{\beta^*}{\beta}\right)^n (a_F - a_L).$$

Rearranging yields the following expression for elastic-plastic crack length[3] as a function of the linear elastic growth:

$$a_F^* = \left(\frac{\beta^*}{\beta}\right)^n (a_F - a_L) + a_L.$$

At this point, this crack length can be directly checked against the Irwin limit to determine if the true crack might be in danger of exceeding this threshold; i.e.,

$$a_F^* < a_i$$

---

[3] This expression is not intended to be an accurate predictor of elastic-plastic crack growth and is based on a number of critical assumptions that affect its accuracy in this regard. It is best to consider a_F^* to be a penalized version of the LEFM prediction, a_F, instead.

should hold. Toward the goal of making the proposed approach easy to interface with current damage tolerance life analysis procedures, this equation can be rearranged to obtain a knockdown on the Irwin plastic zone limit by substituting the definition of a_F^* into the above inequality and rearranging. The new limit is

$$a_i^* = \frac{a_I - a_L}{\left(\frac{\beta^*}{\beta}\right)^n} + a_L$$

where now the analysis is acceptable if $a_F < a_i^*$.

The next step is to choose the driving force parameters β and β^*. As discussed previously, a common choice for a homogeneous linear-elastic material would be $\beta = \Delta K$. However, the stress intensity factor is not applicable to elastic-plastic materials. The *J*-integral is widely used as an EPFM parameter and is convenient in that it can be related directly to K under linear-elastic conditions. It has been shown that range parameters that account for the cyclic nature of the applied stresses such as ΔK or ΔJ provide a more accurate estimate of fatigue crack growth rates.

McClung et al. provide a detailed review of ΔJ as a fatigue parameter [ref. 8], providing additional references and discussing both the merits and theoretical shortcomings of ΔJ. It is important to note that $\Delta J \neq J_{max} - J_{min}$ and must be calculated using the ΔJ-integral [9, 10]. Due to the approximate nature of the modified limit derivation and the lack of a verified code for computing the ΔJ-integral, it was decided that a more simplistic measure of the crack driving force ratio would be used. Specifically, $\beta^*/\beta = J_{\phi_i}^*/J_{\phi_i}$, where $J_{\phi_i}^*$ and J_{ϕ_i} are the elastic and elastic-plastic *J*-integrals evaluated at the initiation angle computed in Appendix C.1. Implicitly, this assumes

$$\frac{J_{\phi_i}^*}{J_{\phi_i}} \propto \frac{\Delta J_{eff}^*}{\Delta J_{eff}}.$$

It should also be noted that the *J*-integral is technically invalid for cyclic loading as it is based on deformation plasticity, which does not allow for unloading. This choice also ignores effects such as crack closure due to plasticity. However, as indicated previously, the goal of this derivation was not an EPFM prediction tool, and the choice was motivated by the simplicity of the analysis and the availability of tools for automating the generation of lookup tables.

Computation of the *J*-integral ratio at ϕ_i rather than taking the maximum value, for example, was an effort to avoid errors associated with computing the *J*-integral near a free surface. An example of the elastic-plastic and elastic *J*-integrals computed along a half crack front ($\phi = [0°, 90°]$) is shown in Figure F.3. Here it can be seen that $J_{max} > J_{max}^*$ (the maximum values occur near the surface). However, the majority of the crack front shows the opposite relation. It was determined that using a maximum was less reliable than using ϕ_i which is already a required calculation as part of the identification of the LEFM limit and has physical significance as the predicted point of initiation under monotonic tension.

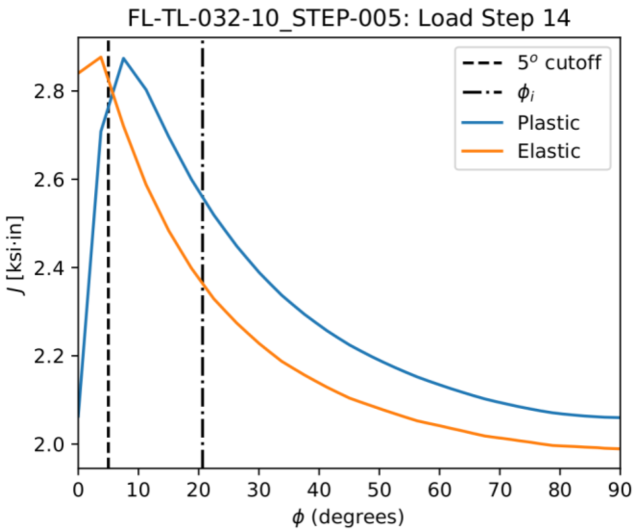

Figure F.3. J-integral computed along the crack front for an example crack size and applied stress.

To simplify the integration of the relative crack growth rate equation, it was assumed that $d\beta/da = d\beta^*/da^* = 0$. In reality, $dJ_{\phi_i}/da = dJ^*_{\phi_i}/da^* \neq 0$. To compensate, conservative values were chosen for $J^*_{\phi_i}$ and J_{ϕ_i}. Specifically, $J_{\phi_i} = \mathcal{M}(a_L, a_L/c_L, \phi_i, \sigma)$ and $J^*_{\phi_i} = \mathcal{M}^*(a_F, a_F/c_F, \phi_i, \sigma)$ where $\mathcal{M}(\cdot)$ is a FEM that computes the *J*-integral at a given crack depth, shape, crack front parametric angle, and the applied stress using the material model denoted by the superscript. This also guarantees the desired behavior that $\left(J^*_{\phi_i}/J_{\phi_i}\right)^n$ (and, thus, the knockdown factor) increases as a_F approaches a_i, since $a_L$is fixed. An example of how the *J*-integral changes with respect to the two available limits (a_L and a_i) prior to the calculation of the modified Irwin limit, a_i^*, as well as the *M*-lifetime crack depth is shown in Figure F.4.

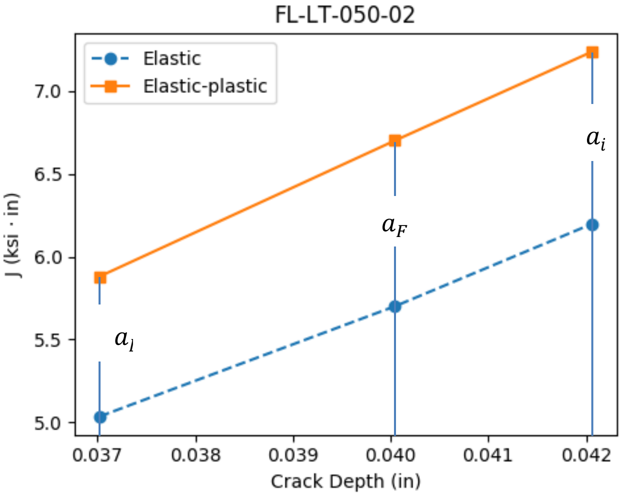

Figure F.4. Example of the elastic-plastic and elastic J_{ϕ_i}at the available crack limits and M-lifetime crack depth.

Finally, the modified Irwin limit is obtained by substituting $J^*_{\phi_i}/J_{\phi_i}$ for β^*/β,

$$a_i^* = \frac{a_I - a_L}{\left(\frac{J^*_{\phi_i}}{J_{\phi_i}}\right)^n} + a_L.$$

References

1. Irwin, G. R., “Crack-Extension Force for a Part-Through Crack in a Plate,” Journal of Applied Mechanics, vol. 29, no. 4, Dec. 1962, pp. 651-654.
2. Orange, T. W., Sullivan, T. L., and Calfo, F. D., “Fracture of Thin Sections Containing Through and Part-through Cracks,” Fracture Toughness Testing at Cryogenic Temperatures, ASTM STP 496, American Society for Testing and Materials, Philadelphia, 1970, pp. 61-81.
3. NASGRO, Fracture Mechanics and Fatigue Crack Growth Analysis Software, Reference Manual, v9.0, May 2018.
4. ASTM E2899-15, “Standard Test Method for Measurement of Initiation Toughness in Surface Cracks Under Tension and Bending,” ASTM International, West Conshohocken, PA, 2015.
5. Paris, P. C., M. P. Gomez, and W. E. Anderson, "A Rational Analytic Theory of Fatigue," The Trend in Engineering, University of Washington, 1961, pp. 9-14.
6. Paris, P. C., 1964, "The Fracture Mechanics Approach to Fatigue," Fatigue - An Interdisciplinary Approach, Proc. 10th Sagamore Army Materials Research Conf., Syracuse Univ. Press, pp. 107-132.
7. Forman, R. G., and Mettu, S. R., “Behavior of Surface and Corner Cracks Subjected to Tensile and Bending Loads in Ti-6Al-4V Alloy,” Fracture Mechanics: Twenty-second Symposium, Vol. 1, ASTM STP 1131, H. A. Ernst, A. Saxena, and D. L. McDowell, eds., American Society for Testing and Materials, Philadelphia, 1992, pp. 519-546.
8. McClung, R. Craig, et al. "Development of a practical methodology for elastic-plastic and fully plastic fatigue crack growth,” NASA Report, NASA/CR-1999-209428, 1999.
9. Tanaka, K. "The cyclic J-integral as a criterion for fatigue crack growth." International Journal of Fracture 22.2, 1983, pp. 91-104.
10. Wüthrich, Ch. "The extension of the J-integral concept to fatigue cracks." International Journal of Fracture, 20.2, 1982.

Appendix G. Small-Scale Testing and Microstructure Evaluation

3D Microstructure Demonstration

While it is well-established that microstructural features influences materials properties, such as strength and ductility, 3D/4D nondestructive characterization opens possibilities for studying deformation and damage mechanisms. Often, these 3D/4D nondestructive tomographic acquisition and processing methods are known as grain mapping, originating from synchrotron X-ray facilities. The Versa 620 equipment used herein provides a means for acquisition of grain mapping data, but in a way that can be utilized in a standard materials lab, LabDCT, thereby greatly expanding the opportunities to study 3D/4D materials mechanisms and to incorporate these methods in the classroom and lab experience. The typical workflow of LabDCT experiments consists of two stages: data acquisition and data reconstruction. Two scans should be acquired: an absorption contrast tomography (ACT) scan to define the sample outline, and a diffraction contrast tomography (DCT) scan in which a specified number of diffraction contrast projections are collected, while the sample rotates. The data are then imported into GrainMapper3D for processing and reconstruction.

Tested subscale coupons were analyzed to acquire the 3D microstructure in relation to the fatigue crack surface. The acquired absorption contrast tomography (ACT), Figure G.1, and diffraction contrast tomography (DCT), Figure G.2, data were used with the GrainMapper3D™ software for volumetric grain reconstruction of the scanned sample volume. The five scanned volumes with 80 μm were reconstructed individually and then stitched together. Figure G.2 shows the rendered volume with the reconstructed 3D grain map embedded in the sample volume. The volume scanned with DCT extended from the fracture surface to the end of the gage region. The DCT scan did not cover the entire sample thickness because the imaged volume was limited by the size of the aperture. As a result, the reconstructed 3D volume had a cylindrical shape.

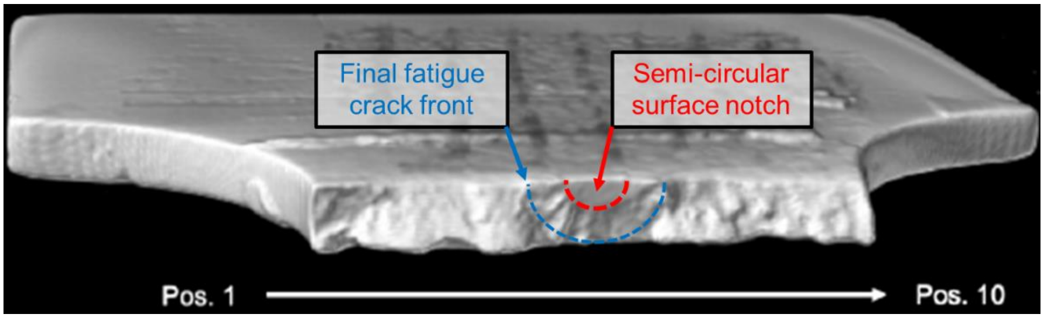

Figure G.1. Post-processed result of ACT measurement from a Versa 620.

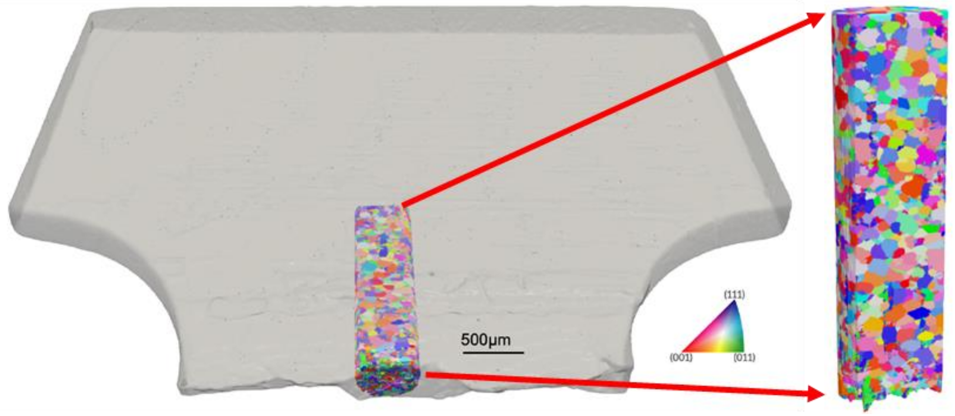

Figure G.2. Post-processed result of DCT measurement with measured grain shapes and crystallographic orientations near the initial semi-circular surface notch.

This proof-of-concept volumetric measurement demonstrates the ability of a commercially-available instrument, the Versa 620, to correlate microstructural features with the observed fatigue crack growth rate and path. Consequently, current material and process qualification procedures could be evolved to incorporate microstructure sensitives upon extracting a multitude of representative coupons from a vessel, testing under an appropriate stress state, and correlating observed crack-growth mechanisms (inter-, intra-, and trans-granular) and rates to the acquired microstructural features.

Small-Scale Test Setup

Gripping these subscale coupons required the use of an extended gripping mechanism, Figure G.3a. First, this helped ensure repeatable alignment within a standard 5 kip load frame. Alignment of the coupons within the extended grips were done in an external jig, before loading the entire assembly into the test stand. Second, the extended grips move the large hydraulic grip component further from the coupon, which allowed room for common DIC cameras, lenses, and lighting. Because the coupons were small and compliant, relative to the extended grips, side braces were additively manufactured to ensure that no inadvertent loads were imposed on the coupon before loading, see Figure G.3a).

For all tests discussed below, two 5 MP Basler Ace cameras with 50 mm Moritex lenses and 25 mm spacers were used for acquiring all DIC images, Figure G.3b). This stereo configuration was placed at the front and back of the coupon that enabled verification of alignment, Figure G.4. The field-of-view of the camera setup was approximately 1 inch, with a 30-degree angle between cameras. White spray paint with airbrushed black speckles were used to pattern the surface for DIC.

This front-and-back DIC setup provided additional data acquisition benefits associated with fatigue crack growth measurements. In fatigue crack growth tests, the system on the front was used to acquire CMOD measurements and the system on the back was used to acquire back-face strains to identify when the crack had nearly progressed across the thickness. Furthermore, these back-face strains could also be used to better understand at what point during the test the remaining ligament began to experience unconstrained plasticity. The VIC3D software from Correlated Solutions was used to analyze displacement and strain fields. With the camerabinning mode set to 2x2, approximately 7 pixels per speckle was achieved and a subset size of 35 and step size of 8 were used for correlation analysis. For all measurements, the noise floor on DIC measurements was found to be approximately 200 microstrain.

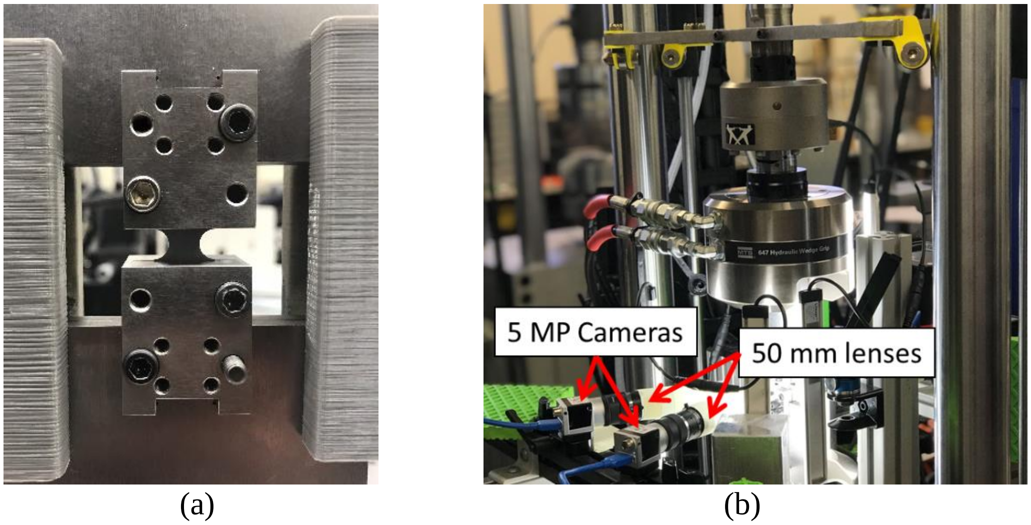

(a) (b)

Figure G.3. (a) Extended grips with inserted coupon and 3D-printed alignment jigs on either side and (b) Test-stand setup with DIC cameras and lenses on front and back.

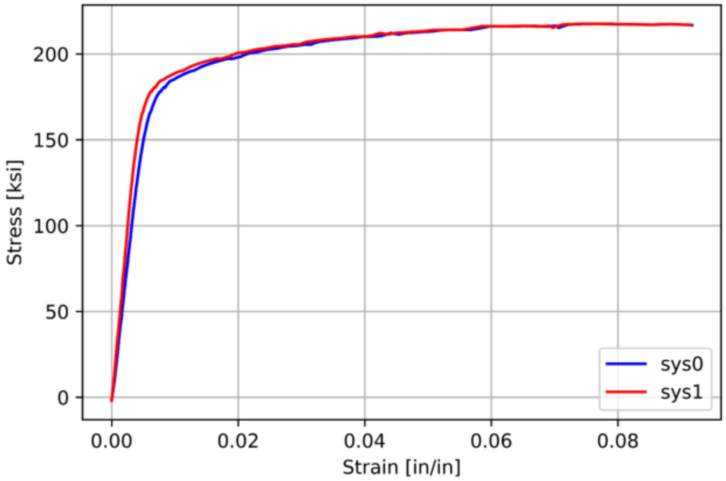

Figure G.4. Engineering stress-strain result with results obtained from front and back DIC.

Commonly, hydraulic grips impose a torsional load upon gripping. This is typically not a major concern, when coupons are relatively stiff and this torsion load is negligible compared to applied tensile loads. However, these subscale coupons were very thin and the torsional stress resulting from this step was not negligible. Consequently, anti-rotation guides were designed and installed, Figures G.5. These guides supported any such torsional load that occurred upon gripping or from drifting during the test. The front-and-back design also provides support against out-of-plan motion of the actuator, which would impose undersirable bending moments on the coupons.

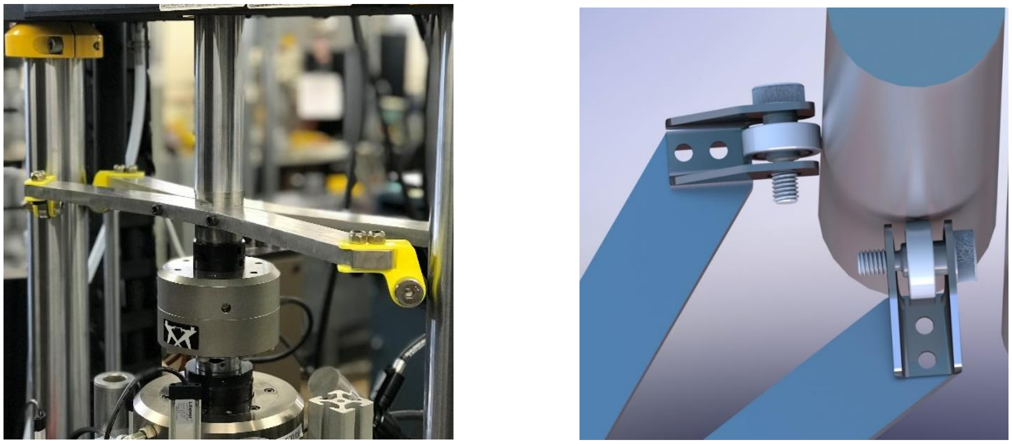

(a) (b)

Figure G.5. Anti-rotation guides used for small-scale testing (a) physical installation and (b) model close-up of roller bearing on vertical column.

Small-scale Fatigue Crack Growth Rate Testing

Small-scale coupons from both the liner and sheet materials were used for small-scale fatigue crack growth testing using the same coupon geometry and extraction method as provided above in the small-scale coupon design and fabrication section. Because a custom coupon design was used for the small-scale tests, any effect of the geometry on measured fatigue crack growth rates was unknown. Running small-scale tests with sheet material provided a baseline comparison between the small- and large-scale coupons. In other words, if the small-scale coupon geometry does not have a significant impact on measured growth rates, then the growth rates of large- and small-scale tests would compare closely. Similarly, any discrepancy in measured growth rates between large- and small-scale sheet material coupons would indicate an effect of the small-scale coupon geometry that could be understood and accounted for.

After extracting the small-scale coupons, a notch was placed on the surface, see Figure G.6, from which a fatigue crack was initiated. Initially, the plasma focused-ion beam (PFIB) at NASA LaRC was used to insert a semi-circular surface notch, see Figure G.7(a). The method proved to be highly-customizable, enabling precise semi-circular notch shapes with high precision and repeatability. Furthermore, because the notch is relatively sharp, much less time was required in the precracking stage. However, the PFIB method is also relatively slow and costly which eventually motivated a change to faster, lower resolution methods, such as laser notching; the result of which is illustrated in Figure G.7(b) and G.7(c). In either case, PFIB or laser notching, fatigue precracks were grown from the notch and propagated until the crack front was beyond the influence of the notch: a distance approximately equal to the notch height.

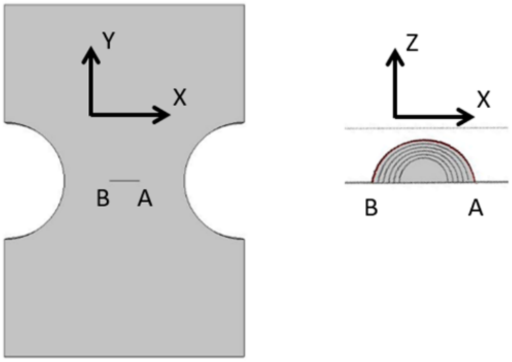

Figure G.6. Small-scale fatigue crack growth coupon with (left) front view and (right) looking down on the crack surface through the thickness.

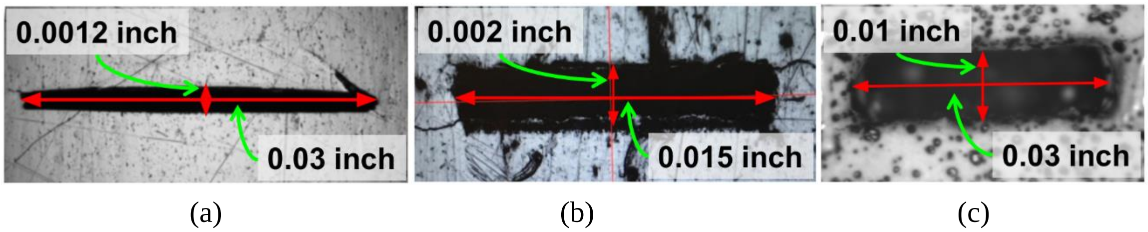

(a) (b) (c)

Figure G.7. Various crack-initiating notches from (a) pFIB, (b) laser spec. #1, (c) laser spec. #2.

Before precracking, the portion of the coupon surface where the crack would eventually propagate was masked off using tape, which is illustrated by the red-box regions (edges) of Figure G.8. White base paint with black airbrush speckles was then applied to the front and back of each coupon. Using this sequence, the crack remained visible on the surface during the test, which enabled direct measurement of 2c with simultaneous crack mouth opening displacement (CMOD) measurements from DIC, Figure G.8. For accurate 2c measurements, a 10X Mitutoyo objective lens was attached to a Navitar 12X fixed focal-length microscope, and placed to focus on the notched surface of the coupon, see Figure G.9(a) and G.9(b).

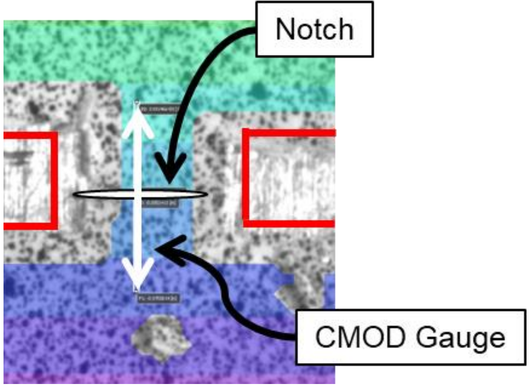

Figure G.8. DIC result with virtual extensometer for CMOD across notch.

With the microscope assembly in place to focus on the crack, Figure G.9(a), the line-of-sight of the DIC cameras was blocked. To accommodate both acquisition methods, the angle between the DIC cameras (on the notched side of coupon) was increased to 39.2°. This allowed for sufficient space to place the microscope assembly on a swivel mount such that it could be rotated into place for 2c measurements, but then rotated back out of the way during image acquisition for DIC. As the crack propagated through the masked region, its surface length (2c) was obtained using a micrometer stage that was attached to the microscope assembly. Consequently, measurements of 2c and CMOD were obtained as a function of the number of cycles, N, throughout the test.

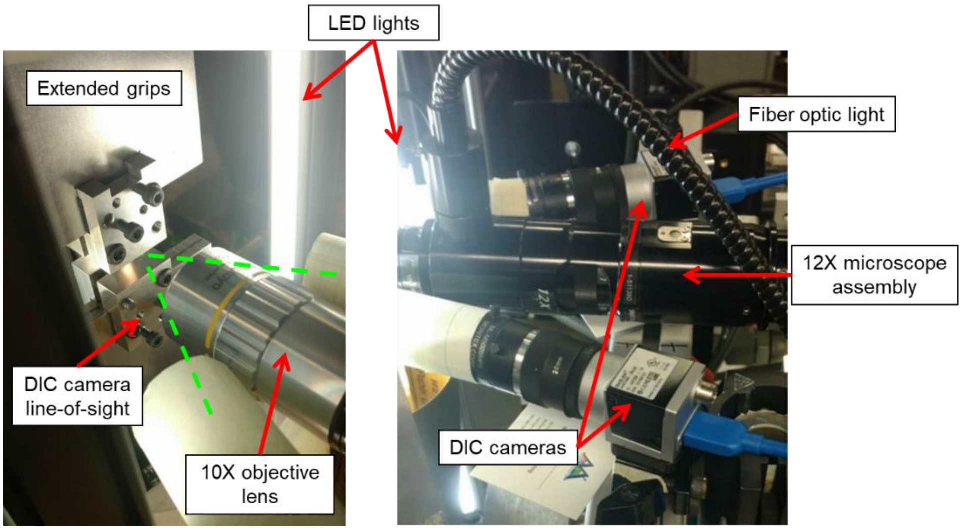

(a) (b)

Figure G.9. (a) 10x objective lens at focal distance, measuring 2c length during fatigue test, (b) Navitar 12x Lens System between two DIC cameras.

As mentioned above, the first set of fatigue cracks initiated from PFIB notches. Because this process was time consuming, a modified approach was adopted whereby EDM notches were inserted on the coupon surface, see Figure G.10. This process milled most of the desired notch length, 0.015 inch. Subsequently, a FIB was used to sharpen the initially-blunt notch by inserted a FIB extension of 0.002 inch. This modified process maintained the ability to mill sharp notches that minimized fatigue precracking time, but also reduced the required PFIB time upfront.

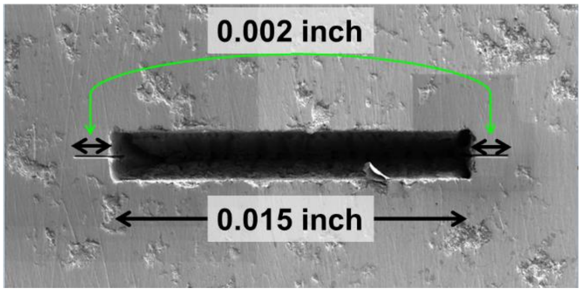

Figure G.10. Blunt laser notches with FIB sharpening.

Initially, the cyclic load peaks were chosen such that an initial $\Delta K = 5\ ksi \cdot \sqrt{inch}$ was achieved at the crack front depth. Fatigue precracks were then propagated under constant-amplitude loading (i.e., an increasing ΔK test). The objective of this similitude was to enable direct comparison of growth rates between the small-scale liner materials with standard coupon geometries from rolled sheet. Differences observed between these two cases would then help quantify the effect of assumptions made in current practice (discussed at the beginning of this subsection). However, upon completion of an initial set of coupons, it was determined that, while matching ΔK, the small-scale coupons experienced increased net section stress leading to larger plastic zones, which resulted in increased growth rates.

In this first round of testing, it was observed that AA6061-T6 coupons extracted from the first-generation liner dome had crack growth rates that were comparable to that of the sheet coupons. However, the liner cylinder coupons demonstrated a much faster (~10X) increase in crack growth rates. Microscopy during and after the test provided observations of two significant changes in crack growth mechanism for the liner cylinder coupons. First, transgranular crack growth was observed for the liner dome and sheet coupons; however, intergranular crack growth was observed in the liner cylinder coupons. Second, the liner dome and cylinder coupons demonstrated secondary cracking as illustrated in Figure G.11. FRASTA analysis was completed on a small-scale AA6061-T6 liner coupon to further study crack propagation path post-mortem, see Figure G.12. In Figure G.12, white regions correspond to crack propagation in stages and clearly illustrate initial growth at approximately 30° and 150° along the crack front. These observations are consistent with testing at lower ΔK tests, discussed in the next section.

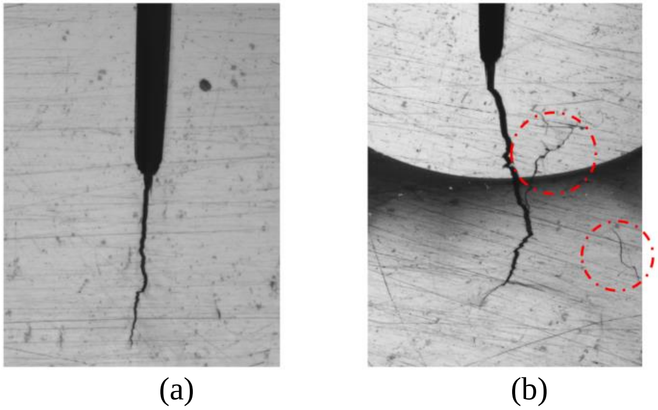
(a) (b)

Figure G.11. AA6061-T6 fatigue crack growth observations from (a) rolled sheet and (b) AA6061-T6 liner.

Subsequent rounds of small-scale fatigue crack growth tests were conducted such that cyclic loads resulted in matched net section stress with the large-scale coupons. As a result, initial ΔK values were reduced to ΔK = 3 $ksi \cdot \sqrt{inch}$, but ultimately provided a better comparison with large-scale coupons. For the AA6061-T6 coupons, this updated procedure resulted in a cyclic load peak of 175 lbf for the 0.032-inch thickness and load peak of 700 lbf for the 0.14-inch thickness. For the IN718 coupons, it was ultimately found that a reduced peak load equating to 33% of yield resulted in reliable initiation from the notch at a reasonable number of cycles, approximately 300K. This resulted in a peak load of 385 lbf for the IN718 coupons. For all cases, R=0.1 and 15 Hz loading frequency was used for crack propagation.

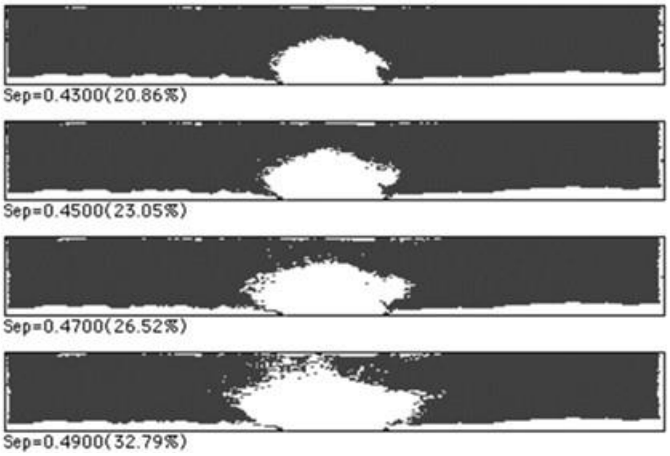

Figure G.12. FRASTA analysis of two post-mortem fracture surfaces.

Quantification of crack growth rates through the thickness of each of the liner and sheet materials was ultimately the required output from these tests. However, crack growth increments through the thickness could not be directly measured. The data obtained from each test was 2c vs. N, CMOD vs. N, and crack depth at the first cycle (N_{init}) and final cycle (N_{final}). These data were obtained through the following procedure (which is equivalent to that used for the large-scale coupons):

1. After notch insertion, precracks were grown to an initial *2c* length.
2. Each coupon was then held at 90% of the peak load while a black Sharpie® pen was pressed against the surface precrack for 60 seconds to mark the initial crack front. The coupon then remained at 90% of max load for 20 minutes to allow for ink to penetrate the depth of crack and dry. This was repeated to ensure adequate coverage of the crack surface at this stage, which provided an initial crack depth data point and for each test. A second data point was measured from the post-mortem fractured surface. The result of this process is illustrated in Section 7.2.1.4, Figure 7.2.1.1-13.
3. Coupons were masked with tape and painted with an airbrush to apply the required DIC pattern for CMOD measurements, recall Figure G.8.
4. Cyclic loading was then applied at levels equivalent to those during precracking to propagate the crack. Periodically throughout each test (every 5K-10K cycles), the load frequency was reduced to 0.1 Hz to allow for measurements of 2c and CMOD (DIC images captured at 320 ms intervals), which were recorded along with the current cycle count.
5. A target for the final crack depth, *a*, was set for each coupon and estimated during the test from the measured 2c values (assuming an a/c=1) and from back face strains obtained for DIC analysis.
6. Once the target crack depth was met the test was concluded by pulling coupon apart in displacement control. This ensured a clear demarcation for the final crack depth, providing the second crack depth data point for each test.

Using this procedure CMOD data are obtained throughout the test (at multiple cycle counts, N), see Section 7.2.1.4, Figure 7.2.1.1-15, and crack depth, *a*, is obtained at the start and end of the fatigue crack growth test, see Figure 7.2.1.1-13. After running a multitude of tests for each material, an averaged relationship between the CMOD and crack depth was obtained. Using this relationship, the value of crack depth was computed at every cycle count at which CMOD data were acquired. In other words, the desired relationship between crack depth and cycle count was obtained. The numerical derivative of this relationship, da/dN, was computed using a 5-point Lagrange polynomial. Finally, for each crack depth at which da/dN was computed a stress-intensity factor was computed using the Raju-Newman equation for an elliptical surface crack to match the SIF solution used in the large-scale data processing. In all of the thin coupon tests completed here, the bounds on the Raju-Newman equation were satisfactorily met. However, for the thick AA6061-T6 coupons the constraint that $0.5 < c/b$ was not met after a $\Delta K = 6\ ksi \cdot \sqrt{inch}$. While this pertains to a subset of the data presented for those cases, it was determined that the error introduced for this subset was negligible compared to the overall scatter in the growth rates. There were too many tests were conducted to permit illustration herein of each result sequence here. Consequently, a representative sample from each is presented to demonstrate the data processing that lead to the final data set upon which the evidence, observations, and recommendations are based.

Appendix H. Strain Measurement in Uniaxial Coupon Testing

Uniaxial coupons can be used to simulate the influence of autofrettage, MDP, proof, and other cycles on the fatigue crack growth behavior of cracks in COPV liners. The coupons are required to replicate the far-field strains in the COPV liner at the crack location. The strains in the COPV liners are typically determined from elastic-plastic finite element analyses (FEA) that model both the metallic liner and the composite overwrap. The experimental simulation of crack growth in the liner assumes that the off-axis strains will have a negligible influence or will be conservative with respect to the crack growth behavior. The worst-case strains (e.g., hoop strains in the cylinder of a cylindrical COPV) determined from the FEA will need to be applied to the uniaxial coupon. The uniaxial tests are typically loaded under displacement control to the specific strains determined from the FEA. The two most common measurements of strains in uniaxial coupons are strain gages and edge extensometers. The choice of strain measurement technique and placement of the strain measurements can influence the understanding of conditions at the crack tip.

Full-field DIC measurements of strain were made during a simulated uniaxial autofrettage loading, as shown in Figure H.1 for the axial strain contours at peak strain. The coupon was 2 inches wide and 0.032-inch thick. The initial surface crack length was 0.063 inch and the initial crack depth was 0.027 inch. The nominal far-field strain level was about 2%. High strain gradients near the crack are readily apparent in Figure H.1. These full-field DIC measurements were used to evaluate the implications of different strain measurements using virtual extensometers and virtual strain gages. The following sub-sections examine the implementation of the strain measurements options for uniaxial coupons using strain gages and edge extensometers.

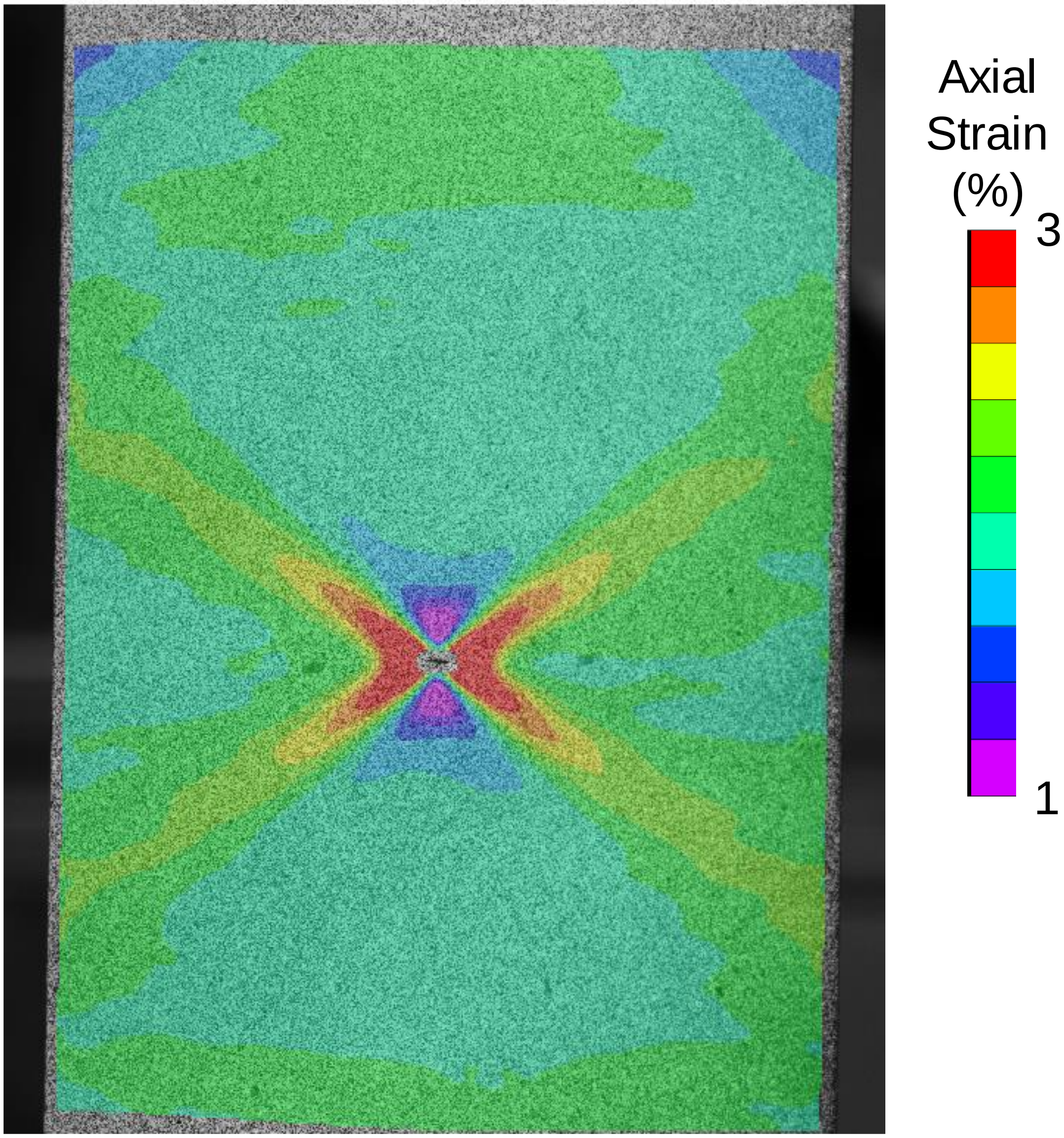

Figure H.1. Axial strain field for a uniaxial autofrettage test.

Strain Gage Measurements

The concept of using a uniaxial coupon to simulate the strain in a COPV liner requires that the far-field strain in the coupon accurately represent the far-field strain at the crack location in the COPV liner. Characterization of the far-field strain using strain gages will require that the gages avoid the high gradient strain field around the crack. Several strain gage locations were simulated using the DIC data, as shown in Figure H.2 along with the recorded stress-strain behavior. Four of the virtual strain gages (shown as black boxes) were located above the center of the crack at different heights above the crack. Two other virtual strain gages were aligned with the crack and located on the left and right edges.

The results indicate the gages placed above the crack have a strong sensitivity to the distance from the plane of the crack (+10% to -20%). The virtual strain gage measurements closest to the crack were below the nominal far-field strain value and increased as the distance from the crack increased. The strain gages furthest from the crack exceeded the nominal far-field strain, possibly influenced by the gripped boundary conditions. The two virtual strain gages near the edges were close to the nominal far-field strain values (±5%). This suggests that the placing strain gages near the edges and in-line with the cracks would provide the most consistent strain measurements.

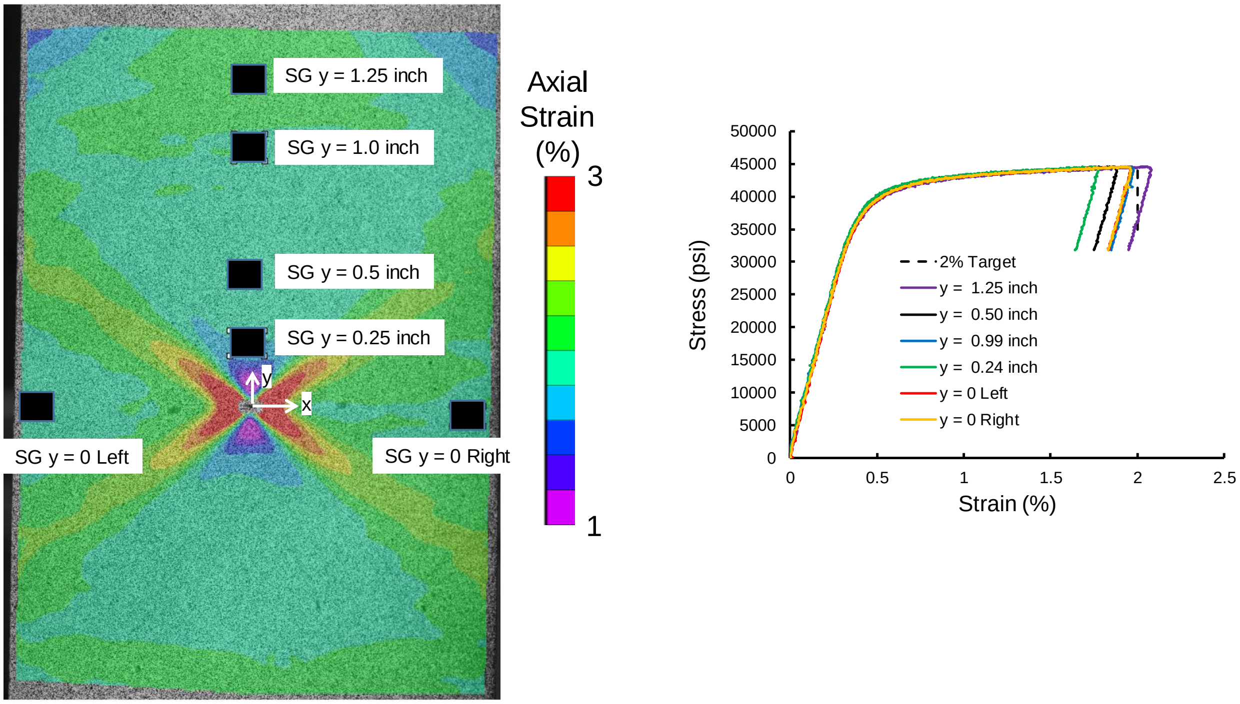

Figure H.2. Virtual strain gage (SG) locations and resulting strains.

Edge Extensometer Measurements

The far-field behavior of the uniaxial coupon was characterized using edge extensometers of different gage length (L) that were centered on the plane of the crack, as shown in Figure H.3. The resulting strain measurements slightly increased with increasing gage length, but all were within ±5%. This suggests that the edge extensometers can produce far-field strains that are largely insensitive to the length of the extensometer.

Best Practice Recommendation

Edge extensometers (physical of DIC virtual) are recommended for measuring far-field strain in uniaxial coupons. The length of the extensometers does not appear to significantly change the strain measurements, but it is recommended that a consistent gage length be used for all tests. The extensometers should be placed on both edges to verify that the loading is uniform. Physical edge extensometers have the limitation of not being able to characterize out-of-plane bending due to misalignment of the loading grips. However, DIC, or other full-field techniques, with virtual extensometers on the front and back surfaces can quantify the amount of out-of-plane bending. Edge extensometers have the advantage of being able to be used with guide plates for cyclic compressive loading if a small (<0.05 inch) amount of the coupon extends beyond the guide plates on both edges.

The use of strain gages is an acceptable alternative to edge extensometers if the gages are placed near the edges and along the plane of the crack. It is recommended that four strain gages be used (left and right edge on both front and back) to characterize any misalignment issues. Strain gages that are placed away from the edges should not be used to characterize far-field strains.

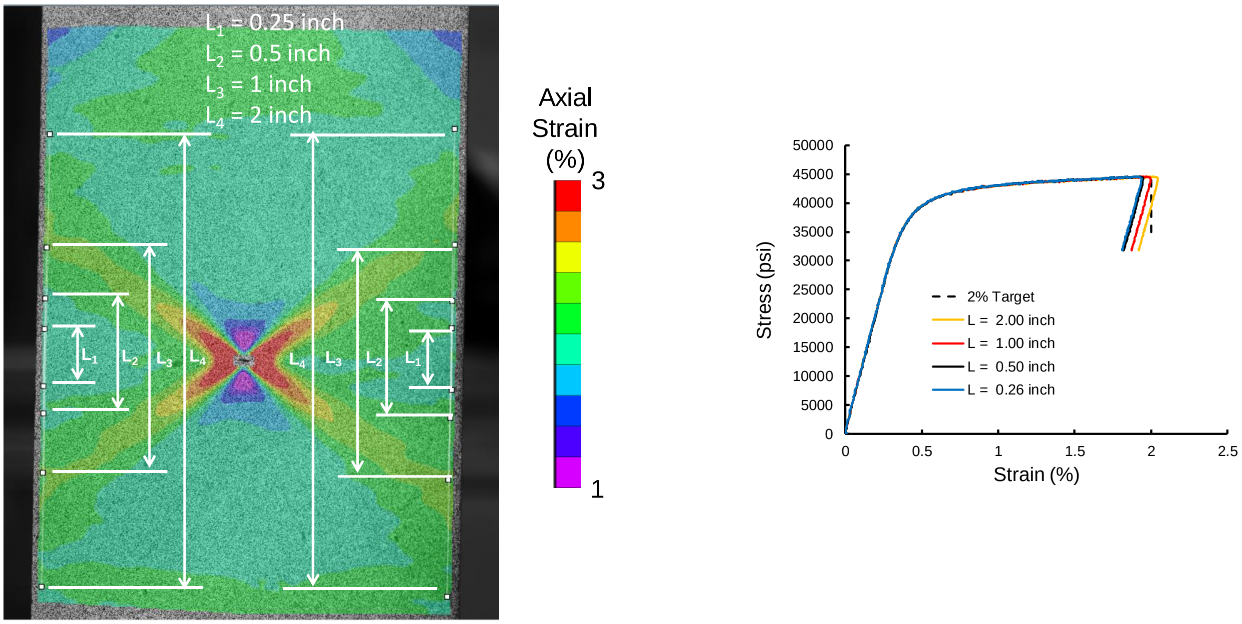

Figure H.3. Virtual edge extensometer locations and resulting strains.

Appendix I. The Use of Guide Plates

Best Practices: Guide Plates for Uniaxial Coupon Testing

Damage tolerance life qualification of COPV liners allows the simulation of the liner behavior using uniaxial coupons. The liner strain history that is applied to the uniaxial coupons generally contains cycles with compressive stresses minimum loads. These compressive stresses, coupled with thin liner material, result in a condition where the uniaxial coupons will buckle before reaching the required minimum loads. Guide plates are recommended to reduce the risk of the coupons buckling during the compressive loads. The need for guide plates could be estimated using the Euler buckling equation given in Equations 1-2.

$$P = \frac{\pi^2 EI}{(KL)^2} \qquad (1)$$

and

$$I = \frac{wt^3}{12} \qquad (2)$$

Where;
P = Estimated buckling load
E = Elastic modulus
I = Area moment of inertia
w = Width of coupon
t = Thickness of coupon
L = Length of coupon between grips
K = Column effective length factor (K = 0.5 for both ends fixed)

Typically, the stress at the minimum strain after autofrettage exceeds the compressive yield stress. So, a rule of thumb is that if the estimated buckling load is less than 1.5 times the ultimate stress of the material, then buckling may occur and guide plates should be used. The following demonstrate how guide plates could be implemented for different uniaxial coupon configurations.

Coupon Thicknesses Greater than 0.05 inch

Coupons that are greater than 0.05-inch thick are relatively easily constrained from buckling using a simple "sandwich" method. Two metallic plates are used to surround the coupon as shown in Figure I.1. The metallic plates should be 3/8-inch thick or greater and match drilled. The inside surfaces of the metallic plates should be flat and parallel, and have a low friction surface, like Teflon tape, to minimize any load transfer through the plates. The bolts should be "finger tight" to allow the plates to slide easily along the coupon. The height of the guide plates should be sized to fit between the grips with a gap at the starting zero load that is about the thickness of a sheet of paper. The length of the coupon will permanently extend during the autofrettage strain, increasing the gap. The subsequent minimum strain will reduce the gap, but verification is required to make sure that contact (load transfer) between the grips and plates does not occur. If contact is observed, then the initial gap needs to be increased and the test repeated. Too large of a gap will result in buckling at the gap, as shown in Figure I.2.

Strain measurements are more difficult with guide plates in place and edge extensometers have been found to be easier to implement than strain gages at the edge. The requirement for edge extensometers is that the width of the guide plate be reduced to 0.1 inch less than the width of the coupon in the gage section. This allows the edge extensometers to make good contact with the edge of the coupon. Springs or rubber bands have been found to be effective at holding the extensometers in contact with the edges of the coupon, as shown in Figure I.1.

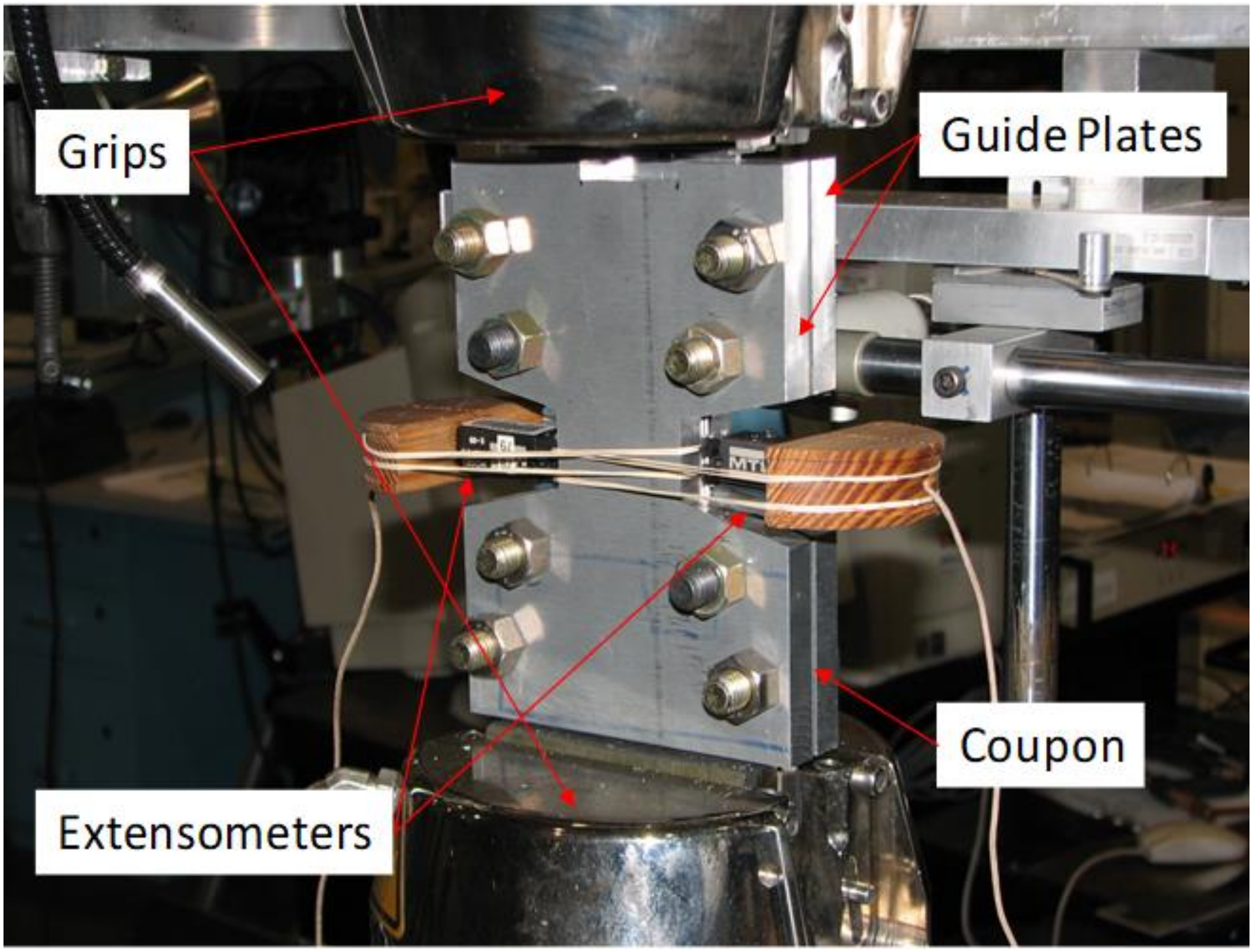

Figure I.1. Example of "sandwich" guide plates [ref. 1].

Figure I.2. Example of coupon buckling at the gap between the guide plates and the grips [ref. 1].

<u>Coupon Thicknesses Less than 0.05 inch</u>

Coupons with a thickness less than 0.05 inch have a strong tendency to buckle at the gap between the guide plate and the grips, as shown in Figure I.2. These coupons can be "sandwiched" with discontinuous sheets cut to the same dimension of the coupon to eliminate gap buckling. The inner discontinuous sheets are then "sandwiched" by the outer guide plates, as shown in Figure I.3. The inner guide plates extend into the grips and provide constraint in the gap region. The discontinuity of each plate prevents load transfer through the inner guides. The inner guide plates must be 0.1-inch narrower in width in the gage section to allow contact between the coupon edge and the extensometers.

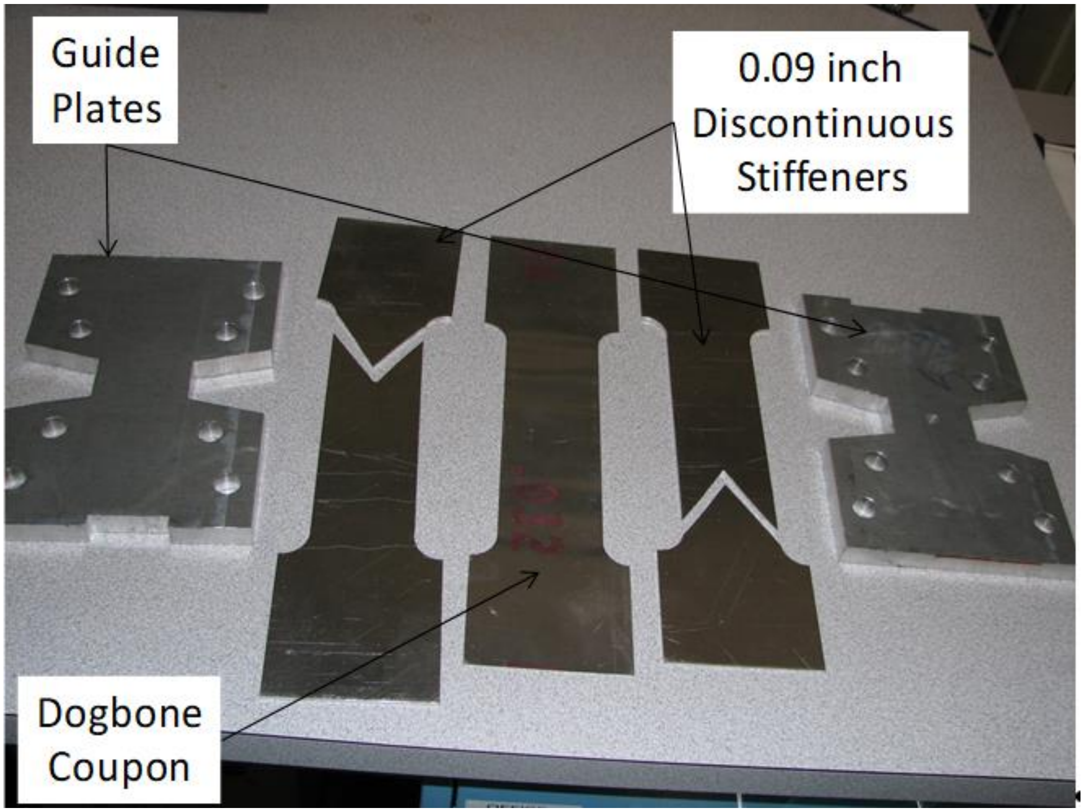

Figure I.3. Inner discontinuous sheets are then "sandwiched" by the outer guide plates.

Coupons Extracted from COPV Liners

Coupons extracted from liner material present an added complexity of the curvature of the tank. Coupons cut from a curved tank will retain a level of curvature that presents difficulties in constraining the buckling behavior. Sub-sized coupons are often used to minimize the curvature. Two options exist: (1) removing the curvature by machining the coupons flat, and (2) mechanically flattening the coupons. Machining the coupons flat is possible in the dome regions where the material is thicker or in other regions if the thickness greater than 0.1 inch. Mechanical flattening is possible for coupons extracted from thin liners, but residual stresses developed in the flattening process must be considered.

Coupons with Welds

Liners with welds may require that the weld and heat affected zone (HAZ) be qualified for damage tolerance. The presence of a weld bead may restrict contact between the guide plates and coupon. Machining the coupon flat, by removing the weld bead, would provide better buckling constraint, but may change the state of stress at the crack front. It is suggested that validated analyses be conducted to demonstrate that the selected method is conservative.

Reference

1. "Fracture Mechanics Based Methods Development for Composite Overwrapped Pressure Vessels (COPVs) with Metallic Liners," NESC-RP-06-065, July 8, 2010.

Appendix J. N/A

This Appendix left intentionally blank.

Appendix K. Eddy Current Inspection of COPV Liners and Coupons

Eddy current background

Eddy current testing is well-established for the detection of surface breaking cracks in metals. An alternating electromagnetic field is established by an eddy current probe. This field induces currents in a conducting material in the vicinity of the probe, altering the impedance of the probe. Monitoring the impedance of the probe can thereby detect defects in the material under test. Currents induced in the metal by the eddy current probe are weighted toward the metal surface, decaying exponentially with depth into the material under test. The rate of decay is governed by the conductivity and permeability of the material under test, the frequency of the eddy current excitation, and probe geometrical effects. The inspection depth of an eddy current technique can be estimated from the skin depth equation:

$$\delta = \sqrt{\frac{\rho}{\pi \mu f}}$$

where the δ = the skin depth (standard depth of penetration), ρ= the material resistivity, μ = the material permeability, and f = the excitation frequency. The skin depth is derived as the depth into a conducting half space at which point a uniform electromagnetic plane wave will decay to e^-1 of its value at the surface of the conductor. Probe geometrical effects are not considered in deriving the skin depth equation resulting, in general, in an underestimate of the decay rate of the induced eddy currents. For most applications the estimate is nonetheless useful. The induced eddy current field decays increasingly gradually beyond the standard depth of penetration such that geometrical effects can be ignored as second order. In critical applications the sensitivity of the eddy current technique to the specific flaw type in the structure under test should be verified by experiment.

In AA6061-T6, the standard depth of penetration at the frequencies used in this study are given in Table K.1.

Table K.1. Standard Depth of Penetration at AA6061-T6Frequencies

f (kHz)	δ (mm)	Comment
4000	.05	High current density very near inspection surface. Detection capabilities limited to surface breaking cracks.
1000	.1	High frequency with limited depth of penetration. Provides some separation between lift-off effects and surface breaking cracks.
25	.6	Inspection depth on the order of thickness of .032-inch (0.8 mm) samples. Near full through the thickness capability with back surface variations muted.
10	1.0	Inspection depth greater than thickness of .032- inch (0.8 mm) samples. Good through the thickness coverage but highly sensitive to changes in material thickness.

Through-thickness Crack Detection

During a previous NESC assessment on fracture mechanics methods for COPVs [ref. 1] it was found that naturally occurring cracking can initiate on the liner ID during the high cycle fatigue process used to initiate and grow precracks on the liner OD. In that work a screening technique was developed to stop the fatigue process on a liner if an internal flaw was detected that had potential to grow into a through crack during the next fatigue interval. The applied technique was a low frequency eddy current inspection applied from the liner OD. At regular intervals during the fatigue process the liners would be removed from the load system, dried, and mounted on a computer controlled multi-axis stepper motor scanning system. Acquired data were processed to highlight changes in the eddy current response related to ID flaw growth.

In the current work a modified version of the technique used in [ref. 1] was applied to screen for ID flaw growth during precracking of the liners. As the liner thickness was reduced to approximately 0.030 inch in this study, the inspection frequency was increased from the prior work. A Zetec MIZ-27 SI eddy current impedance plane instrument was used to drive a Uniwest US3160 eddy current probe at 10 and 25 kHz. As shown in the table above, these frequencies should give good through the thickness coverage of the liner and allow frequency mixing techniques to help remove wall thickness effects and highlight ID flaw growth.

A phase rotation was applied to the eddy current response to rotate the lift-off response to the negative horizontal direction. Subsurface flaws would then have a response rotated clockwise from the lift-off line, with a phase shift approximately equal to 1 radian per skin depth at the flaw location. Calibration of the technique was performed on a 0.032-inch thick AA6061-T6 flat sheet specimen with a surface fatigue crack 0.040 inch long. Eddy Current scans of this sample performed with the scan surface opposite the flaw found good flaw detectability, with the signal response at 25 kHz nearly vertical and the response at 10 kHz rotated approximately 50 degrees away from the negative horizontal axis.

Scans were performed with the probe mounted in a customized probe holder incorporating a spring-loaded miniature profile rail guide and pivot mounts to maintain contact and orthogonality between the probe and liner during all scans. 5 mil thick Ultra High Molecular Weight (UHMW) Tape [CS Hyde Company Part Number 19-3A-.5-5] was used as a replaceable, low friction wear surface on the face of the probe. Analog output eddy current response data from the MIZ-27 were collected through a National Instruments analog to digital converter with acquisition rate timed to scan speed to produce the targeted spatial resolution. Four channels of data (real and imaginary components of the eddy current signal at the two inspection frequencies) where stored at each measurement point. The liners were mounted vertically and held by the port in the port down position. The liners were then rotated by the port while the separately mounted eddy current probe was fixed at a constant radial position and scanned in the z direction. Due to limitations in the length of the z-axis on the scanning system, two scans where required to cover the cylindrical section of the liners. A port scan started approximately 1 inch above the cylinder to dome transition and covered 8 inches vertically (along the axis of the cylinder). The second, dome end scan, began 1-inch lower than the end point of the port scan and continued 8 inches in the vertical direction ending approximately 1 inch from the opposite cylinder to dome transition. Specific settings used for the scans are given below.

Scan and Eddy Current Tester Settings

Z-Theta, 1500 steps second circumferential, .025" step size z, .0221" theta step (.4 degrees)

Scan circumference set at 22.5"

Uniwest US3160 D/P circular probe
Miz 27, 500 samples/sec 16avg
10 kHz, 20V, 40db, 64 degrees, 16avg, 0-200Hz BPF
25 kHz, 20V, 20db, 33 degrees, 16avg, 0-200Hz BPF
6.3" diameter x 20"length cylindrical bottle
360 deg x 8" scan, port end, start 1 inch away from port
bottle rotates clockwise as viewed from port side

All liners were scanned at the notched, uncycled state and then again periodically during the fatigue process. Scan data were process using ECgui eddy current data processing and visualization software [ref. 2]. C-scan plots of the initial eddy current data for liner 18072 are shown below in Figures K.1 through K.5. In this port end data, the changing liner thickness at the dome/cylinder transition is evident at approximately 1inch along the z-axis. Applying a high pass filter line by line along the circumferential (x-axis) direction removes this signal response along with the horizontal banding caused by thickness variations due to the liner forming process. Finally, performing a frequency mix removes other artifacts, highlighting the flow pattern of the liner metal developed during the liner forming process. Note that the 9 fatigue crack starter notches in the liner are also observable in Figure K.6, which shows the processed data for the port and dome end scans overlaid. The eddy current signature from these notches can be seen at x,z locations {(1.7, 3.2), (8.3, 3.2), 15.2, 3.2), (4, 7.2), (10.8, 7.2), (17.6, 7.2), (6.2, 11.3), (13, 11.3), (19.8, 11.3)}.

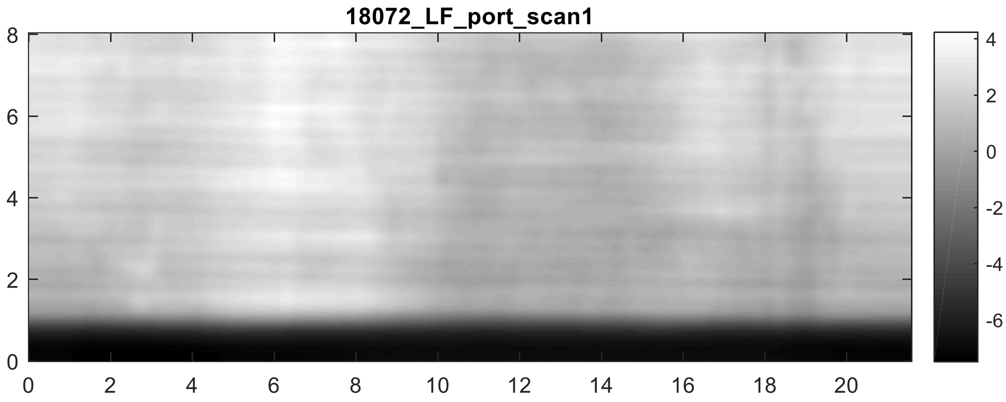

Figure K.1. 10kHz vertical channel response on liner 18072 at notched, unfatigued state.

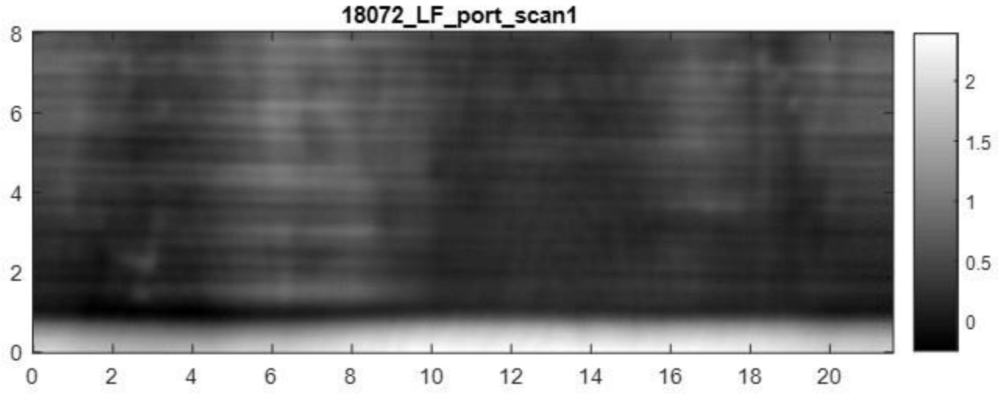

Figure K.2. 25kHz vertical channel response on liner 18072 at notched, unfatigued state.

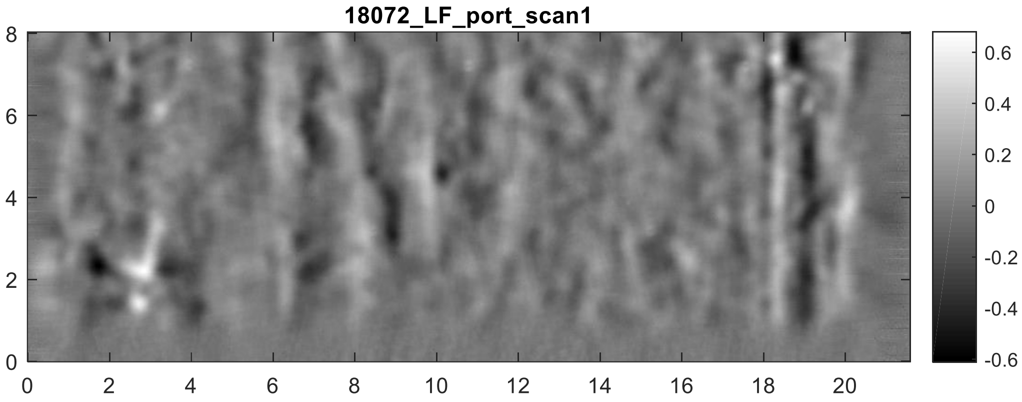

Figure K.3. 10kHz HPF vertical channel response on liner 18072 at notched, unfatigued state.

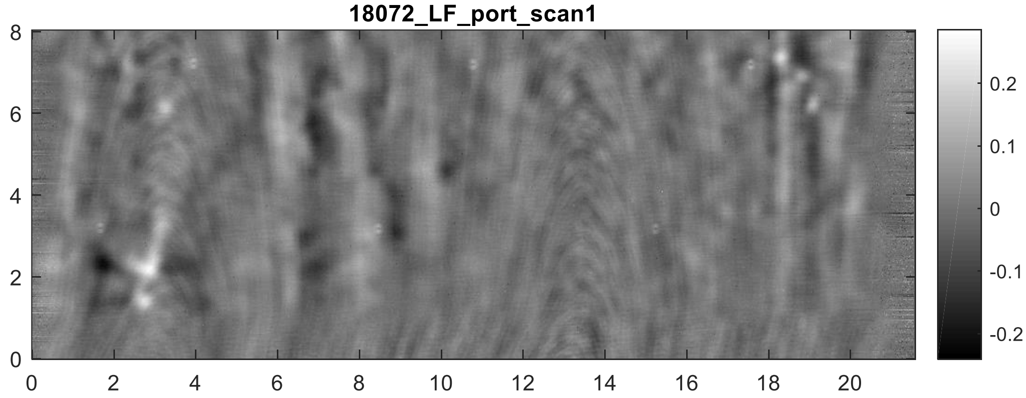

Figure K.4. 25kHz HPF vertical channel response on liner 18072 at notched, unfatigued state.

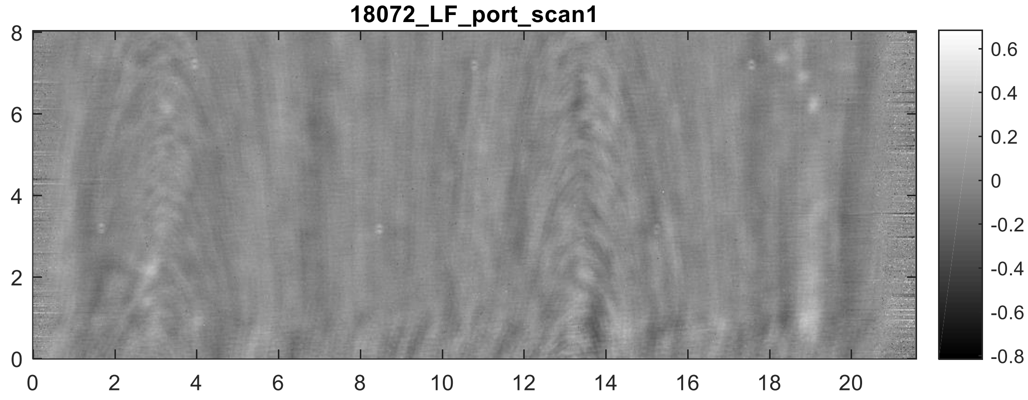

Figure K.5. 10/25 kHz HPF frequency mix response on liner 18072 at notched, unfatigued state.

The feature rich data shown in the previous plots make identification of ID flaw growth difficult. A data processing procedure was thus employed in which the baseline data was subtracted from subsequent data sets. Figure K.7 display the processed 25 kHz results for the port end scan of liner 18072 for multiple fatigue cycle counts. The color map has been held consistent through the plots to more easily see the increase in the flaw signals. The signal response at the locations of the OD starter notches increases as fatigue cracks initiate and grow, becoming visible in the baseline subtracted plots at 60,000 cycles. In the final data set, at 100,000 cycles, the location of cracks grown from all 6 OD notches in the port half scan are clearly visible. Two ID flaws are also detected. The ID indications, both appearing near x,z = (8,4.5), are barely visible at 60,000 cycles but dominate the response at 100,000 cycles. These two ID flaws are the second and third largest ID flaws detected in the liner set.

A close up view of the three flaws near (8,4) is shown in Figure K.8. The lowest flaw in this figure is a crack grown from an OD notch while the two higher flaws are ID indications. While the eddy current C-Scan response of the OD and ID flaws are similar, they can be clearly distinguished by their Lissajous responses. As seen in Figure K.9, the OD flaw has a phase angle close to the horizontal axis, while signature of the ID flaw is rotated approximately 90 degrees in a clockwise direction.

The largest ID indication was detected in liner 18086. Figures K.10 and K.11 show the 25 kHz response of the ID flaw at 10,000 cycles and again at 41,000 cycles. At this point it was decided to stop further cycling of the liner as the ID flaw was assessed to be approaching breakthrough of the liner wall. In these figures the top C-scan shows the vertical channel response at the labeled cycle count and the lower C-scan shows the baseline subtracted plot.

The complete results of the through the thickness eddy current inspections are given in Table K.2. The tabulated data shows the eddy current response versus cycle count for all tracked ID flaws, at both 10 kHz and 25 KHz. Figure K.12 displays a graph of the eddy current response versus cycle count for the seven largest ID indications at 10 kHz eddy current inspection frequency. Figure K.13 displays the corresponding 25 kHz data.

Three of the ID cracks identified during the eddy current through-thickness inspections where excavated from the liners following the damage tolerance testing of Section 7.2.3. In Table K.2 these three flaws are listed as 18072 C3, 18092 C2, and 18086 C1. Analysis of the fracture surface under SEM reported the (a x 2c) size of these flaws to be .0177” x .0347”, .0082” x .0171”, and .0098” x 0.45” respectively. Images of the fracture surfaces are shown in Figures N.39, N.50, and 7.2.3-8.

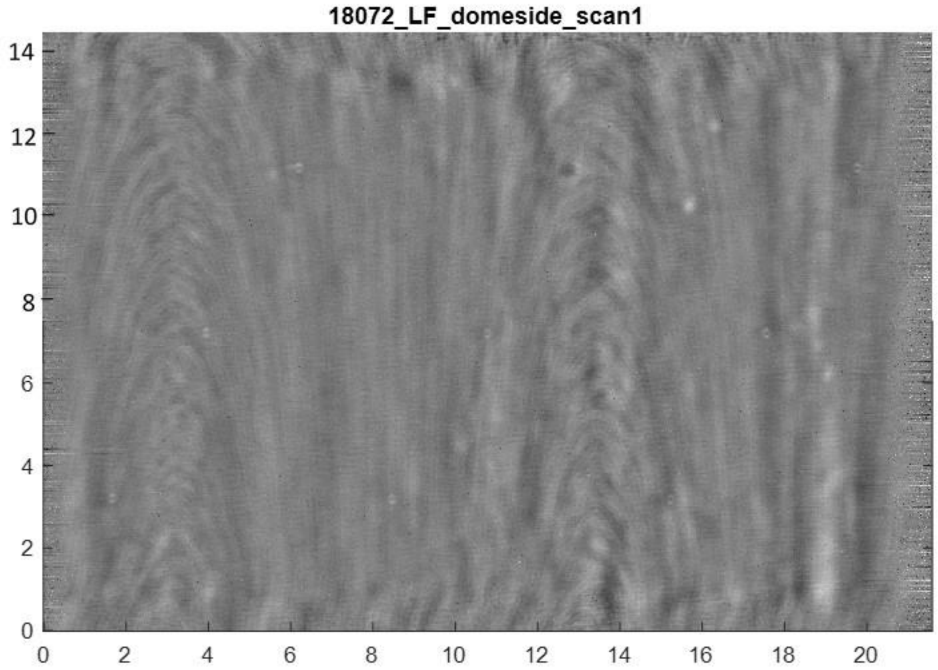

Figure K.6. 10/25 kHz HPF frequency mix response, port end scan overlapped with dome-side scan.

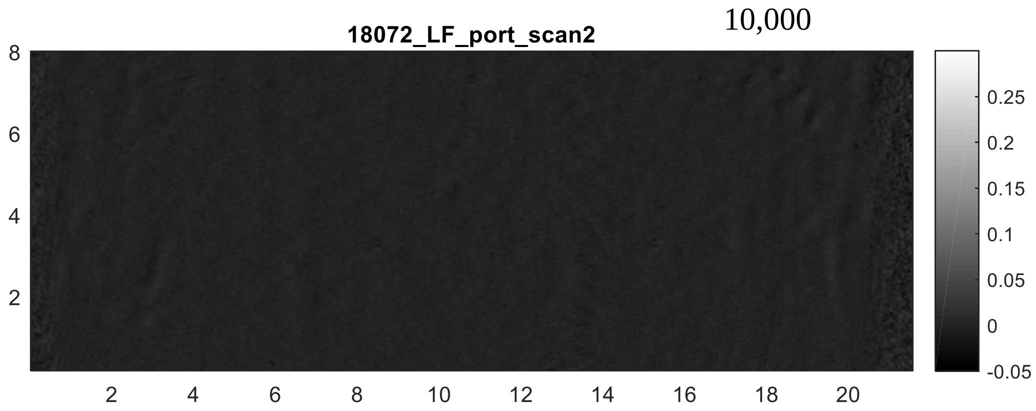

10,000

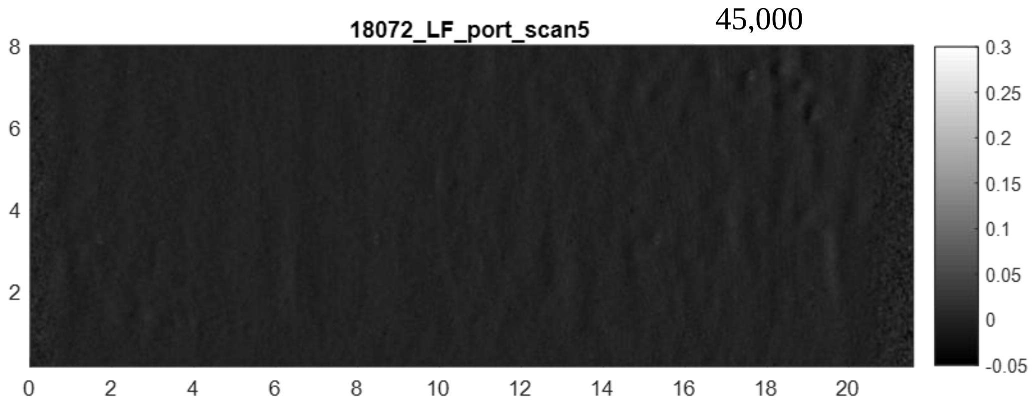

45,000

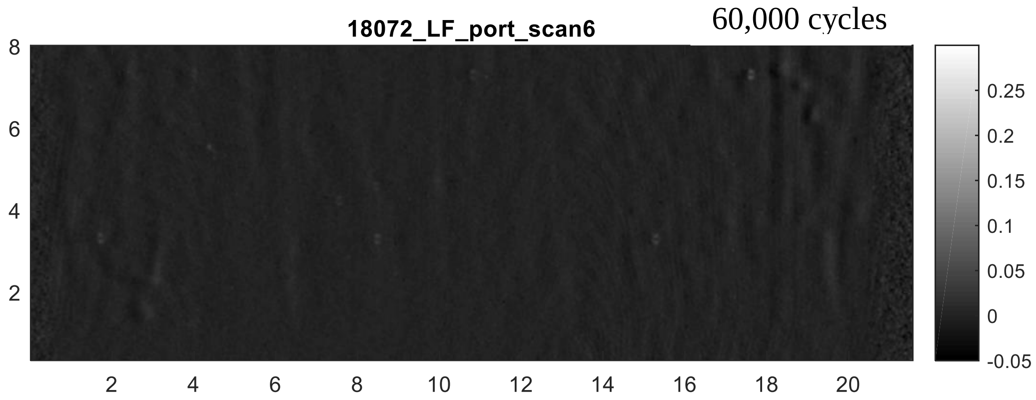

60,000 cycles

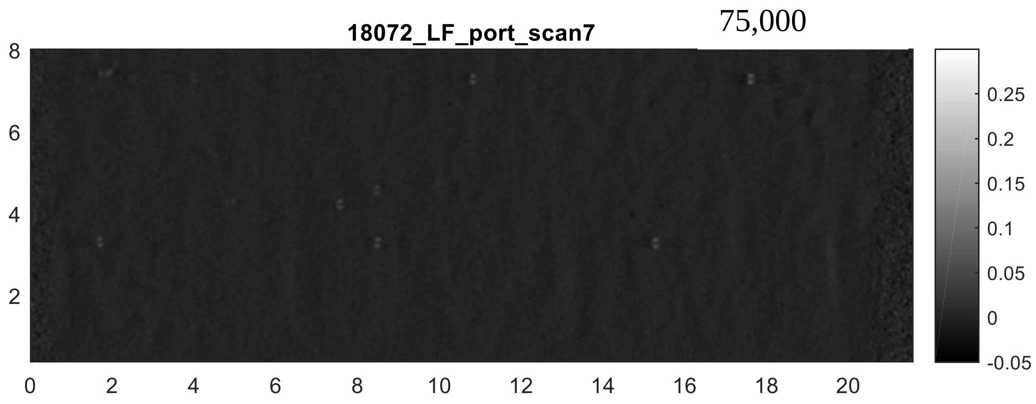

75,000

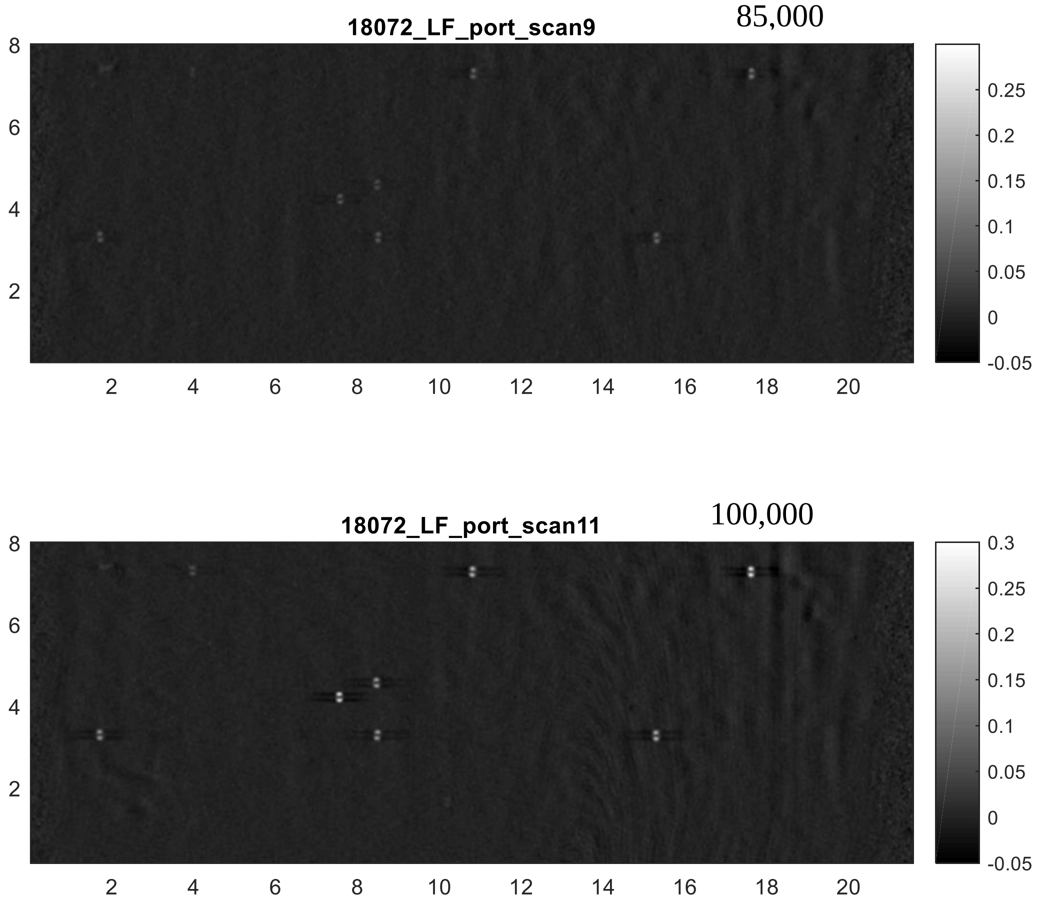

Figure K.7. Baseline subtracted eddy current results at 25 kHz for Liner 18072 at increasing fatigue cycle count. X and Y axes are in inches relative to the scan start position.

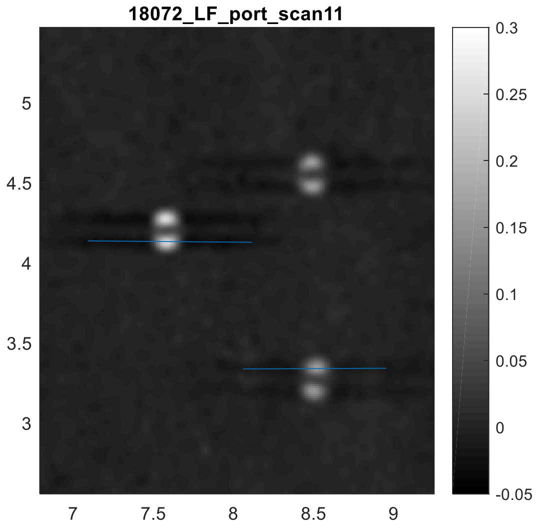

Figure K.8. Zoom in on figure K. 7 showing area containing three nearby flaws in liner 18072 at 100,000 cycles. Lowest flaw corresponds to a crack grown from an OD starter notch while two higher flaws are naturally occurring ID flaws. Data extracted along blue lines is used to generate the Lissajous plots in Figure K.9.

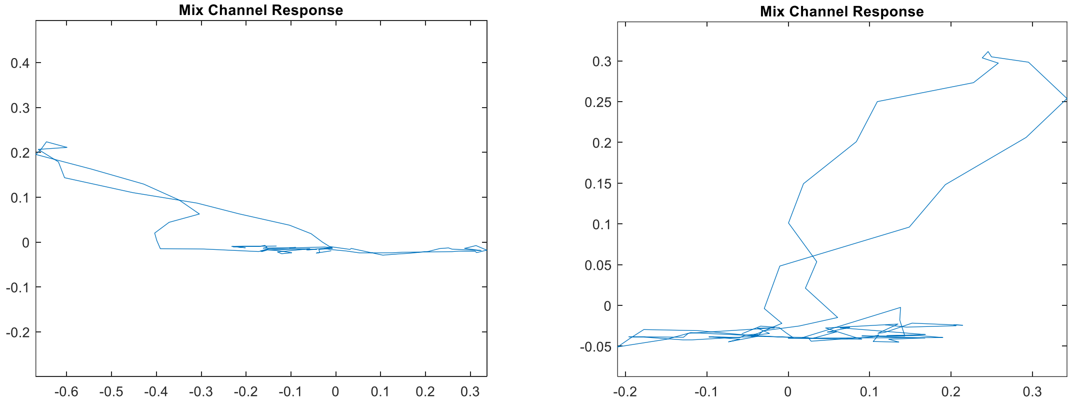

Figure K.9. Lissajous response for OD flaw (8.5,3.25) in Figure K.7, and ID flaw (7.5, 4.1) in Figure K.8 in liner 18072.

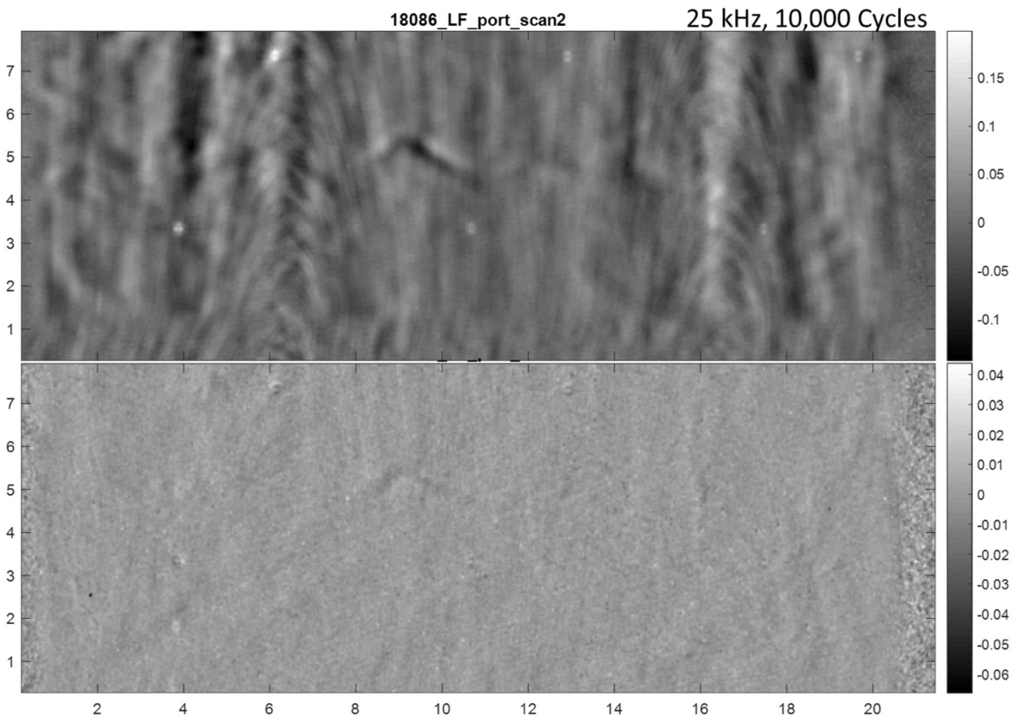

Figure K.10. HPF (upper) and background subtracted (lower) 25 kHz eddy current response for liner 18086 at 10,000 cycles.

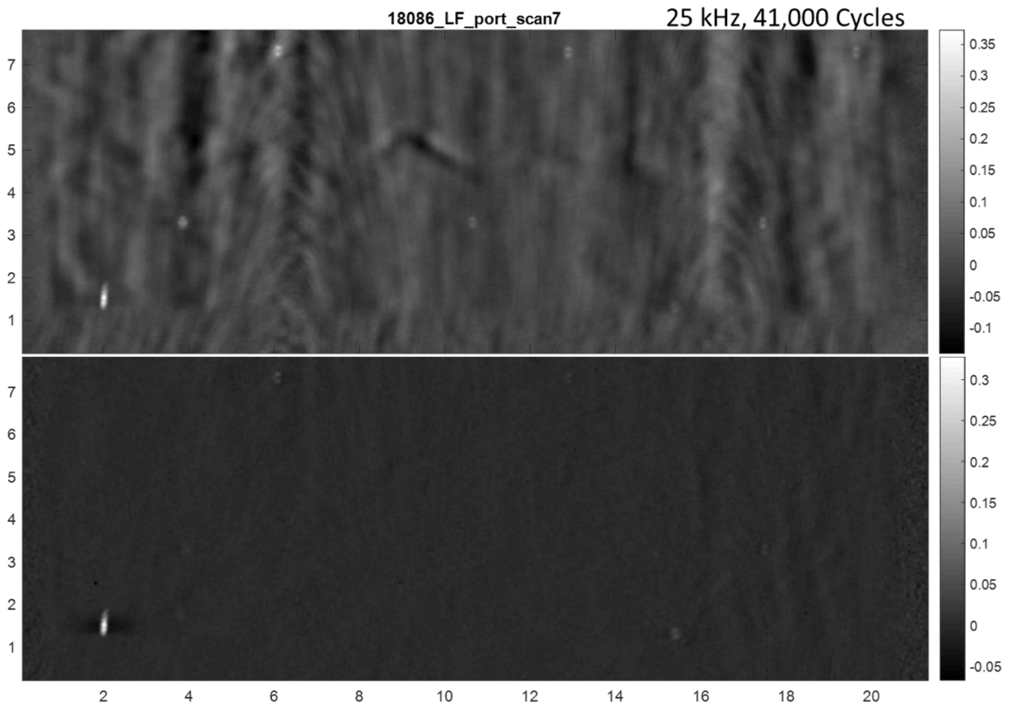

Figure K.11. HPF (upper) and background subtracted (lower) 25 kHz eddy current response for liner 18086 at 41,000 cycles. Indication at (1.98, 1.54) is the largest naturally occurring flaw detected in the liner data set.

Table K.2. Eddy Current Signal Response from all Tracked ID Indications During Fatigue Cycling Process

Eddy Current Response Liner 18072 (Volts)

Cycle Count	18072 C1 (7.6,4.2)P		18072 C2 (8.5,4.55)P		18072 C4 (10.2, 1.6)P		18072 C3 (19.5, 3.5)D	
	10KHz	25KHz	10KHz	25KHz	10KHz	25KHz	10KHz	25KHz
10000	0	0	0	0	0	0	0	0
20000	0	0	0	0	0	0	0	0
45000	0	0	0	0	0	0	0	0
60000	0.039	0.023	0.043	0.022	0	0	0	0
75000	0.081	0.048	0.072	0.036	0	0	0	0
80000	0.0985	0.065	0.0795	0.045	0	0	0	0
85000	0.12	0.074	0.099	0.054	0	0	0.047	0.028
90000	0.151	0.103	0.121	0.074	0.038	0.019	0.061	0.032
100000	0.335	0.249	0.227	0.158	0.058	0.031	0.134	0.087

Eddy Current Response Liners 18092 and 18099 (Volts)

Cycle Count	18092 C1 (19.25,1.61)P		18092 C2 (19.33, 1.91)P		18099 C1 (2.66, 5.22)P		18099 C2 (13.4, 4.7)P	
	10KHz	25KHz	10KHz	25KHz	10KHz	25KHz	10KHz	25KHz
10000	0	0	0	0	0	0	0	0
15000								
20000	0	0	0	0				
30000					0	0	0	0
35000	0	0	0	0				
45000					0	0	0	0
50000	0	0	0	0				
55000					0	0	0	0
70000	0.054	0.023			0.032	0.02		
75000	0.063	0.028						
80000	0.075	0.043			0.053	0.028		
85000	0.087	0.047	0.044	0.018	0.068	0.035		
90000	0.106	0.064	0.049	0.027	0.089	0.047		
95000	0.144	0.074	0.061	0.027	0.102	0.056	0.058	0.03

Eddy Current Response Liners 18074 and 18086 (Volts)

Cycle Count	**18074 C1 (11.88,1.95)P**		**18074 C2 (13.3, 2.4)P**		**18086 C1 (1.98,1.54)P**	
	10Khz	25KHz	10Khz	25KHz	**10KHz**	**25KHz**
10000	0	0	0	0	**0**	**0**
15000					**0.029**	**0**
25000	0	0	0	0		
35000					**0.28**	**0.12**
39000					**0.447**	**0.202**
40000	0	0	0	0	**0.541**	**0.252**
41000					**0.665**	**0.328**
55000	0	0	0	0		
70000	0.048	0.024	0	0		
80000	0.069	0.035	0	0		
85000	**0.081**	**0.051**	0	0		
90000	**0.102**	**0.058**	0	0		
100000	**0.14**	**0.077**	0.071	0.034		

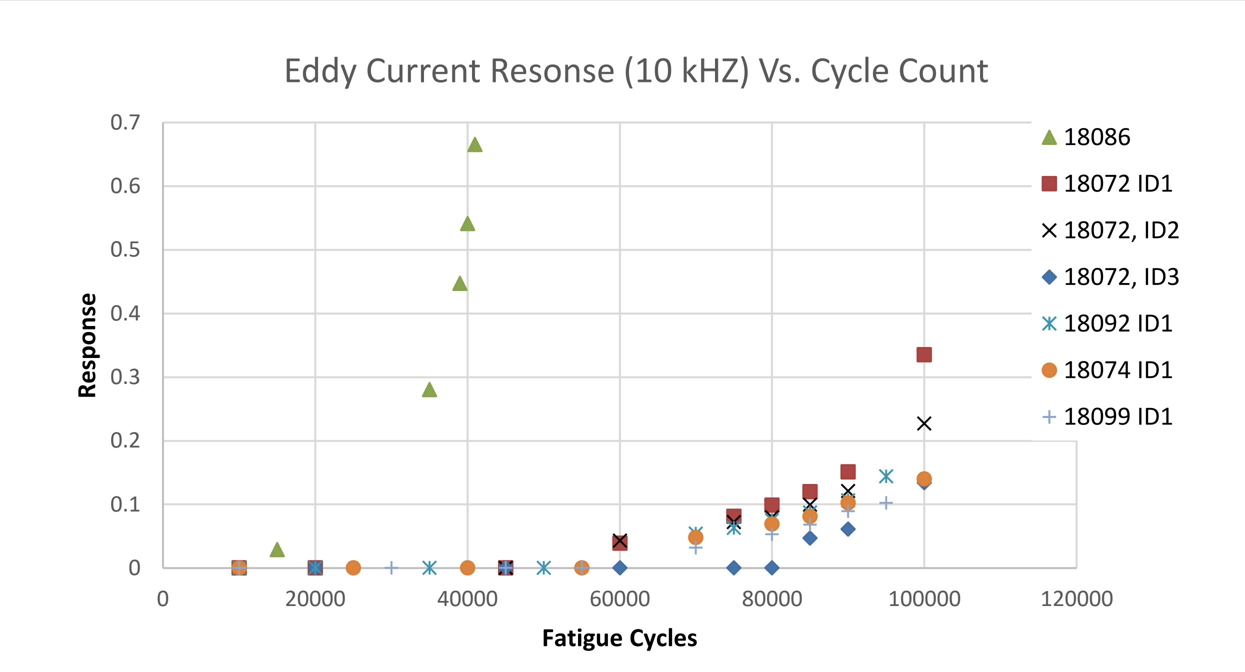

Figure K.12. Eddy Current signal response at 10 kHz versus cycle count for largest 7 ID indications monitored during the fatigue cycle process.

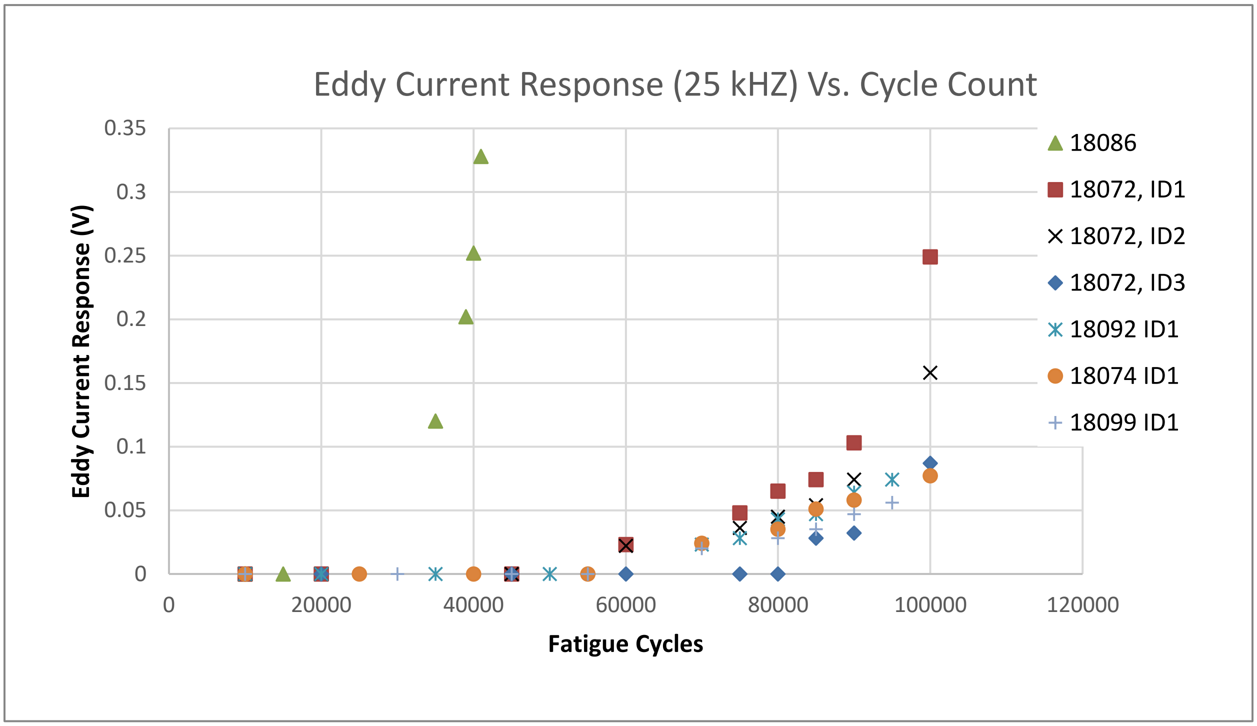

Figure K.13. Eddy Current signal response at 25 kHz versus cycle count for largest 7 ID indications monitored during the fatigue cycle process.

Surface Breaking Crack Inspections:

Eddy current inspections for surface breaking cracks in the COPV liners and coupons were performed using a modified version of the procedure described in [ref. 3]. This procedure was also applied in [ref. 4]. In the current work a Zetec MIZ-27 SI eddy current impedance plane instrument was used to drive a Uniwest 3151 dual element eddy current probe at 1 MHz and 4 MHz.

The articles under test where scanned using a computer controlled multi-axis stepper motor scanning system. A customized probe holder an incorporating spring-loaded miniature profile rail guide and pivot mounts was used to maintain contact and orthogonality between the probe and part under test during all scans. 5-mil thick Ultra High Molecular Weight (UHMW) Tape [CS Hyde Company Part Number 19-3A-.5-5] was used as a replaceable, low friction wear surface on the face of the probe. Analog output eddy current response data from the MIZ-27 were collected through a National Instruments analog to digital converter with acquisition rate timed to scan speed to produce the targeted spatial resolution. Eight channels of data (real and imaginary components of the eddy current signal at two frequencies for each of the two probe elements) were stored at each scan point.

Three different scan setups for surface crack detection and sizing were used during this study. A brief description of the requirement of the eddy current test and the specific eddy current settings for each of these tests is described below.

High Frequency OD

This eddy current test was designed to help monitor the growth of the fatigue cracks from notches during the fatigue process of the COPV liners. Tanks were scanned in the as-notched condition and then again periodically at increasing fatigue cycle counts as the cracks were grown. The liners were mounted vertically and held by the port in the port down position. The liners were then rotated by the port while the separately mounted eddy current probe was fixed at a constant radial positioned and scanned in the z direction. A scan length of 10 inches in the z direction was used, covering an area from approximately 1 inch below to 1 inch above the nine starter notches. Data was processed using [ref. 2] to monitor the state of the cracking at the notch locations while also inspecting for natural crack initiation at other locations on the outer diameter of the cylindrical section of the liners. No significant outside diameter cracks away from the notch locations were detected in any of the liners. As the cracks at the notch locations could be visually inspected under optical magnification between cycle steps, eddy current data were used as supplemental information on analyzing the state of cracking damage at the notches. A secondary objective of the high frequency outside diameter eddy current scans was to refine eddy current crack sizing techniques. This can be accomplished by comparing eddy current signals recorded during the fatigue process to crack sizes destructively measured from coupons extracted from the liners following the damage tolerance testing.

Specific settings used for the scans are given below.

Scan and Eddy Current Tester Settings

Theta - Z2 scan, 1500 steps second circumferential, .005" step size z, .044” theta step (.08 degrees)

Uniwest US3151 driver/differential pickup EC probe
Miz 27, 0-275Hz BPF, 600 samples/sec, 16avg

1 MHz, 5V, 36db, 138 deg, circumferential
1 MHz, 5V, 36db, 138 deg, axial
4 MHz, 1V, 36db, 293 deg, circumferential
4 MHz, 1V, 36db, 272 deg, axial
6.3" diameter x 20"length cylindrical bottle
360 deg x 10" scan
Scan circumference set at 22.5"

Cal on Al notch sample, (.012, .020, .040), Al 7075, SN 10010
bottle rotates clockwise as viewed from port side

Figure K.14 displays the full high frequency OD scan results for liner 18072 after 100,000 fatigue cycles. In the full scan the grown fatigue cracks are difficult to see as the crack lengths, on the order of 0.05 inch, are more than two orders of magnitude smaller than the scan axis lengths. An automated flaw detection technique, modified from [ref. 3], was applied to analyze the data set for indications corresponding to fatigue cracks. The phase rotation listed in the eddy current test settings above was applied to produce a vertical eddy current response for surface breaking crack in AA6061-T6. The 4 MHz vertical channel response was used as input to the automated flaw detection routine. A surface fit using a structural element size of .025” x .075” was applied, followed by a convolution filter using the point response signature of the probe. Table K.3 displays the output of this processing routine for the data plotted in Figure K.14. Of the 12 indications reported, analysis found three indications not associated with the starter notches but instead due to surface residue or dings on the liner surface. These indications have been marked red in Table K.3. The flaw with the largest EC response is seen to be located at (x,y) location (3.6869, 5.4607). This EC signature for this flaw is highlighted in the bottom plot in Figure K.14 which plots a 1-inch square area centered at the indication. The indication is due to the crack grown from starter notch #4 on the liner. The Eddy Current Lissajous response for the flaw, extracted from the C-scan data along the blue line across the flaw in the bottom plot of Figure K.14, is shown in Figure K.15.

Table K.4 shows the OD fatigue crack response from each of the liners at the end of the fatigue cycle testing. Here, the tabulated eddy current response is calculated at the sum of the top eighteen pixels across the crack indication. The large ID indication of liner 18086 forced the fatigue cycle process to be stopped with OD crack sizes well below the targeted flaw size. As such, only the fatigue cracks within the axial band containing the two largest indications at the previous fatigue cycle increment (35,000 cycles) were recorded at the final fatigue count (41,000).

A log-log plot of the eddy current response after precracking versus the destructively measured crack size is given in Figure K.16. In this plot, the crack length is the precrack length (a_i, $2c_i$ in Table 7.2.3-1), corresponding to the crack size when the eddy current measurements were acquired.

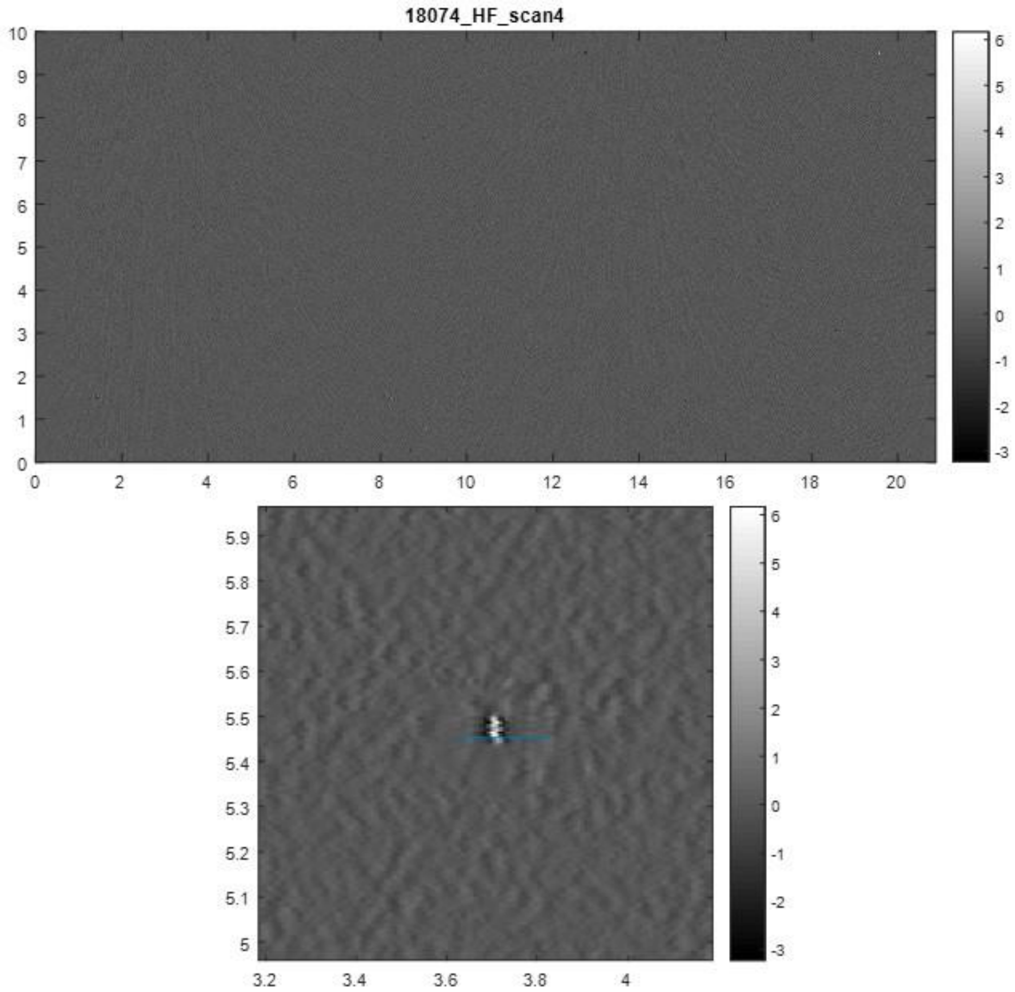

Figure K.14. Full area view of processed eddy current data at 4 MHz. Fatigue cracks are barely visible as small area bright spots in the top figure. Bottom figure is a zoom in view of crack formed at notch number four. X, Y axes are in inches from scan start position. Blue line across the indication area in bottom figure is the location of the extracted Lissajous signals in Figure K.15.

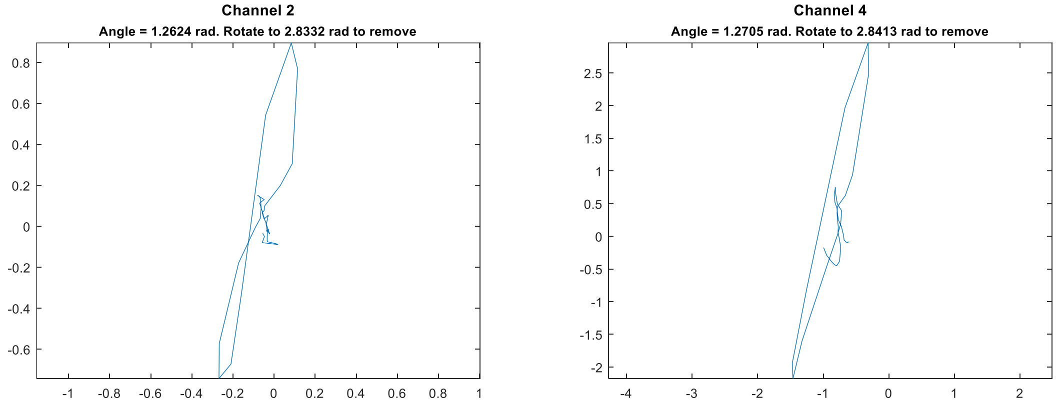

Figure K.15. 10 kHz and 25-kHz eddy current Lissajous response for the flaw shown the bottom plot of Figure K.14.

Table K.3. Detected flaws with locations in COPV liner 18074 after 100K cycles. Amplitude calculated as peak signal at flaw location.

xpos	ypos	xsize	ysize	volume	peak	s_n
8.729	0.2547	0.012	0.033	7.46E-05	3.7035	5.5507
1.4576	1.4621	0.0102	0.0352	1.20E-04	3.8981	5.8425
8.2621	1.4667	0.0198	0.0392	3.53E-04	4.6885	7.0271
15.0789	1.4706	0.0098	0.03	1.72E-04	4.451	6.6711
18.5785	3.0301	0.0026	0.0158	2.11E-05	3.7372	5.6013
17.4468	4.2341	0.0106	0.0143	7.31E-05	3.672	5.5036
3.6869	5.4607	0.0224	0.0492	6.95E-04	6.1619	9.2355
17.3186	5.4651	0.0103	0.0286	1.51E-04	4.5495	6.8188
10.4862	5.4741	0.0146	0.0404	3.45E-04	4.3608	6.536
19.5621	9.4627	0.016	0.0329	2.67E-04	4.6768	7.0096
5.9409	9.4651	0.0135	0.0421	2.91E-04	4.8452	7.262
12.7625	9.4762	0.0116	0.0379	2.72E-04	4.8838	7.3198

Table K.4. High Frequency Eddy Current Response at Final Cycle Count for all Liners. Amplitude calculated as some of 18 peak points contained in the flaw.

	18099 @90K		18099 @95K		18092 @95K		18074 @100K		18072 @100K		18086 @41K	
	4 MHz	1 MHz	4 MHz	1 MHz	4 MHz	1 MHz	4 MHz	1 MHz	4 MHz	1 MHz	4 MHz	1 MHz
c1	49.75	15.9	56.494	18.439	77.432	23.65	60.679	18.96	79.169	24.72		
c2	68.8	22.7	80.684	26.051	54.026	15.574	48.197	13.787	80.847	26.213		
c3	70.8	23.8	84.018	25.859	95.908	30.603	51.109	14.637	75.94	23.555		
c4	78.5	26.9	83.439	27.639	70.901	22.98	82.623	26.201	89.847	28.722		
c5	64.8	20.4	68.35	20.677	93.549	29.141	52.475	15.394	88.878	28.075		
c6	72.9	23.75	77.542	25.262	85.542	27.448	54.132	15.462	76.908	23.477		
c7	90.4	30.5	101.023	33.539	77.098	23.832	62.387	18.393	56.908	16.743	69.532	20.958
c8	59	17.85	61.355	18.171	59.825	18.192	60.87	17.204	60.223	17.83	62.343	17.875
c9	70.1	22.1	85.966	28.151	85.045	26.993	62.316	18.557	78.222	25.343	63.73	18.805

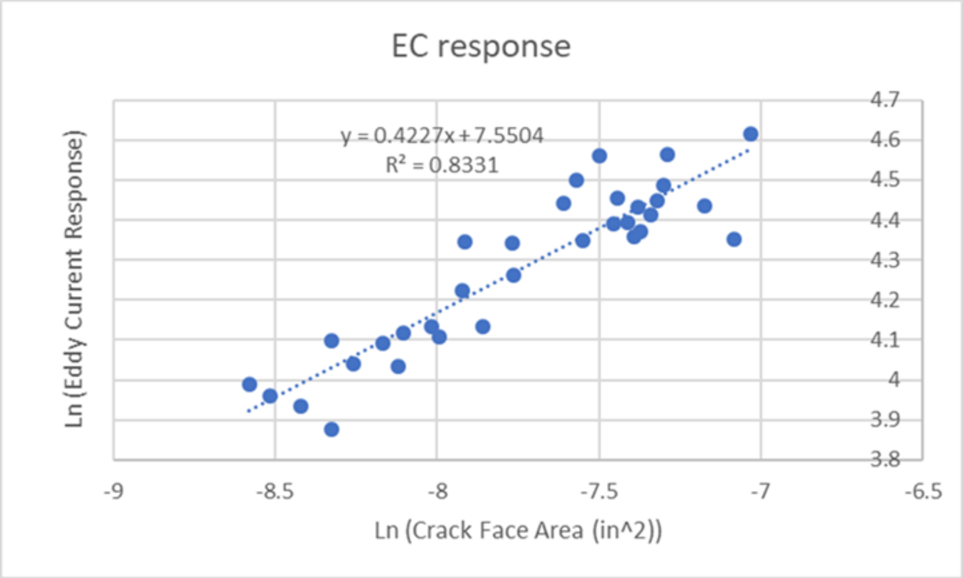

Figure K.16. Eddy Current Response measured at final step in liner precracking versus destructively measured crack face area of the precracks.

Post Mission Cycle ID

In previous work [ref. 1] it was discovered that naturally occurring cracking can initiate on the ID of the liner during the high cycle fatigue process used to initiate and grow the precracks on the liner OD. Inside diameter high-frequency eddy current testing provides an efficient technique for locating these naturally occurring defects so that they may be included in the crack growth study. The work was accomplished by removing the dome ends and longitudinally sectioning the mission cycled COPVs into two halves, resulting in semi-cylindrical sections approximately 15” long x 180 degrees. The tank halves were positioned horizontally on a pair of conveyor rollers and attached at the port end to a rotary table. The eddy current probe was positioned separately in contact with and along the center-line of the tank and scanned horizontally along the length of the cylinder while the tank half was rotated. Data were processed in alignment with [ref. 3]. As with the high frequency OD eddy current inspections, the 4 MHz vertical channel response was used as input to the automated flaw detection routine. A convolution filter using the point response signature of the probe was applied, followed by a line by line normalization of the data along the cylindrical axis of the cylinder. All indications above a 2V threshold were marked. Pitting, to some degree, was detected on all liners. Cracking, initiating from pits, OD notches that grew through the thickness, and other sources was detected on all liners. The locations of all indications were marked on the liners. Destructive analysis of a limited number of the detected ID cracks proceeded with the results included in the main body of this report.

Scan and Eddy Current Tester Settings

Y - theta scan, 2500 steps second, .0075" step size, 0.14 degree theta setup

Uniwest US3151 driver/differential pickup EC probe
Miz 27, 0-275Hz BPF, 600 samples/sec, 16avg

1 MHz, 5V, 36db, 138 deg, circumferential
1 MHz, 5V, 36db, 138 deg, axial
4 MHz, 1V, 36db, 293 deg, circumferential
4 MHz, 1V, 36db, 272 deg, axial

Cal on Al notch sample, (.012, .020, .040), Al 7075, SN 10010

Figure K.17 is a photograph of one section of liner 18072 following high frequency ID eddy current inspections. Twelve indications above a 2V threshold were detected and marked on the liner. The tabulated inspection results for all liners are shown in Tables K.5 through K.13. In these charts Xpos and Ypos list the location of the indication relative to the scan start position, Indication Length is the length of the indication along the cylindrical axis of the cylinder, and Indication Strength is the peak eddy current signal of the indication. Red text is used to highlight the larger indications. In some of the data sets locations where high frequency ID indications match with low frequency OD indications (performed on bare liners prior to wrapping, as discussed above) or OD starter notch locations are noted in the comments. Low frequency OD inspections for ID cracks were also performed on liner 18074 post damage tolerance testing, after removal of the composite but prior to sectioning the liner. Comments of LFP and LFD for that liner correspond to indications detected from the port or dome end scans during this inspection. All other comments of LF correspond to low frequency OD indications observed at the pre-crack stage prior to wrapping of the liners.

Two liners can be seen to be out of family in terms of number of ID indications detected, Liners 18074 and 18086. Liner 18074 was the first wrapped liner to undergo autofrettage and mission cycle testing. A failure of the hydraulic system occurred in reaching the autofrettage pressure on this first test. Repairs to the system occurred but the liner interior remained wet during this time period. Upon sectioning 18074 after damage tolerance testing corrosion pitting on the ID surface was prominently observed and resulted in the abundance of high frequency ID eddy current indications. Liner 18086 is the liner with the large ID indication detected by low frequency OD EC inspections in which precracking was halted early. During mission cycle testing this COPV failed during the first autofrettage pressure cycle. After sectioning and High Frequency ID EC inspections, no flaws beyond the one monitored during precracking were detected.

Figure K.17. Marked section of liner 18072 following high frequency ID Eddy Current inspection.

Table K.5. High Frequency ID Indications for 0-Degree Side of Liner 18074

Flaw #	Xpos (in)	Ypos (degrees)	Indication Length (in)	Signal Strength (V)	Comment
1	0.2344	103.1076	0.0466	5.4829	
2	0.4017	75.5249	0.0549	5.8085	
3	0.541	153.0255	0.0712	9.8657	
4	0.9787	125.0725	0.0295	2.409	
5	1.2133	20.5351	0.0766	8.8902	LFD1
6	1.7758	25.1718	0.042	3.6262	
7	1.7995	36.3058	0.0547	5.2369	
8	2.2405	83.896	0.0761	9.7267	LFD13
9	2.6536	41.9281	0.0717	7.1368	
10	3.2869	133.7206	0.0844	12.3476	LFD11
11	3.4527	80.8639	0.0872	10.105	LFD14
12	3.6081	21.7389	0.4637	15.2888	LFD2a
13	3.7438	124.732	0.0398	3.229	
14	3.9258	17.1038	0.1722	13.589	LFD2b
15	3.9988	104.4941	0.0644	5.5433	
16	4.0632	8.068	0.0569	8.9747	
17	4.3383	125.8712	0.0358	3.2386	
18	5.5612	101.0825	0.0577	5.4186	
19	5.7248	13.6372	0.0858	7.6327	
20	5.9467	167.4961	0.0737	7.6231	LFD10
21	5.9733	13.4632	0.0326	2.4889	Notch4, LFD4
22	6.0786	52.7655	0.0755	6.8192	
23	6.3439	128.5651	0.0723	6.3283	LFD12, LFP21
24	6.3605	17.6199	0.1338	10.6549	LFD3, LFP3
25	7.0138	43.0367	0.1012	8.2734	
26	7.4835	133.7238	0.067	8.6403	LFP20
27	7.617	13.2155	0.0285	2.743	
28	7.69	183.2293	0.0394	4.1837	
29	7.9156	158.5661	0.0728	9.4632	LFP19
30	8.2702	183.1504	0.0302	3.2062	
31	8.2783	9.109	0.0837	7.3941	
32	8.5668	9.9747	0.1106	11.6128	
33	8.6735	69.8353	0.1571	12.5798	LFP1
34	8.7765	158.6692	0.1277	14.9477	LFP18
35	8.8584	78.4728	0.0839	9.7894	
36	8.9305	2.2556	0.1069	10.8439	
37	9.1084	73.7089	0.0981	10.5396	
38	9.4796	119.0899	0.0356	4.495	
39	9.691	5.083	0.0402	4.98	
40	9.9716	23.0179	0.1331	10.9042	LFP2
41	10.556	78.9162	0.0558	5.0057	
42	10.8188	8.0342	0.0493	4.0468	
43	10.8942	18.4102	0.0229	2.938	
44	10.9179	1.4066	0.0325	3.4428	
45	10.918	59.1071	0.0583	6.8708	
46	10.9531	48.0918	0.0642	7.3724	
47	11.062	91.6999	0.0472	6.7279	
48	11.1004	24.6803	0.0976	8.7461	
49	11.5406	70.7092	0.0488	3.3556	
50	11.6315	162.5902	0.0943	9.2379	
51	11.9744	167.7965	0.0555	6.7073	
52	11.9996	10.5603	0.1708	16.7271	LFP5
53	12.1219	182.9451	0.0826	10.0933	
54	12.1267	84.2058	0.0476	4.6914	
55	12.1452	172.7607	0.0429	2.7057	
56	12.2759	154.1286	0.0597	6.7306	

Flaw #	Xpos (in)	Ypos (degrees)	Indication Length (in)	Signal Strength (V)	Comment
57	12.5612	76.0637	0.0828	7.6369	
58	12.7619	81.8006	0.0487	5.1209	
59	12.846	117.5914	0.0604	8.522	

Table K.6 High Frequency ID indications for 180-degree side of Liner 18074

Flaw #	Xpos (in)	Ypos (degrees)	Indication Length (in)	Signal Strength (V)	Comment
1	0.0172	80.404	0.0302	4.9329	
2	0.0362	11.6333	0.0667	5.3884	
3	0.0639	53.4528	0.1027	10.106	
4	0.3498	65.9274	0.0875	8.2992	
5	0.3949	59.3948	0.0952	9.2966	
6	0.4888	56.2944	0.1205	12.1695	
7	0.5706	51.1444	0.0532	6.4504	
8	0.645	116.1322	0.108	6.9373	
9	0.6586	142.4763	0.1606	12.7527	
10	0.7133	69.1781	0.0262	2.8786	
11	1.0644	142.4797	0.0906	5.8896	
12	1.2058	139.3854	0.0261	2.1836	
13	1.5261	53.9928	0.0829	9.8944	
14	1.7523	118.7191	0.0949	11.4553	
15	2.0826	103.3277	0.1302	12.5651	
16	2.088	79.5633	0.1106	9.4337	
17	2.4146	25.5737	0.035	3.2811	
18	2.4378	144.212	0.0181	2.7399	
19	2.4779	133.6138	0.0324	3.215	
20	2.5852	113.4725	0.091	8.9748	
21	2.755	51.288	0.0594	5.9722	
22	3.1237	73.9759	0.1428	13.5283	
23	3.1991	22.9512	0.0781	8.773	
24	3.2126	56.8653	0.0087	2.8952	
25	3.5745	142.2631	0.0231	2.3507	
26	3.6667	91.3621	0.7447	15.6194	
27	4.0437	95.9025	0.0436	2.6964	
28	4.1157	114.6692	0.0557	5.9251	
29	4.2808	62.9208	0.0771	9.2666	
30	4.3055	39.5797	0.0478	4.6823	
31	4.572	107.92	0.1862	14.5021	
32	5.1905	86.2584	0.3951	15.7901	
33	5.7191	66.8316	0.1038	12.1356	
34	5.7759	2.9479	0.0644	8.3626	
35	5.8319	88.0651	0.1851	12.8998	
36	5.8418	73.673	0.0351	4.6943	
37	6.4709	85.394	0.0383	4.2942	
38	7.4115	56.5624	0.0827	7.7626	
39	7.9709	1.0037	0.0265	3.5644	
40	8.1924	42.6917	0.0739	7.8626	
41	11.0124	3.1172	0.0479	3.9072	
42	11.2254	5.0078	0.0446	4.3319	
43	11.375	37.9467	0.0978	13.0281	
44	12.2354	71.228	0.0761	8.6872	
45	12.4393	44.5963	0.0512	6.2082	
46	12.5721	50.9552	0.0289	2.8113	

Table K.7. High Frequency ID Indications for 90-degree Side of Liner 18072

Flaw #	Xpos (in)	Ypos (degrees)	Indication Length (in)	Signal Strength (V)	Comment
1	0.3124	40.5954	0.0266	2.8390	
2	0.7938	154.7802	0.0657	4.8647	
3	1.3928	63.7964	0.0274	2.6444	
4	1.6410	117.1076	0.0513	3.7962	
5	2.3092	129.0153	0.0262	2.6332	
6	2.3522	63.7852	0.0286	2.4734	
7	2.5025	116.6990	0.0496	3.5399	
8	2.9300	126.2807	0.0493	3.4363	
9	3.3875	107.3227	1.1710	12.1655	LF indication (#1)
10	3.7281	123.5614	0.1193	9.0411	LF indication (#2)
11	3.9236	86.6212	0.0352	2.8679	
12	8.1689	87.9125	0.0394	3.1032	
13	10.4699	83.5100	0.1485	8.1784	N9

Table K.8. High Frequency ID Indications for 270-degree Side of Liner 18072

Flaw #	Xpos (in)	Ypos (degrees)	Indication Length (in)	Signal Strength (V)	Comment
1	0.4790	42.9577	0.0140	2.2839	
2	0.7638	11.1613	0.0183	2.2861	
3	0.9704	86.5909	0.0024	2.1621	
4	1.5039	39.0791	0.0315	3.2487	
5	2.2451	57.7335	0.0429	3.1848	
6	4.3197	116.8310	0.0456	3.1400	
7	5.2218	108.2753	0.0401	2.7119	
8	5.4976	107.6458	0.0545	3.5969	
9	6.0287	79.9532	0.0292	3.4998	
10	6.0362	127.1046	0.0221	2.8263	
11	6.4757	43.1915	0.0339	2.7083	
12	9.2694	127.0350	0.0986	7.0205	LF Indication (#3)

Table K.9. High Frequency ID Indications for 0-degree Side of Liner 18099

Flaw #	Xpos (in)	Ypos (degrees)	Indication Length (in)	Signal Strength (V)	Comment
1	1.6787	123.4468	0.0369	2.8405	
2	2.8496	159.8817	0.0169	2.6856	
3	3.1119	160.5272	0.0168	2.1789	
4	3.2248	161.8902	0.0395	3.8057	
5	4.0163	154.7812	0.0280	2.6205	
6	4.3471	76.9543	0.0303	3.3691	
7	4.3625	4.9154	0.0168	2.9872	
8	4.3981	140.6462	0.0708	4.7137	
9	4.7160	144.0896	0.1228	7.5980	
10	5.0907	69.6226	0.0203	2.8491	
11	5.1336	22.7835	0.0679	7.3577	
12	7.6600	34.1335	0.0426	3.7200	
13	8.8486	20.4009	0.0664	6.3719	

Table K.10. High Frequency ID Indications for 180-degree Side of Liner 18099

Flaw #	Xpos (in)	Ypos (degrees)	Indication Length (in)	Signal Strength (V)	Comment
1	1.1151	157.5399	0.0354	2.497	
2	2.0827	155.9356	0.0495	5.1406	
3	2.7269	149.7757	0.0542	5.6881	
4	3.4193	78.9895	0.0465	7.1729	
5	3.7334	1.8917	0.0415	3.5956	
6	4.0956	31.4484	0.0445	3.6638	
7	4.174	152.8909	0.0714	8.3501	
8	4.8137	157.1961	0.0446	4.3952	
9	6.2755	55.6509	0.0391	2.9153	
10	6.8588	97.3317	0.032	2.7317	
11	6.8669	88.8323	0.0245	2.7737	
12	6.8672	105.3445	0.0259	2.4414	
13	7.8132	33.9378	0.0339	2.6485	
14	10.5492	147.3233	0.4015	10.8342	N7

Table K.11. High Frequency ID Indications for 0-degree Side of Liner 18092

Flaw #	Xpos (in)	Ypos (degrees)	Indication Length (in)	Signal Strength (V)	Comment
1	0.1640	87.7316	0.1901	4.2924	
2	0.9546	90.7280	0.2488	9.7646	LF Indication (#1)
3	1.4054	89.3961	0.0580	2.8079	
4	1.4142	92.1297	0.1037	6.1988	LF Indication (#2)
5	1.5428	89.0040	0.0325	2.2369	
6	1.7175	77.3568	0.0205	2.7142	
7	1.8151	51.1850	0.0281	3.2910	
8	3.0899	81.0337	0.0326	2.9849	
9	3.9007	148.9785	0.0302	2.3993	
10	4.3249	7.6529	0.0286	3.1756	
11	4.6664	90.3522	0.0351	2.8245	
12	7.8549	84.5121	0.0357	2.9066	
13	10.7670	60.8040	0.0434	3.7066	

Table K.12. High Frequency ID Indications for 180-degree Side of Liner 18092

Flaw #	Xpos (in)	Ypos (degrees)	Indication Length (in)	Signal Strength (V)	Comment
1	1.3989	37.2758	0.0244	2.6719	
2	1.7176	142.9336	0.0234	2.9140	
3	2.3828	39.5242	0.0399	2.9672	
4	4.0421	149.9686	0.0579	4.1817	
5	5.1959	32.3460	0.0467	3.3441	
6	5.5762	125.8045	0.0391	3.3695	
7	10.6522	119.5570	0.0310	2.6203	

Table K.13. High Frequency ID Indications for 0-degree Side of Liner 18086

Flaw #	Xpos (in)	Ypos (degrees)	Indication Length (in)	Signal Strength (V)	Comment
1	0.8516	101.5878	0.6353	18.5509	LF Indication (#1)

Compression Test Coupons

Earlier work looking at compressive loading between smooth surfaces in AA6061-T6 found a drop in signal of approximately 3X with compressive loading of -32 ksi [ref. 5]. In this work, the effect of compressive loading on the eddy current detectability of surface fatigue cracks in liner materials was examined. Surface cracks where grown from starter notches in 0.090-inch thick AA6061-T6 aluminum sheet. The notches were then polished away, reducing the sheet thickness to approximately 0.078” and leaving only the surface fatigue cracks. Inversion of the crack dimensions from the eddy current response estimated the crack sizes at 0.04” long x 0.015” deep and 0.030” long x 0.010”. Post-test destructive analysis of the smaller flaw, shown in Figure K.18, measured the fatigue crack at 0.027” long x 0.010” deep.

Cracked coupons were fitted with anti-buckling guide plates and loaded into a hydraulic test system. Eddy current scanning was performed in situ, with a 2-axis scanning system mounted to the hydraulic frame. Eddy current data were acquired over the crack area at varying load levels, beginning in the unloaded state, increasing to 80% yield, decreasing to -80% yield, and then increasing back to zero load. Two cycles on each coupon, occurring on different days, were run. In the first set of tests onset of buckling was observed so the maximum compressive load was not reached. Modified guide plates were then designed and incorporated that allowed the full load range to be tested.

The results, plotted in Figures K.19 and K.20 below, showed that load levels between +/- 80 yield had very little effect on the eddy current response to the surface fatigue cracks. A small uptick in the response with initial loading is believed to be due to opening of a smeared surface layer developed during polishing to remove the starter notch. It is not apparent on the second cycled using the new guide plates. The other perturbation of the data occurs near max compressive load for sample EC-yy-090-01 during the first run. Small buckling of the sample in a direction to open the fatigue crack was observed when trying to approach -70% compressive load. The load was therefore reduced to -40% compressive load and were the next data point was acquired. The data suggests that the contact resistance between crack faces of a surface crack formed during high cycle fatigue varies little with loading between +/-80% yield in AA6061-T6. While this would need to be tested for other materials, systems, and eddy current techniques, it is encouraging to the further development of inside diameter eddy current crack detection methods which could be applied for fracture control after COPV autofrettage.

COPV Life Test Compression Tests

Uniwest US3151 driver/differential pickup EC probe
Miz 27, 0-275Hz BPF, 600 samples/sec, 16avg

X-Z scan on load frame, 0.5” x 0.375”, 0075” step
0-275Hz BPF, 600 samples/sec, 16avg
4 MHz, 1V, 36db, 293 deg, circumferential
4 MHz, 1V, 36db, 272 deg, axial

Cal on Al notch sample, (.012, .020, .040), Al 7075, SN 10010

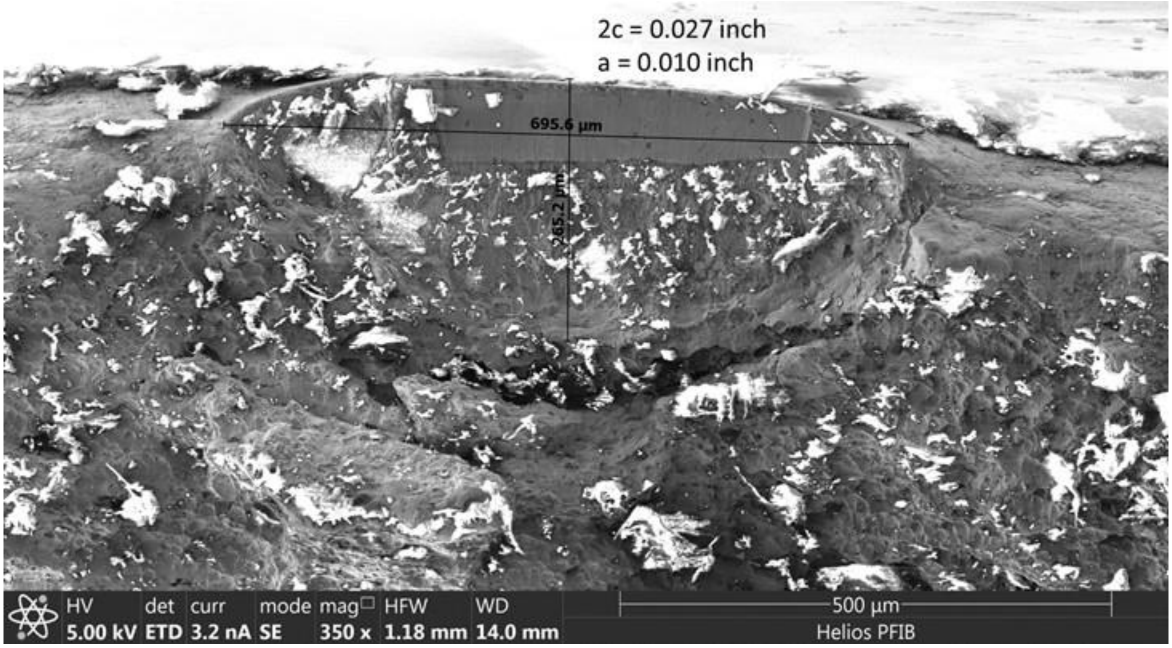

Figure K.18. Fracture surface of fatigue crack in panel EC-yy-090-02.

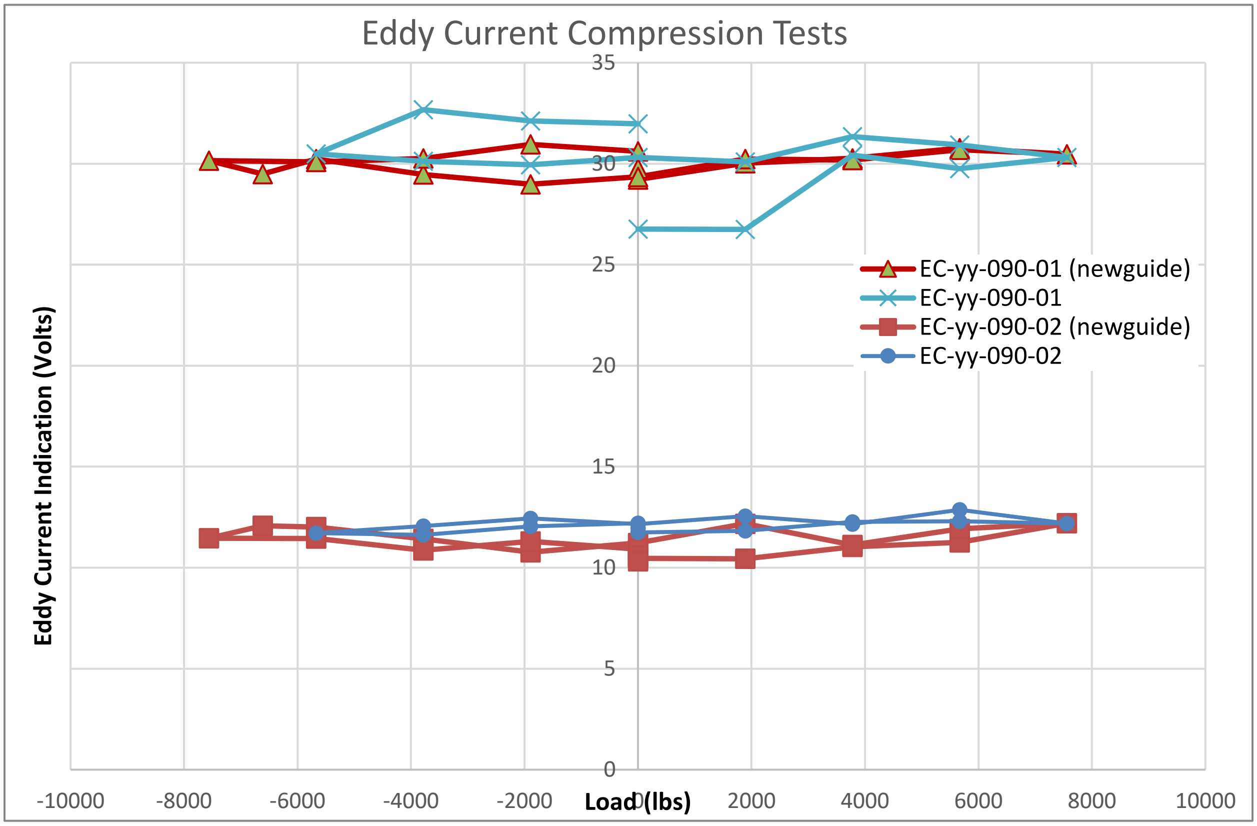

Figure K.16. Eddy current response vs. load for surface cracks in 3" wide x .078" thick AA6061-T6 sheets. Crack in EC-yy-090-01 is approximately .04" long x .015" deep and crack in EC-yy-02 is .027" long x .010" deep.

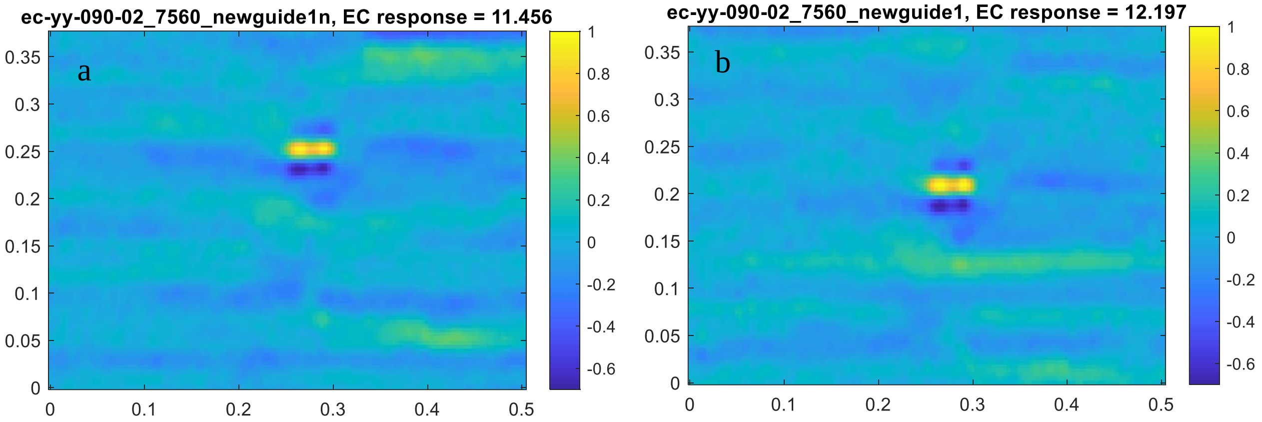

Figure K.17. Eddy current C-scan plots for sample EC-yy-090-02 at (a) 80% compressive and (b) 80% tensile loading.

References

1. Development for Composite Overwrapped Pressure Vessels with Metal Liners, NESC Assessment TI-06-065.
2. "ECgui eddy current data processing and visualization software", LAR-18978-1, 2016.
3. "Procedure for Automated Eddy Current Crack Detection in Thin Titanium Plates", NASA/TM–2012-217782.
4. "COPV Liner Inspection Capability Development Assessment", NESC-RP-14-00954, 2019.
5. AA&S 2010, "Eddy Current Evaluation of Fatigue Crack Growth in Integral Structures", http://meetingdata.utcdayton.com/agenda/airworthiness/2010/proceedings/presentations/P3207.pdf, 2010.

Appendix L. Truncation

Damage tolerant qualification testing of COPVs can be a costly and time intensive process. Uniaxial coupons have been demonstrated to simulate the crack growth behavior of COPVs for AA6061-T6 (see Section 7.2.3). The uniaxial coupons are required to replicate the far-field liner strain history at the crack location with the largest crack that could be missed by NDE. However, uniaxial coupons have limitations: (1) uniaxial coupons cannot replicate the influence of bi-axial loading present in COPV liners, (2) uniaxial coupons also cannot replicate the influence of the composite on crack on the outside of the liner, and (3) uniaxial coupons cannot replicate the influence of the internal pressure on cracks on the inside of the liner. These limitations must be negligible, conservative, and otherwise accounted for in the analysis.

The replication of the far-field liner strain history in a uniaxial coupon presents the problem of the thin uniaxial coupons buckling under the compressive loads that are generally present in a COPV liner after depressurization from the autofrettage pressure. Fatigue testing of thin coupons under combined tension-compression loading cycles will require restraints to prevent buckling from occurring. Guide plates that “sandwich” the coupon are a common method of restraining the buckling (see Appendix I on anti-buckling guide plates), but add complexity to the testing and measurement of the applied strains. Coupon testing would be made much easier if the compressive loads could be ignored, eliminating the need for guide plates. However, a common misconception of fatigue testing is that the compressive portion of a tensile-compressive loading spectrum does not contribute to the fatigue crack growth damage. The assumption is that the crack tip is closed during the compressive loads, as exemplified by the convention of using the tensile portion of the stress range when calculating the stress intensity factor range (ΔK) [ref. 1]. However, as cautioned [ref. 1], the existence of a large tensile overload, as occurs with the autofrettage cycle, and subsequent loading into compression will negate the assumption.

The influence of compressive loading, following an overload, can be demonstrated by running fatigue tests on identical coupons; one with the compression portion of the load truncated and the other with the full cycle, as illustrated in Figure L.1. The loading cycle is a simulation of a COPV liner spectrum with an autofrettage strain of 1.25%, and minimum strain of 0%, and maximum MDP strain of about 0.65% and minimum MDP strain of about 0.5%. Two AA6061-T6 coupons were precracked to a target crack depth of a = 0.025 inch and an aspect ratio of a/c = 1. One coupon was tested with the complete loading cycle (using guide plates to restrain the out-of-plane buckling). This coupon experienced compressive yielding at the minimum stress following the autofrettage cycle. The subsequent MDP cycles experienced tension-tension loading. The second coupon experienced the same autofrettage strain, but unloaded only to zero stress (truncation of the compression loading). The subsequent MDP cycles were identical to the tension-tension loading of the first coupon. Both coupons were fatigue cycled until the surface crack length was about 0.12 inch. Crack mouth opening displacements (CMOD) were made using DIC (see Section 7.2.1) periodically during the test. The coupons were failed by monotonic loading to failure after the target crack size was achieved. The fracture surfaces of the two coupons were examined using a scanning electron microscope (SEM), as shown in Figure L.2. The autofrettage cycle marked the fracture surface at the end of the precracking and the ductile fracture marked the fracture surface at the end of the fatigue cycles. The coupon with the complete loading history (SC-LT-090-15) reached the target surface crack length in fewer cycles, even though the initial crack depth was less than that of the truncated coupon (SC-LT-

090-16). The CMOD measurements were used to estimate the crack growth in the depth direction as a function of loading cycles, as shown in Figure L.3. The crack depth measurements demonstrated that the coupon that was truncated, excluding the compressive loading following the autofrettage cycle, grew significantly slower than the coupon with the full loading history. This suggests that truncation would be unconservative for a COPV loading spectrum. The difference in crack growth rate would be expected to increase as the minimum load of the MDP cycles become more compressive. Thus, the best practice is to use the entire loading spectrum when using uniaxial coupons to simulate the fatigue crack behavior in COPV liners.

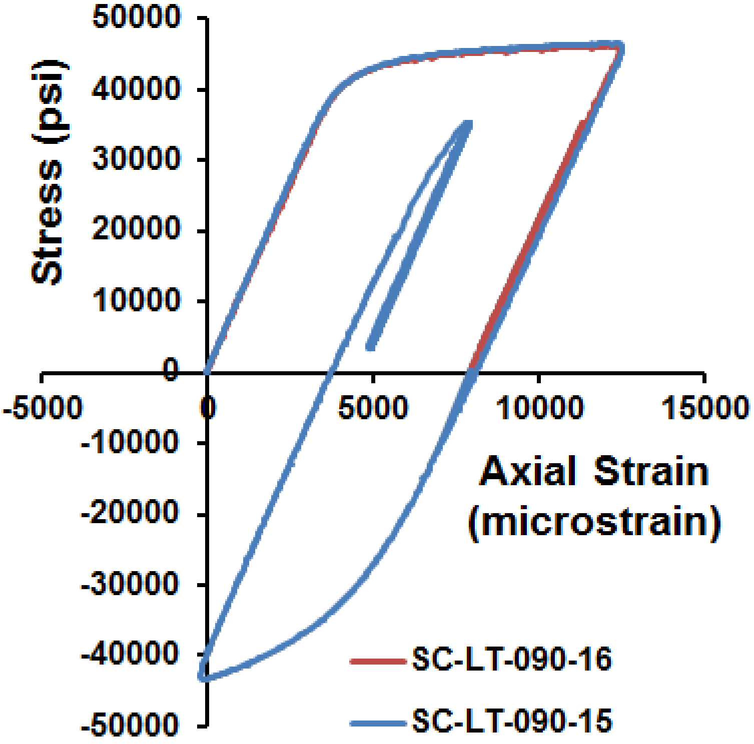

Figure L.1. Two loading histories with the same peak strain and one truncated at zero stress and the other compressed to zero strain.

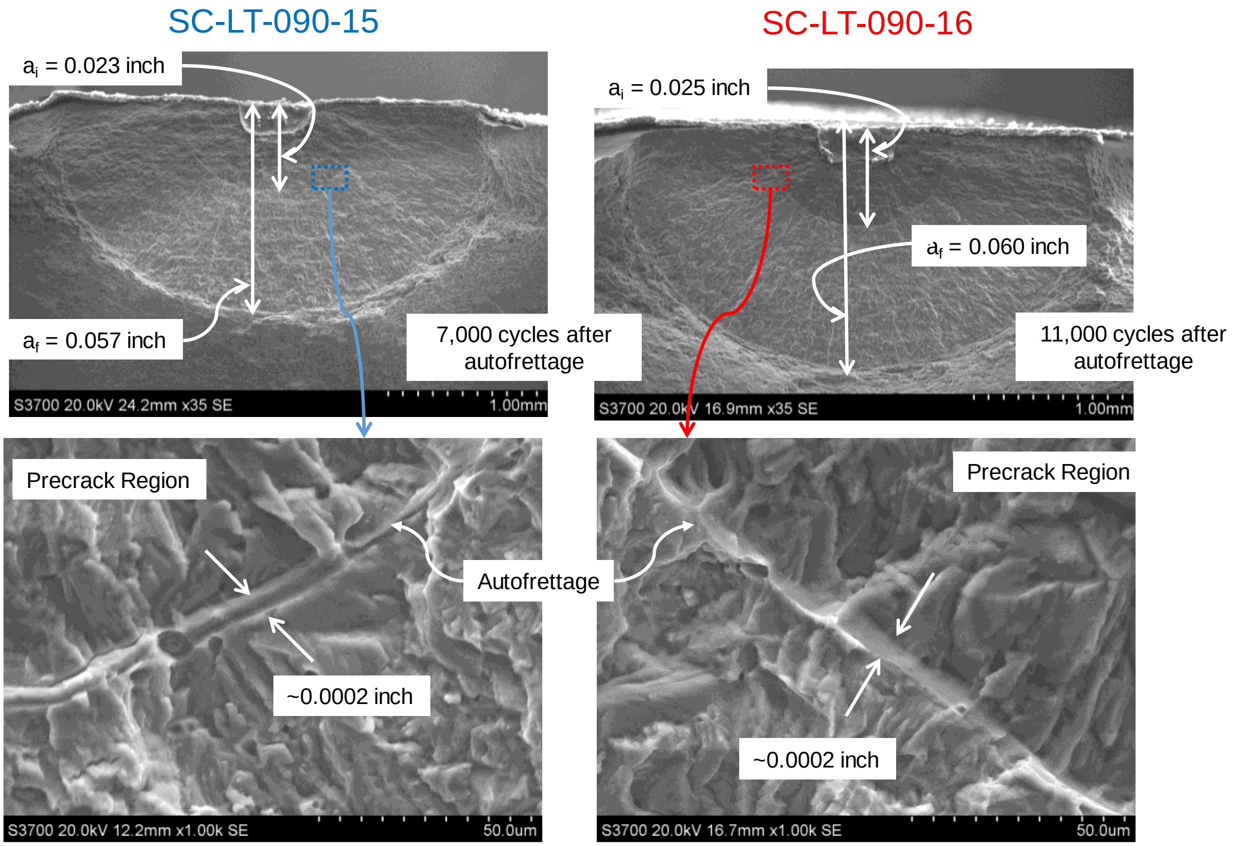

Figure L.2. SEM images of the fracture surfaces from Al fatigue tests without truncation (SC-LT-090-15) and with truncation at zero stress (SC-LT-090-16).

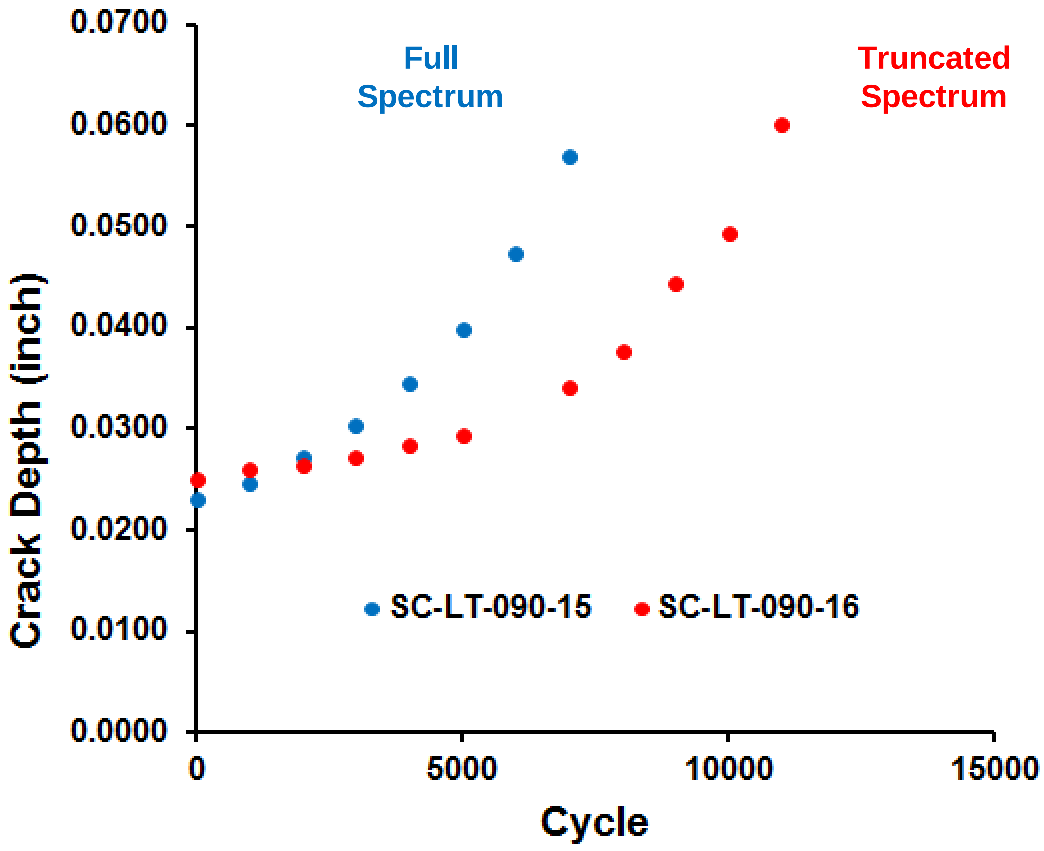

Figure L.3. Fatigue crack growth in the depth direction as a function of the number of fatigue cycles for AA6061-T6 fatigue tests without truncation (SC-LT-090-15) and with truncation at zero stress (SC-LT-090-16).

Reference:

1. “Standard Test Method for Measurement of Fatigue Crack Growth Rates,” ASTM E647-15, July 2016.

Appendix M. Fracture Surfaces from the Uniaxial Coupon Autofrettage Tests

Autofrettage tests were performed on uniaxial coupons made from three materials: AA6061-T6, IN718, and Ti-6Al-4V. Each coupon was precracked elastically before being loaded to the desired strain. The coupons were again fatigue cycled elastically at a peak load that was 70% of the load during the autofrettage cycle and a stress ratio of R = 0.8. The autofrettage testing procedure is described in detail in Section 7.2.2. Some of the tests were conducted with four repeated autofrettage cycles. The changes in the loading created marks on the fracture surface that allowed the determination of: (1) the crack size and shape at the end of the elastic precracking, (2) the amount of crack growth during autofrettage, and (3) if stable tearing was present. The autofrettage tests are summarized in Tables M.1 to M.3 for the AA6061-T6, IN718, and Ti 6Al-4V materials, respectively. Each fracture surface is presented in Figures M.1 to M.87.

Table M.1. AA6061-T6 Autofrettage Uniaxial Tests

ID	Thickness (inch)	a (inch)	a/c	Strain (%)	Delta-a (inch)
F-LT-032-002A	0.0305	0.024	0.98	1.50	0.00110
F-LT-032-003A	0.0310	0.027	0.74	2.00	0.00323
F-LT-032-004A	0.0310	0.023	0.88	1.25	0.00107
F-TL-032-003A	0.0325	0.024	0.94	1.75	0.00223
F-TL-032-002A	0.0325	0.026	1.06	2.00	0.00180
F-LT-032-007	0.0325	0.023	0.94	2.00	0.03825
F-LT-032-17	0.0315	0.023	0.92	2.25	0.00800
F-LT-032-009	0.0315	0.027	0.90	2.50	0.01000
F-LT-032-16	0.0315	0.023	0.94	1.75	0.00163
F-LT-032-02	0.0315	0.025	1.06	1.26	0.00109
F-LT-032-03	0.0315	0.023	1.02	1.49	0.00108
F-LT-050-011	0.0490	0.024	1.04	1.28	0.00028
F-TL-050-018	0.0500	0.027	1.08	1.78	0.00048
F-LT-090-018	0.0885	0.027	1.00	1.50	0.00028
F-LT-090-009	0.0895	0.028	1.04	2.00	0.00032
F-LT-090-011	0.0885	0.024	1.00	1.75	0.00010
F-TL-090-17	0.0875	0.029	1.09	2.25	0.00038

Table M.2. IN718 Autofrettage Uniaxial Tests

ID	Thickness (inch)	a (inch)	a/c	Strain (%)	Delta-a (inch)
IN718 F-LT-030-20	0.0295	0.019	0.8	1.77	0.0006
IN718 F-LT-030-18	0.03	0.028	0.92	1.73	0.0020
IN718 F-LT-030-19	0.03	0.024	0.84	1.68	0.0060
IN718 F-LT-030-16	0.03	0.027	0.93	1.73	0.0030
IN718 F-LT-030-01	0.0295	0.019	0.93	1.75	0.0007
IN718 F-LT-030-02	0.0305	0.022	0.88	1.70	0.0029
IN718 F-LT-030-17	0.0295	0.02	1.08	1.74	0.0005

Table M.3. Ti 6Al-4V Autofrettage Uniaxial Tests

ID	Thickness (inch)	a (inch)	a/c	Strain (%)	Delta-a (inch)
Ti-Dome-01-04-060	0.0585	0.025	1.06	1.07	0.0018
Ti-Dome-01-05-060	0.0585	0.027	1.02	1.02	0.0010
Ti-Dome-01-03-060	0.06	0.021	0.93	1.04	0.0008
Ti-Dome-01-06-060	0.059	0.026	1.04	1.02	0.0011
Ti-Dome-01-08-060	0.059	0.028	1.08	1.03	0.0009
Ti-Dome-03-01-060	0.064	0.035	0.99	1.10	0.0010
Ti-Dome-03-02-060	0.061	0.034	1.04	1.07	0.0020
Ti-Dome-060-03-03	0.06	0.035	0.85	1.17	0.0250
Ti-Dome-03-04-060	0.0615	0.038	1.01	1.08	0.0019 (0.016 at 30°)
Ti-Dome-03-05-060	0.058	0.025	1.06	1.02	0.0010
Ti-Dome-03-06-060	0.058	0.036	1.04	1.13	0.007 (0.023 at 30°)
Ti-Dome-03-07-060	0.0595	0.037	1.06	1.07	0.002 (0.022 at 30°)
Ti-Dome-03-08-060	0.0595	0.027	1.04	1.00 (4xAF)	0.0003
Ti-Dome-00-01-082	0.084	0.029	1.16	2.66	0.0038
Ti-Dome-00-02-082	0.082	0.032	1.19	2.53	0.0500
TI-Dome-00-03-082	0.0835	0.039	1.22	1.71	0.0445
Ti-Dome-00-04-082	0.082	0.025	1.00	2.72	0.0019
Ti-Dome-00-05-082	0.078	0.025	1.02	2.69	0.0008
Ti-Dome-00-06-082	0.081	0.023	1.15	2.68	0.0009
Ti-Dome-01-01-082	0.082	0.0123	0.18	2.72	0.0019
Ti-Dome-02-01-082	0.082	0.014	0.17	2.63	0.0019
Ti-Dome-02-02-082	0.081	0.019	0.27	2.77	0.0013

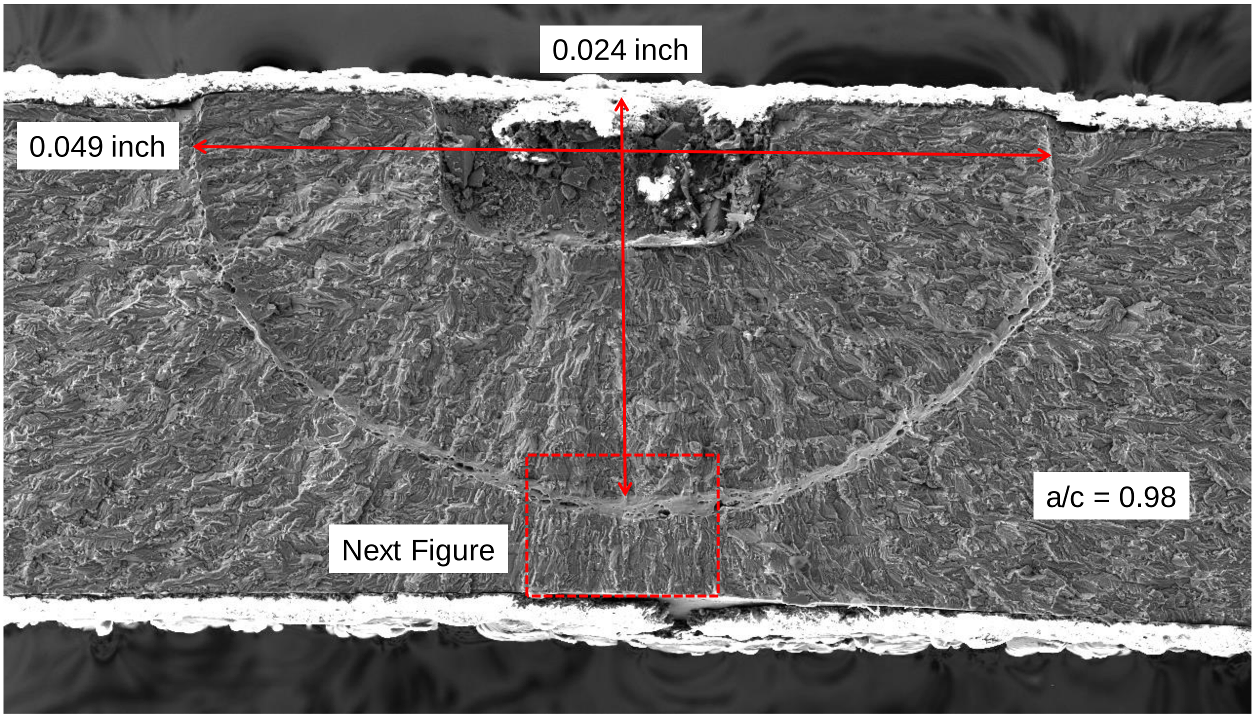

Figure M.1. Fracture surface for AA6061-T6 coupon F-LT-032-002A that was loaded to an autofrettage strain level of 1.5%.

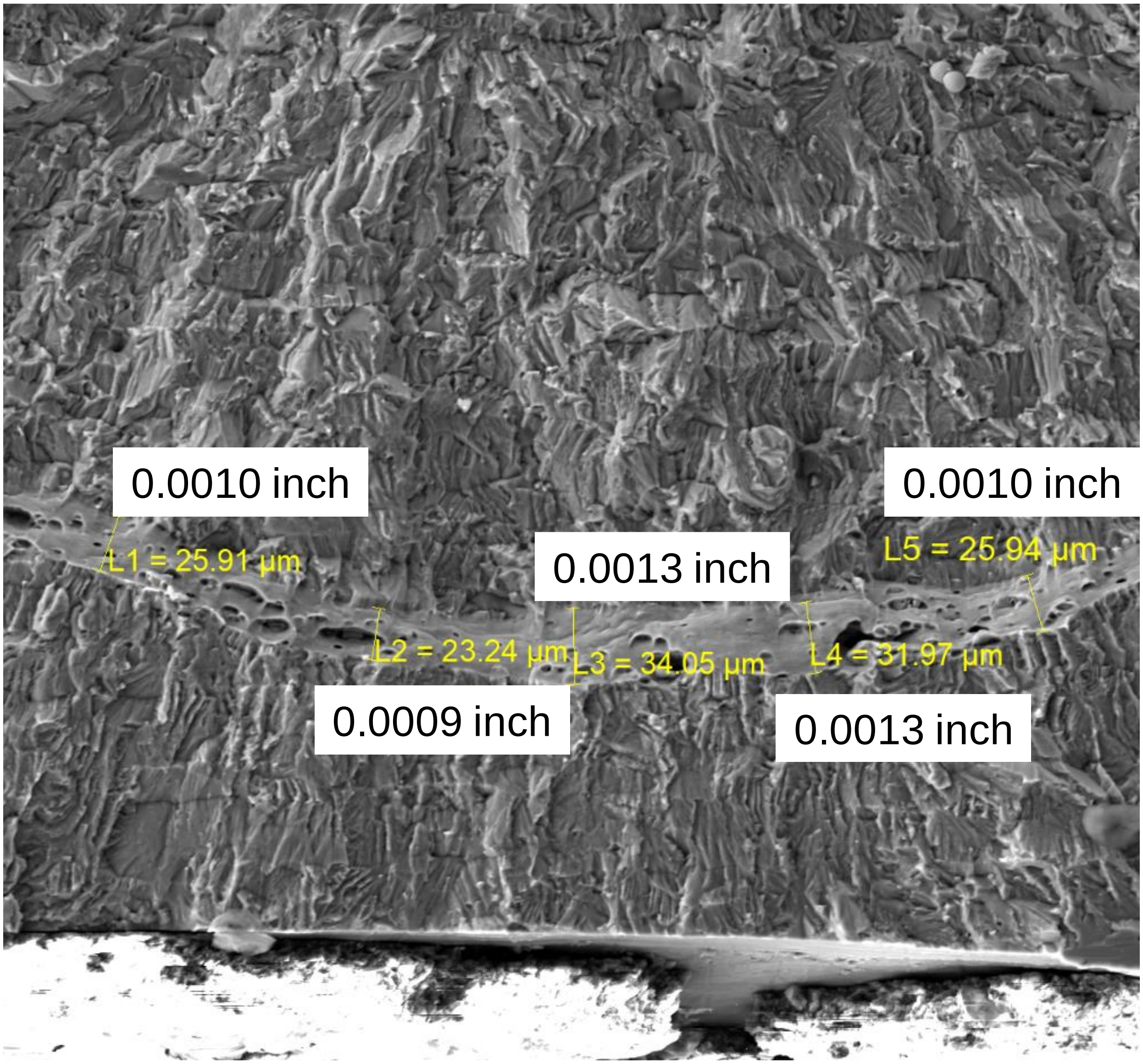

Figure M.2. Autofrettage measurements for AA6061-T6 coupon F-LT-032-002A that was loaded to an autofrettage strain level of 1.5%.

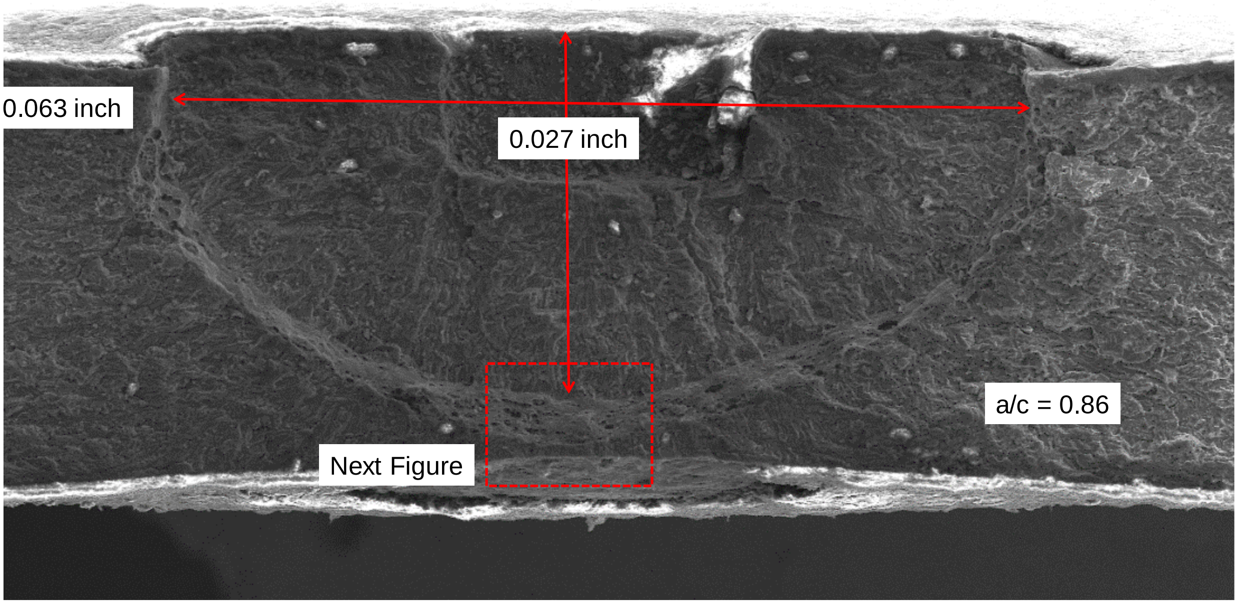

Figure M.3. Fracture surface for AA6061-T6 coupon F-LT-032-003A that was loaded to an autofrettage strain level of 2%.

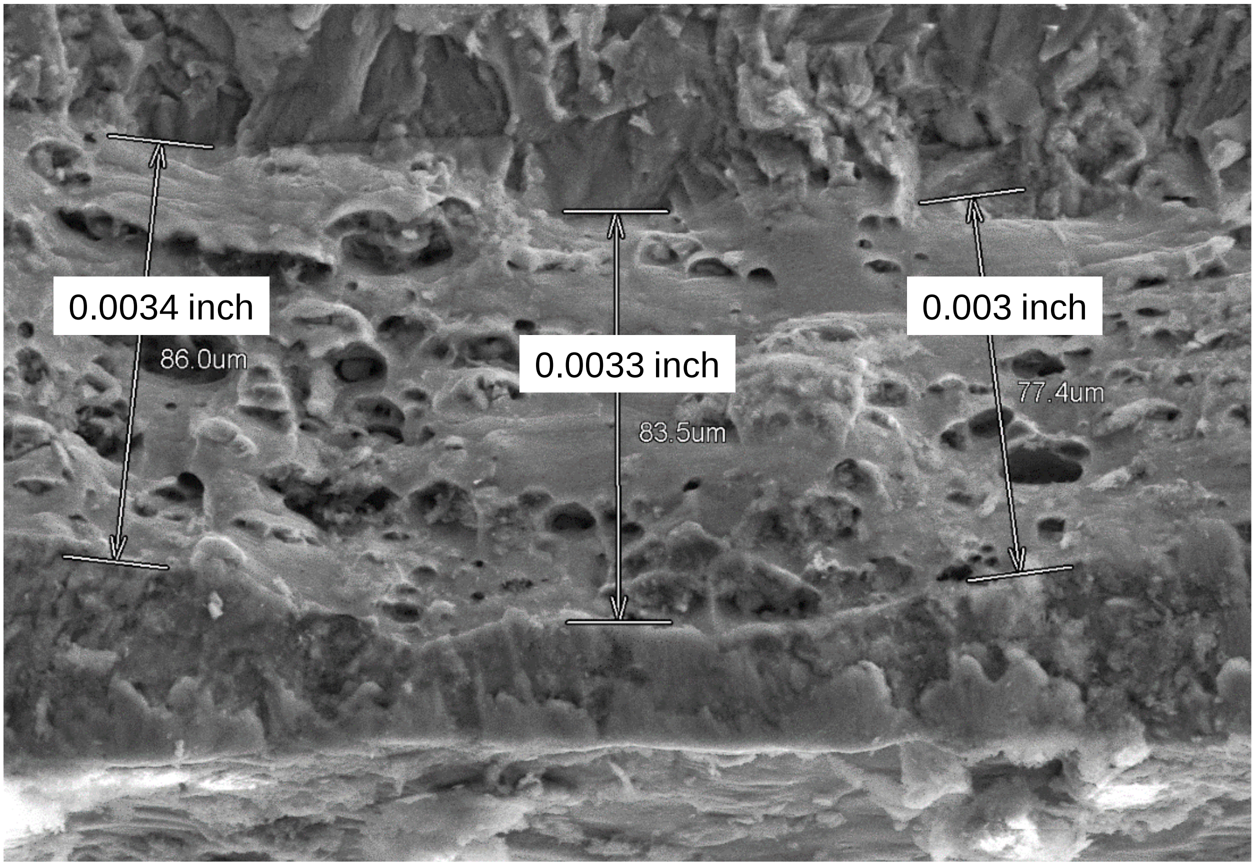

Figure M.4. Autofrettage measurements for AA6061-T6 coupon F-LT-032-003A that was loaded to an autofrettage strain level of 2%.

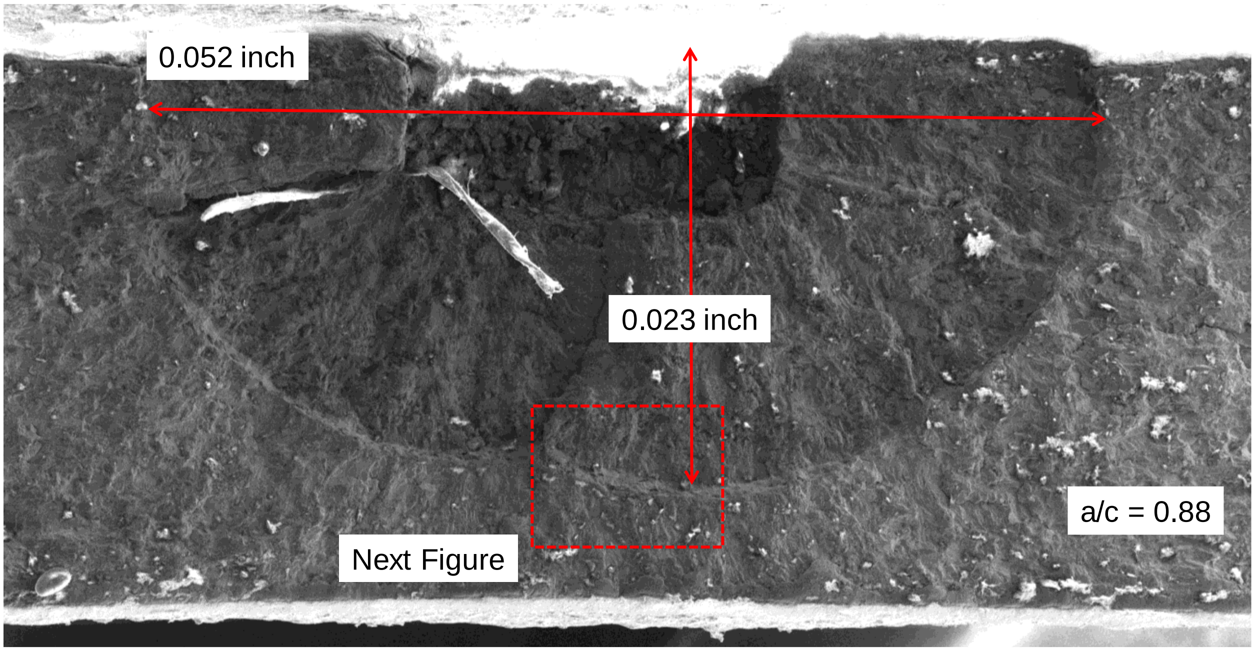

Figure M.5. Fracture surface for AA6061-T6 coupon F-LT-032-004A that was loaded to an autofrettage strain level of 1.25%.

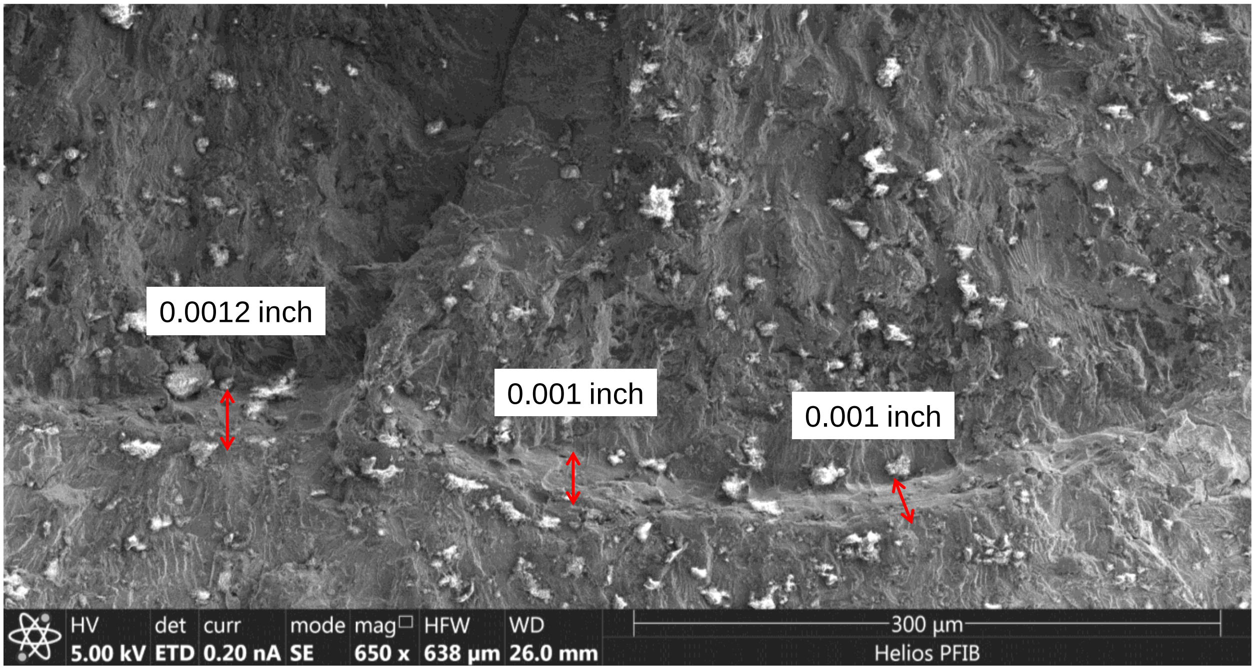

Figure M.6. Autofrettage measurements for AA6061-T6 coupon F-LT-032-004A that was loaded to an autofrettage strain level of 1.25%.

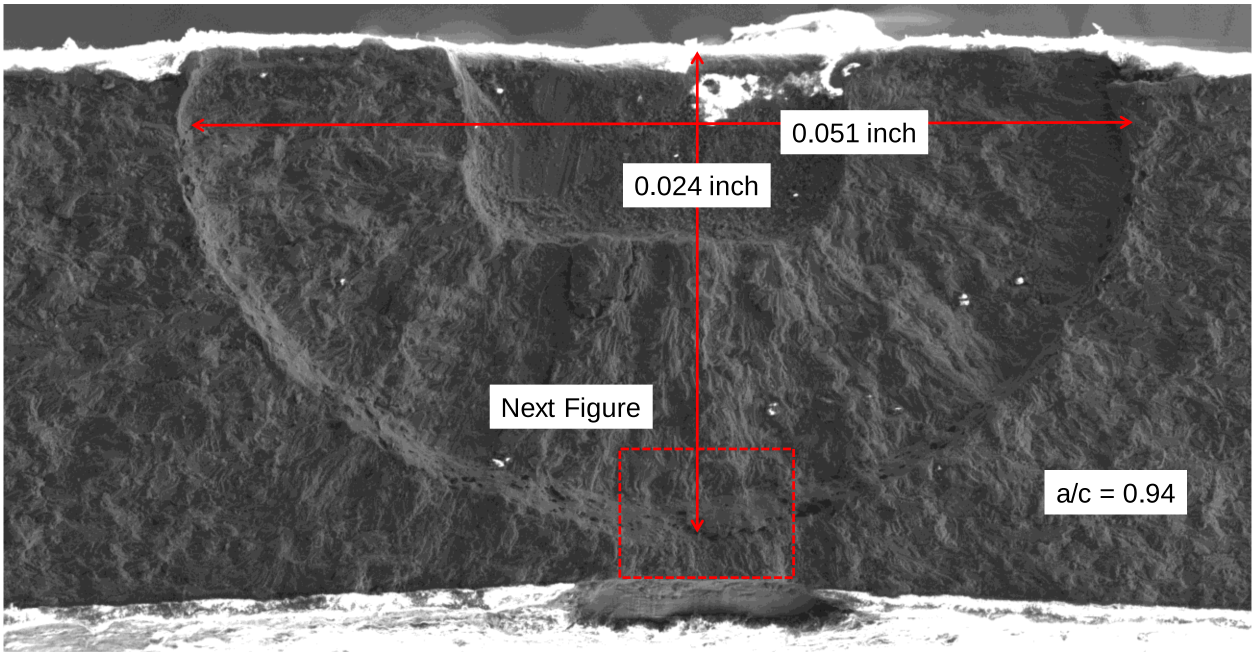

Figure M.7. Fracture surface for AA6061-T6 coupon F-TL-032-003A that was loaded to an autofrettage strain level of 1.75%.

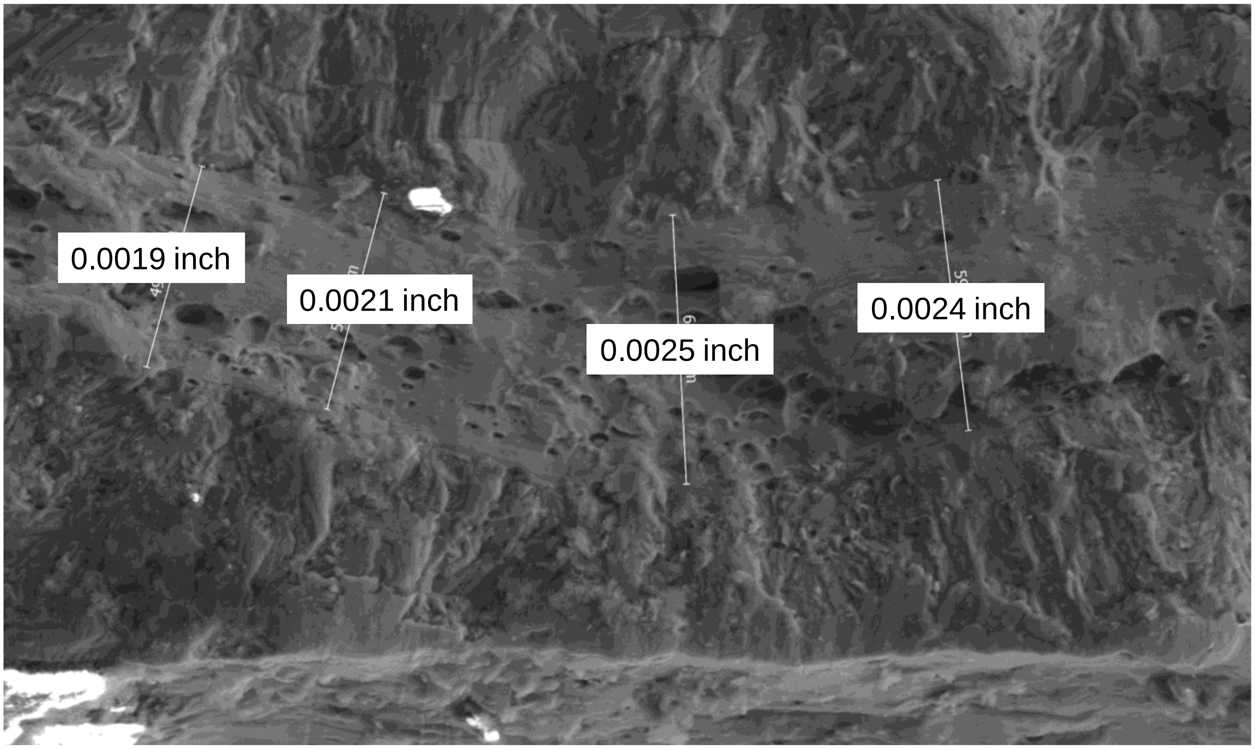

Figure M.8. Autofrettage measurements for AA6061-T6 coupon F-TL-032-003A that was loaded to an autofrettage strain level of 1.75%.

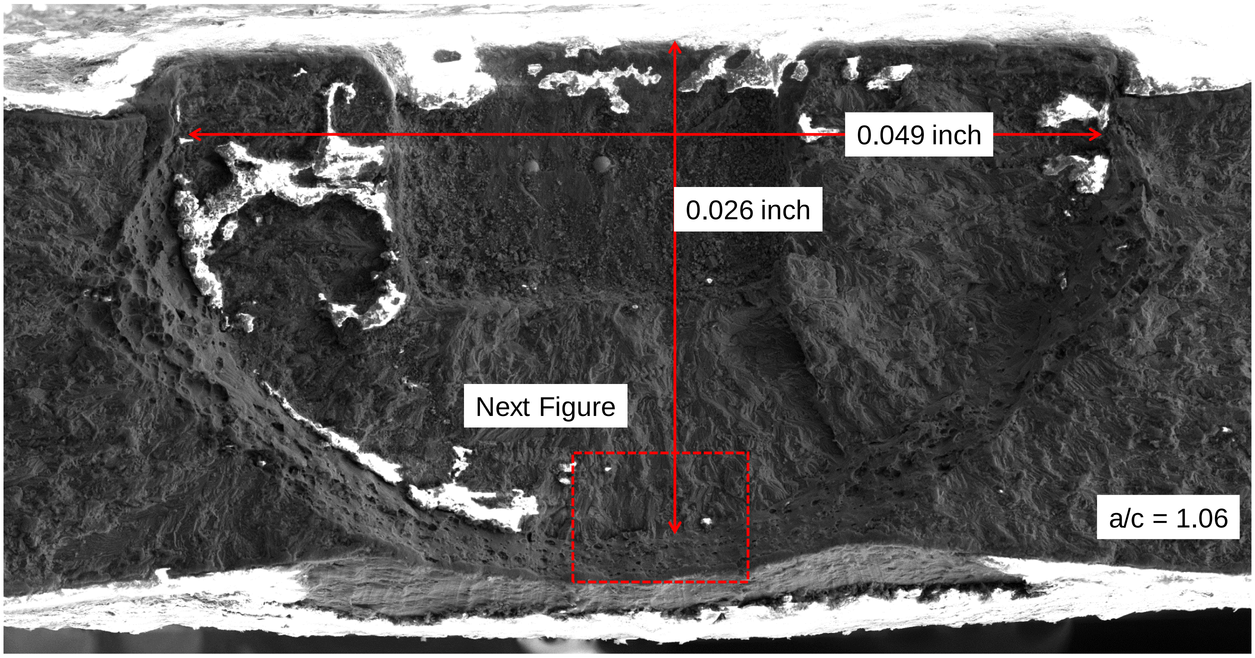

Figure M.9. Fracture surface for AA6061-T6 coupon F-TL-032-002A that was loaded to an autofrettage strain level of 2%.

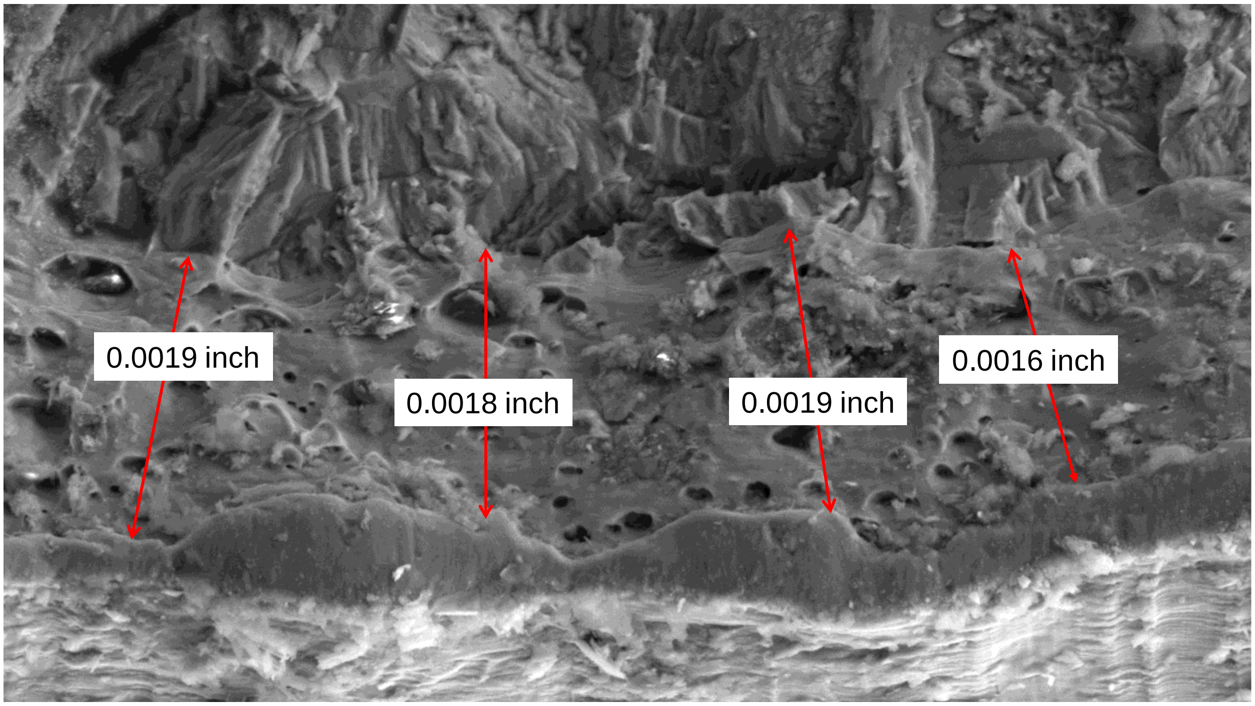

Figure M.10. Autofrettage measurements for AA6061-T6 coupon F-TL-032-002A that was loaded to an autofrettage strain level of 2%.

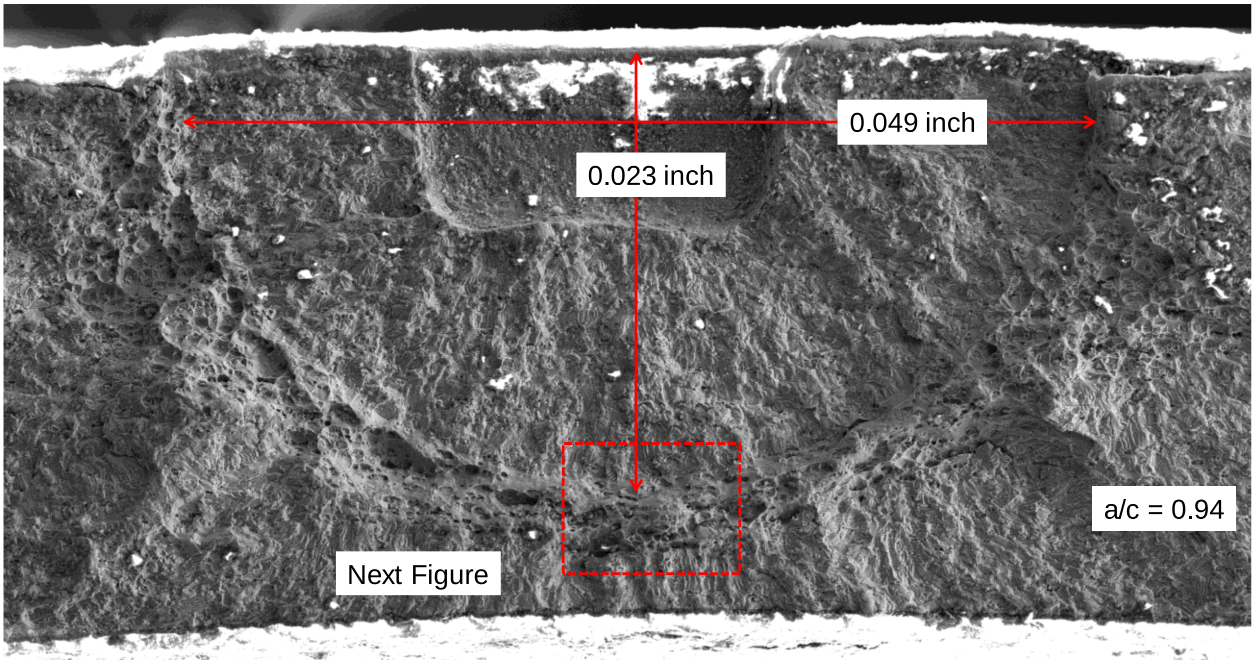

Figure M.11. Fracture surface for AA6061-T6 coupon F-LT-032-007 that was loaded to an autofrettage strain level of 2%.

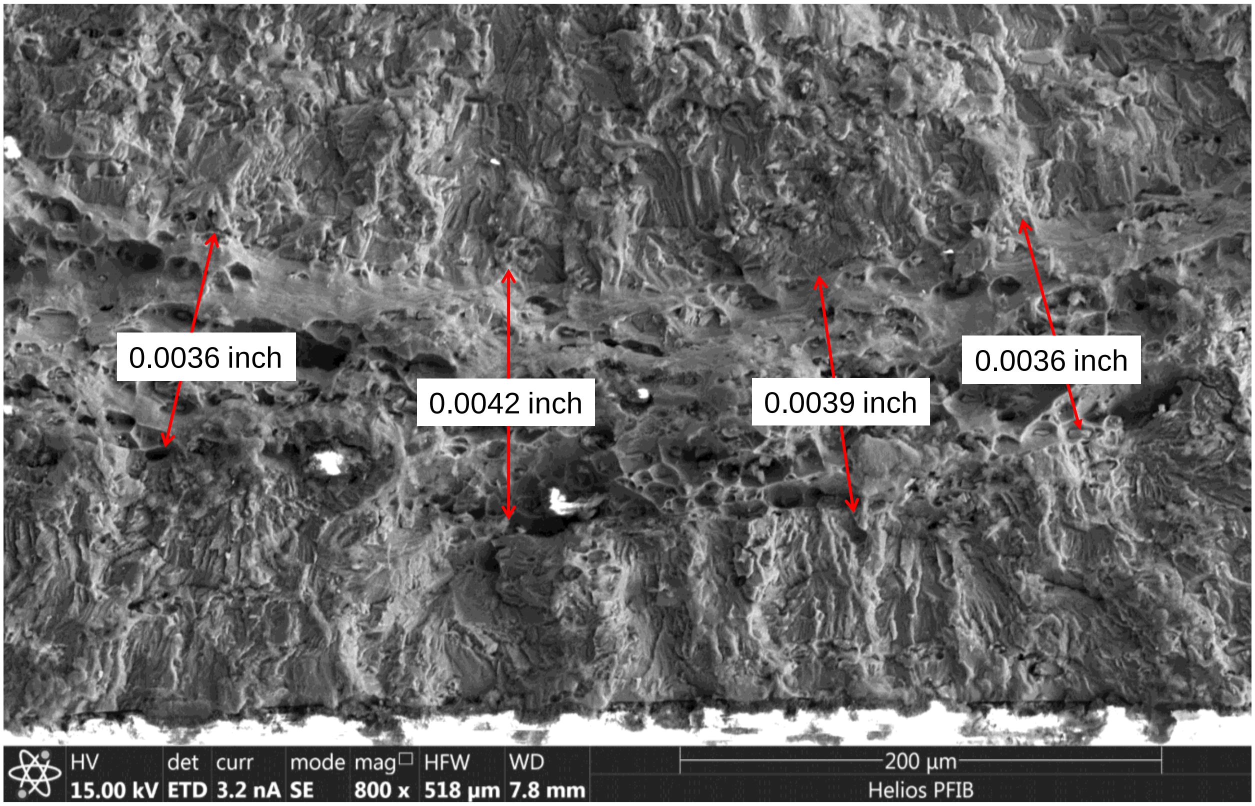

Figure M.12. Autofrettage measurements for AA6061-T6 coupon F- LT-032-007 that was loaded to an autofrettage strain level of 2%.

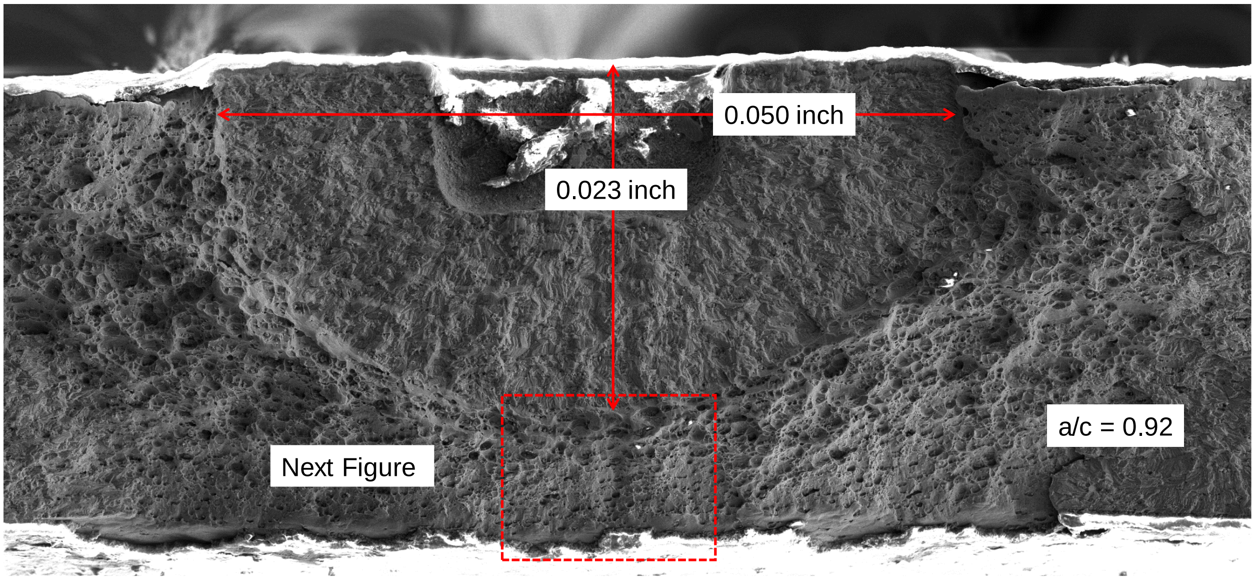

Figure M.13. Fracture surface for AA6061-T6 coupon F-LT-032-17 that was loaded to an autofrettage strain level of 2.25%.

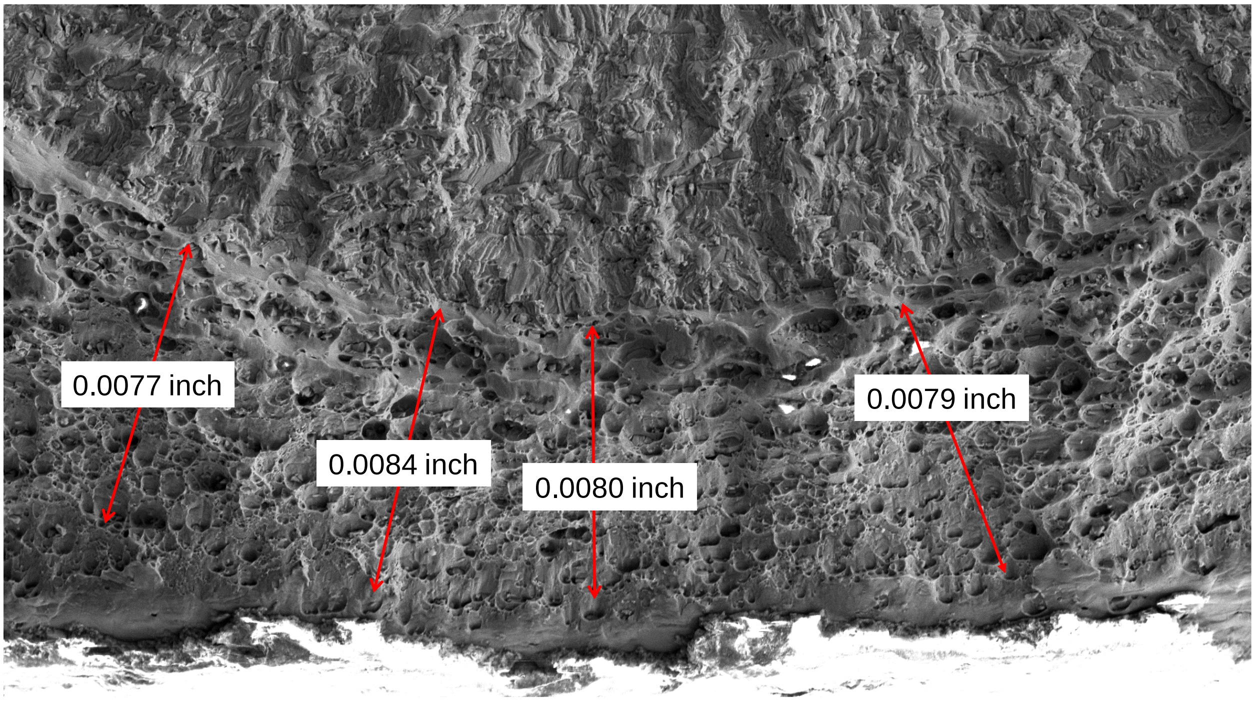

Figure M.13. Autofrettage measurements for AA6061-T6 coupon F- LT-032-17 that was loaded to an autofrettage strain level of 2.25%.

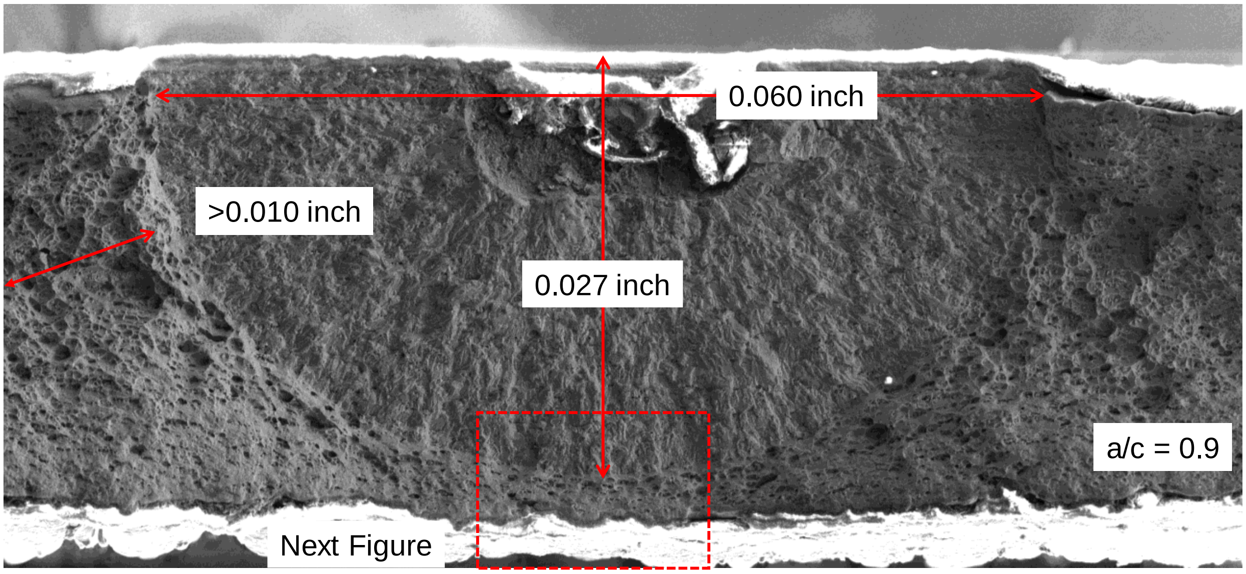

Figure M.14. Fracture surface for AA6061-T6 coupon F-LT-032-009 that was loaded to an autofrettage strain level of 2.5%.

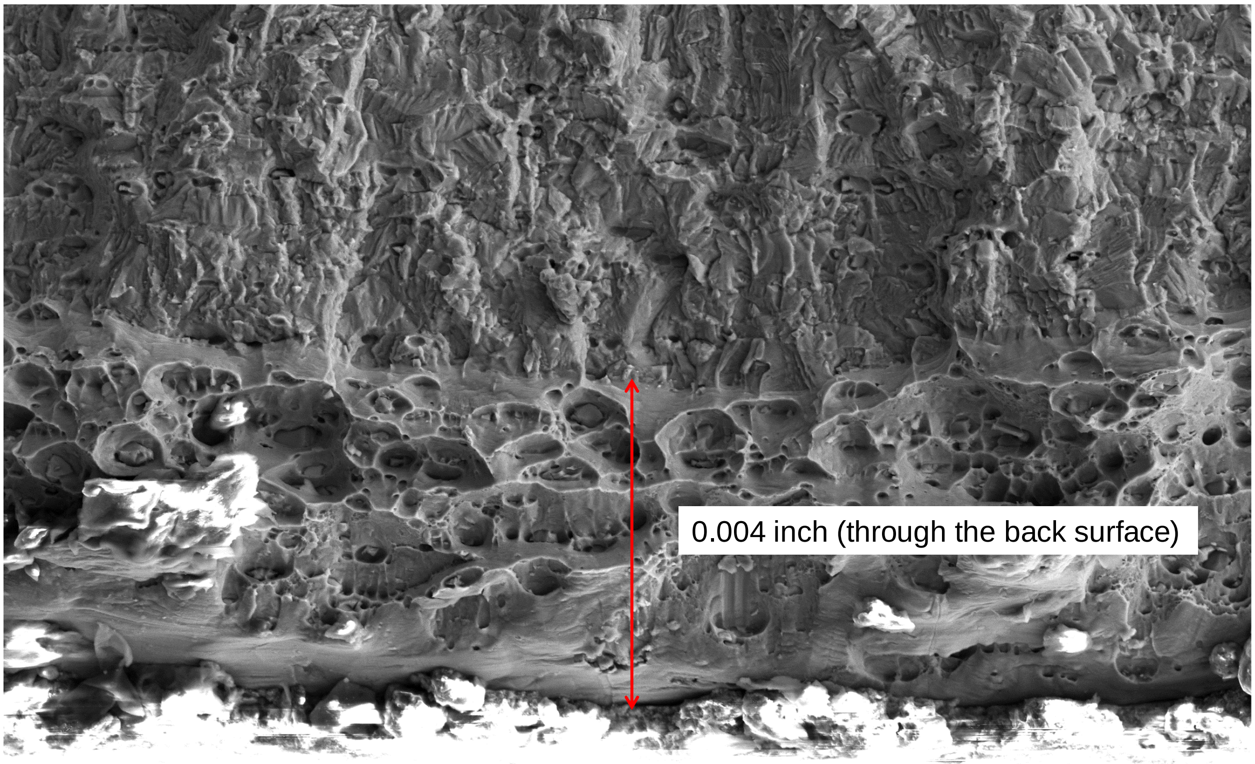

Figure M.15. Autofrettage measurements for AA6061-T6 coupon F- LT-032-009 that was loaded to an autofrettage strain level of 2.5%.

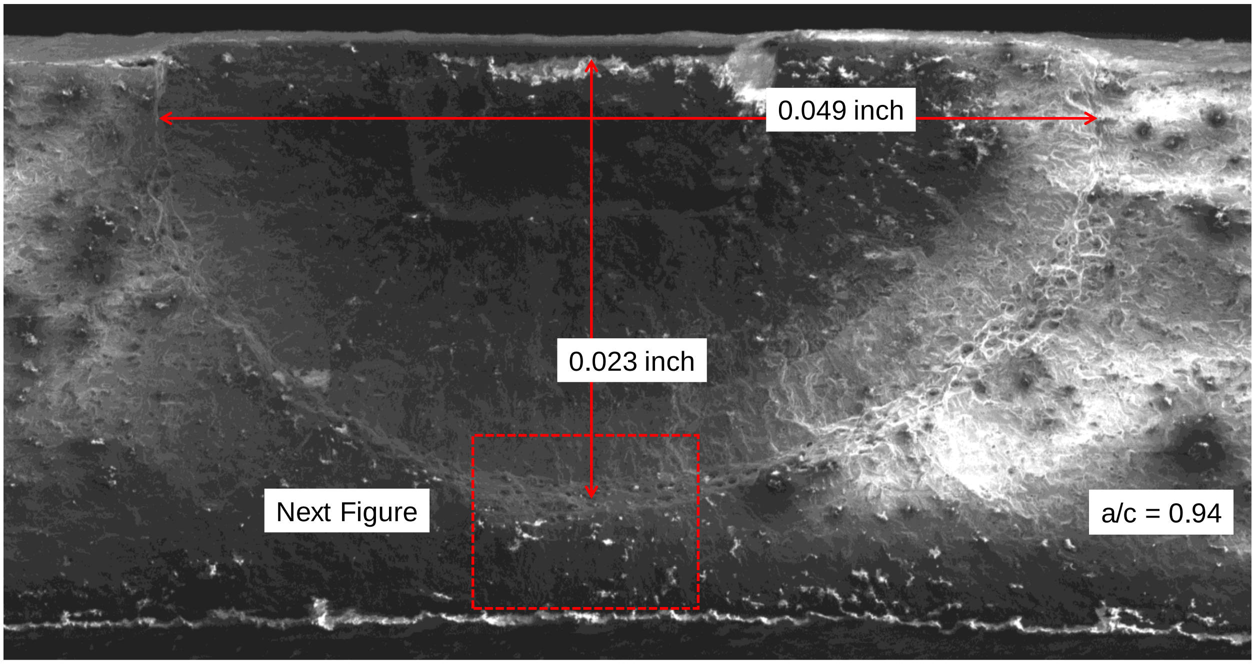

Figure M.1.6 Fracture surface for AA6061-T6 coupon F-LT-032-16 that was loaded to an autofrettage strain level of 1.75%.

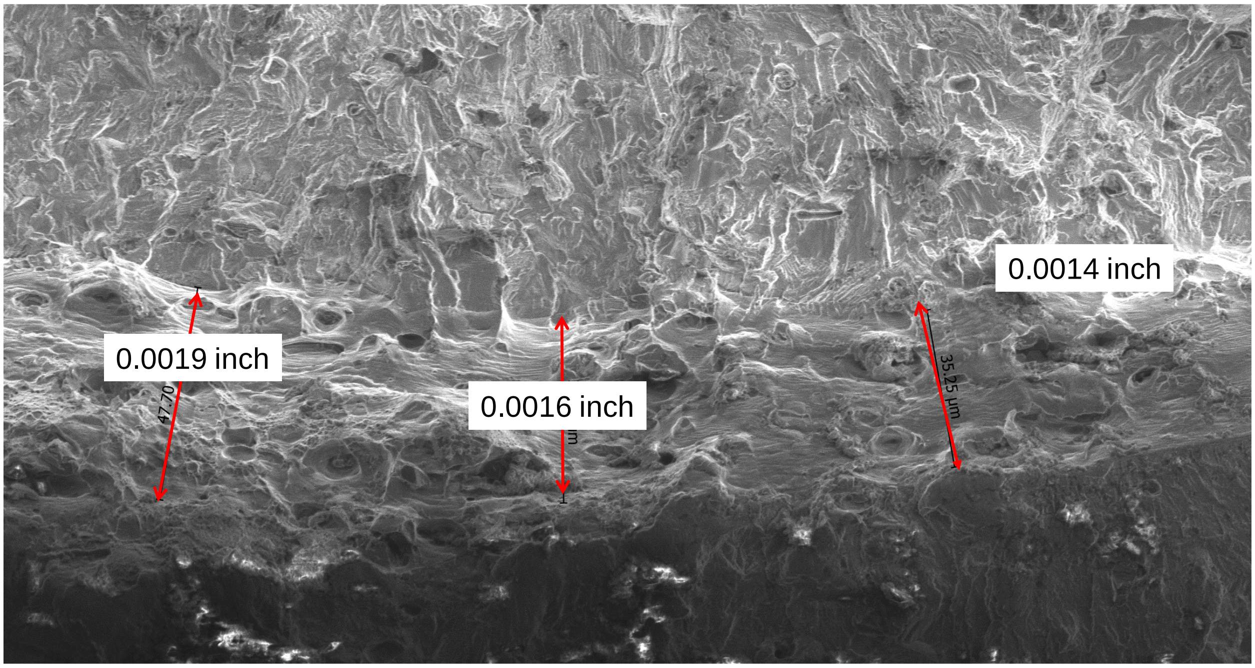

Figure M.17. Autofrettage measurements for AA6061-T6 coupon F- LT-032-16 that was loaded to an autofrettage strain level of 1.75%.

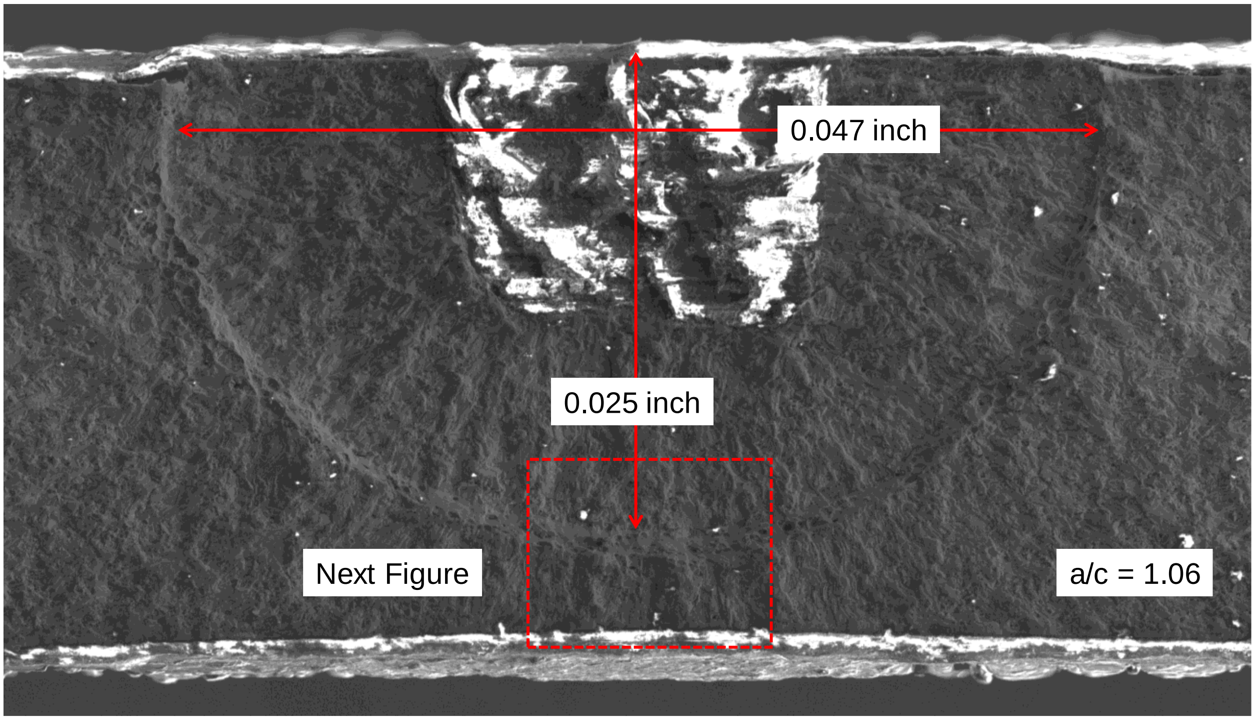

Figure M.18. Fracture surface for AA6061-T6 coupon F-LT-032-02 that was loaded to an autofrettage strain level of 1.26%.

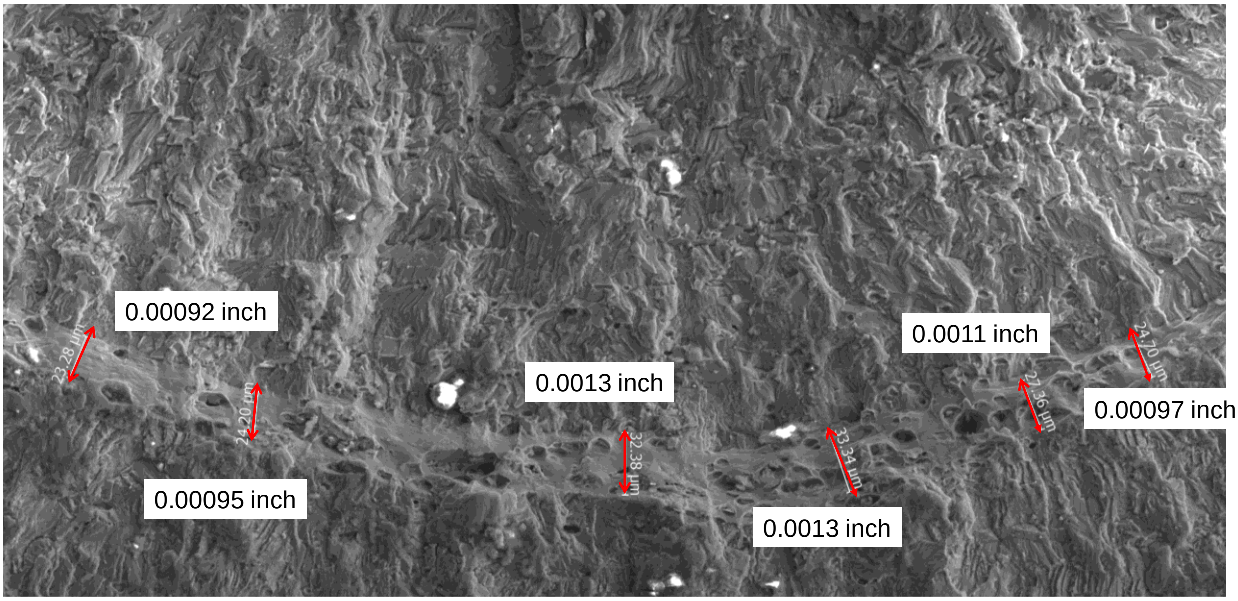

Figure M.19. Autofrettage measurements for AA6061-T6 coupon F- LT-032-02 that was loaded to an autofrettage strain level of 1.26%.

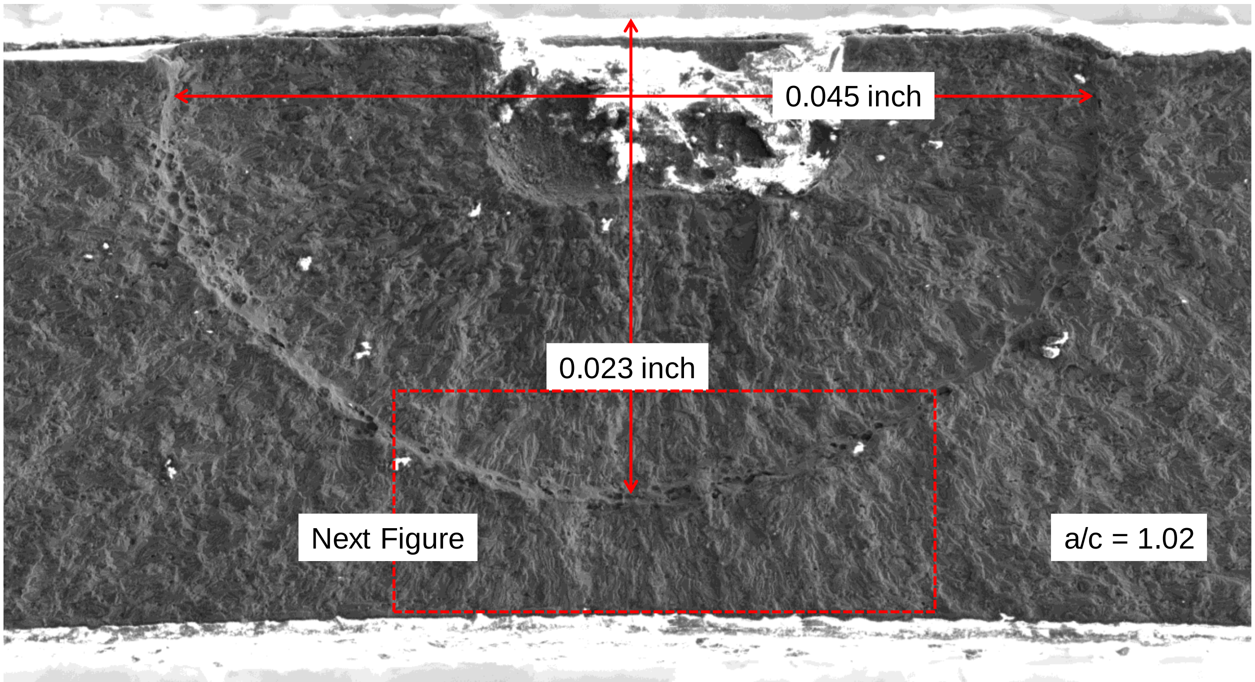

Figure M.20. Fracture surface for AA6061-T6 coupon F-LT-032-03 that was loaded to an autofrettage strain level of 1.49%.

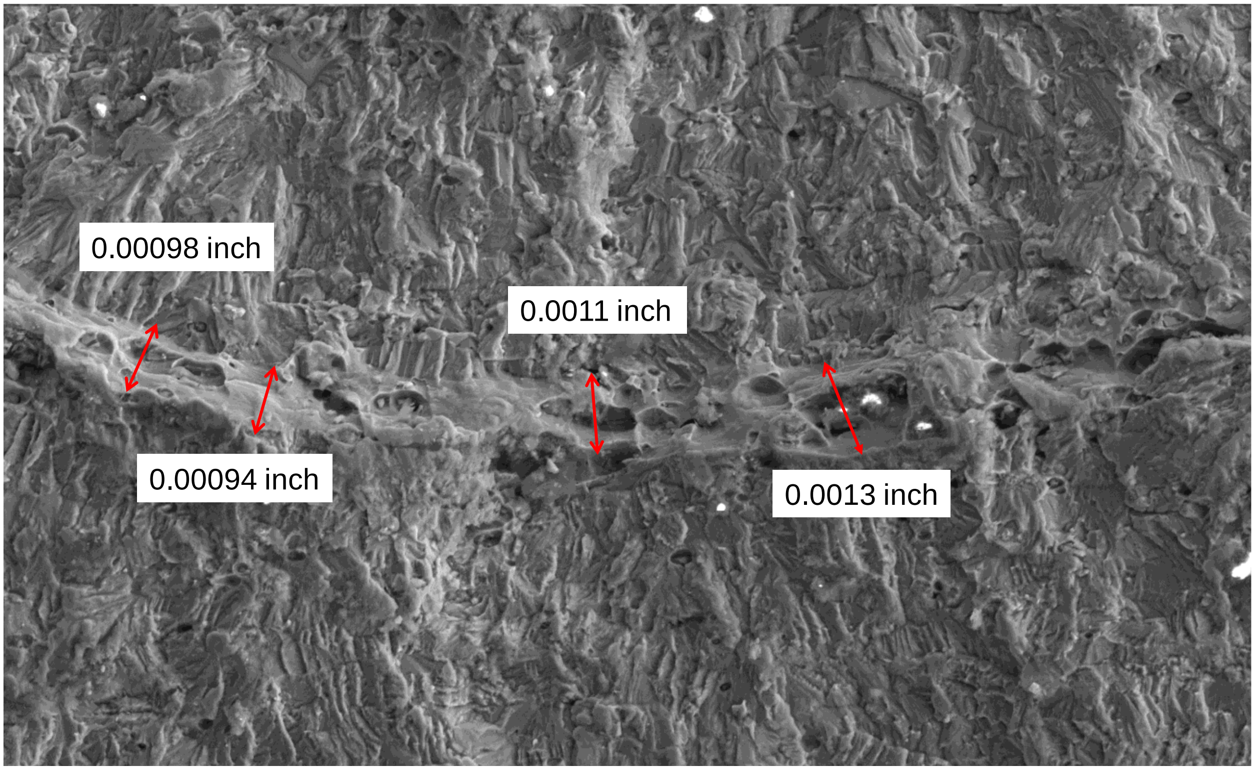

Figure M.21. Autofrettage measurements for AA6061-T6 coupon F- LT-032-03 that was loaded to an autofrettage strain level of 1.49%.

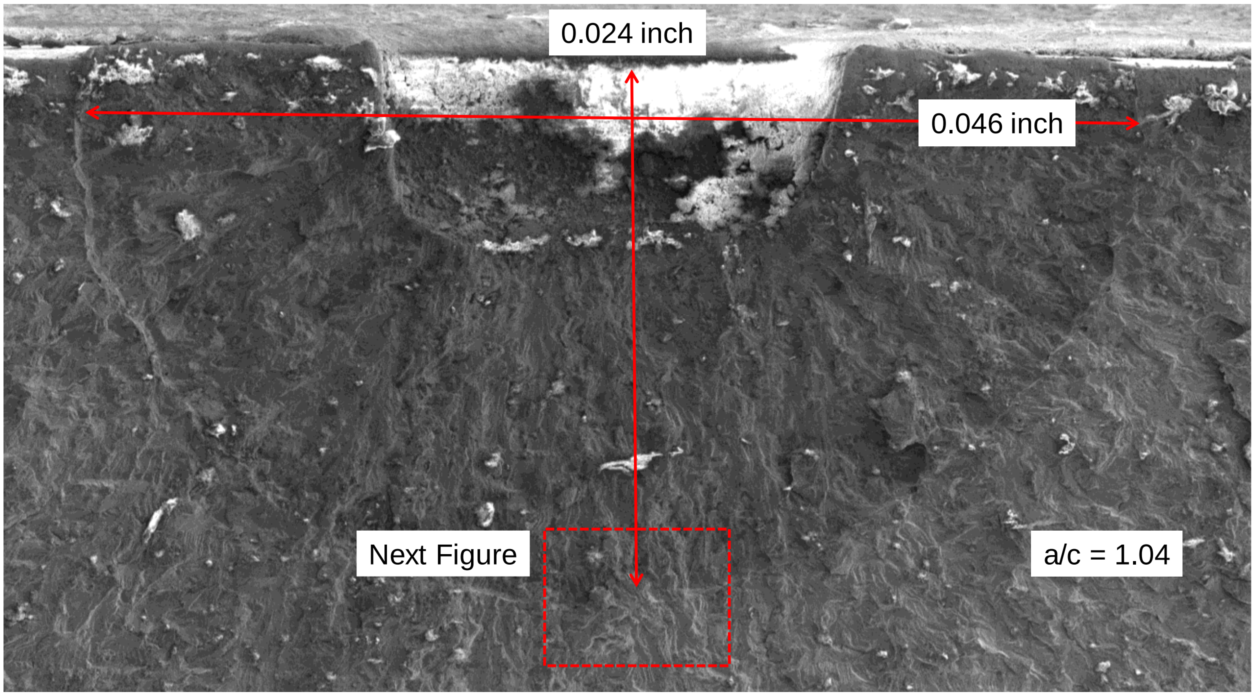

Figure M.22. Fracture surface for AA6061-T6 coupon F-LT-050-11 that was loaded to an autofrettage strain level of 1.28%.

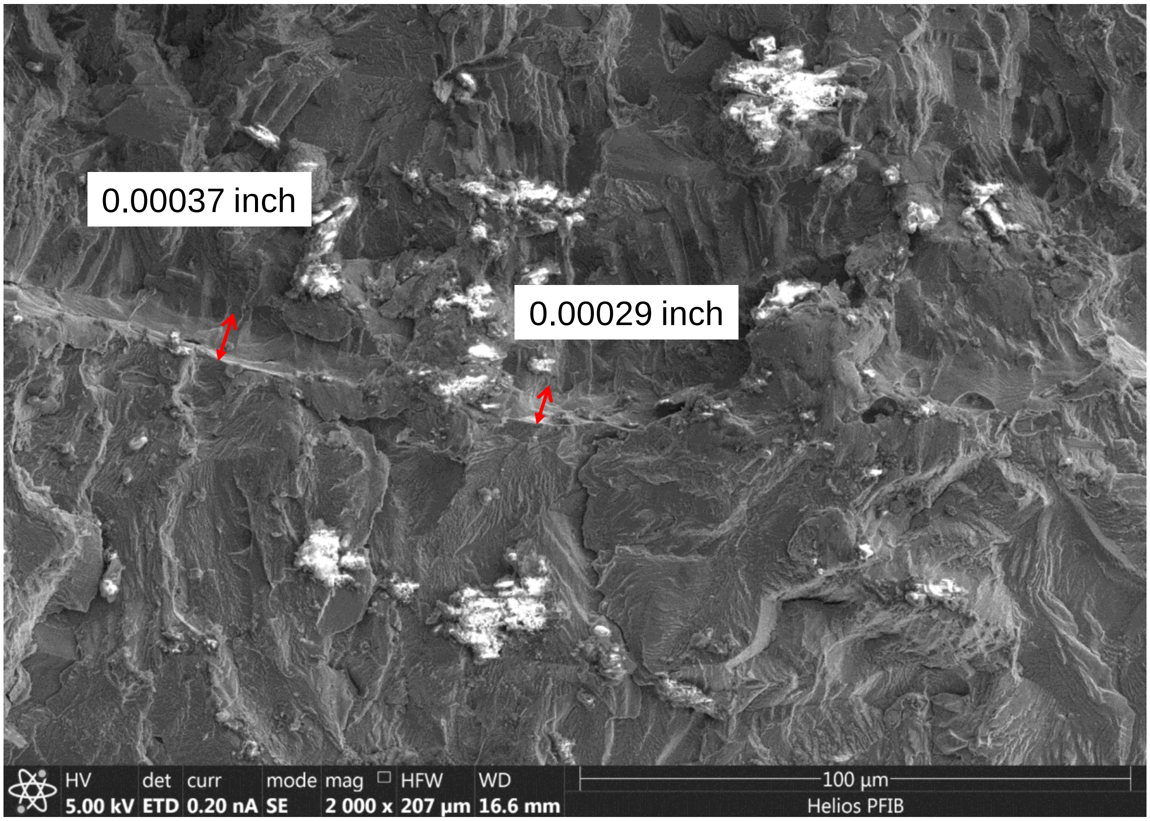

Figure M.23. Autofrettage measurements for AA6061-T6 coupon F- LT-050-11 that was loaded to an autofrettage strain level of 1.28%.

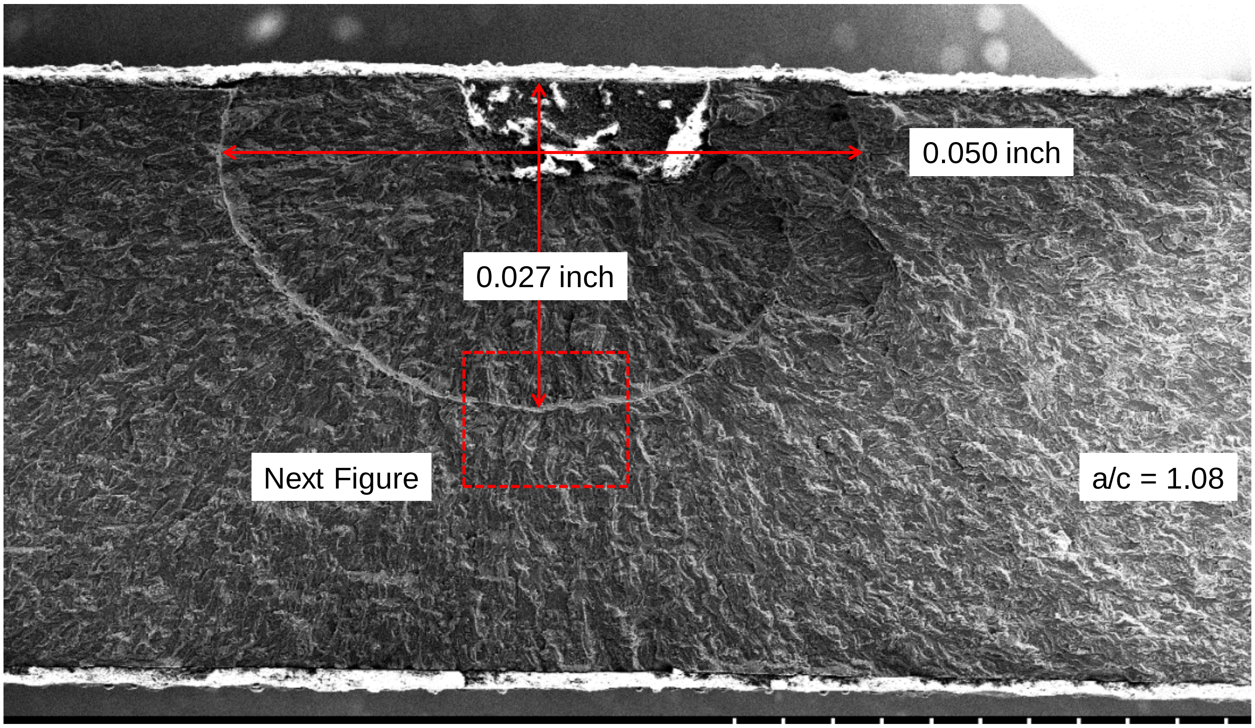

Figure M.24. Fracture surface for AA6061-T6 coupon F-LT-050-18 that was loaded to an autofrettage strain level of 1.78%.

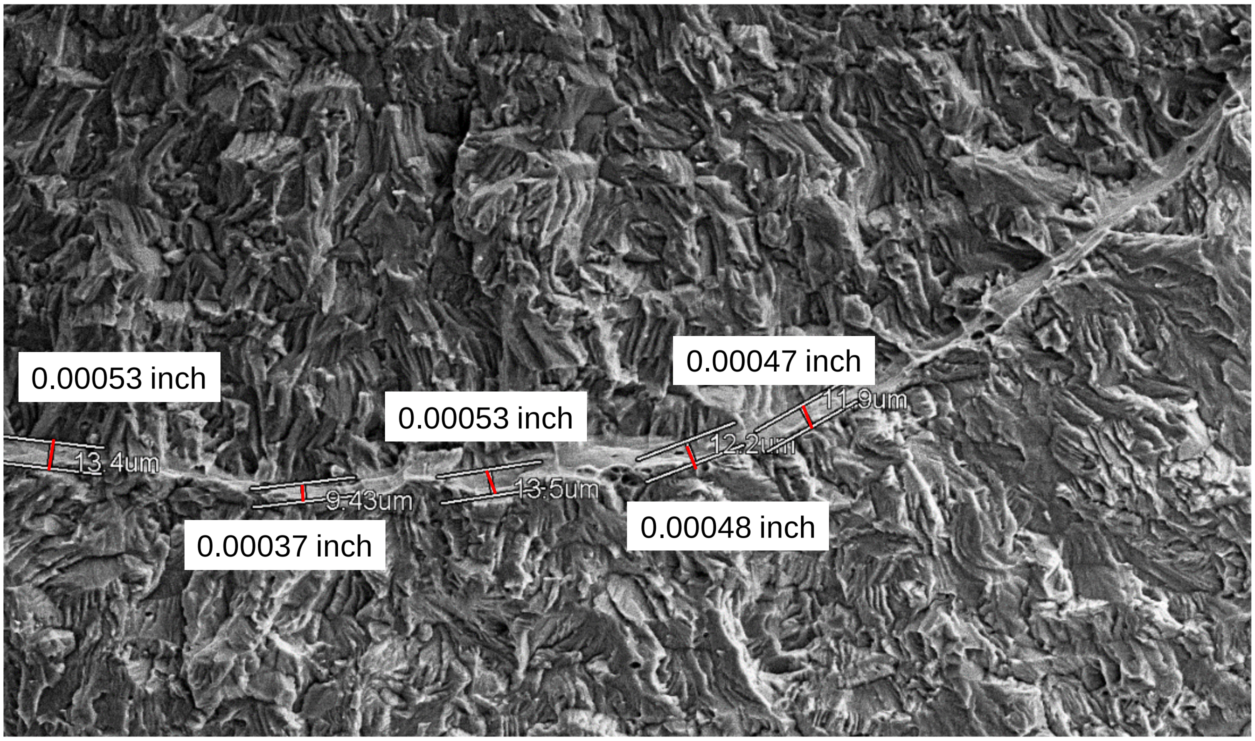

Figure M.25. Autofrettage measurements for AA6061-T6 coupon F- LT-050-18 that was loaded to an autofrettage strain level of 1.78%.

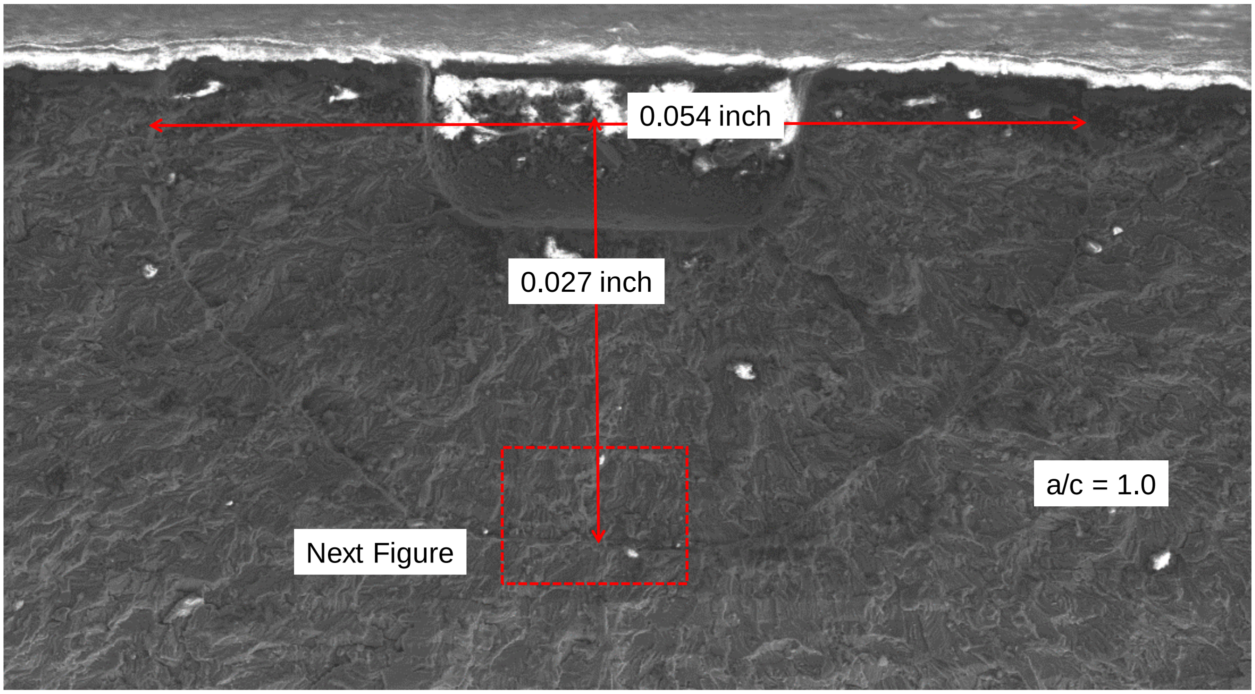

Figure M.26. Fracture surface for AA6061-T6 coupon F-LT-090-18 that was loaded to an autofrettage strain level of 1.5%.

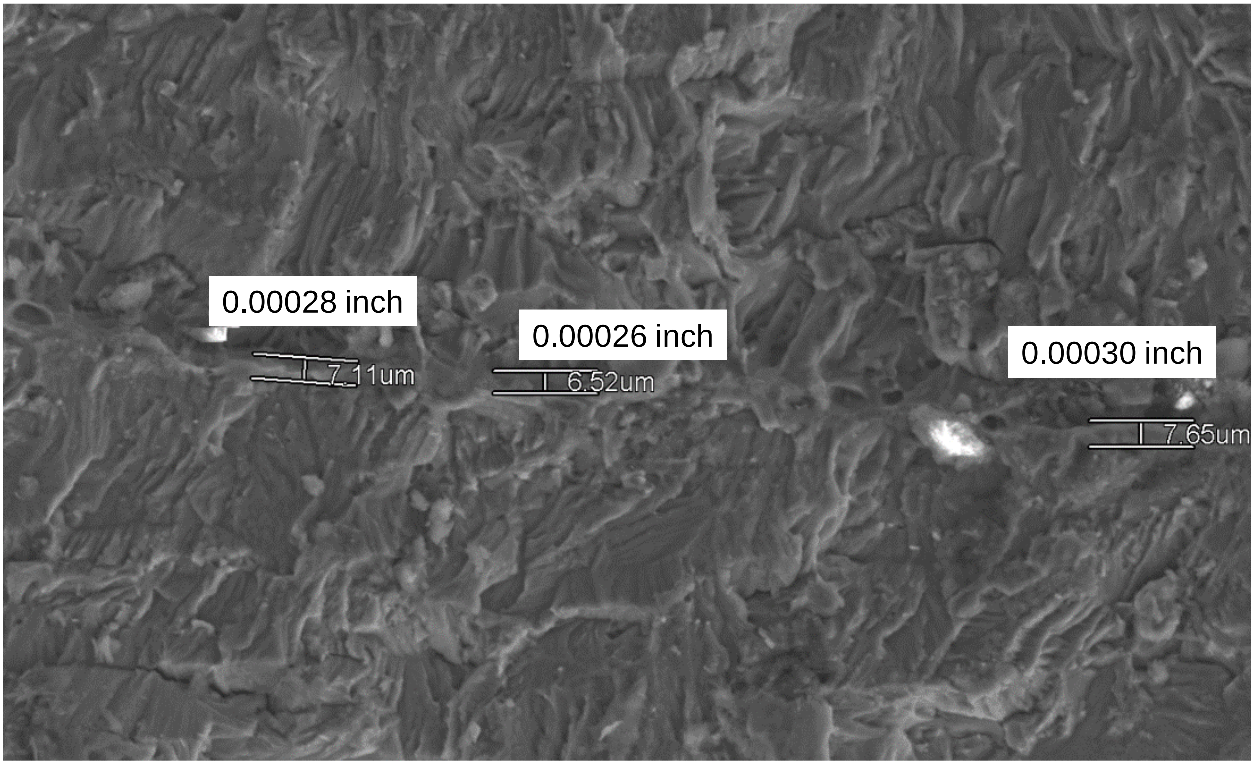

Figure M.27. Autofrettage measurements for AA6061-T6 coupon F- LT-090-18 that was loaded to an autofrettage strain level of 1.5%.

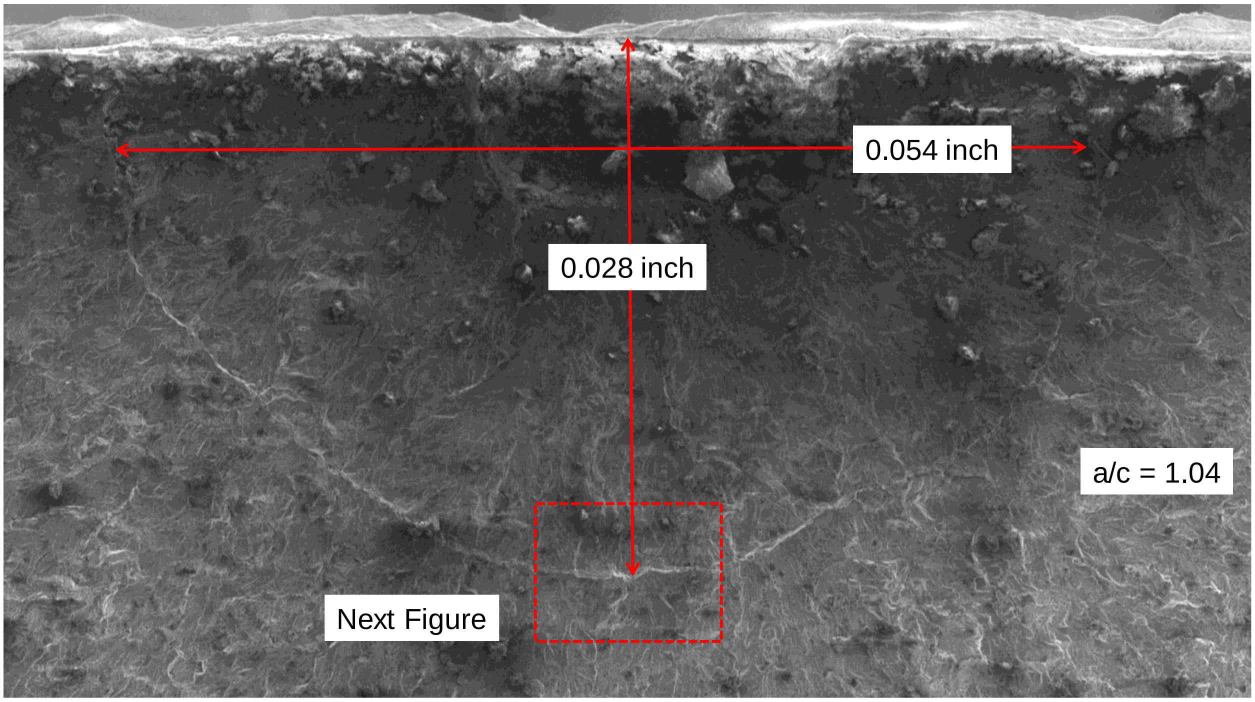

Figure M.28. Fracture surface for AA6061-T6 coupon F-LT-090-009 that was loaded to an autofrettage strain level of 2%.

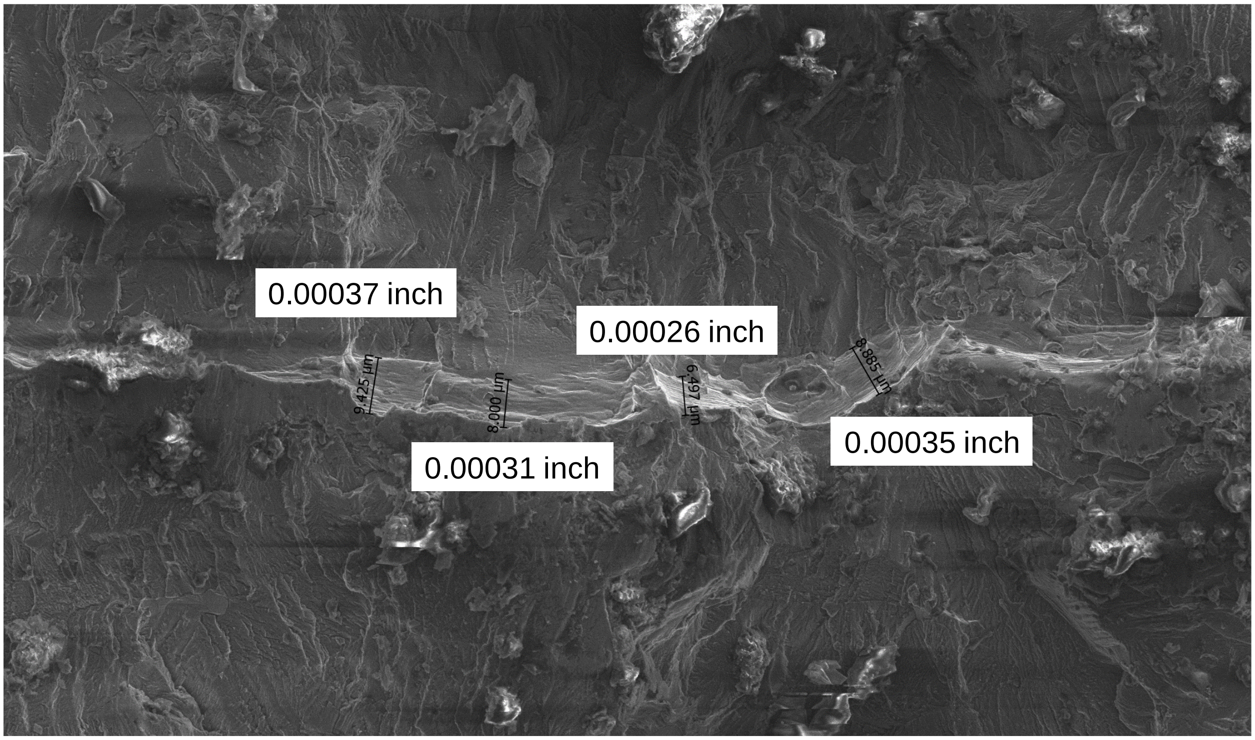

Figure M.29. Autofrettage measurements for AA6061-T6 coupon F- LT-090-009 that was loaded to an autofrettage strain level of 2%.

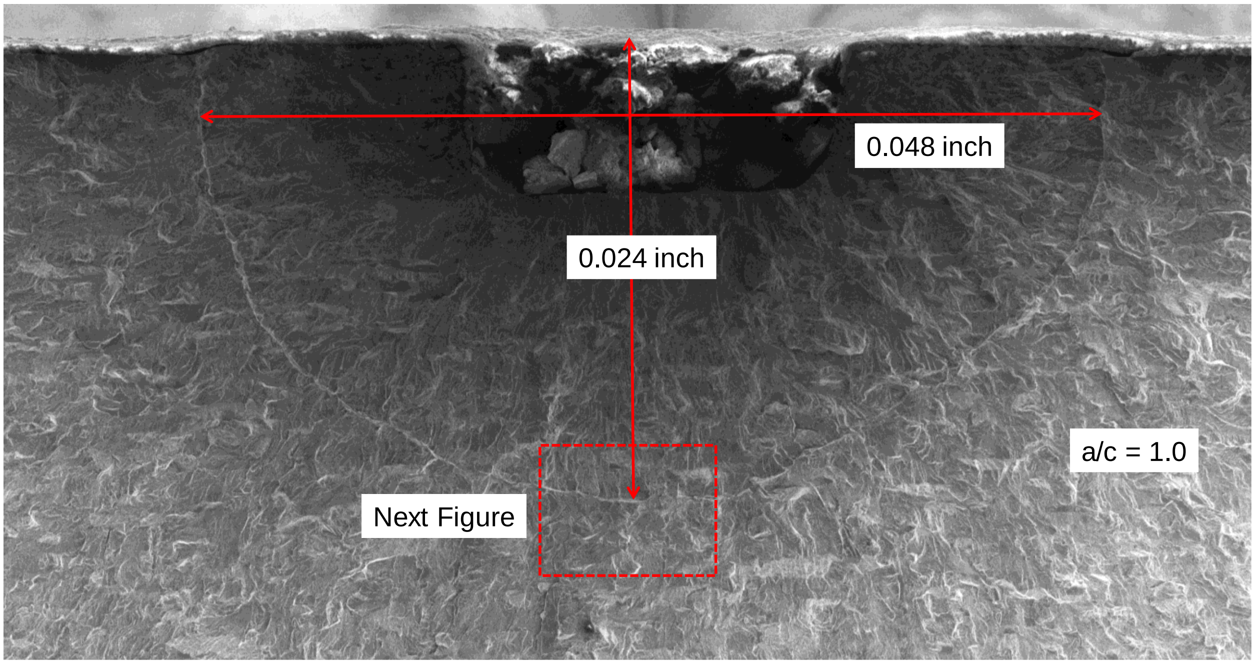

Figure M.30. Fracture surface for AA6061-T6 coupon F-LT-090-11 that was loaded to an autofrettage strain level of 1.75%.

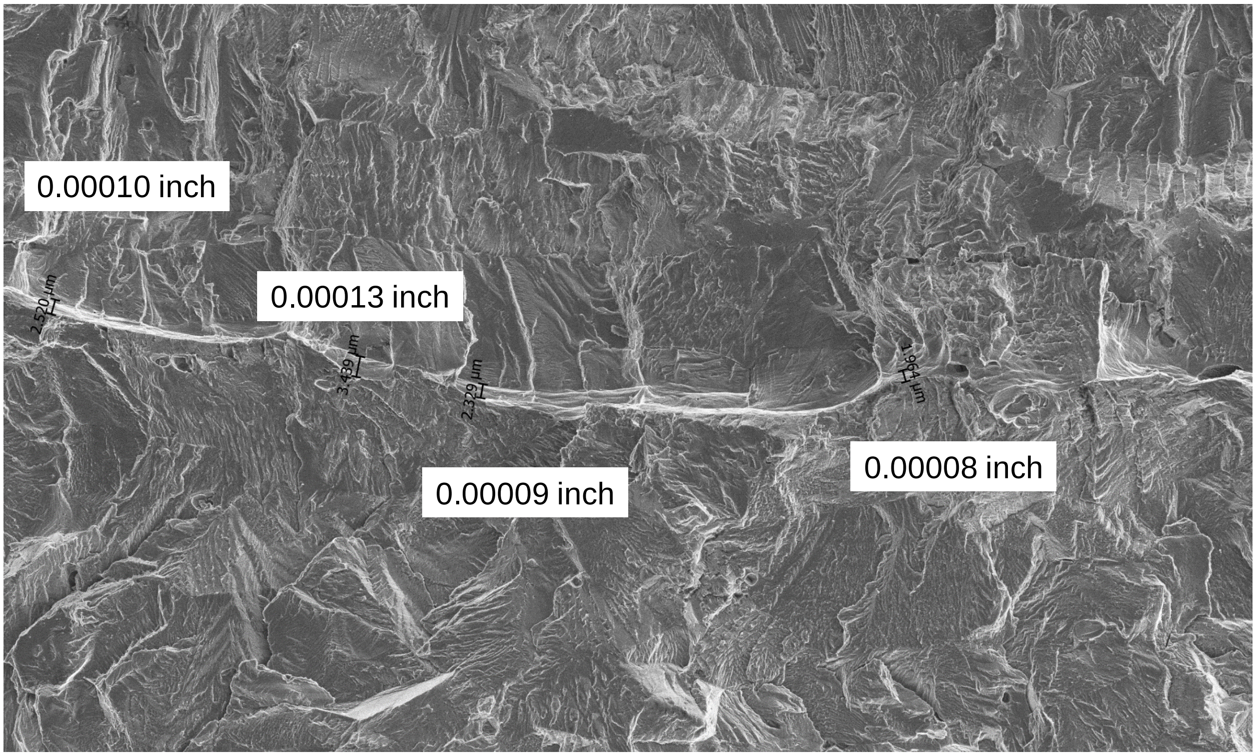

Figure M.3.1 Autofrettage measurements for AA6061-T6 coupon F- LT-090-11 that was loaded to an autofrettage strain level of 1.75%.

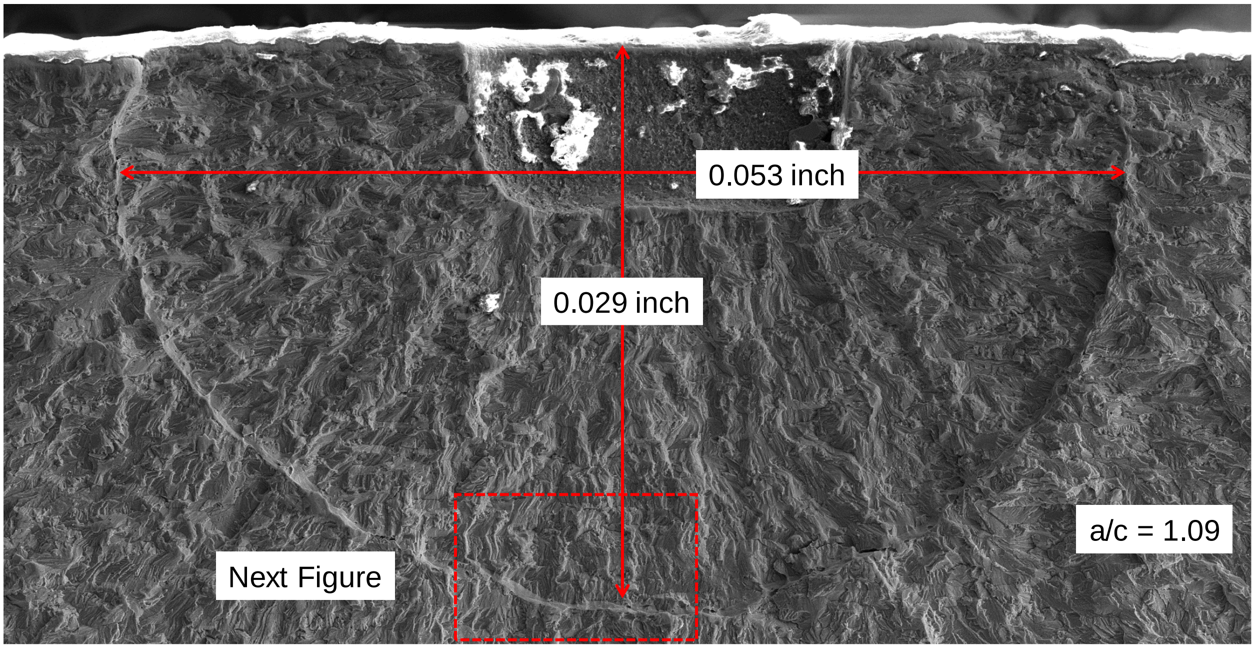

Figure M.32. Fracture surface for AA6061-T6 coupon F-LT-090-17 that was loaded to an autofrettage strain level of 2.25%.

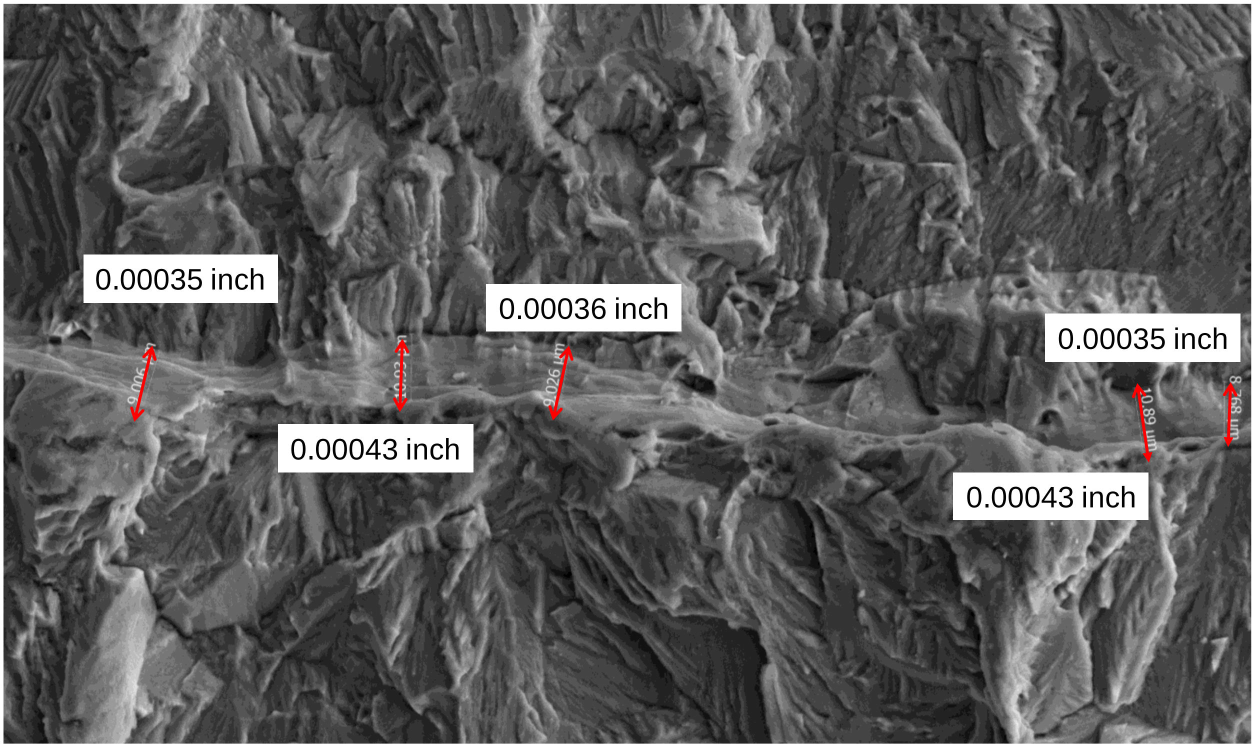

Figure M.33. Autofrettage measurements for AA6061-T6 coupon F- LT-090-17 that was loaded to an autofrettage strain level of 2.25%.

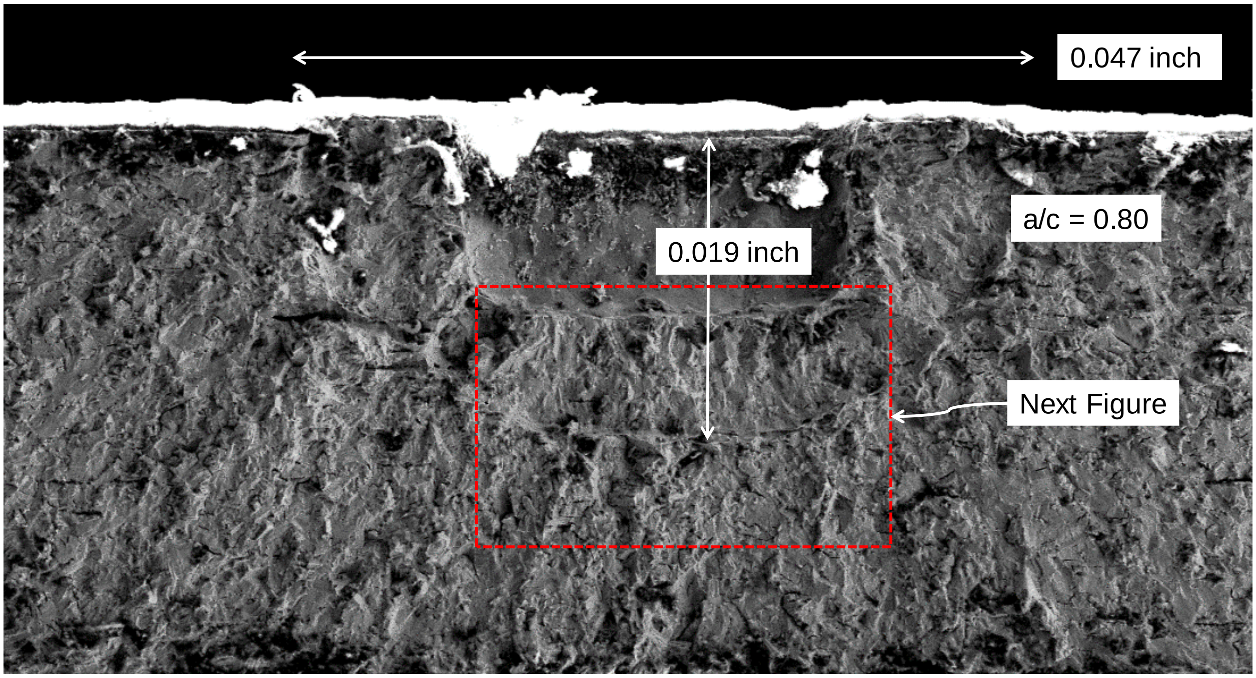

Figure M.34. Fracture surface for IN718 coupon F-LT-030-20 that was loaded to an autofrettage strain level of 1.77%.

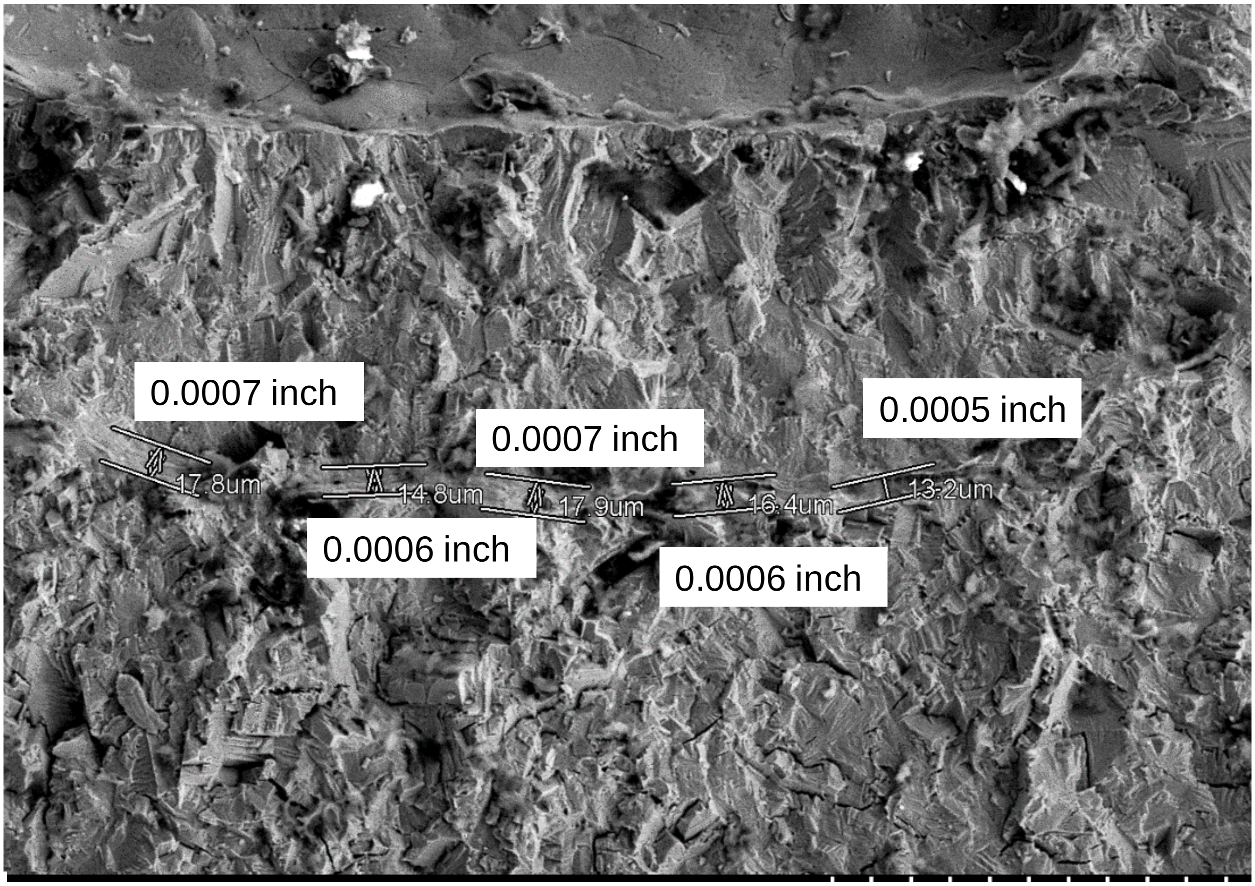

Figure M.35 Autofrettage measurements for IN718 coupon F-LT-030-20 that was loaded to an autofrettage strain level of 1.77%.

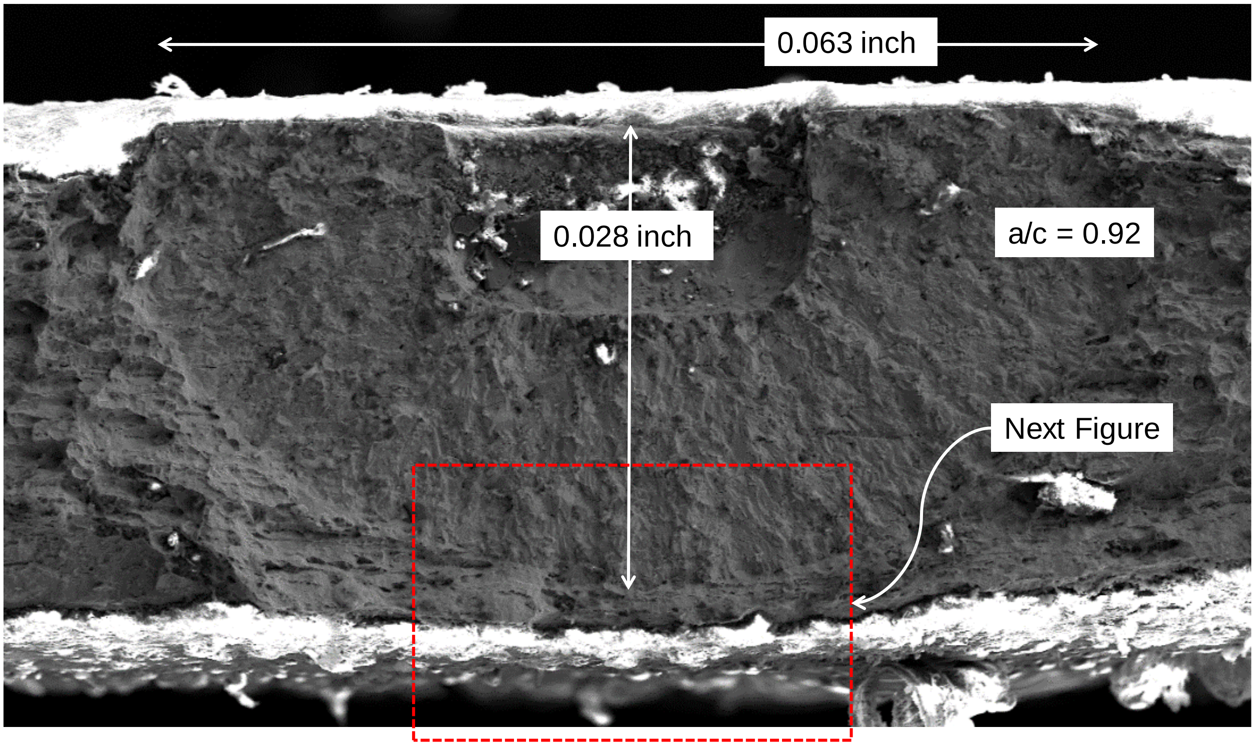

Figure M.36. Fracture surface for IN718 coupon F-LT-030-18 that was loaded to an autofrettage strain level of 1.77%.

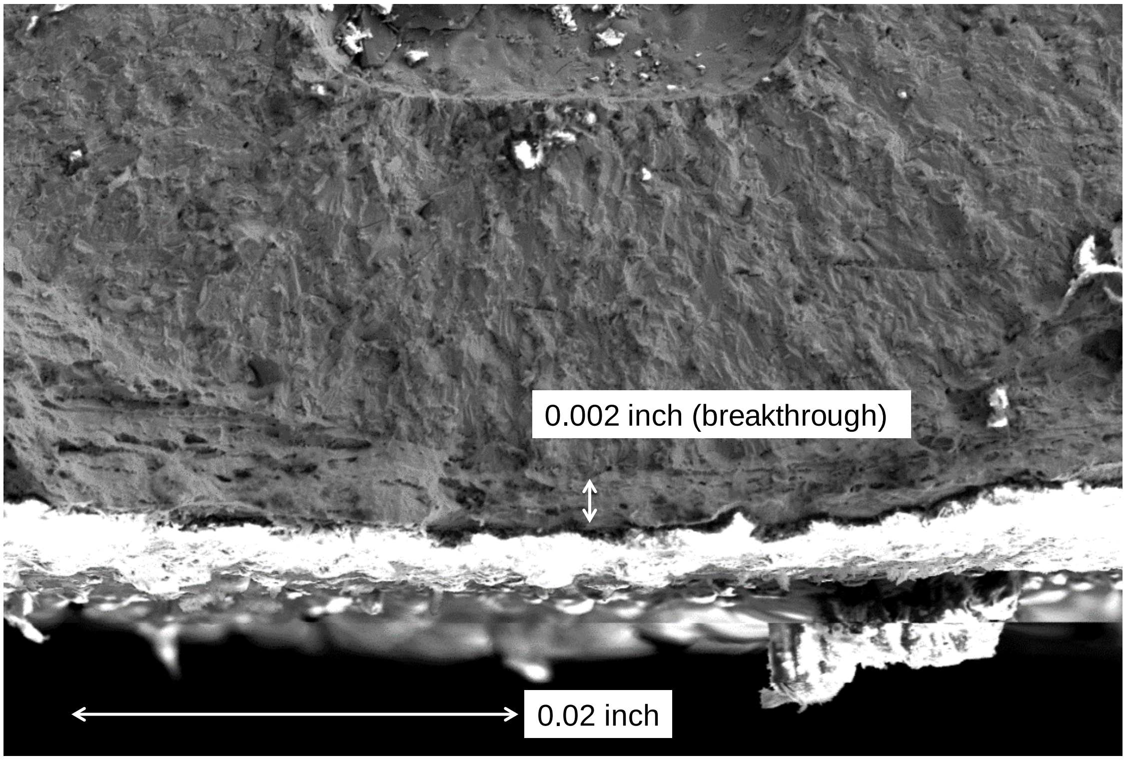

Figure M.37. Autofrettage measurements for IN718 coupon F-LT-030-20 that was loaded to an autofrettage strain level of 1.77%.

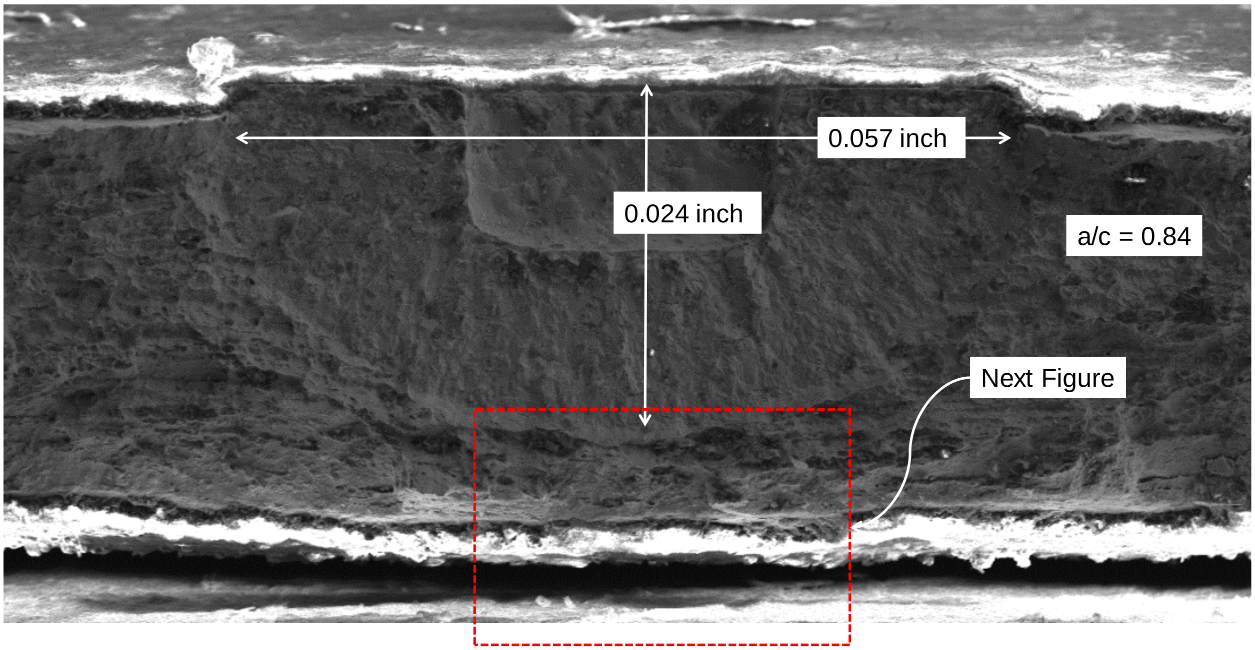

Figure M.38. Fracture surface for IN718 coupon F-LT-030-19 that was loaded to an autofrettage strain level of 1.68%.

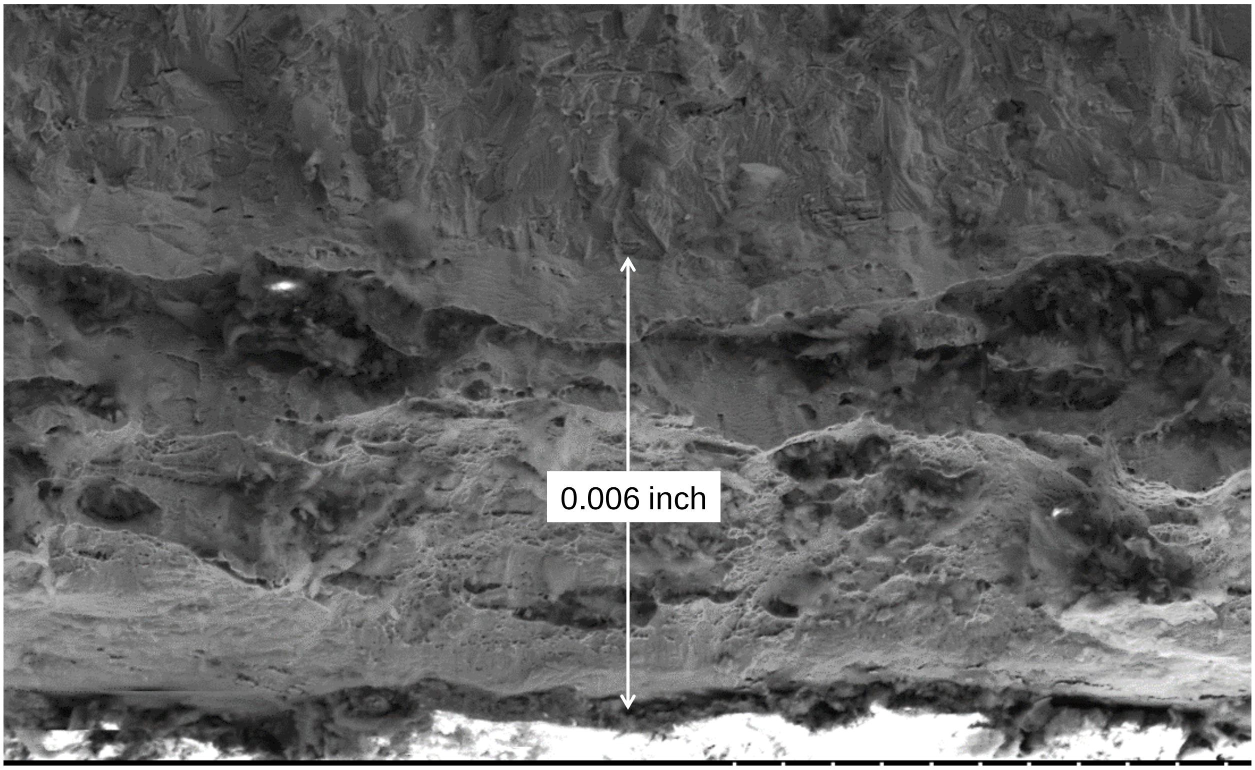

Figure M.39. Autofrettage measurements for IN718 coupon F-LT-030-19 that was loaded to an autofrettage strain level of 1.68%.

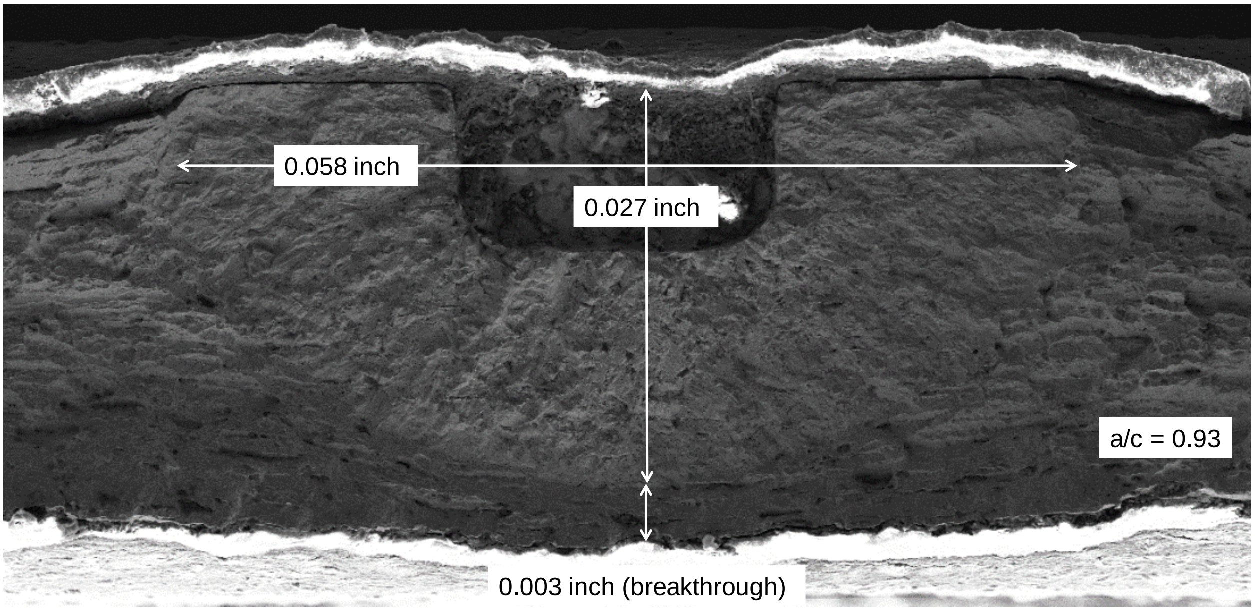

Figure M.40. Fracture surface for IN718 coupon F-LT-030-16 that was loaded to an autofrettage strain level of 1.73%.

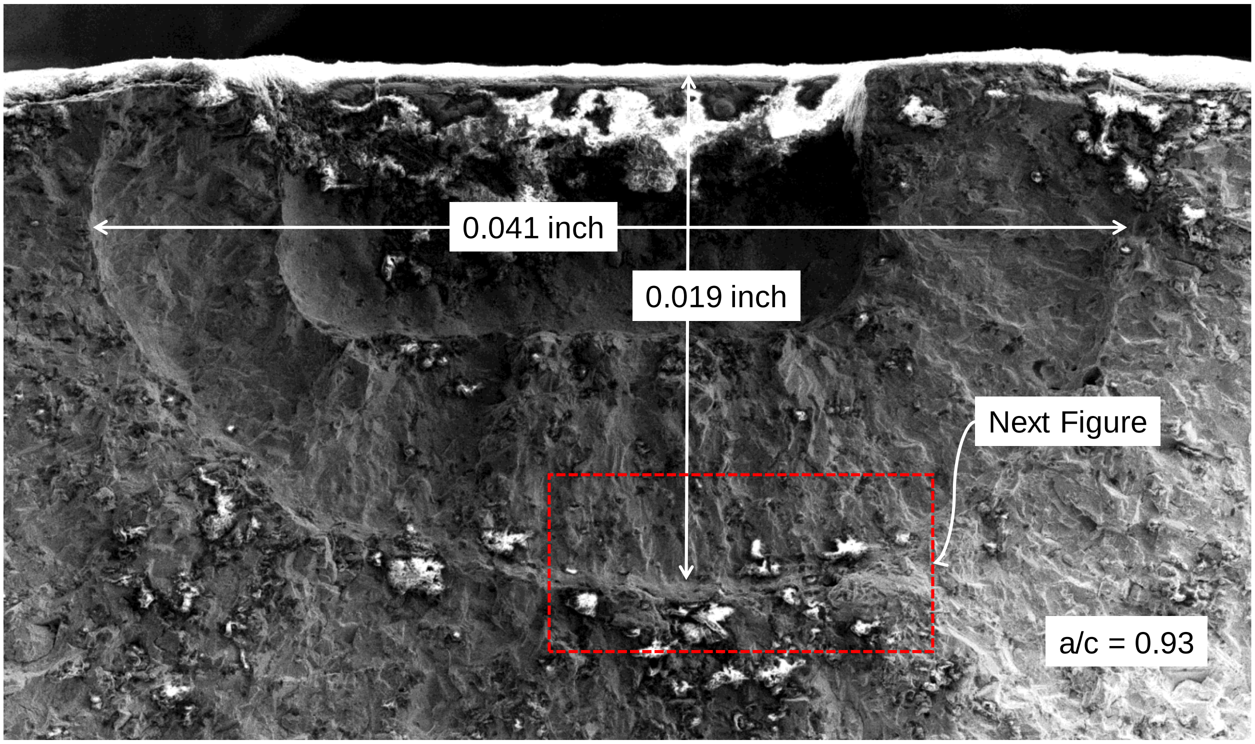

Figure M.41. Autofrettage measurements for IN718 coupon F-LT-030-01 that was loaded to an autofrettage strain level of 1.75%.

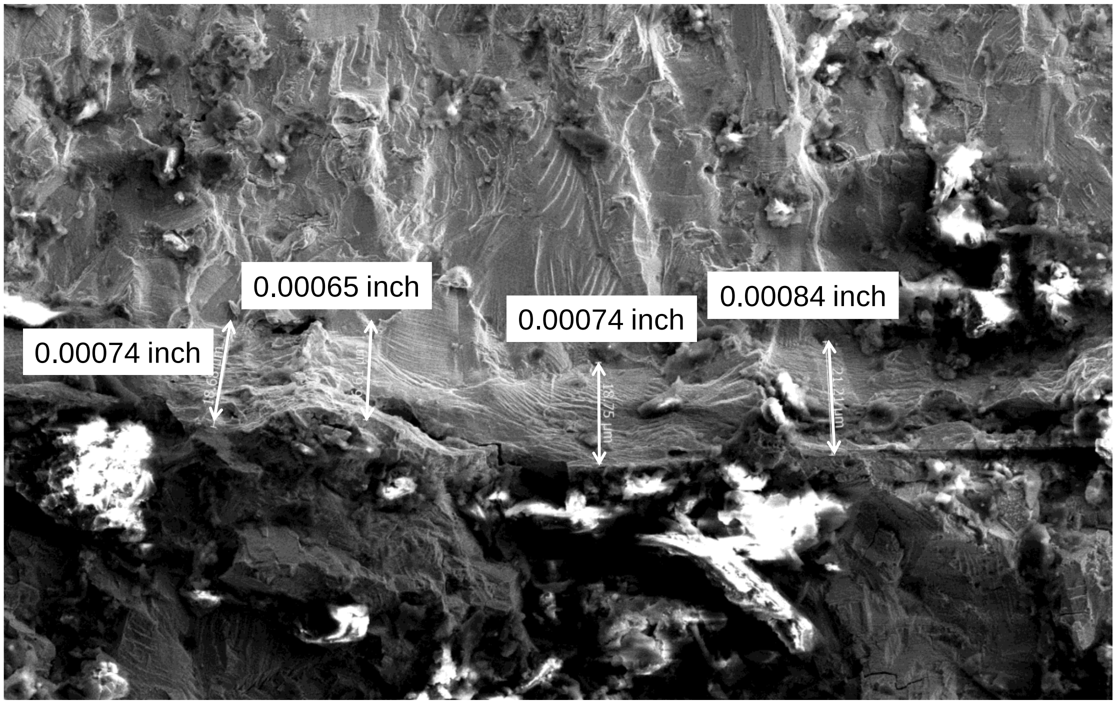

Figure M.42. Autofrettage measurements for IN718 coupon F-LT-030-01 that was loaded to an autofrettage strain level of 1.75%.

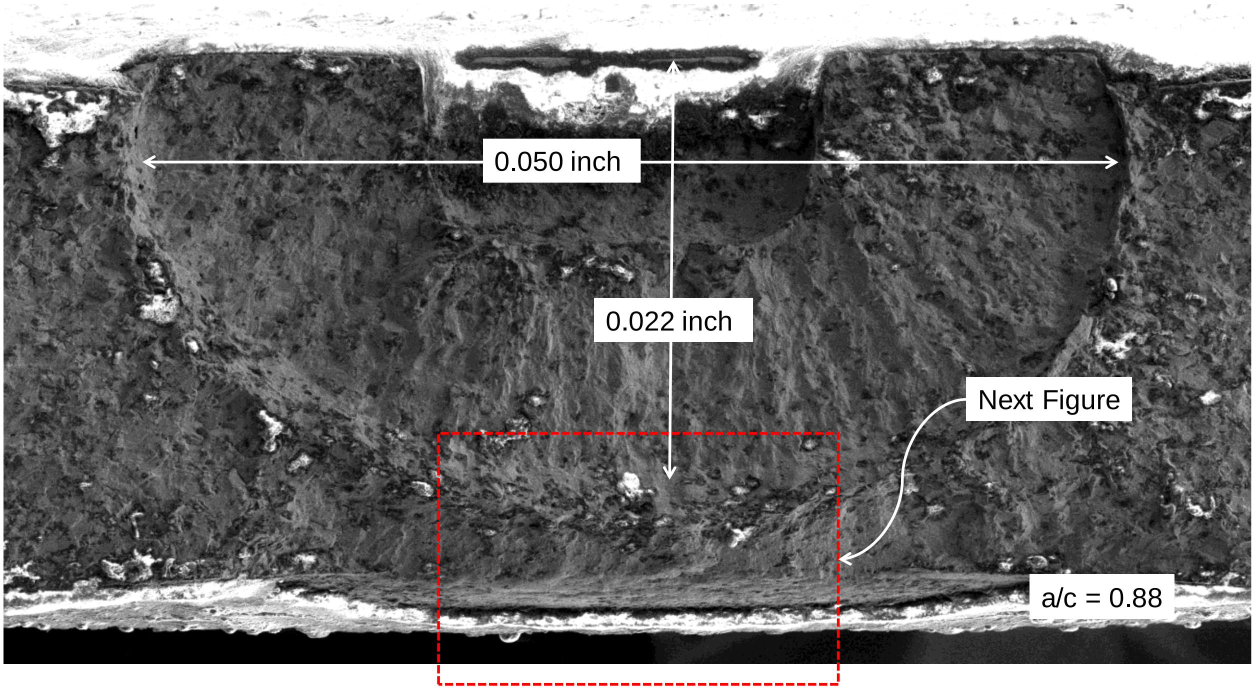

Figure M.42 Fracture surface for IN718 coupon F-LT-030-02 that was loaded to an autofrettage strain level of 1.70%

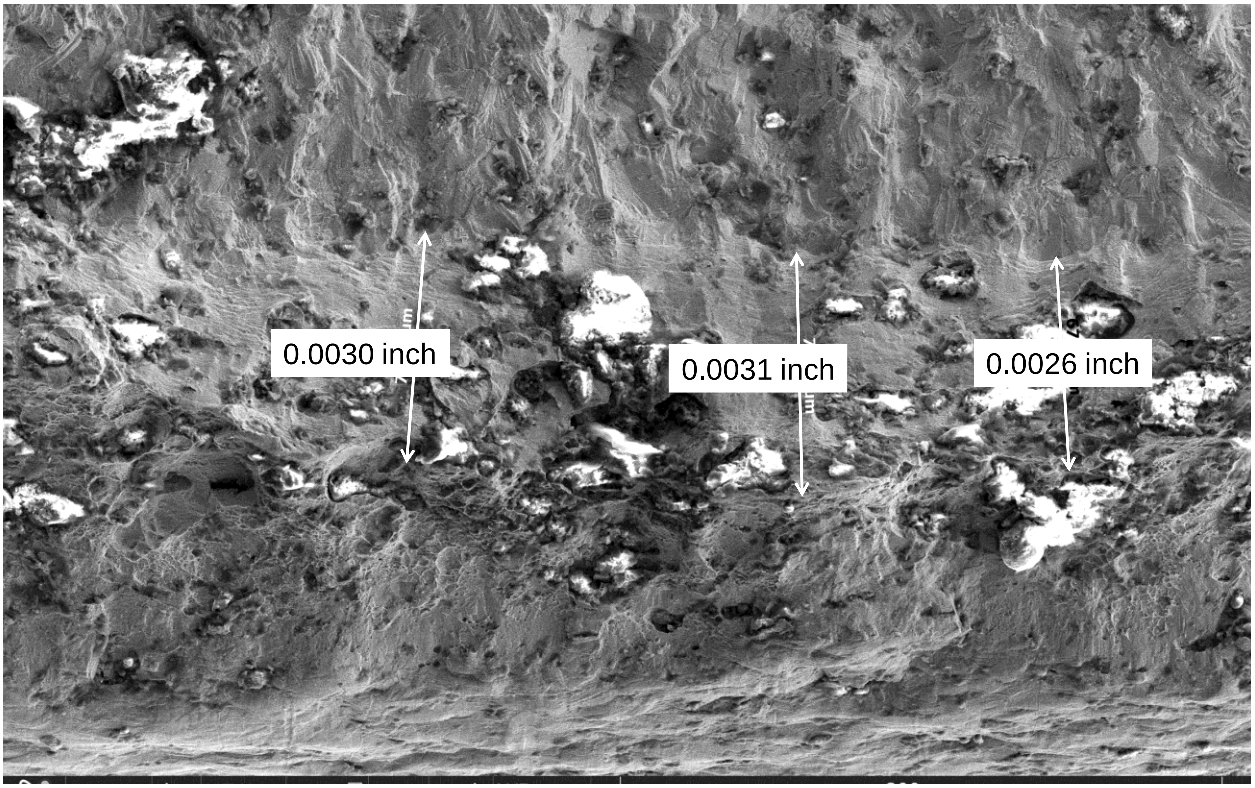

Figure M.43. Autofrettage measurements for IN718 coupon F-LT-030-02 that was loaded to an autofrettage strain level of 1.70%.

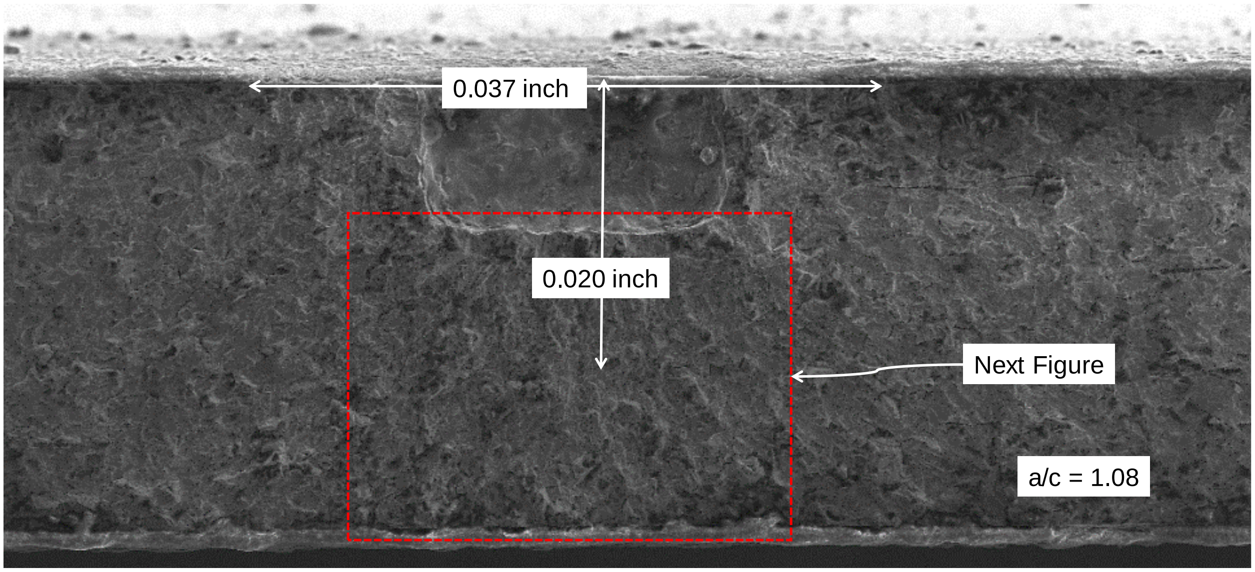

Figure M.44. Fracture surface for IN718 coupon F-LT-030-17 that was loaded to an autofrettage strain level of 1.74%.

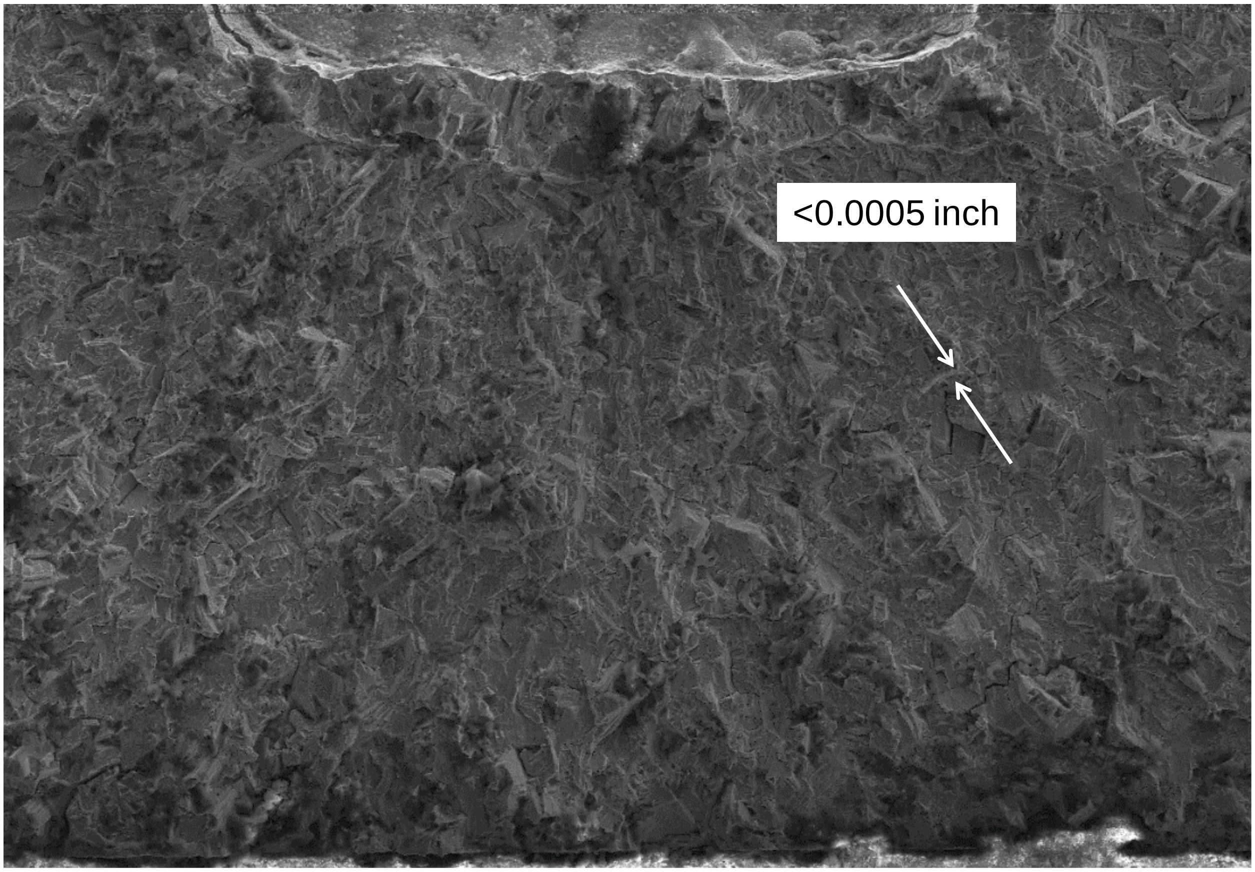

Figure M.45. Autofrettage measurements for IN718 coupon F-LT-030-17 that was loaded to an autofrettage strain level of 1.74%.

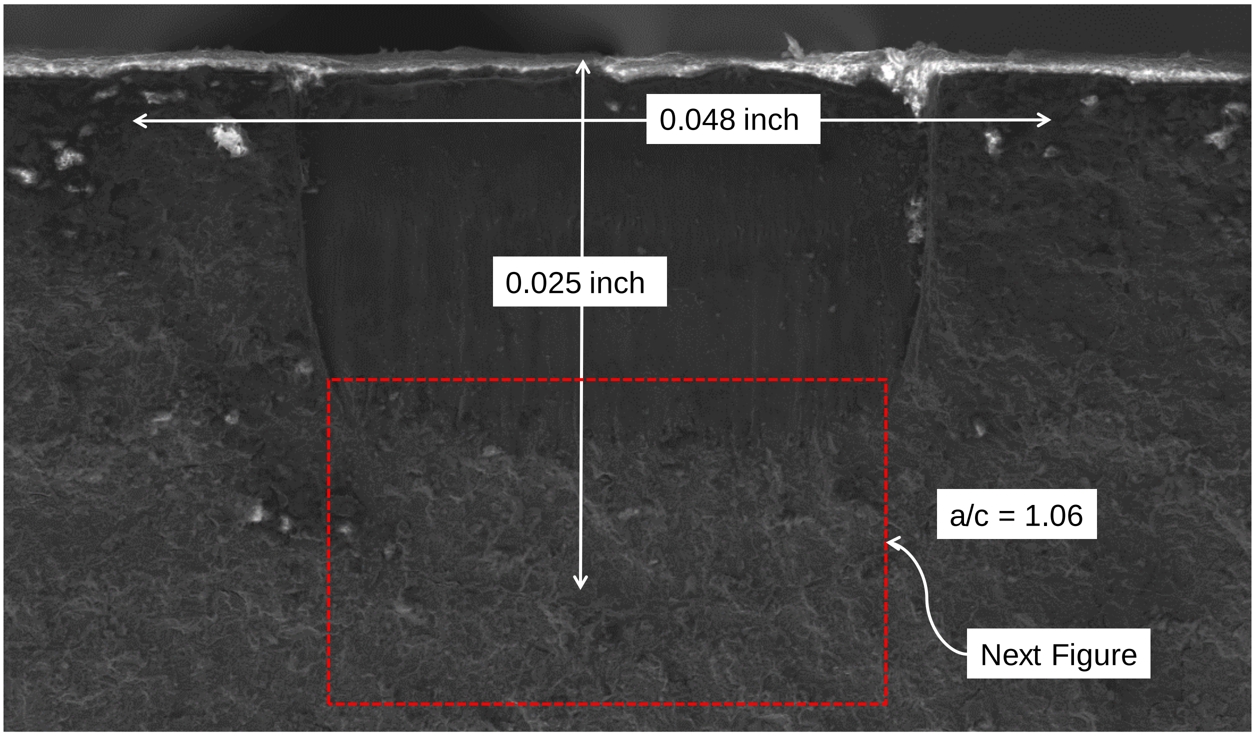

Figure M.46. Fracture surface for Ti 6Al-4V coupon Ti-Dome-01-04-060 that was loaded to an autofrettage strain level of 1.07%.

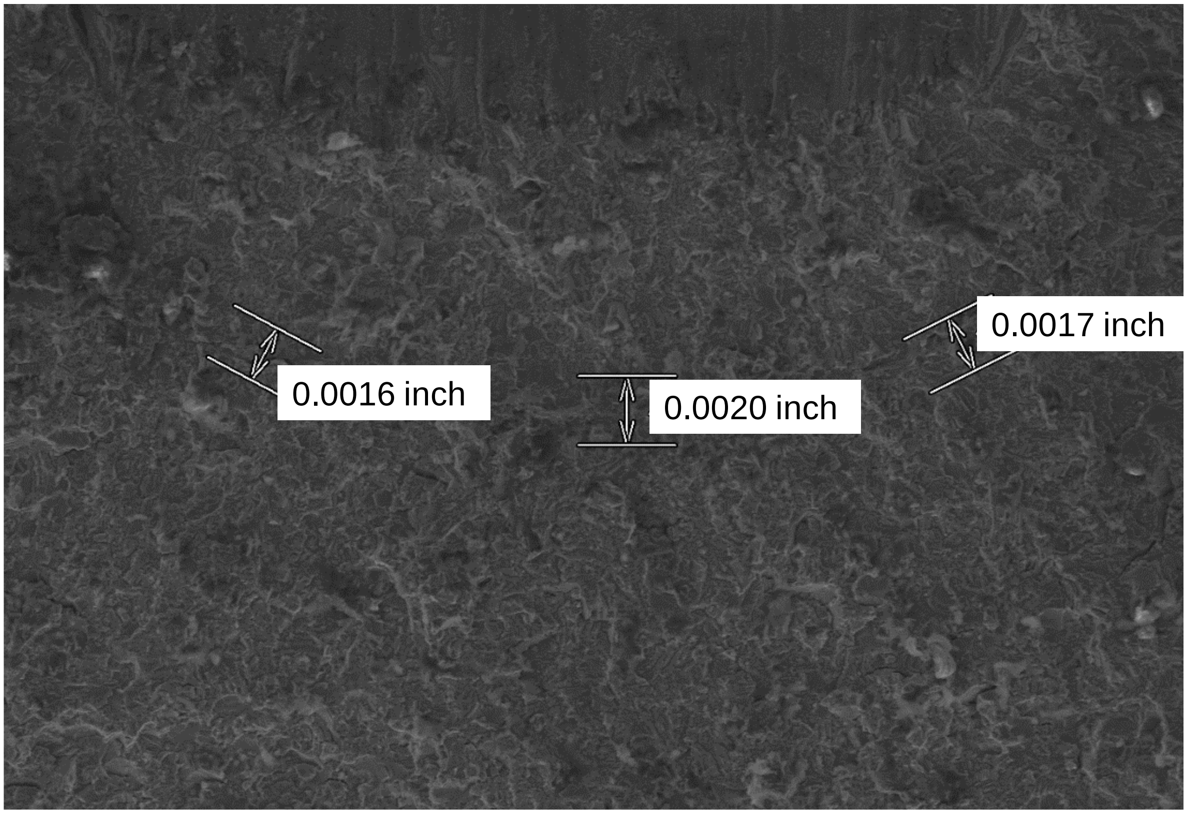

Figure M.47. Autofrettage measurements for Ti 6Al-4V coupon Ti-Dome-01-04-060 that was loaded to an autofrettage strain level of 1.07%.

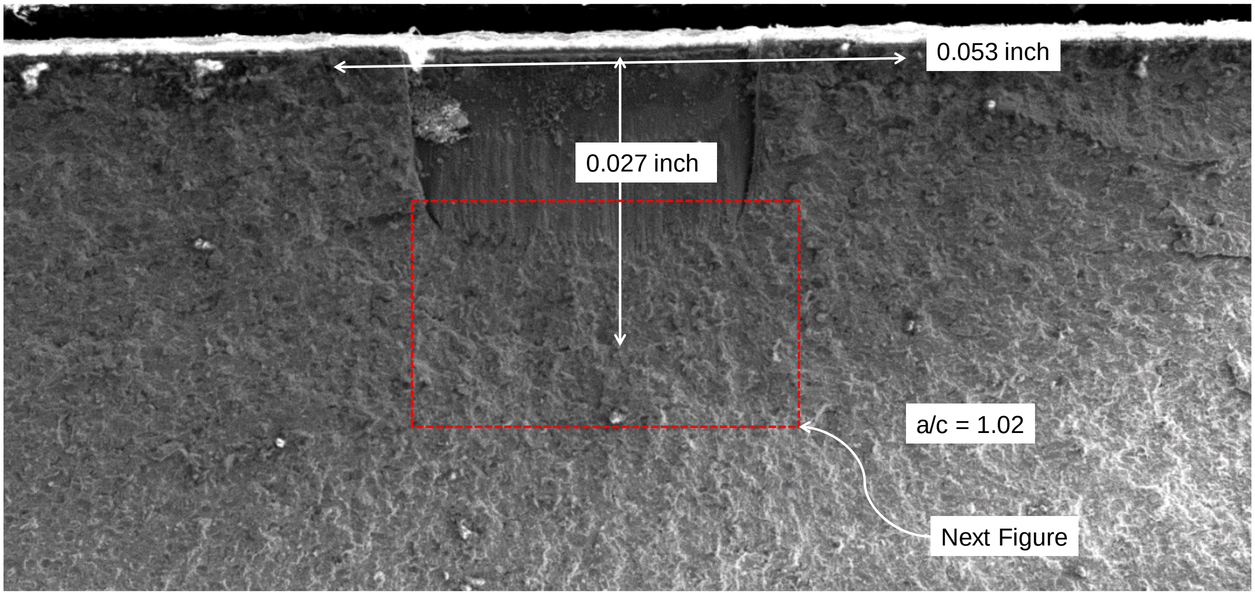

Figure M.48. Fracture surface for Ti 6Al-4V coupon Ti-Dome-01-05-060 that was loaded to an autofrettage strain level of 1.02%.

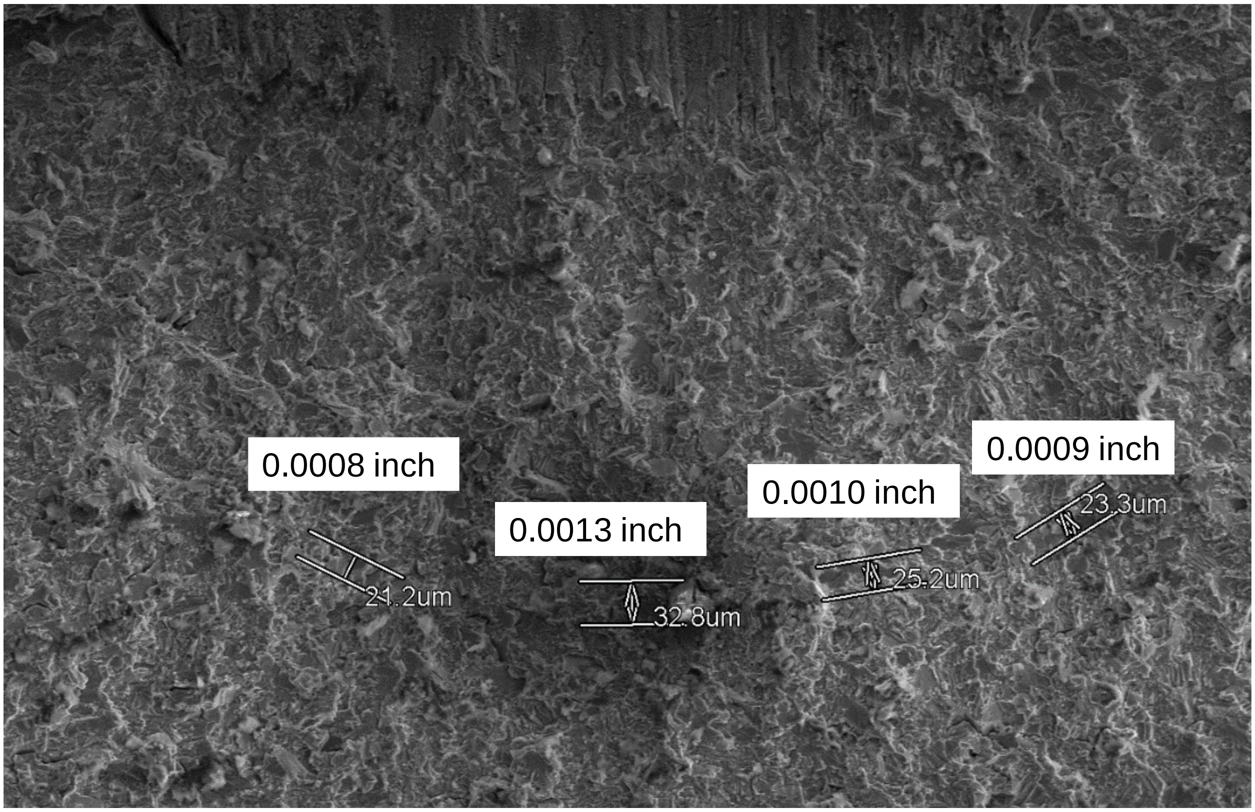

Figure M.49. Autofrettage measurements for Ti 6Al-4V coupon Ti-Dome-01-05-060 that was loaded to an autofrettage strain level of 1.02%.

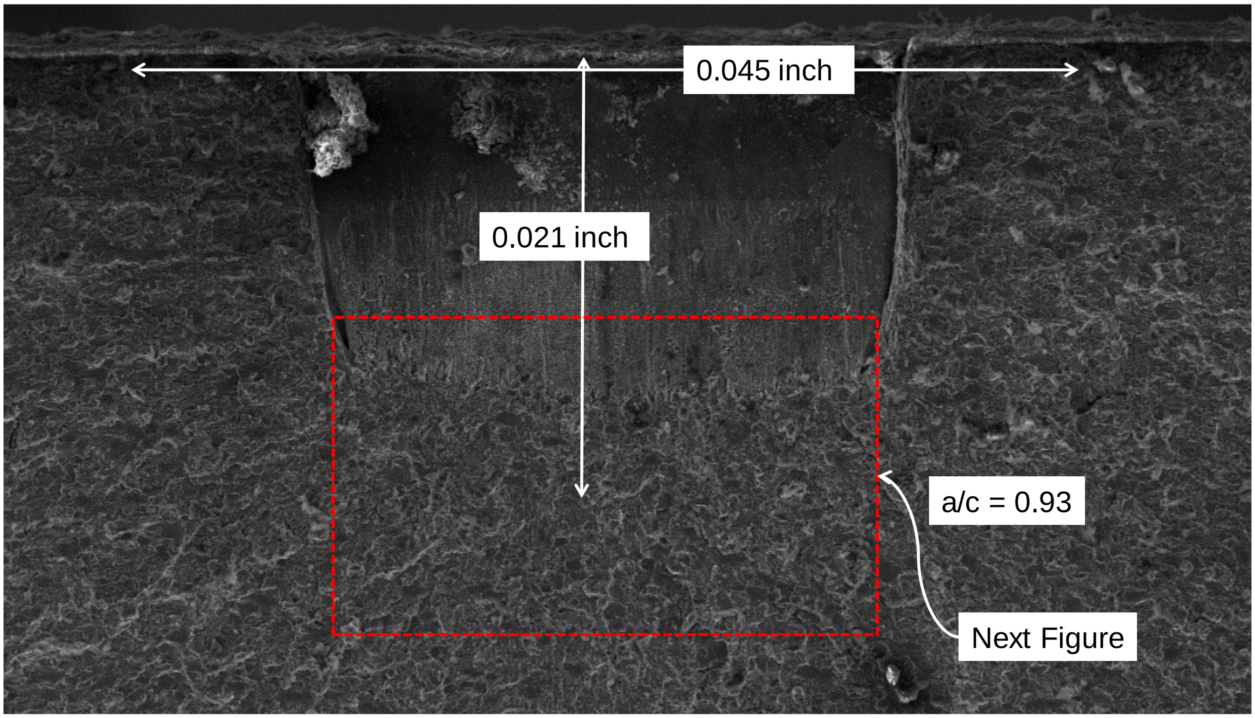

Figure M.50. Fracture surface for Ti 6Al-4V coupon Ti-Dome-01-03-060 that was loaded to an autofrettage strain level of 1.04%.

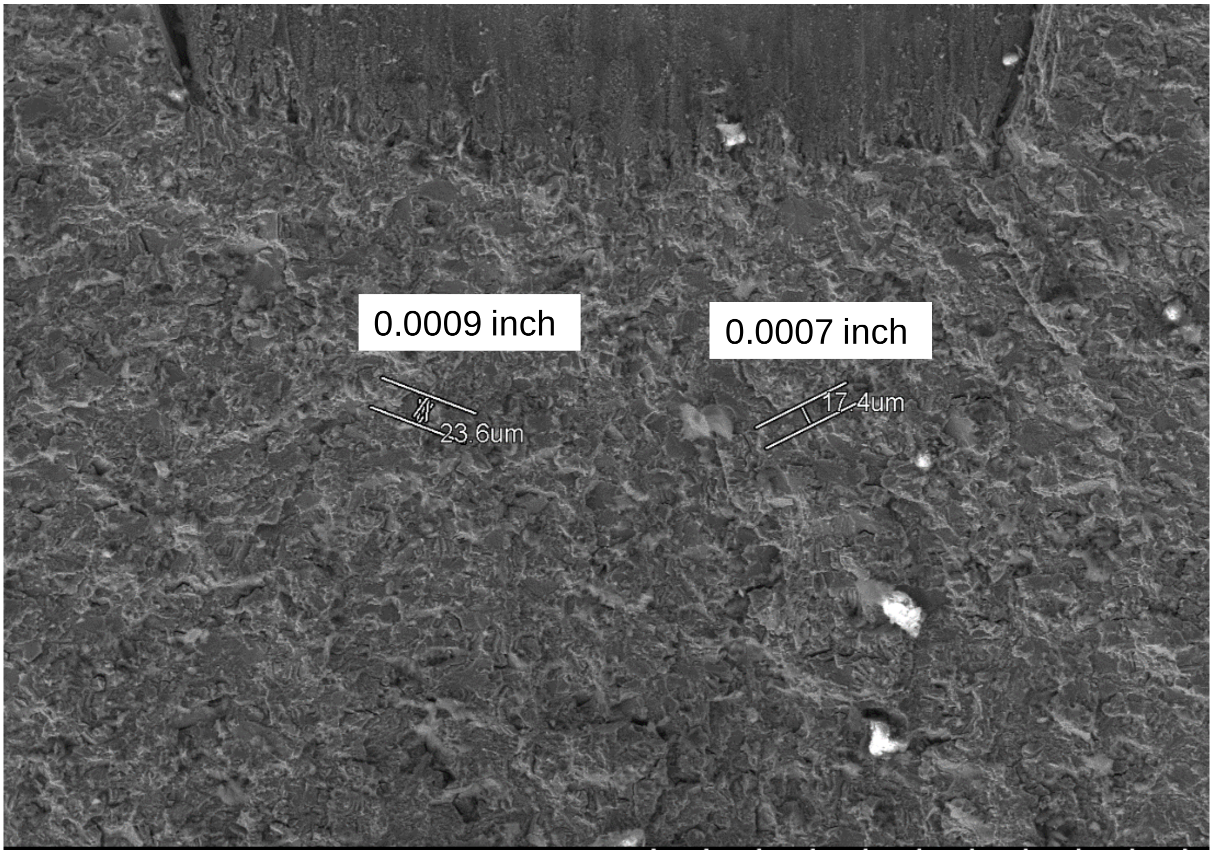

Figure M.51. Autofrettage measurements for Ti 6Al-4V coupon Ti-Dome-01-03-060 that was loaded to an autofrettage strain level of 1.04%.

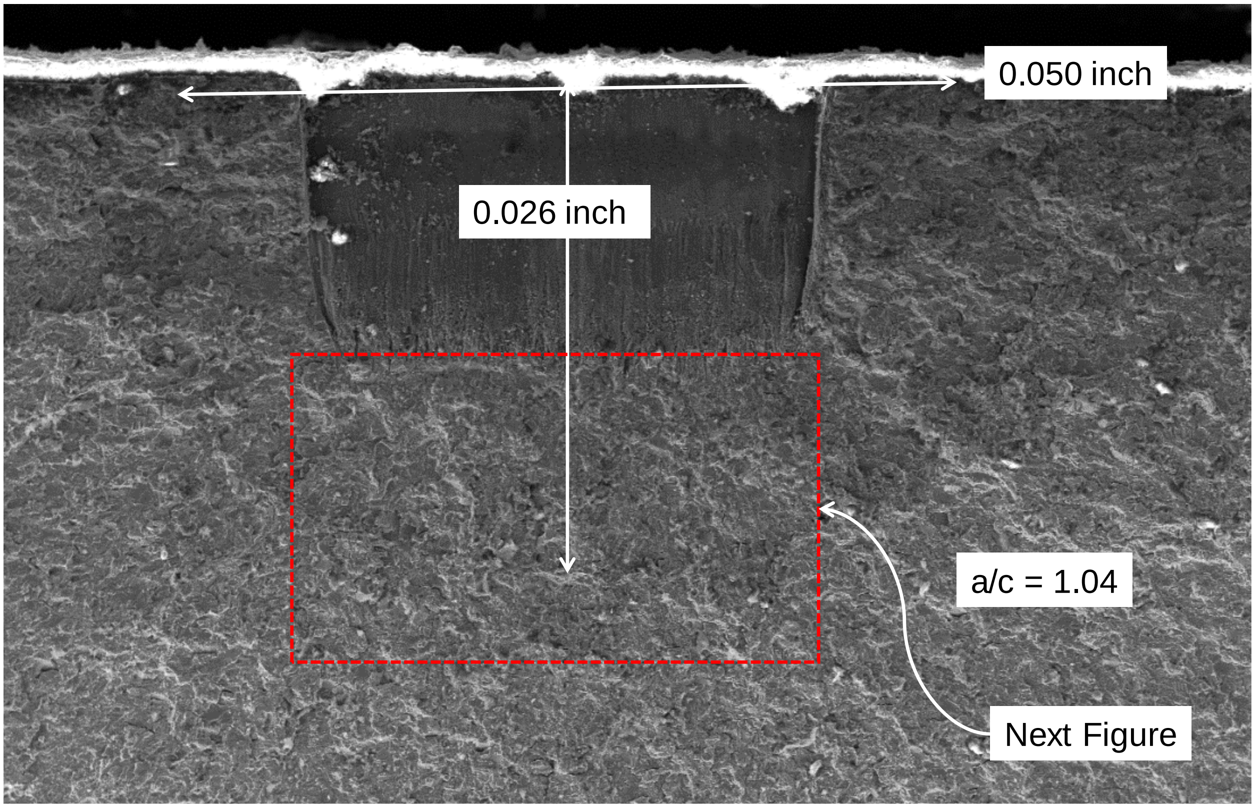

Figure M.52. Fracture surface for Ti 6Al-4V coupon Ti-Dome-01-06-060 that was loaded to an autofrettage strain level of 1.02%.

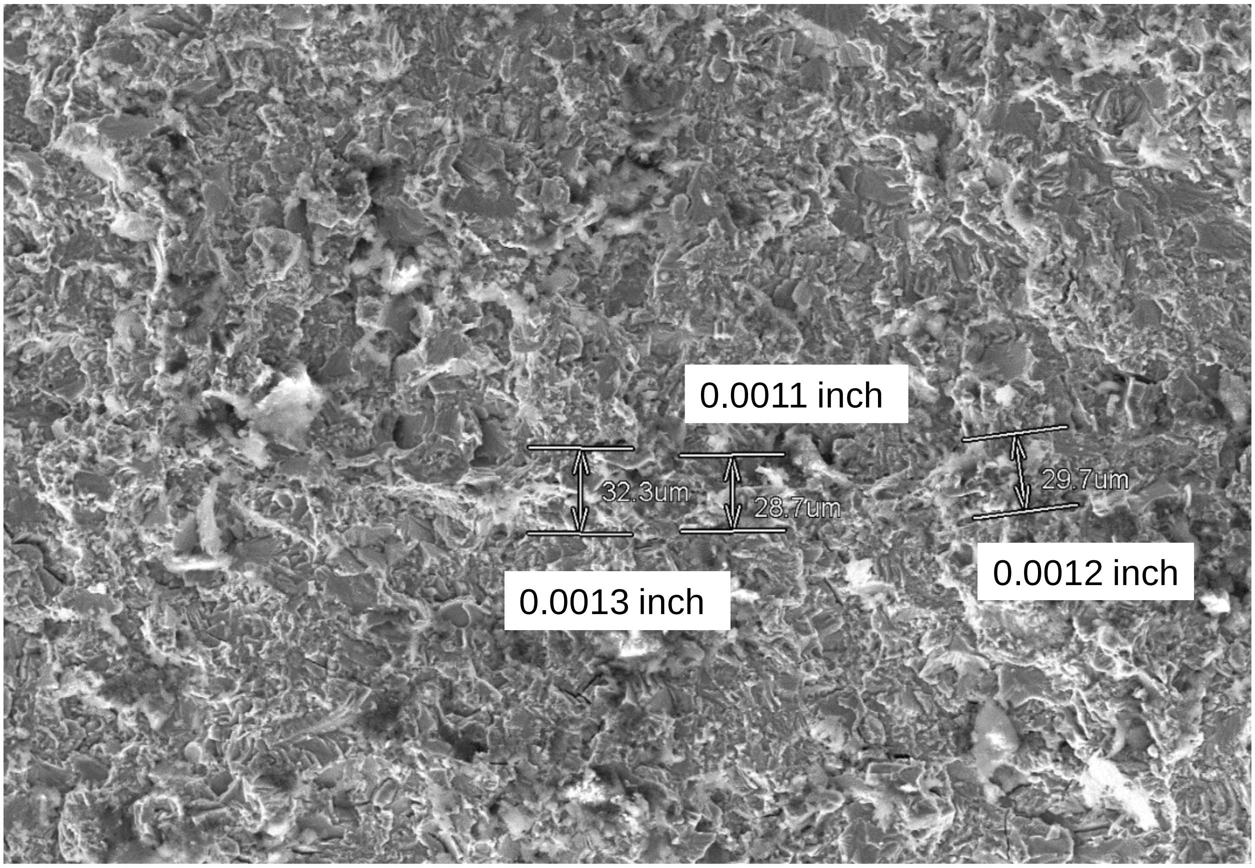

Figure M.53. Autofrettage measurements for Ti 6Al-4V coupon Ti-Dome-01-06-060 that was loaded to an autofrettage strain level of 1.02%.

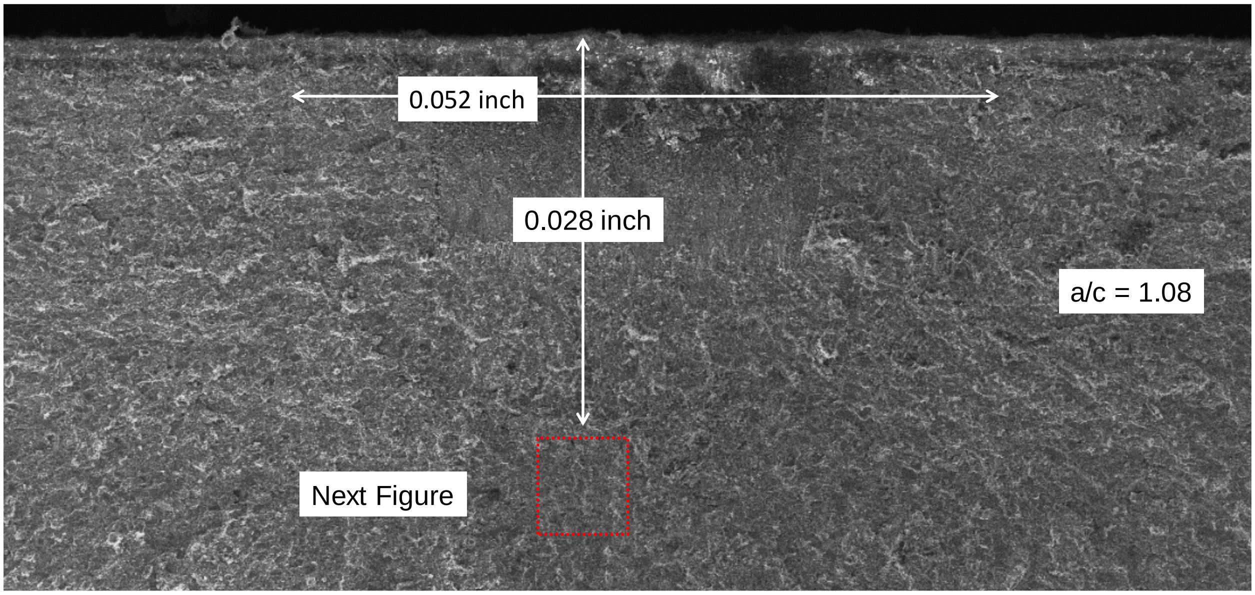

Figure M.54. Fracture surface for Ti 6Al-4V coupon Ti-Dome-01-08-060 that was loaded to an autofrettage strain level of 1.02%.

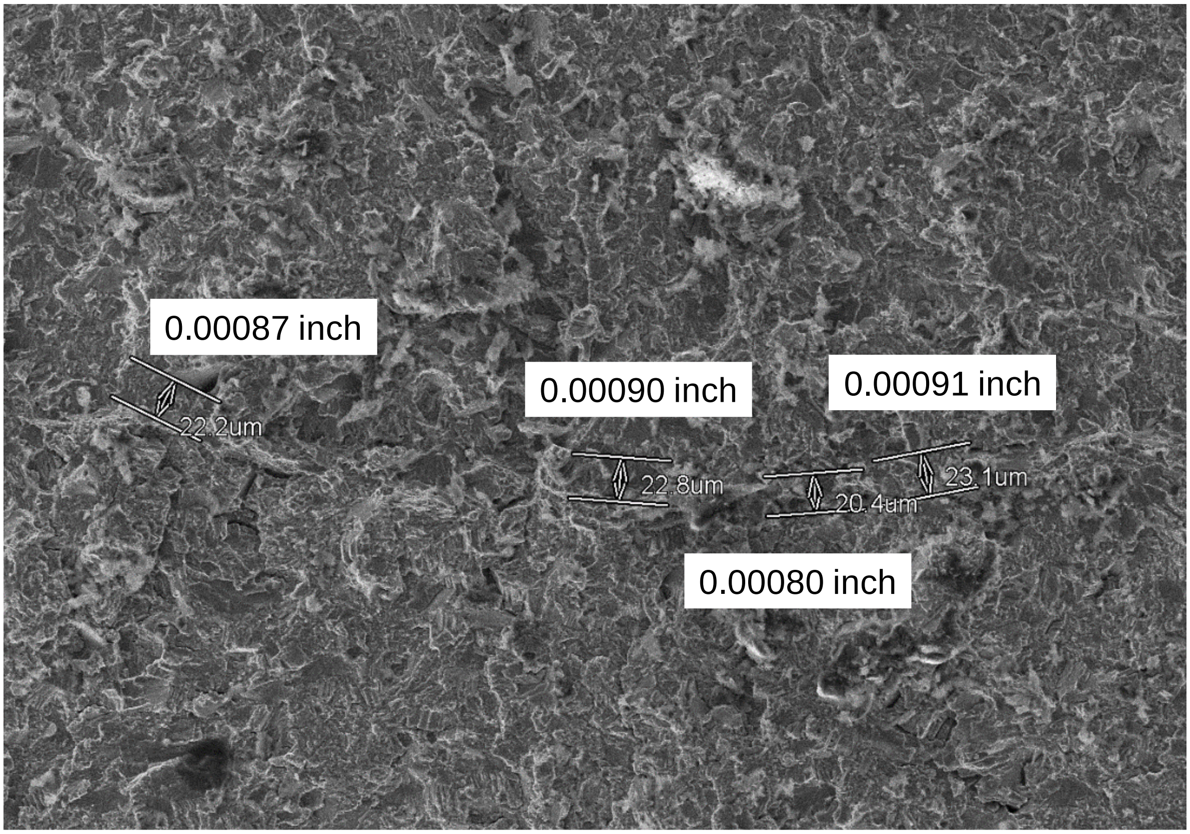

Figure M.55. Autofrettage measurements for Ti 6Al-4V coupon Ti-Dome-01-08-060 that was loaded to an autofrettage strain level of 1.02%.

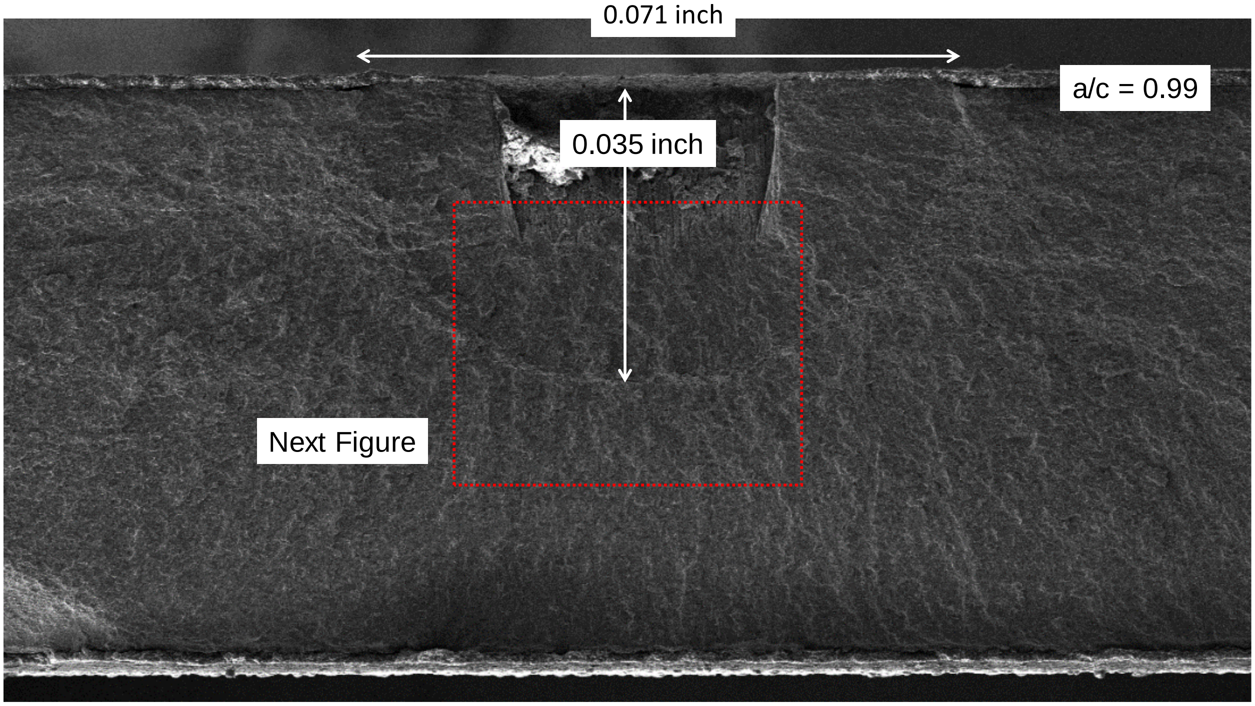

Figure M.56. Fracture surface for Ti 6Al-4V coupon Ti-Dome-03-01-060 that was loaded to an autofrettage strain level of 1.10%.

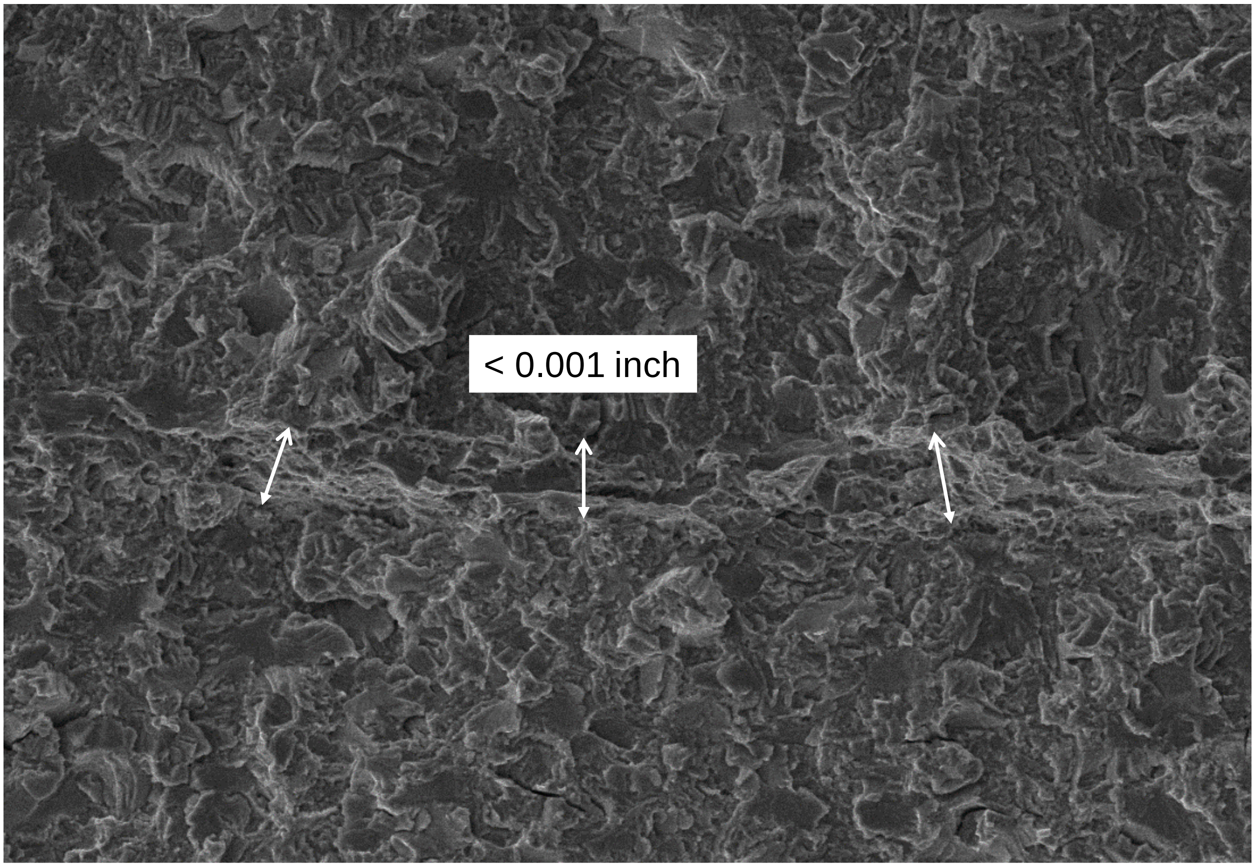

Figure M.57. Autofrettage measurements for Ti 6Al-4V coupon Ti-Dome-03-01-060 that was loaded to an autofrettage strain level of 1.10%.

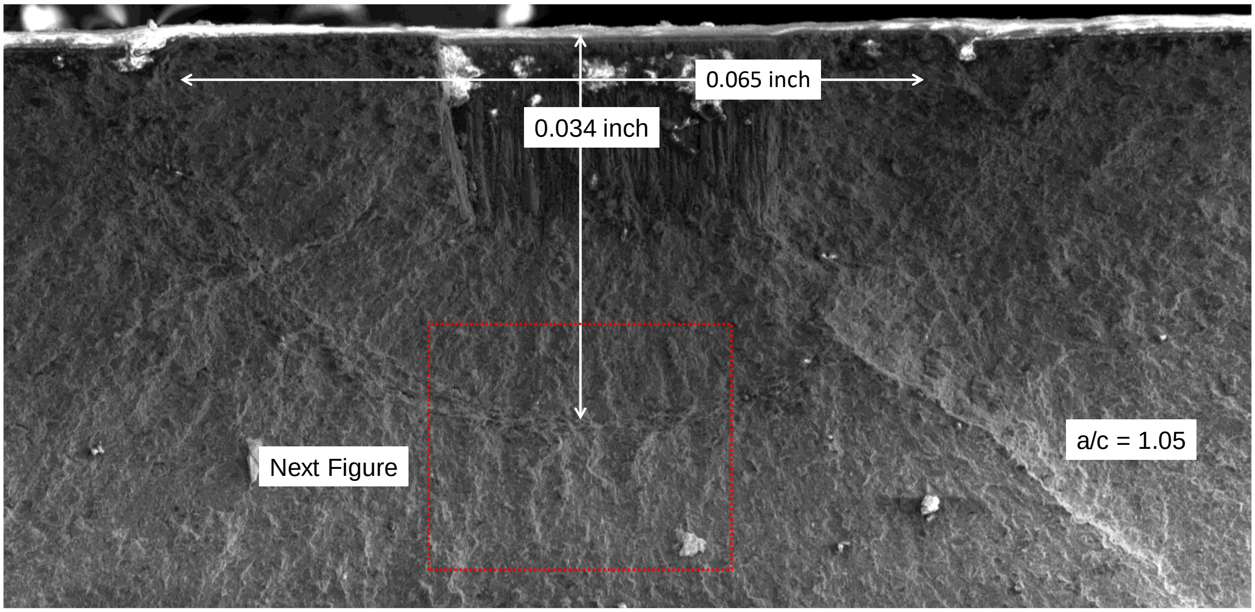

Figure M.58. Fracture surface for Ti 6Al-4V coupon Ti-Dome-03-02-060 that was loaded to an autofrettage strain level of 1.07%.

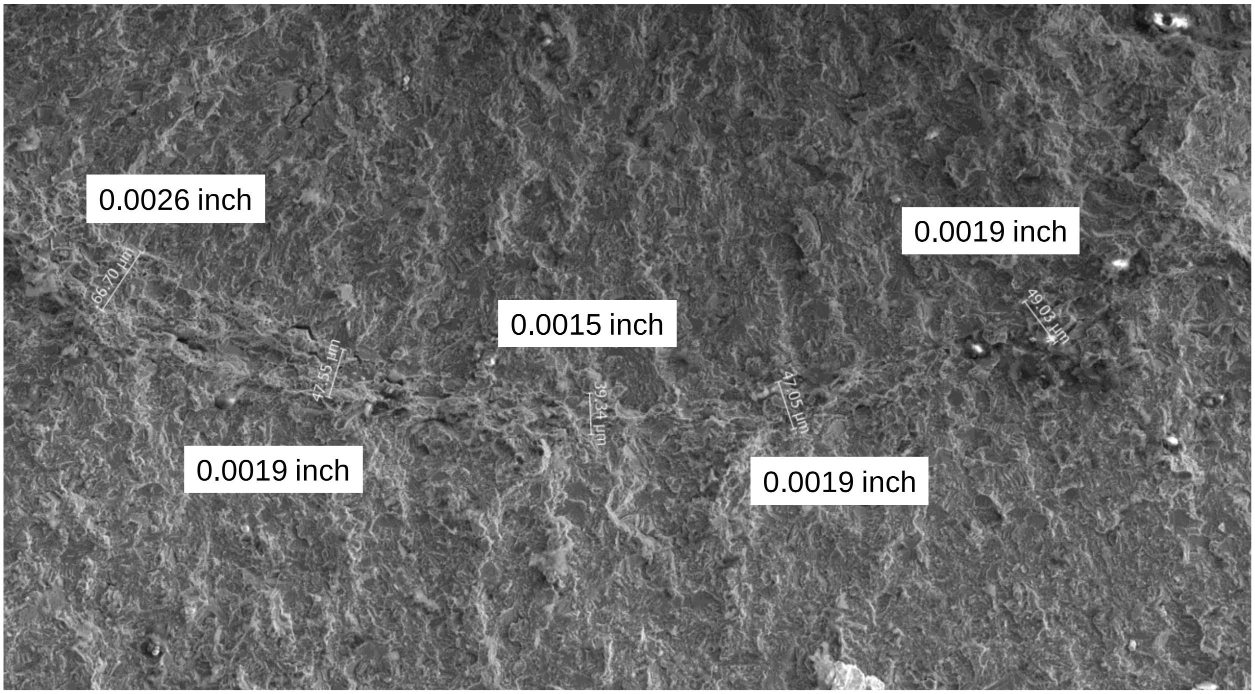

Figure M.59. Autofrettage measurements for Ti 6Al-4V coupon Ti-Dome-03-02-060 that was loaded to an autofrettage strain level of 1.07%.

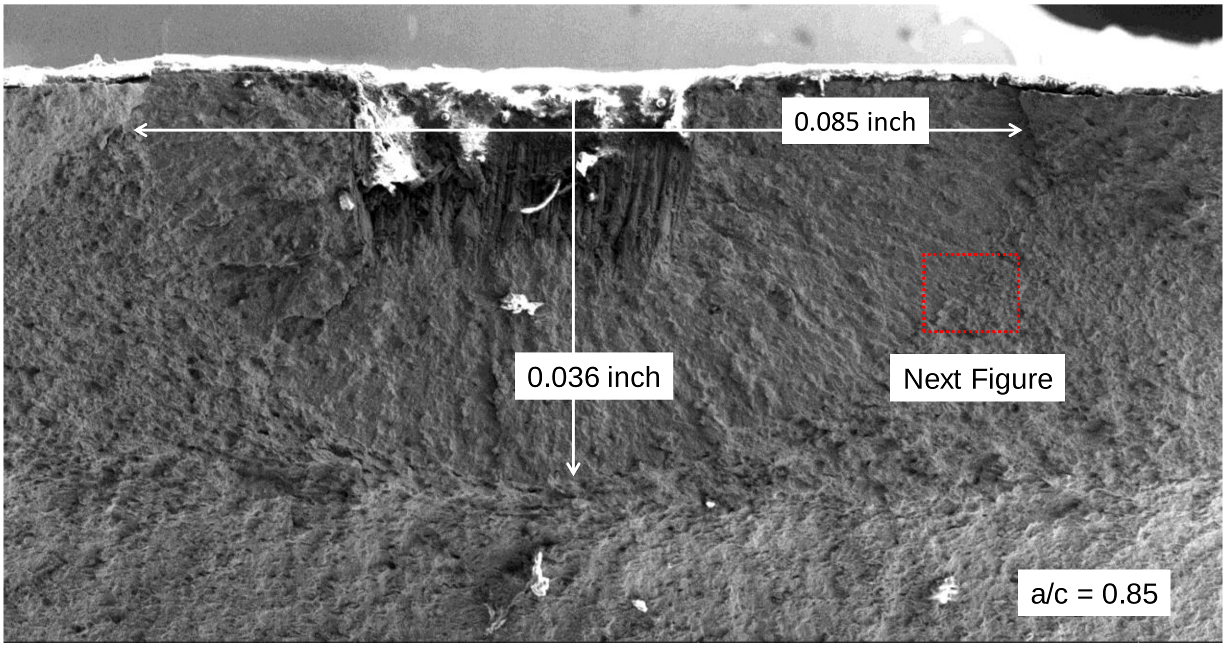

Note: The displacement was held constant after 1% strain was achieved and the coupon failed before the loading could be reversed.

Figure M.60. Fracture surface for Ti 6Al-4V coupon Ti-Dome-03-03-060 that was loaded to an autofrettage strain level of 1.07%.

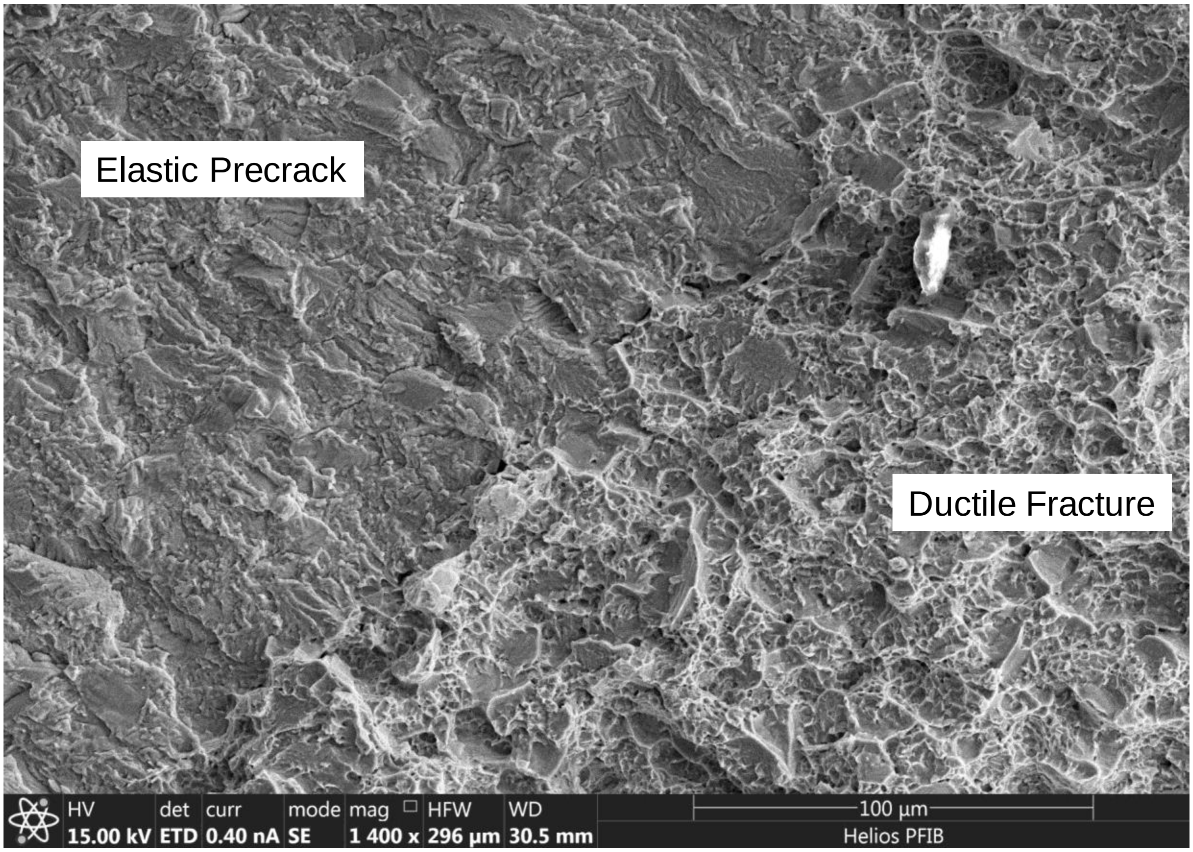

Figure M.61. Autofrettage measurements for Ti 6Al-4V coupon Ti-Dome-03-03-060 that was loaded to an autofrettage strain level of 1.07%.

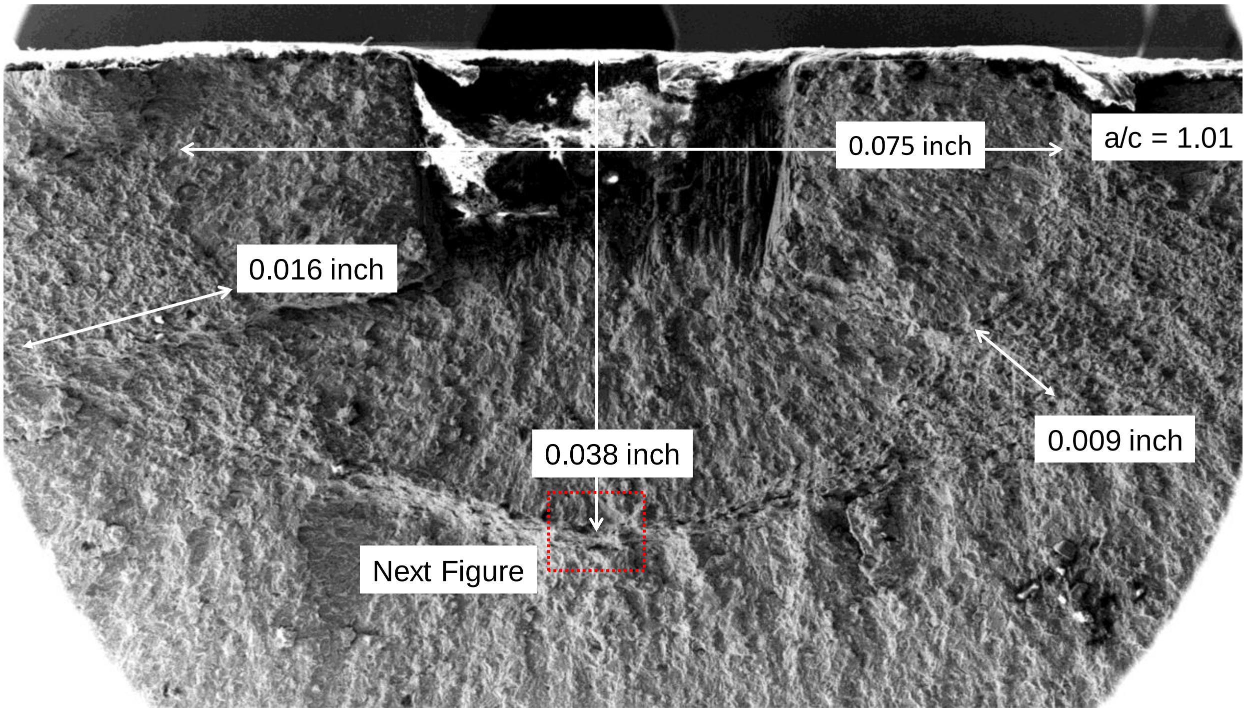

Figure M.62. Fracture surface for Ti 6Al-4V coupon Ti-Dome-03-04-060 that was loaded to an autofrettage strain level of 1.01%.

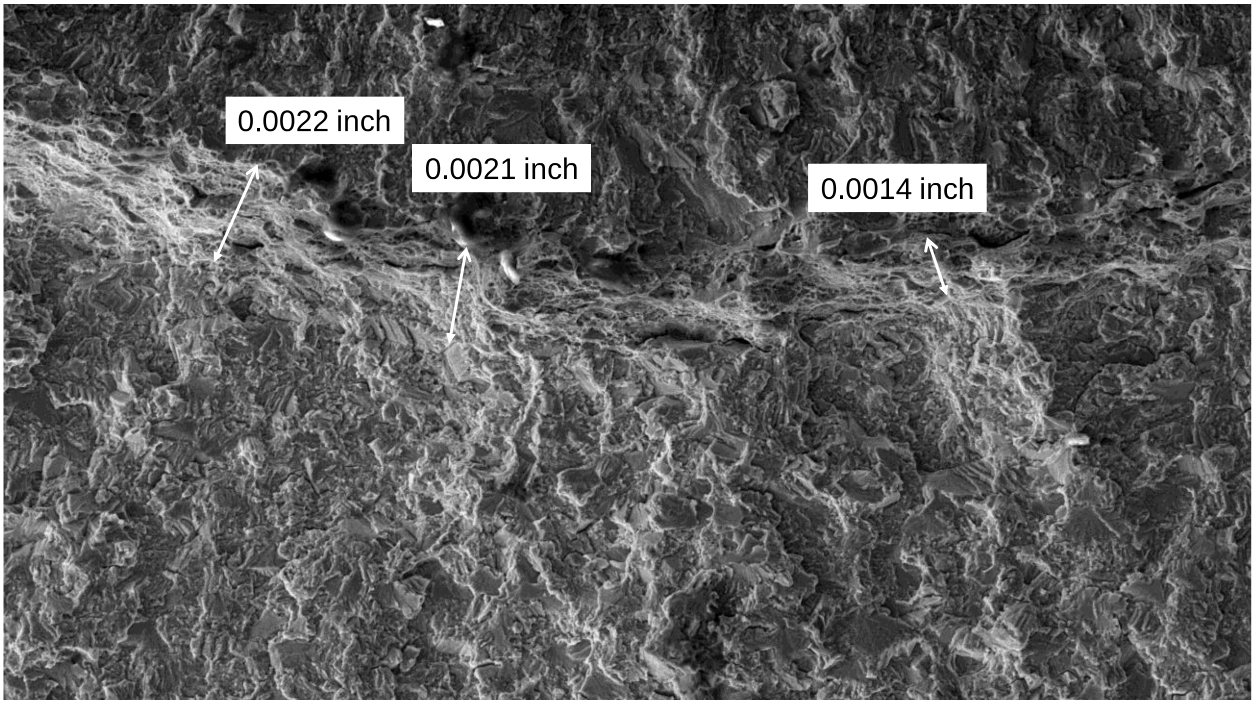

Figure M.63. Autofrettage measurements for Ti 6Al-4V coupon Ti-Dome-03-04-060 that was loaded to an autofrettage strain level of 1.01%.

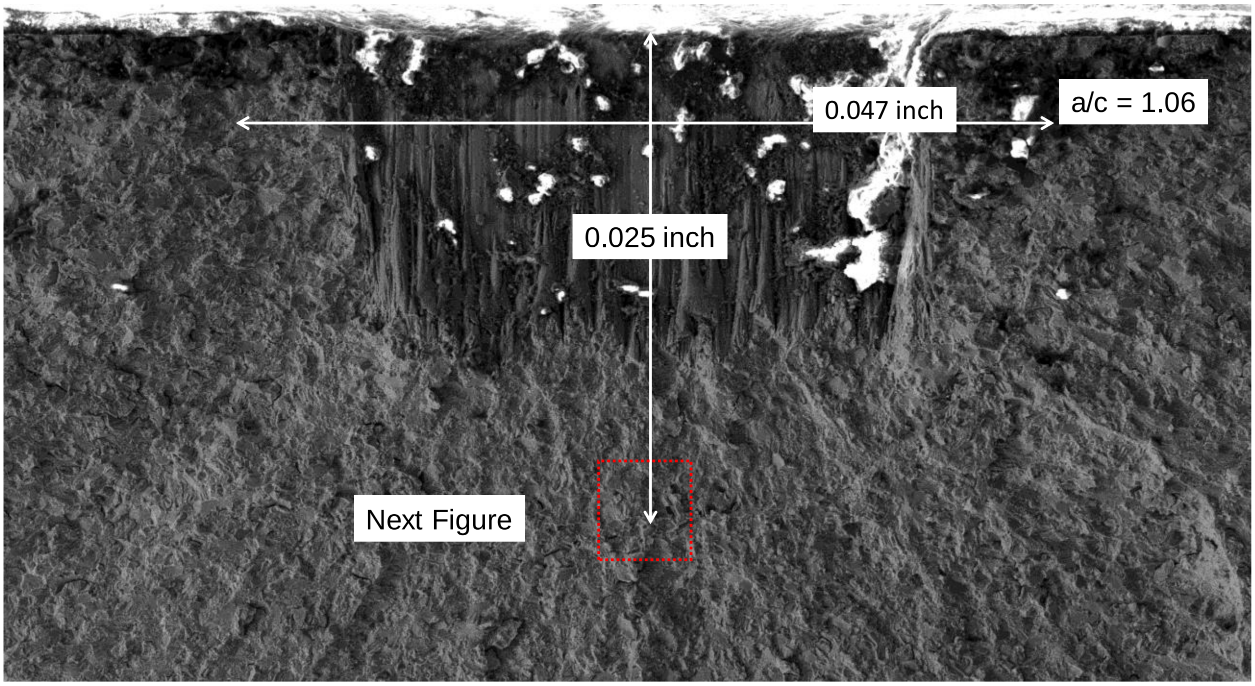

Figure M.64. Fracture surface for Ti 6Al-4V coupon Ti-Dome-03-05-060 that was loaded to an autofrettage strain level of 1.02%.

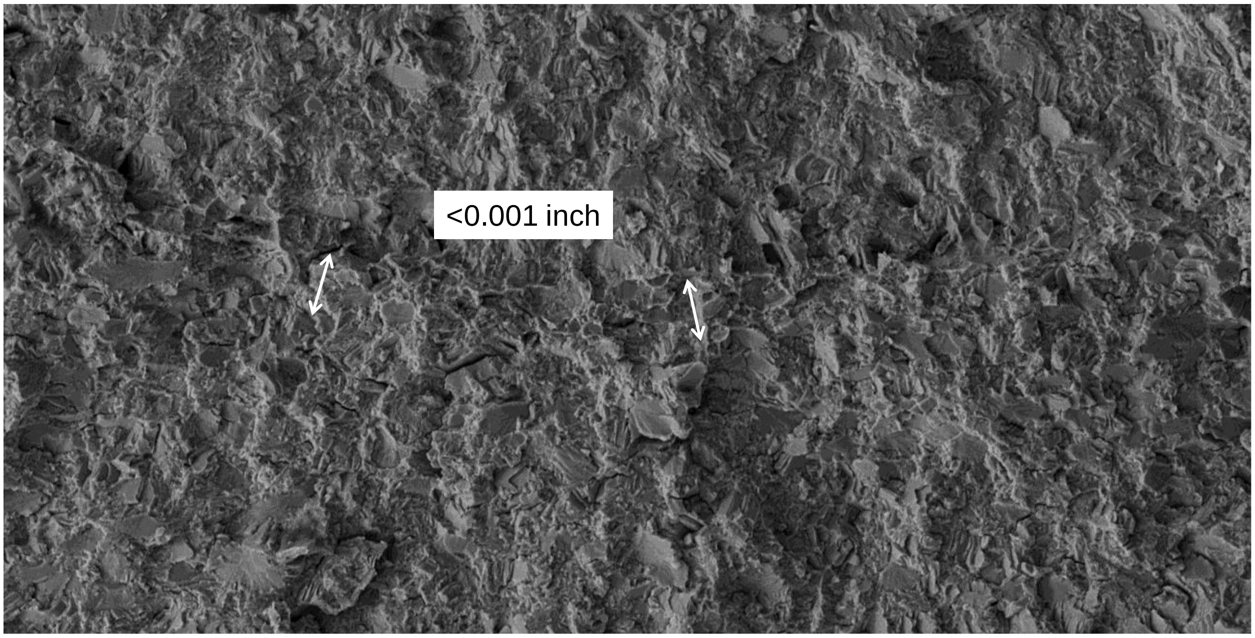

Figure M.65. Autofrettage measurements for Ti 6Al-4V coupon Ti-Dome-03-05-060 that was loaded to an autofrettage strain level of 1.02%.

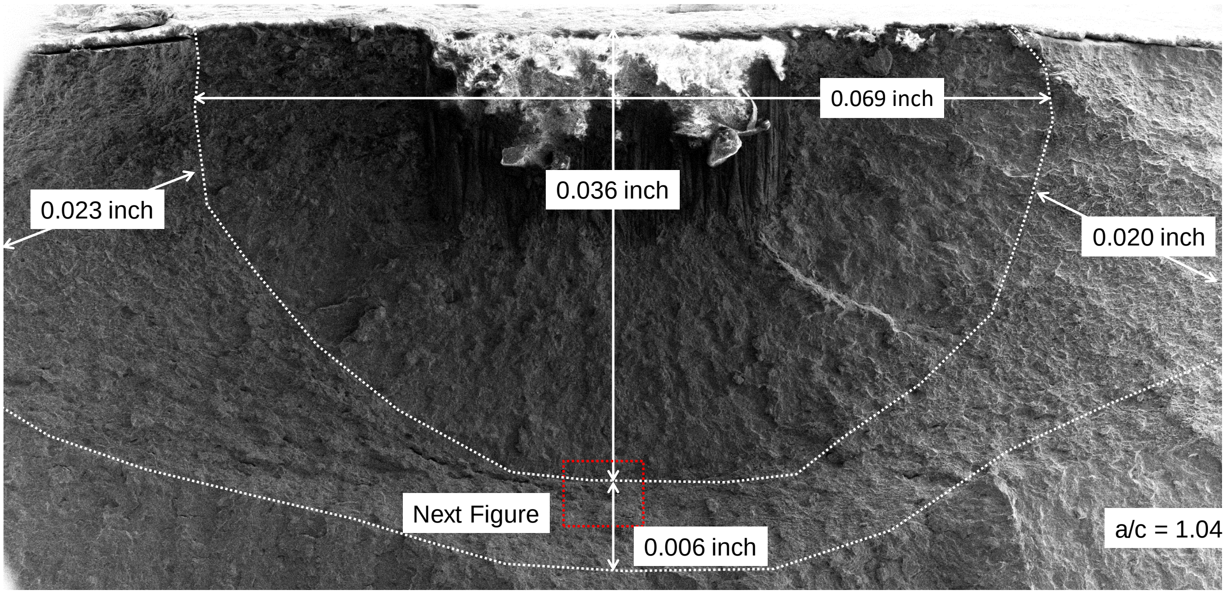

Figure M.66. Fracture surface for Ti 6Al-4V coupon Ti-Dome-03-06-060 that was loaded to an autofrettage strain level of 1.13%.

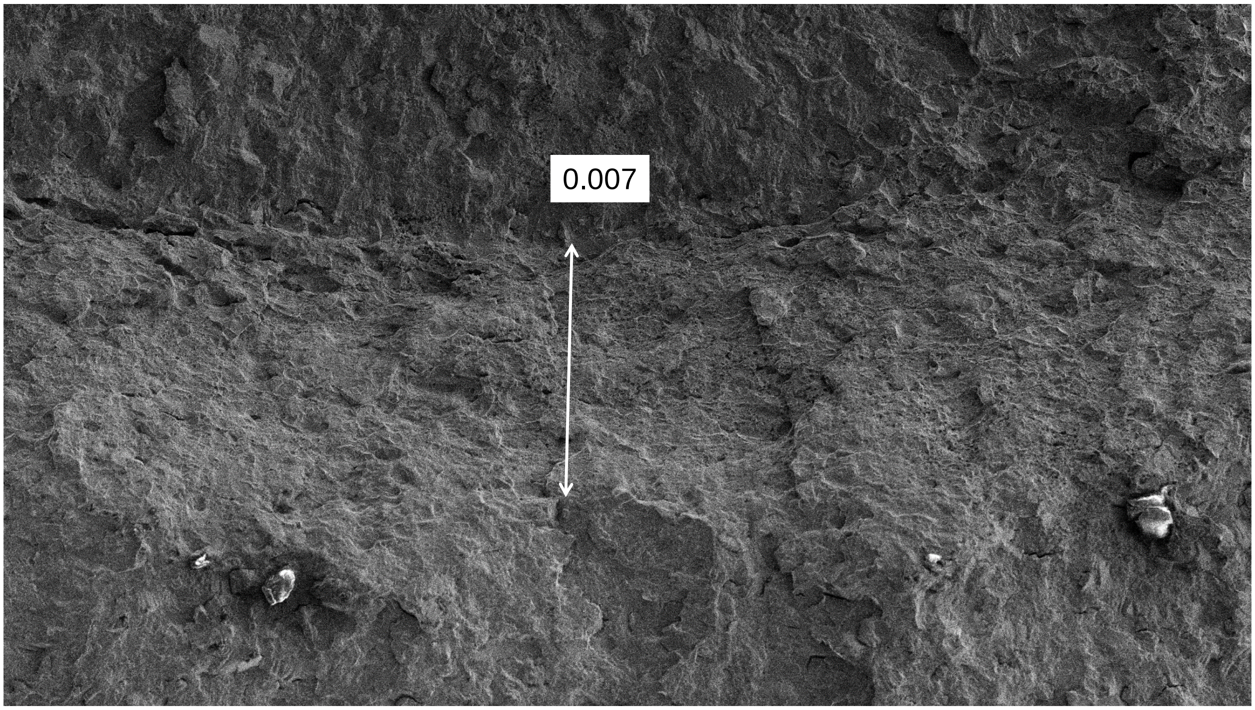

Figure M.67. Autofrettage measurements for Ti 6Al-4V coupon Ti-Dome-03-06-060 that was loaded to an autofrettage strain level of 1.13%.

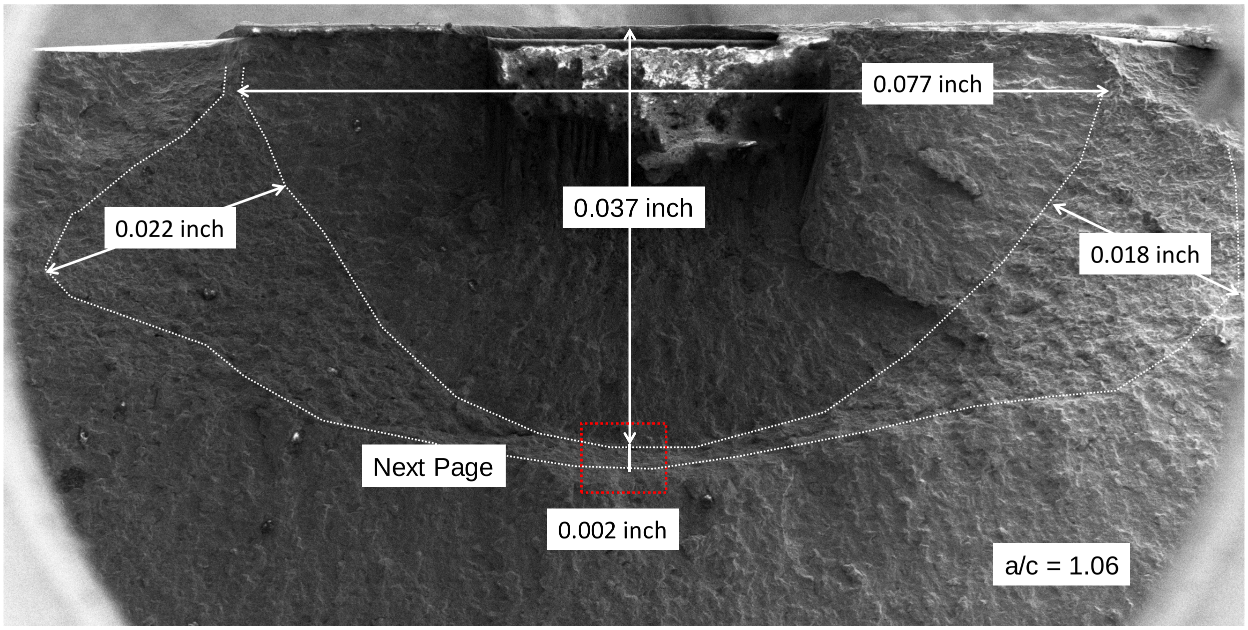

Figure M.68. Fracture surface for Ti 6Al-4V coupon Ti-Dome-03-07-060 that was loaded to an autofrettage strain level of 1.13%.

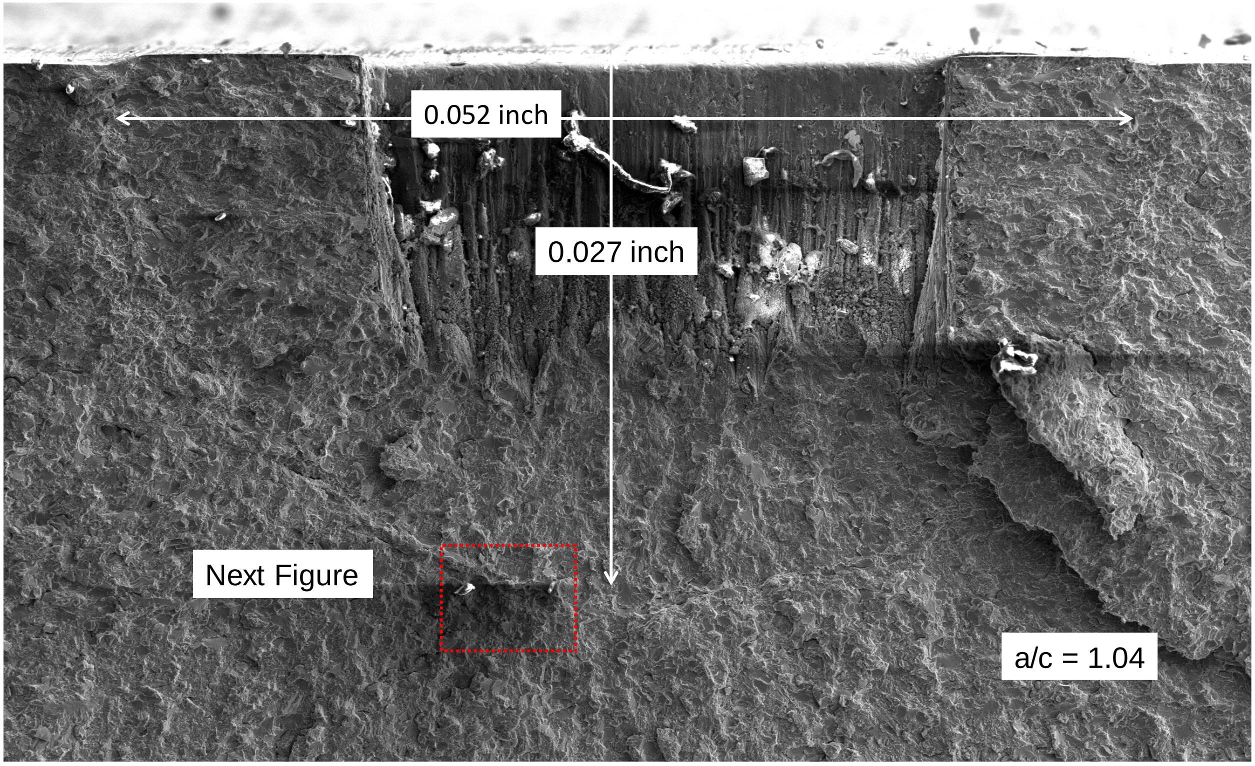

Figure M.69. Fracture surface for Ti 6Al-4V coupon Ti-Dome-03-08-060 that was loaded to an autofrettage strain level of 1.0% (4 autofrettage cycle repeats).

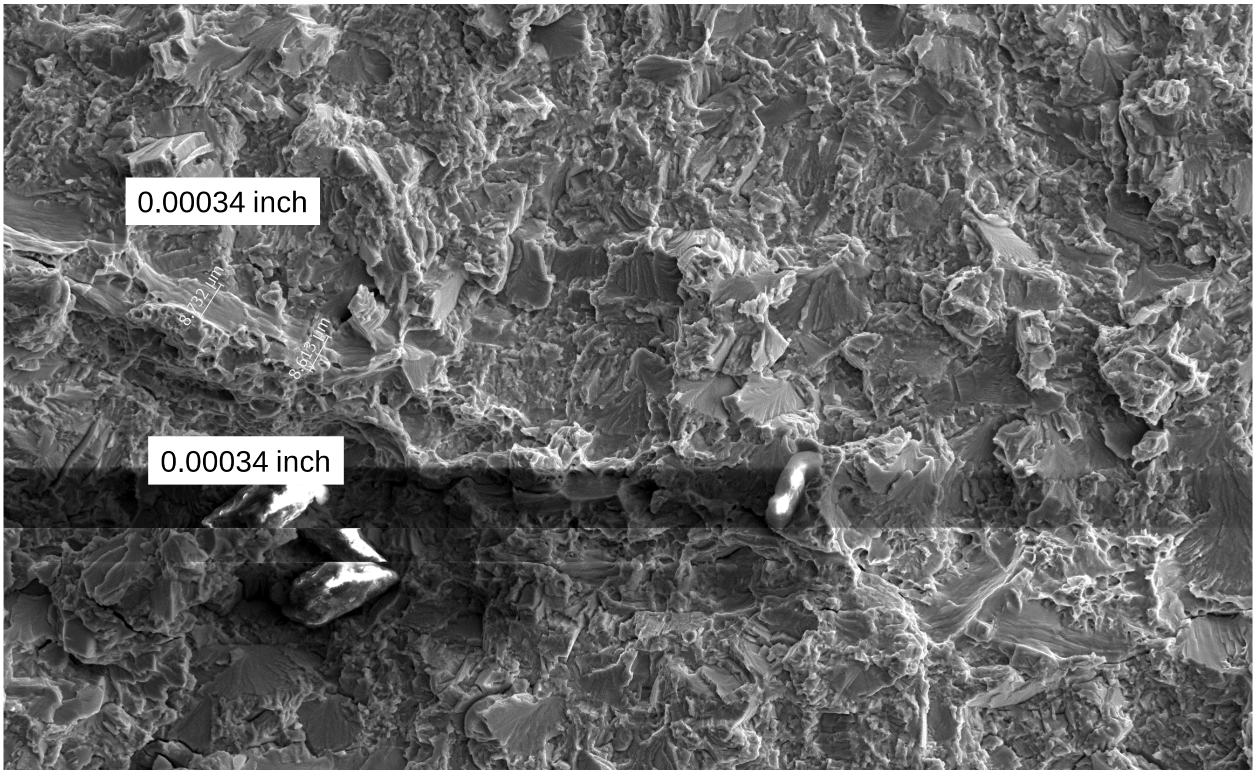

Figure M.70. Autofrettage measurements for Ti 6Al-4V coupon Ti-Dome-03-08-060 that was loaded to an autofrettage strain level of 1.0% (4 autofrettage cycle repeats).

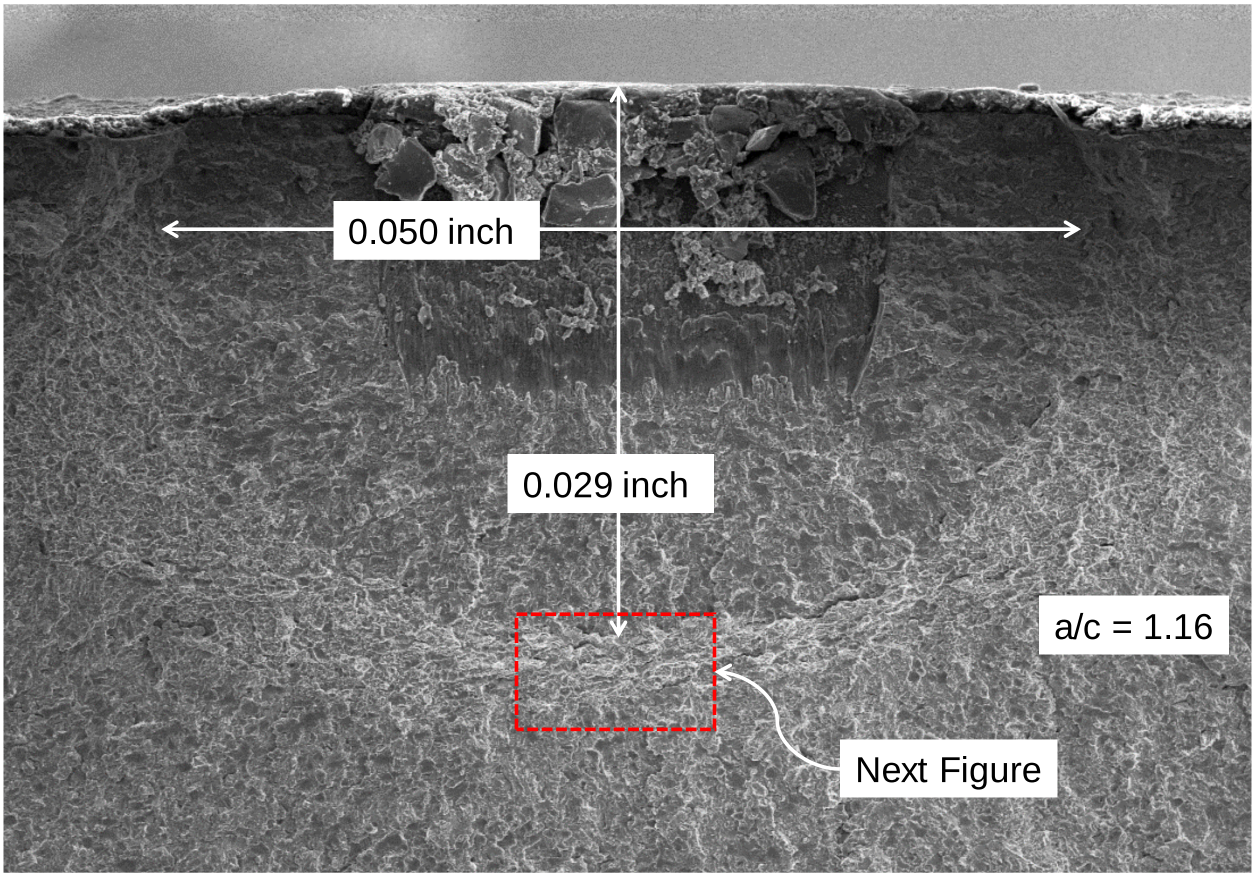

Figure M.71. Fracture surface for Ti 6Al-4V coupon Ti-Dome-00-01-082 that was loaded to an autofrettage strain level of 2.66%.

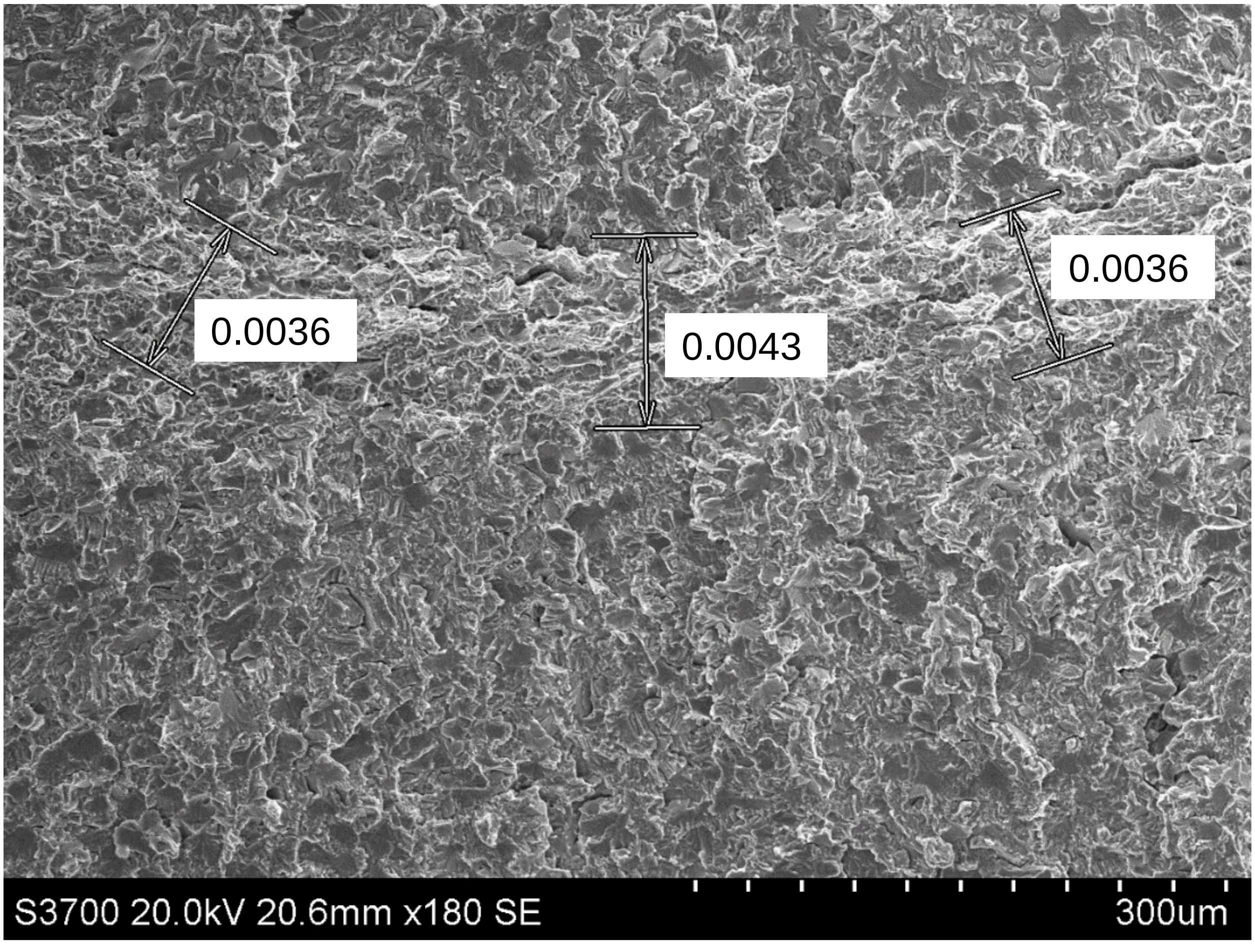

Figure M.72. Autofrettage measurements for Ti 6Al-4V coupon Ti-Dome-00-01-082 that was loaded to an autofrettage strain level of 2.66%.

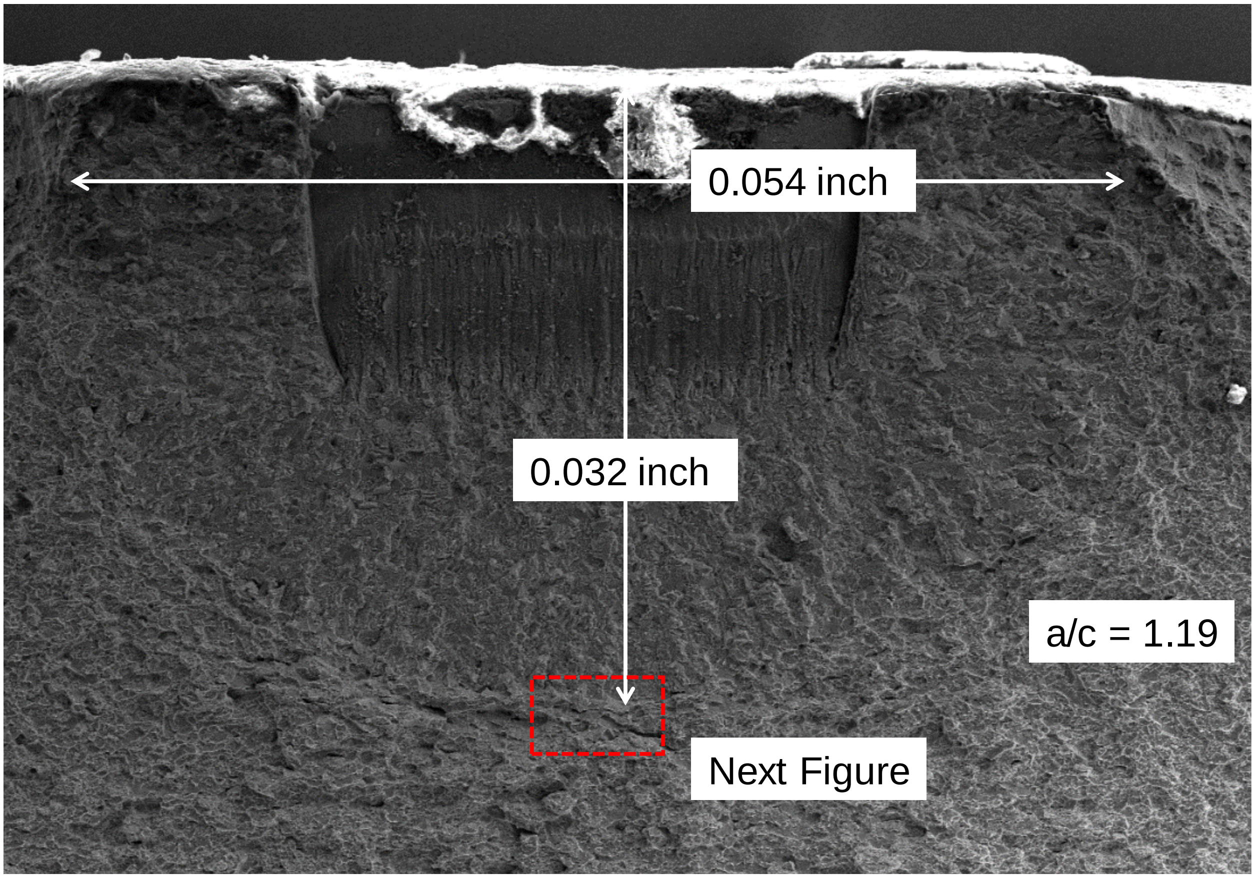

Figure M.73. Fracture surface for Ti 6Al-4V coupon Ti-Dome-00-02-082 that was loaded to an autofrettage strain level of 2.53%.

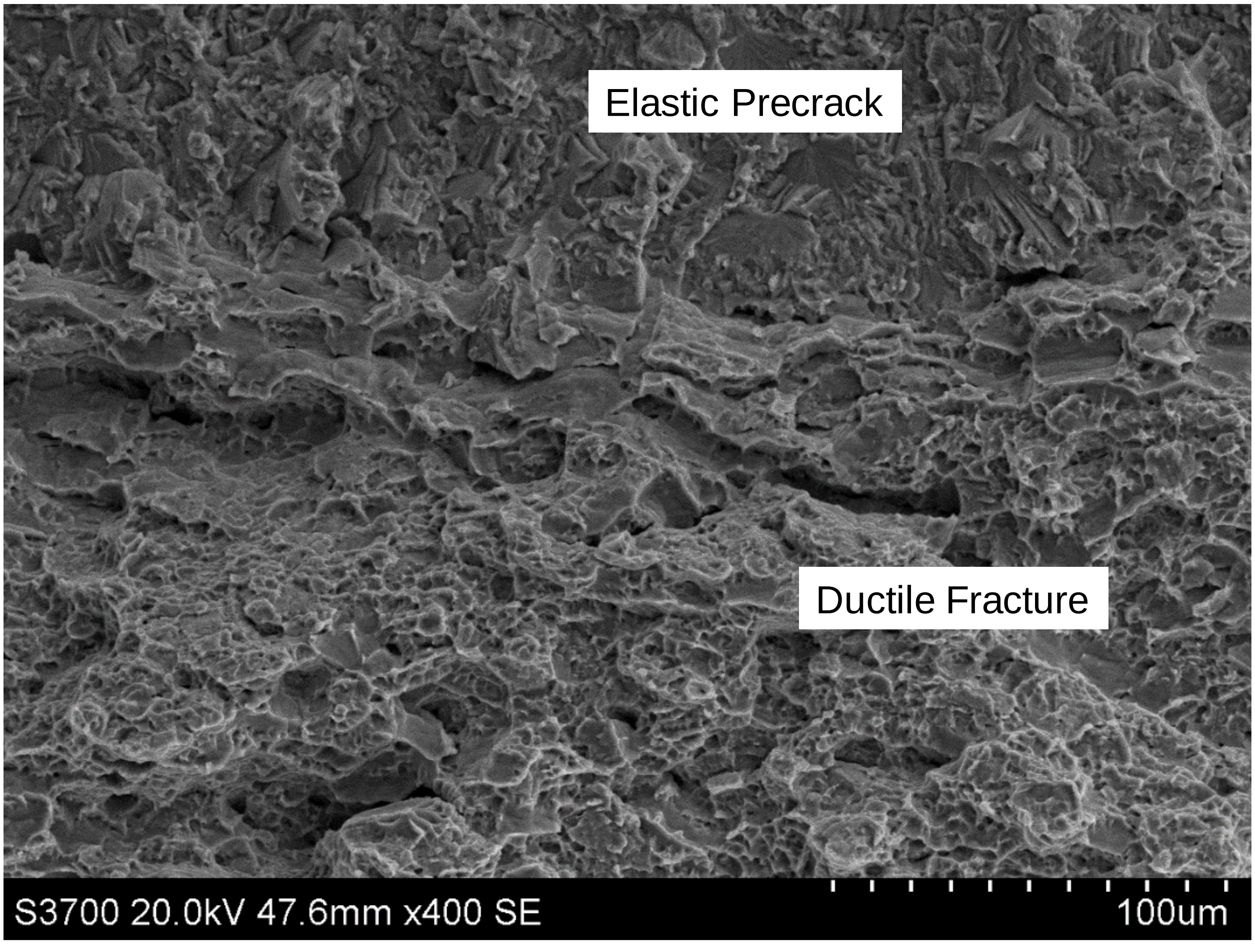

Figure M.74. Autofrettage measurements for Ti 6Al-4V coupon Ti-Dome-00-02-082 that was loaded to an autofrettage strain level of 2.53%.

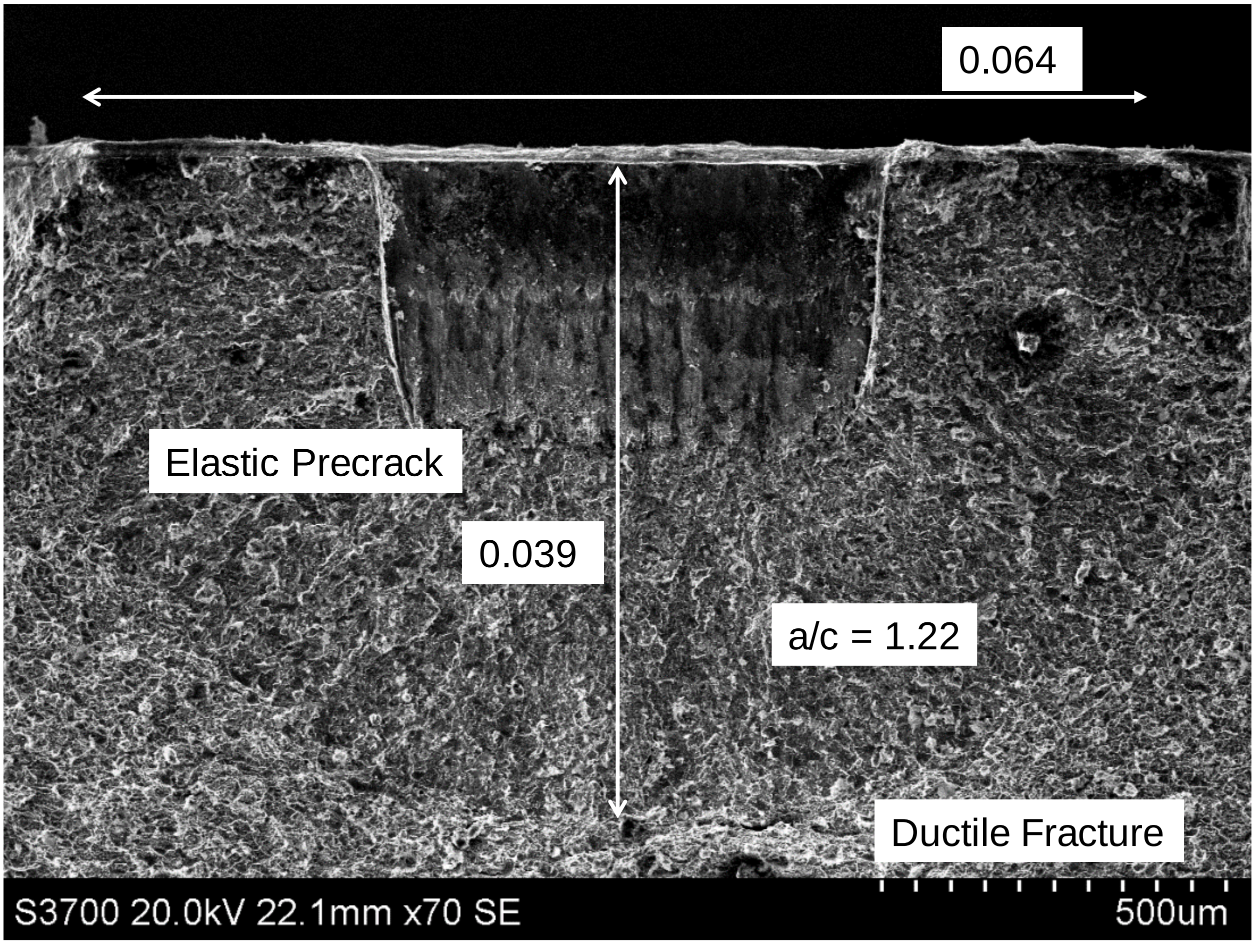

Figure M.75. Fracture surface for Ti 6Al-4V coupon Ti-Dome-00-03-082 that was loaded to an autofrettage strain level of 1.71%.

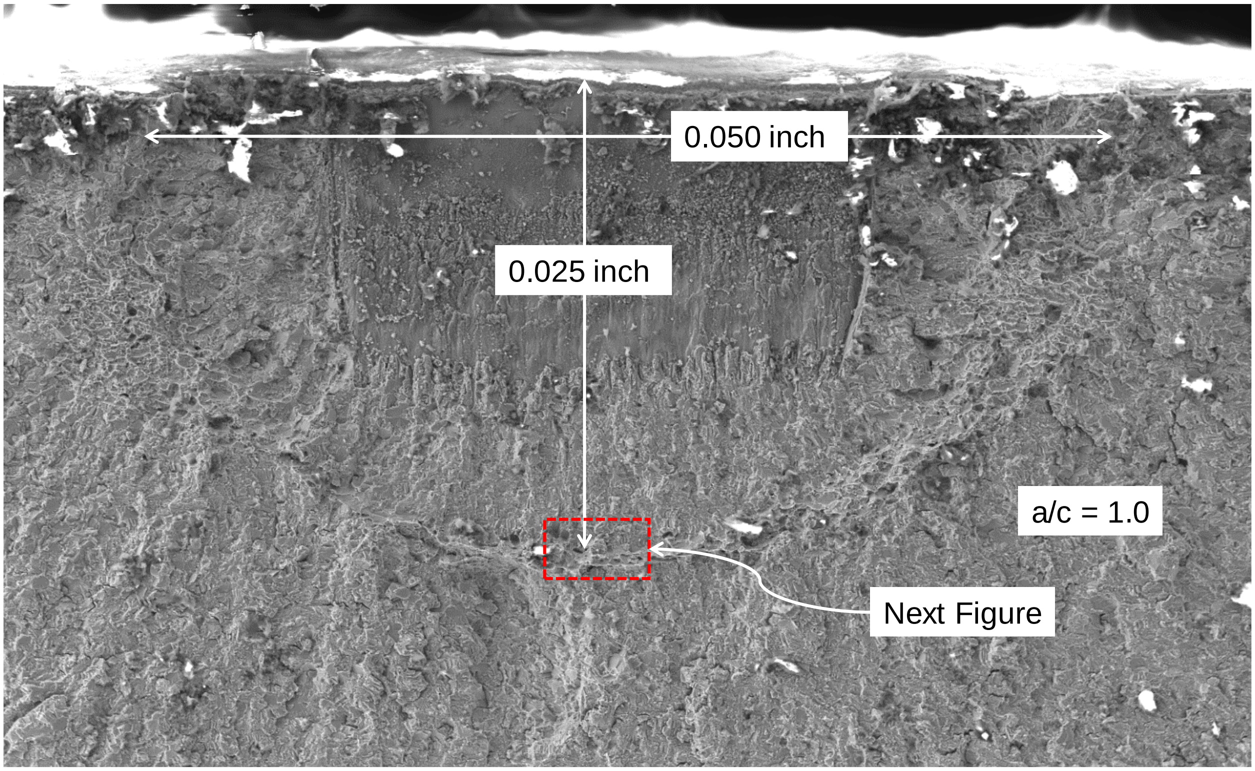

Figure M.76. Fracture surface for Ti 6Al-4V coupon Ti-Dome-00-04-082 that was loaded to an autofrettage strain level of 2.72%.

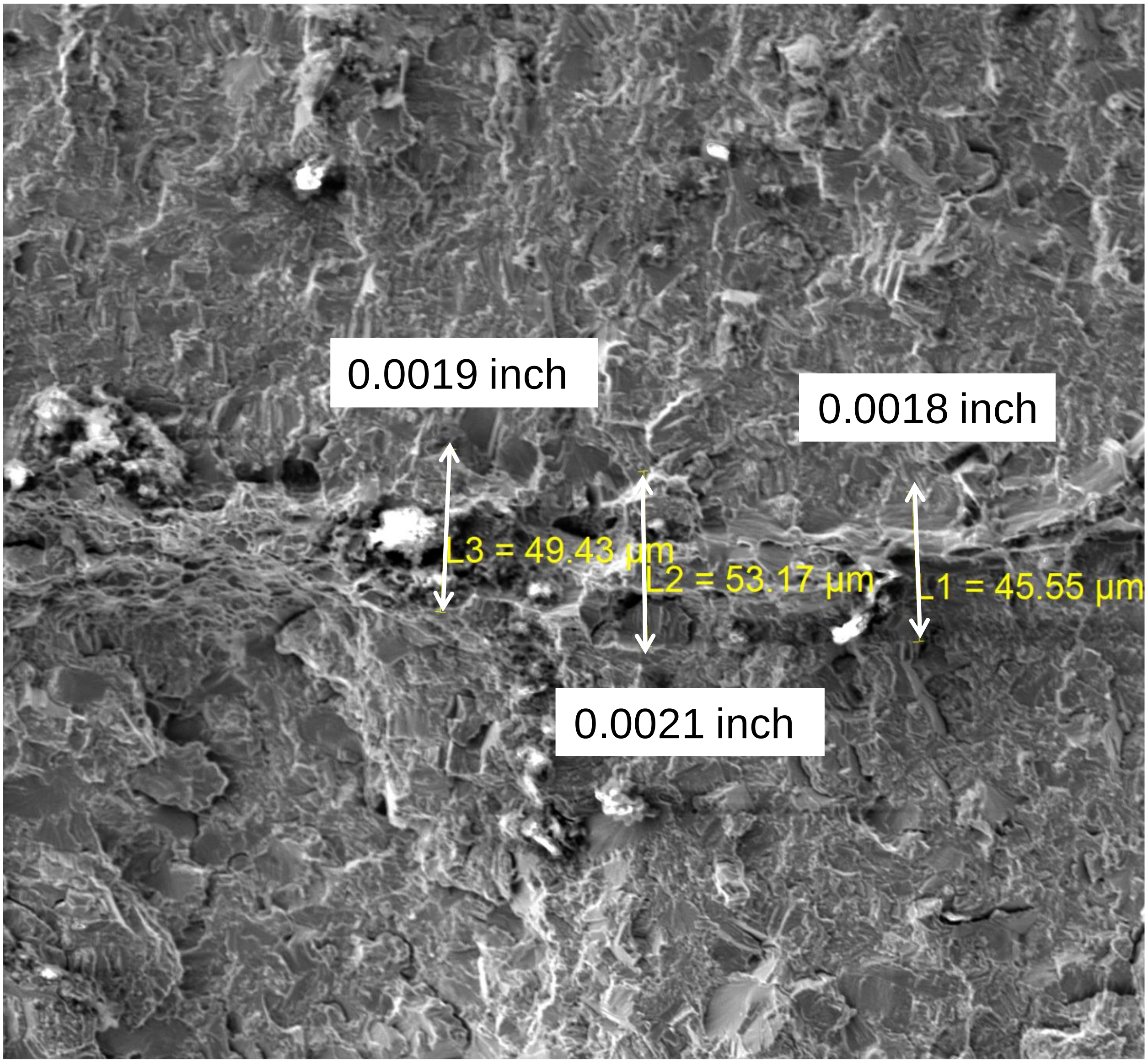

Figure M.77. Autofrettage measurements for Ti 6Al-4V coupon Ti-Dome-00-04-082 that was loaded to an autofrettage strain level of 2.72%.

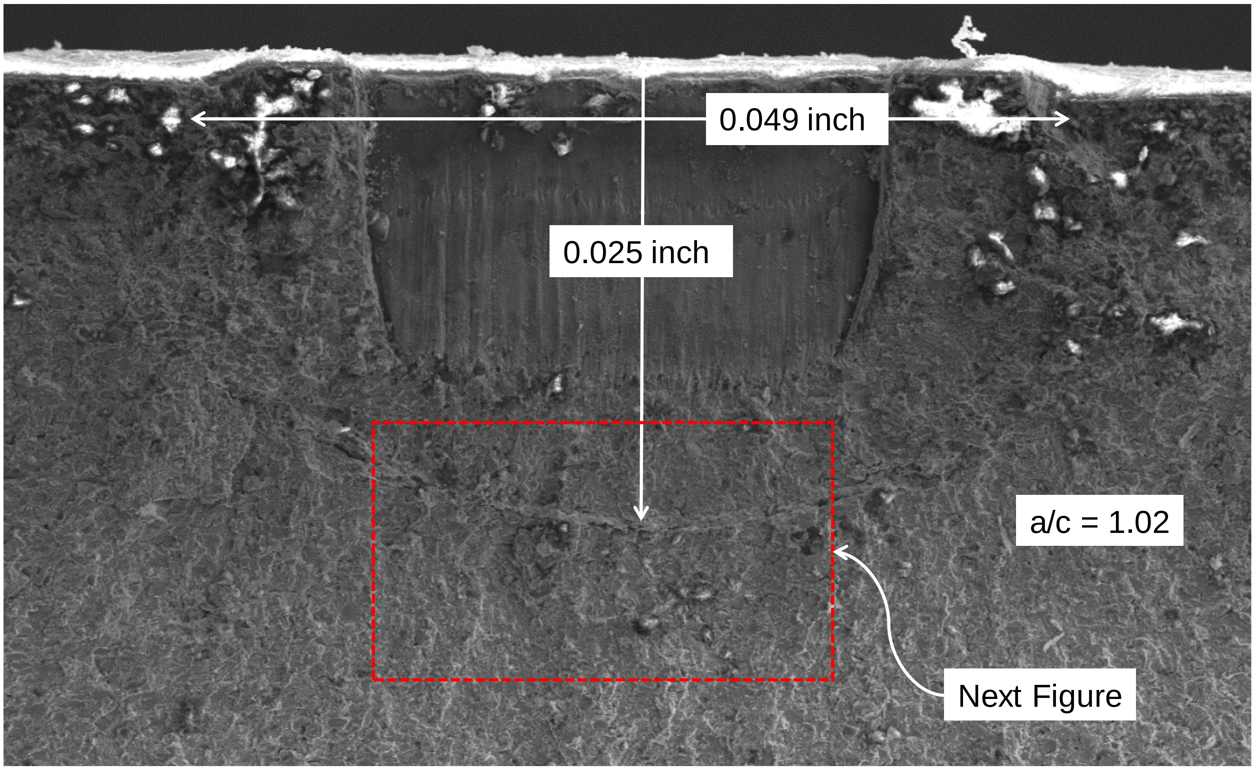

Figure M.78. Fracture surface for Ti 6Al-4V coupon Ti-Dome-00-05-082 that was loaded to an autofrettage strain level of 2.69%.

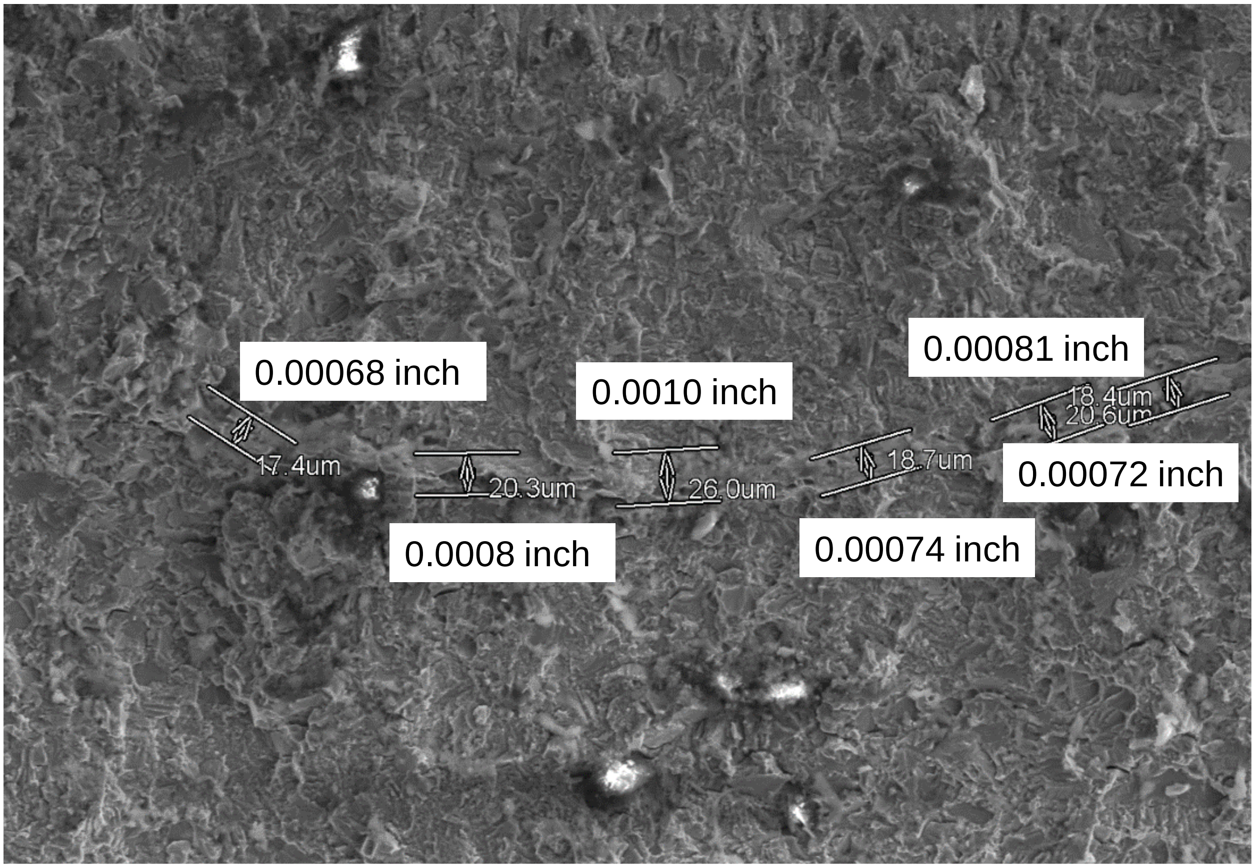

Figure M.79. Autofrettage measurements for Ti 6Al-4V coupon Ti-Dome-00-05-082 that was loaded to an autofrettage strain level of 2.69%.

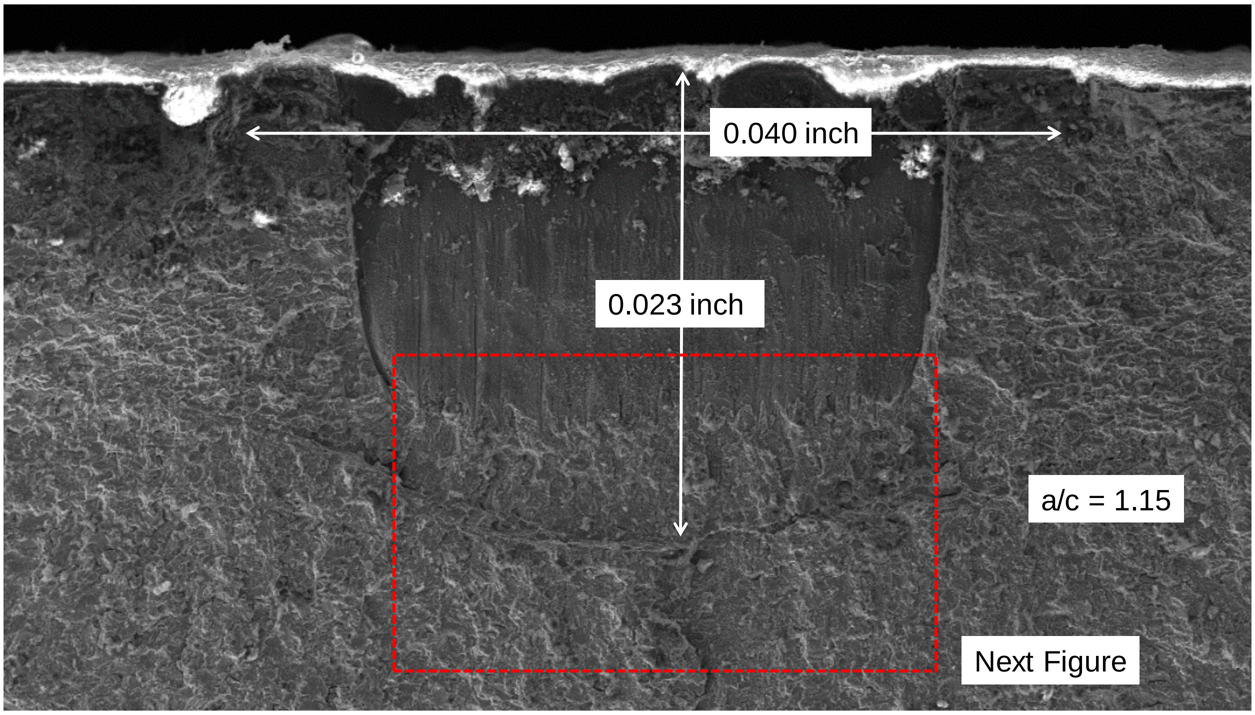

Figure M.80. Fracture surface for Ti 6Al-4V coupon Ti-Dome-00-06-082 that was loaded to an autofrettage strain level of 2.68%.

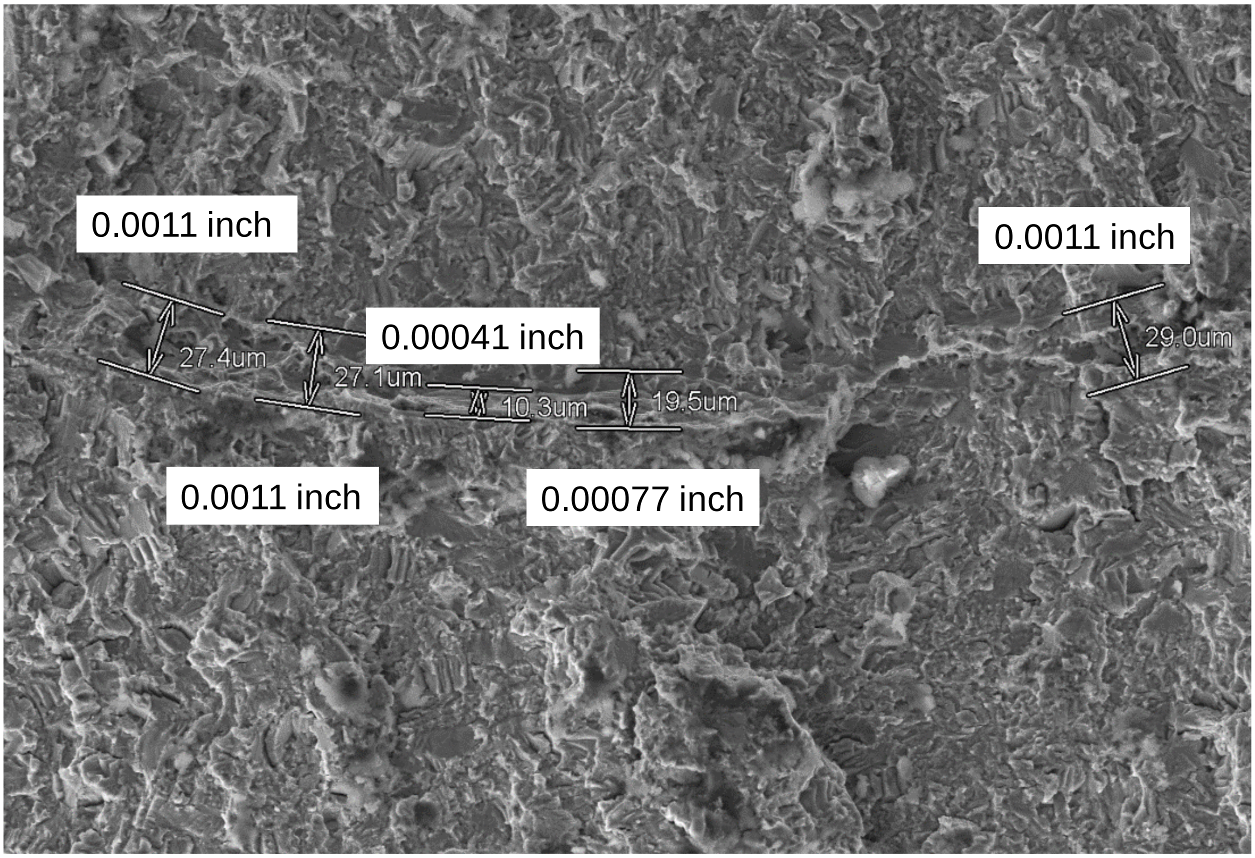

Figure M.81. Autofrettage measurements for Ti 6Al-4V coupon Ti-Dome-00-06-082 that was loaded to an autofrettage strain level of 2.68%.

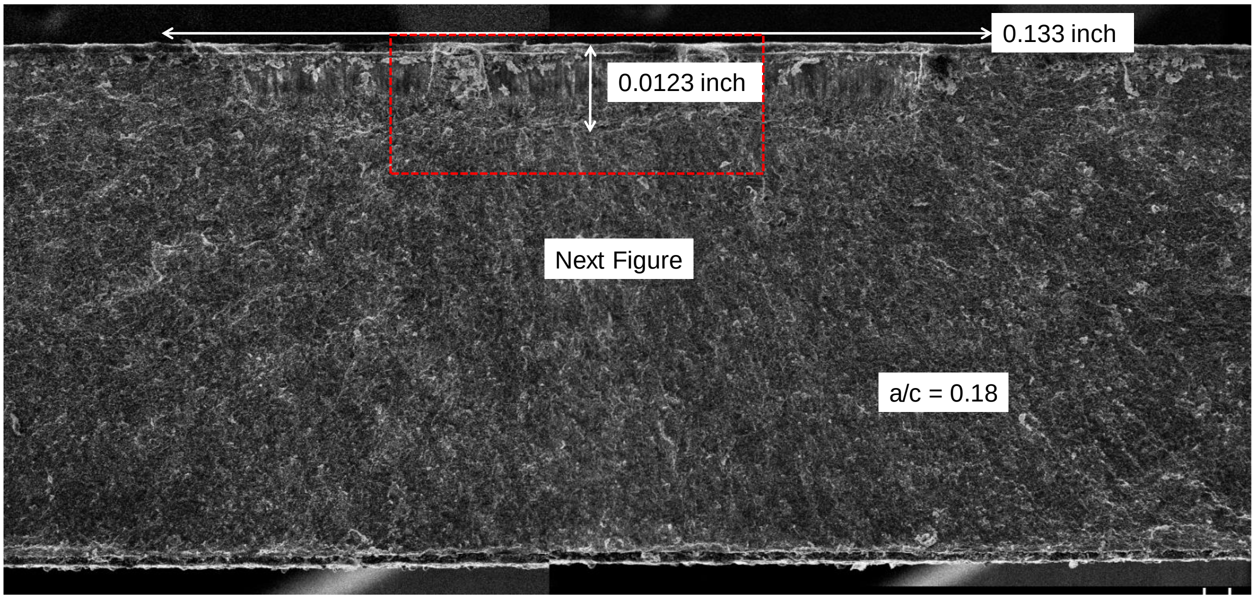

Figure M.82. Fracture surface for Ti 6Al-4V coupon Ti-Dome-01-01-082 that was loaded to an autofrettage strain level of 2.72%.

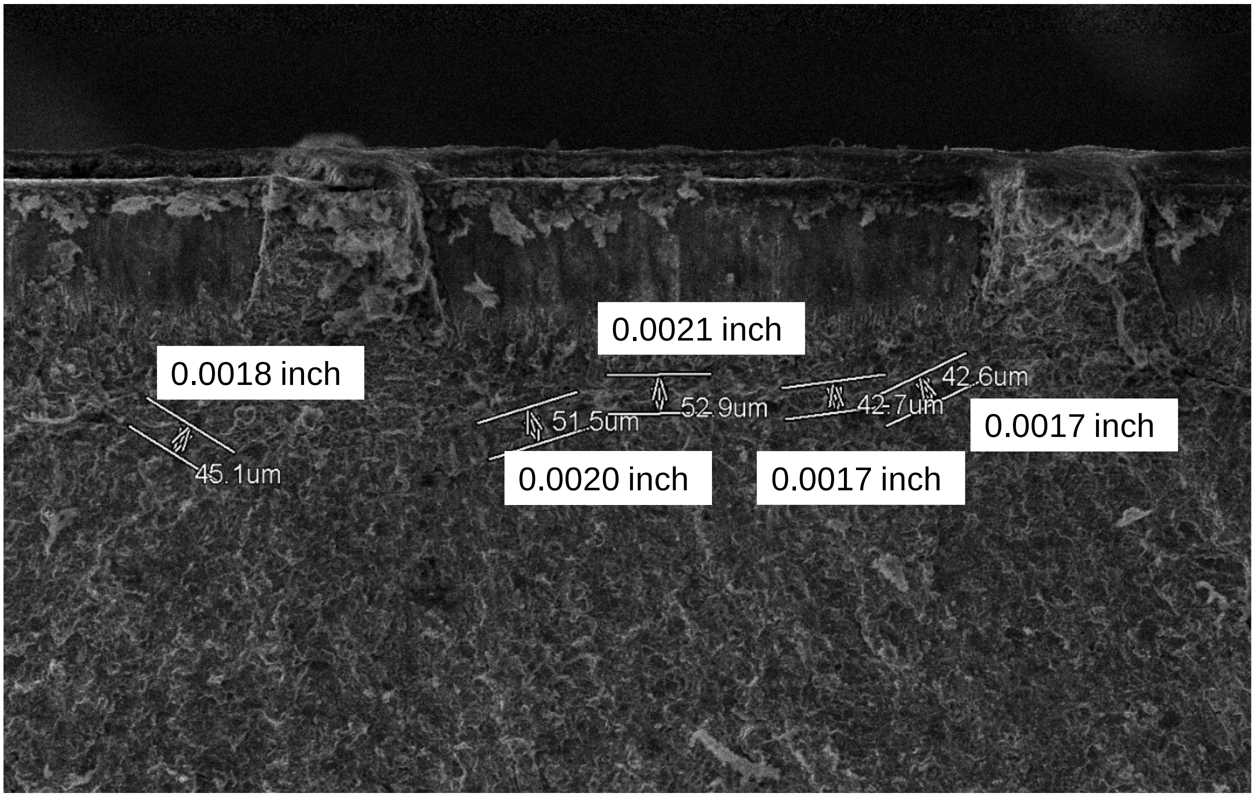

Figure M.83. Autofrettage measurements for Ti 6Al-4V coupon Ti-Dome-01-01-082 that was loaded to an autofrettage strain level of 2.72%.

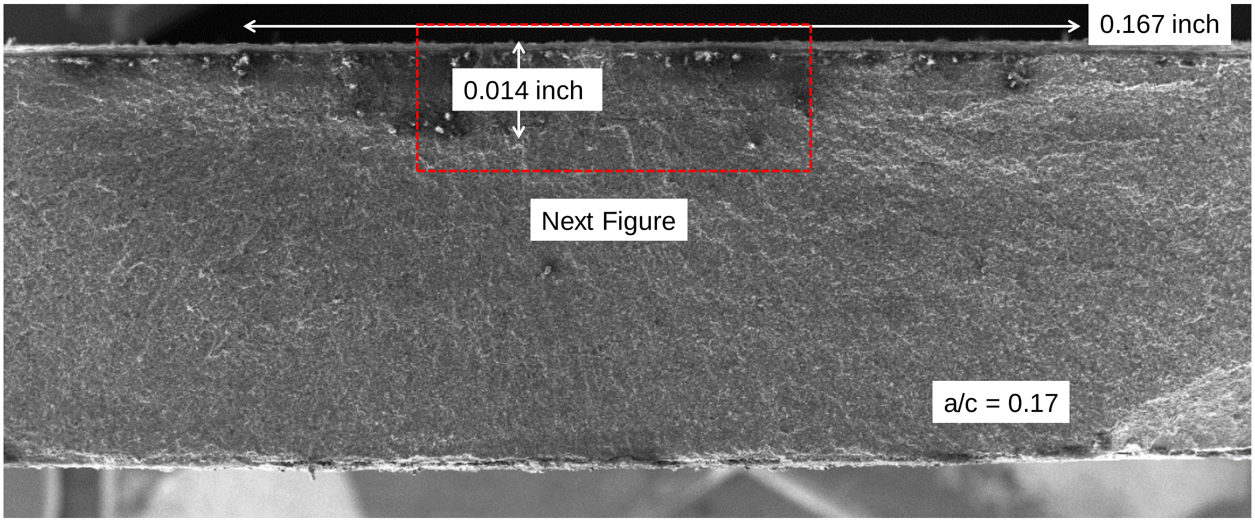

Figure M.84. Fracture surface for Ti 6Al-4V coupon Ti-Dome-02-01-082 that was loaded to an autofrettage strain level of 2.63%.

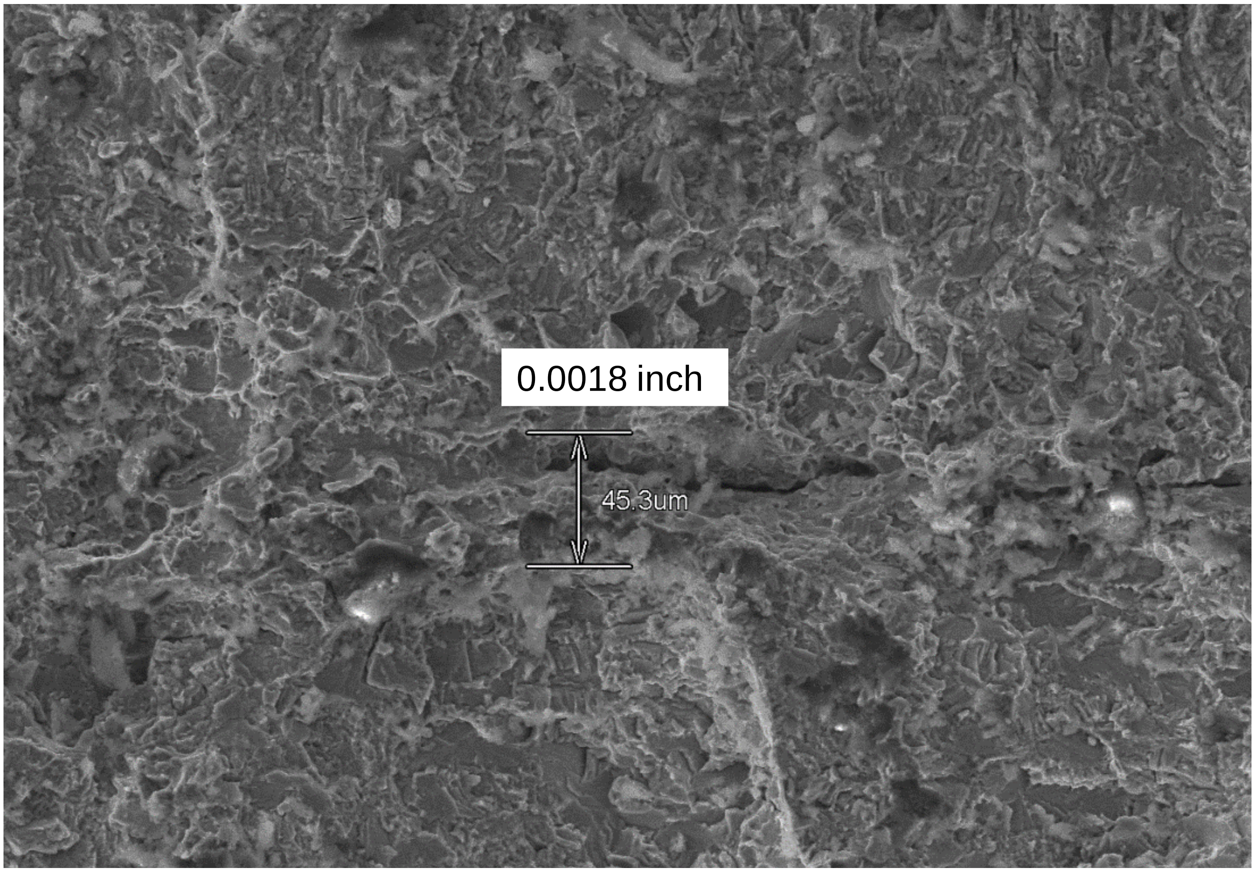

Figure M.85. Autofrettage measurements for Ti 6Al-4V coupon Ti-Dome-02-01-082 that was loaded to an autofrettage strain level of 2.63%.

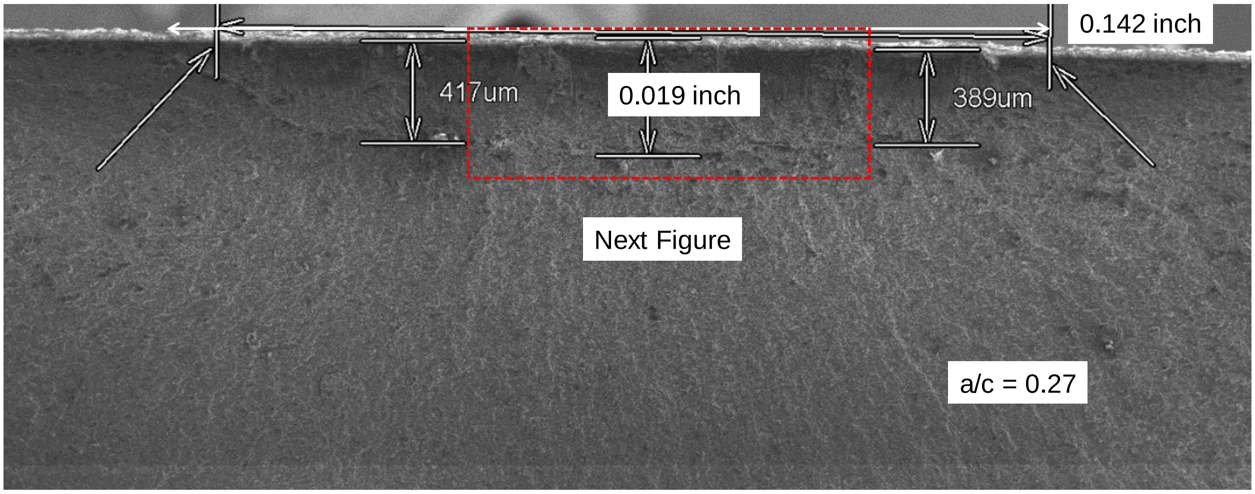

Figure M.86. Fracture surface for Ti 6Al-4V coupon Ti-Dome-02-02-082 that was loaded to an autofrettage strain level of 2.77%.

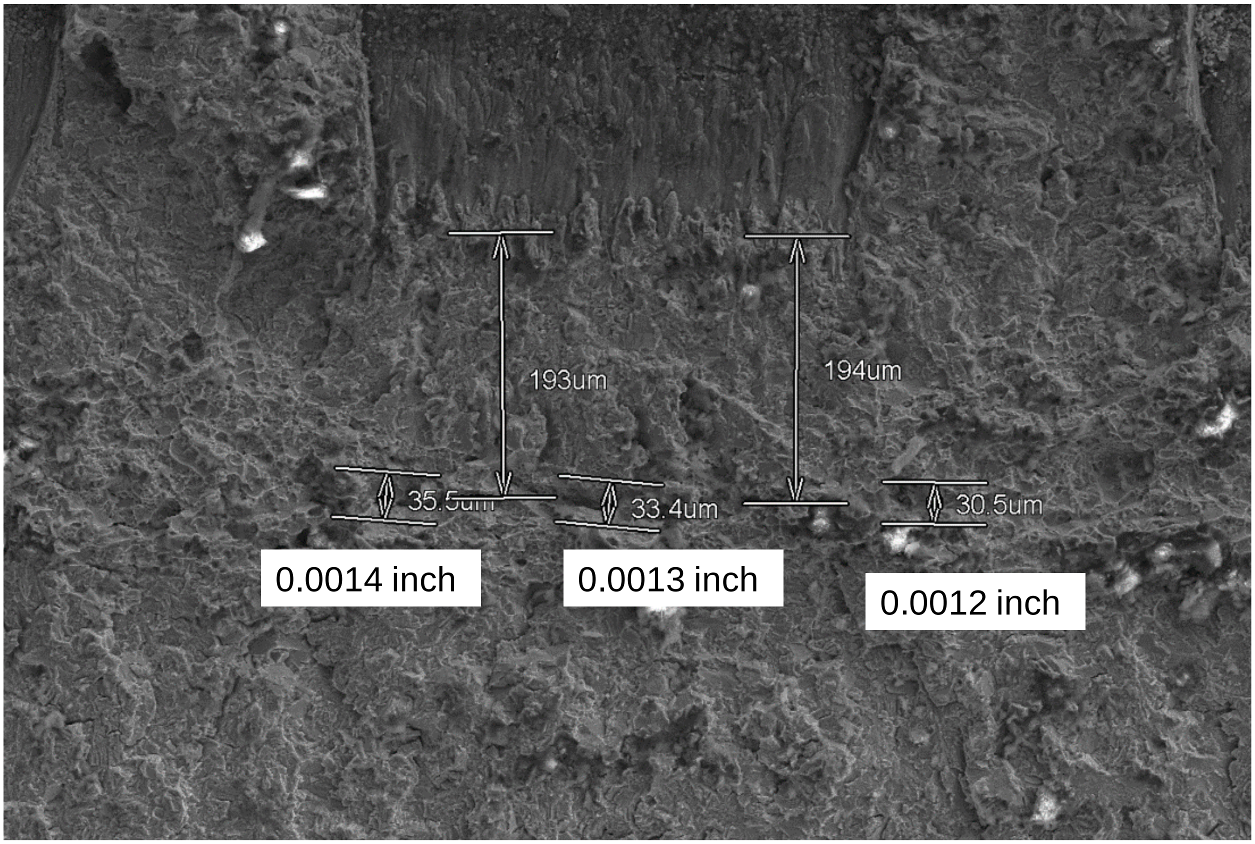

Figure M.87. Autofrettage measurements for Ti 6Al-4V coupon Ti-Dome-02-02-082 that was loaded to an autofrettage strain level of 2.77%.

Appendix N. Fracture Surfaces from the COPV Pressure Tests

Four COPVs (18072, 18074, 18092, and 18099) were successfully pressure tested. The liner of each COPV had nine EDM notches that were introduced on the outer surface (OD) as crack nucleation sites. The bare liners were pressure cycled elastically. Eddy current inspections were performed to determine if cracks were nucleating at natural defects on the inside surface (ID). The pressure cycles were stopped when the largest OD or ID crack reached the target size. The liners were wrapped and pressure cycled at simulated conditions (autofrettage and MDP). The COPVs were cut open and the crack surfaces revealed after the completion of the pressure cycles. The crack surfaces that were successfully harvested from each COPV liner were examined using a scanning electron microscope (SEM). Measurements of the starting and ending crack sizes were made using marks left on the surface by the different pressure cycles and are summarized in **Tables N.1** to **N.4** and presented in **Figures N.1** to **N.53**.

Table N.1. Crack Measurements for COPV 18072 Subjected to Pressurization Cycles of 3x(AF & 200 MDP) + AF & 116 MDP

Tank ID	Crack #	Surface	Initial (a)	Initial (2c)	Initial a/c	Final (a)	Final (2c)	Final a/c
18072	C1	OD	0.0194	0.0413	0.9395	0.029	0.0646	0.8978
18072	C2	OD	0.0193	0.0398	0.9698	0.0252	0.0614	0.8208
18072	C4	OD	0.0164	0.0401	0.8180	0.0295	0.065	0.9077
18072	C5	OD	0.0197	0.0436	0.9037	0.0305	0.0718	0.8496
18072	C6	OD	0.0157	0.0343	0.9155	0.02	0.0475	0.8421
18072	C9	OD	0.0216	0.0364	1.1868	0.0297	0.0571	1.0403
18072	C7	OD	0.0116	0.0284	0.8169	0.0161	0.0393	0.8193
18072	C8	OD	0.0122	0.0253	0.9644	0.018	0.0379	0.9499
18072	ID 12	ID	0.0177	0.0347	1.0202	0.041	0.094	0.8723

Table N.2. Crack Measurements for COPV 18074 Subjected to Pressurization Cycles of AF & 916 MDP

Tank ID	Crack #	Surface	Initial (a)	Initial (2c)	Initial a/c	Final (a)	Final (2c)	Final a/c
18074	C2	OD	0.0123	0.0251	0.98	0.0162	0.0312	1.04
18074	C3	OD	0.0109	0.0257	0.85	0.0148	0.034	0.87
18074	C4	OD	0.0206	0.0401	1.03	0.0343	0.0787	0.87
18074	C5	OD	0.0116	0.022	1.05	0.0134	0.028	0.96
18047	C7	OD	0.0147	0.0335	0.88	0.0210	0.0518	0.81
18074	C8	OD	0.0145	0.0297	0.98	0.0195	0.0518	0.75
18074	C9	OD	0.0147	0.0286	1.03	0.0204	0.0419	0.97
18074	N2	OD	0.0245	0.0509	0.96	0.0352	0.0871	0.81
18074	ID34	ID	0.0169	0.0583	0.58	0.0367	0.133	0.55

Table N.3. Crack Measurements for COPV 18092 Subjected to Pressurization Cycles of AF & 916 MDP

Tank ID	Crack #	Surface	Initial (a)	Initial (2c)	Initial a/c	Final (a)	Final (2c)	Final a/c
18092	C1	OD	0.0176	0.0381	0.92	0.026	0.0614	0.85
18092	C2	OD	0.01	0.0239	0.84	0.0144	0.028	1.03
18092	C3	OD	0.0214	0.0406	1.05	0.0369	0.0725	1.02
18092	C4	OD	0.018	0.0301	1.20	0.0252	0.0524	0.96
18092	C5	OD	0.0179	0.0394	0.91	0.0278	0.0704	0.79
18092	C6	OD	0.0216	0.039	1.11	0.0357	0.0804	0.89
18092	C7	OD	0.014	0.0333	0.84	0.022	0.0543	0.81
18092	C8	OD	0.0126	0.0287	0.88	0.0188	0.0407	0.92
18092	C9	OD	0.0169	0.0373	0.91	0.029	0.0681	0.85
18092	ID1	ID	0.0024	0.099	0.05	0.0066	0.111	0.12
18092	ID4	ID	0.0082	0.0338	0.49	0.0171	0.0661	0.52

Table N.4. Crack Measurements for COPV 18099 Subjected to Pressurization Cycles of 4xAF & 800 MDP

Tank ID	Crack #	Surface	Initial (a)	Initial (2c)	Initial a/c	Final (a)	Final (2c)	Final a/c
18099	N1	OD	0.0127	0.0298	0.85	0.0174	0.0424	0.82
18099	N2	OD	0.0201	0.0366	1.10	0.0325	0.0796	0.82
18099	N3	OD	0.019	0.0418	0.91	0.0307	0.0715	0.86
18099	N4	OD	0.0227	0.043	1.06	0.0331	0.0756	0.88
18099	N5	OD	0.0141	0.0327	0.86	0.017	0.0437	0.78
18099	N6	OD	0.0242	0.0441	1.10	0.0352	0.0833	0.85
18099	N7	OD	0.0227	0.0496	0.92	0.037	0.114	0.65
18099	N8	OD	0.0118	0.0326	0.72	0.0173	0.0424	0.82
18099	N9	OD	0.019	0.0393	0.97	0.0288	0.0685	0.84

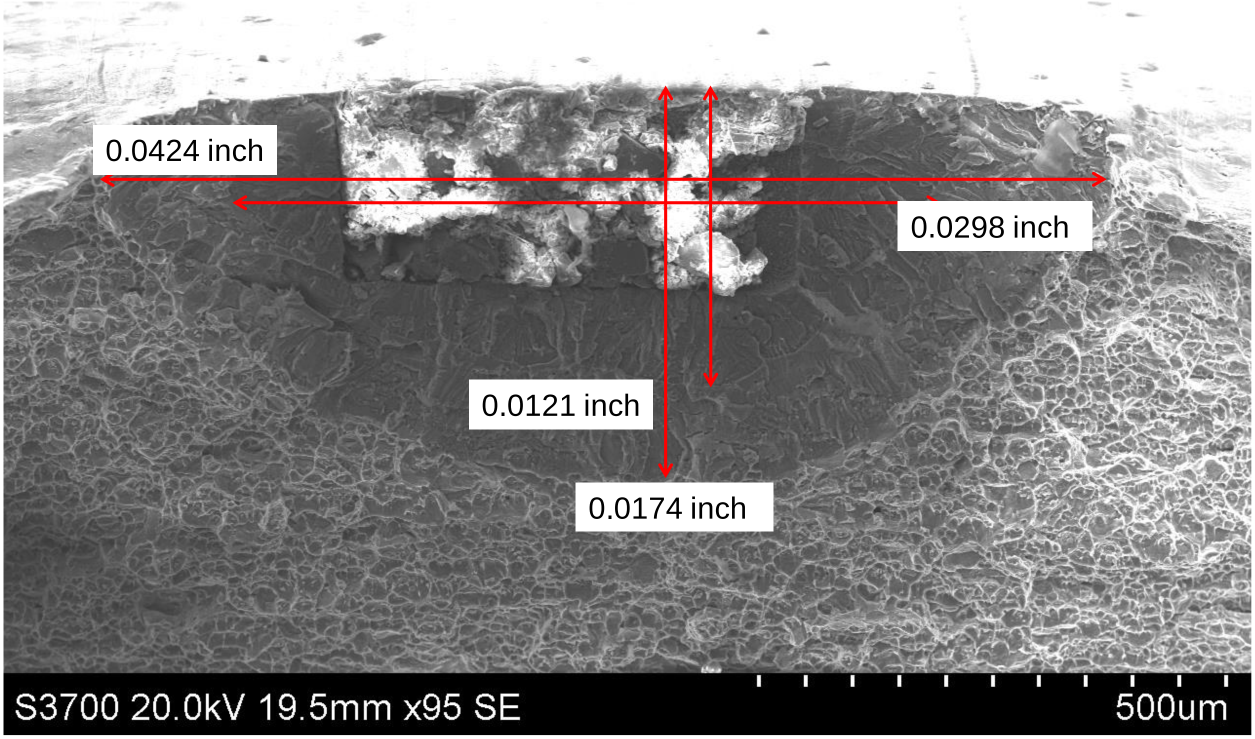

Figure N.1. Fracture surface and crack sizes for crack N1 of COPV 18099.

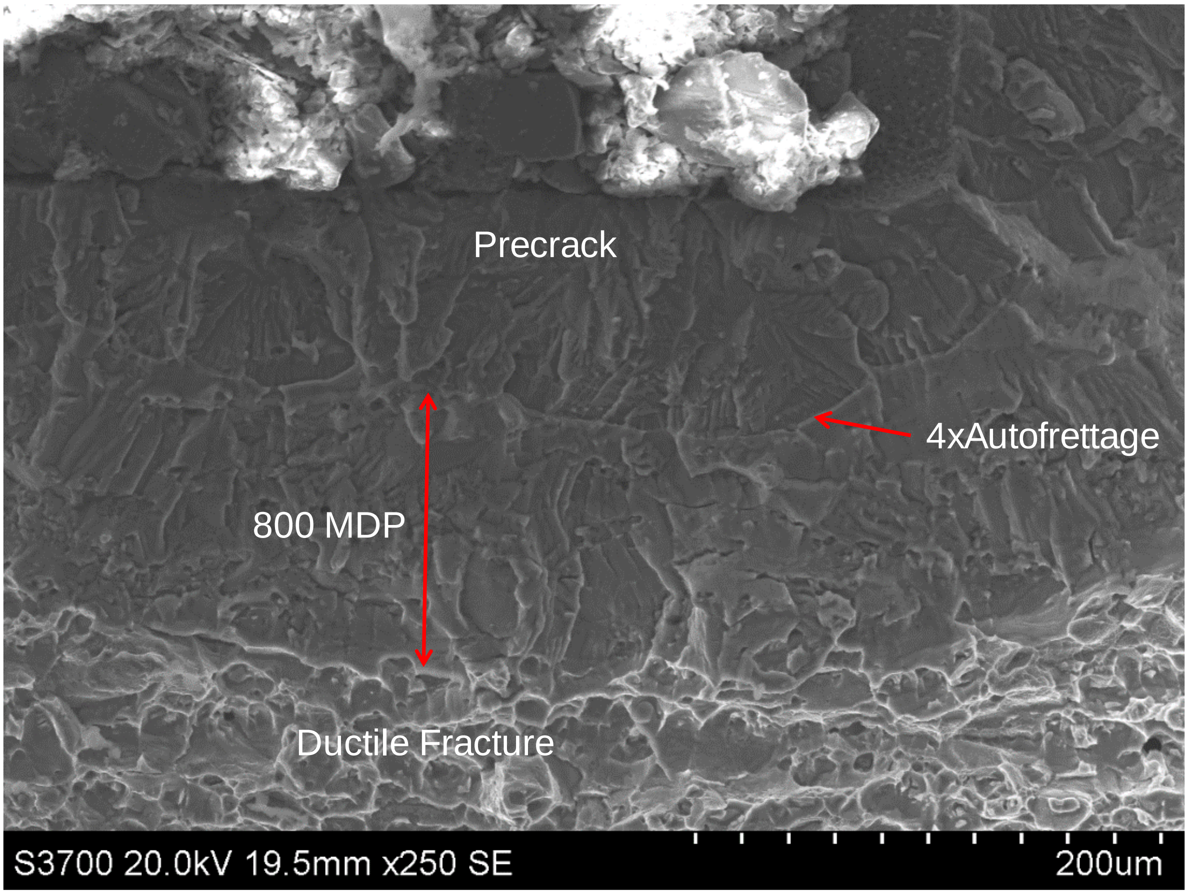

Figure N.2. Higher magnification of the fracture surface for crack N1 of COPV 18099.

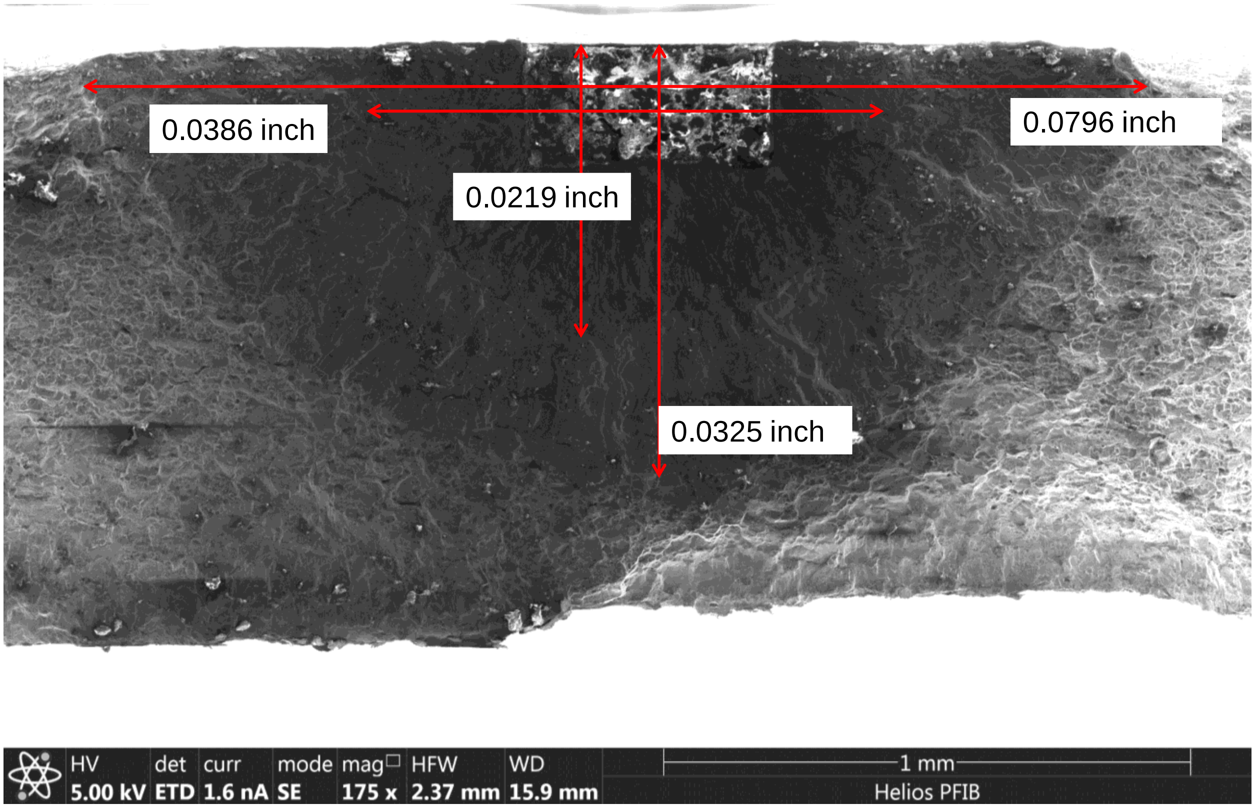

Figure N.3. Fracture surface and crack sizes for crack N2 of COPV 18099.

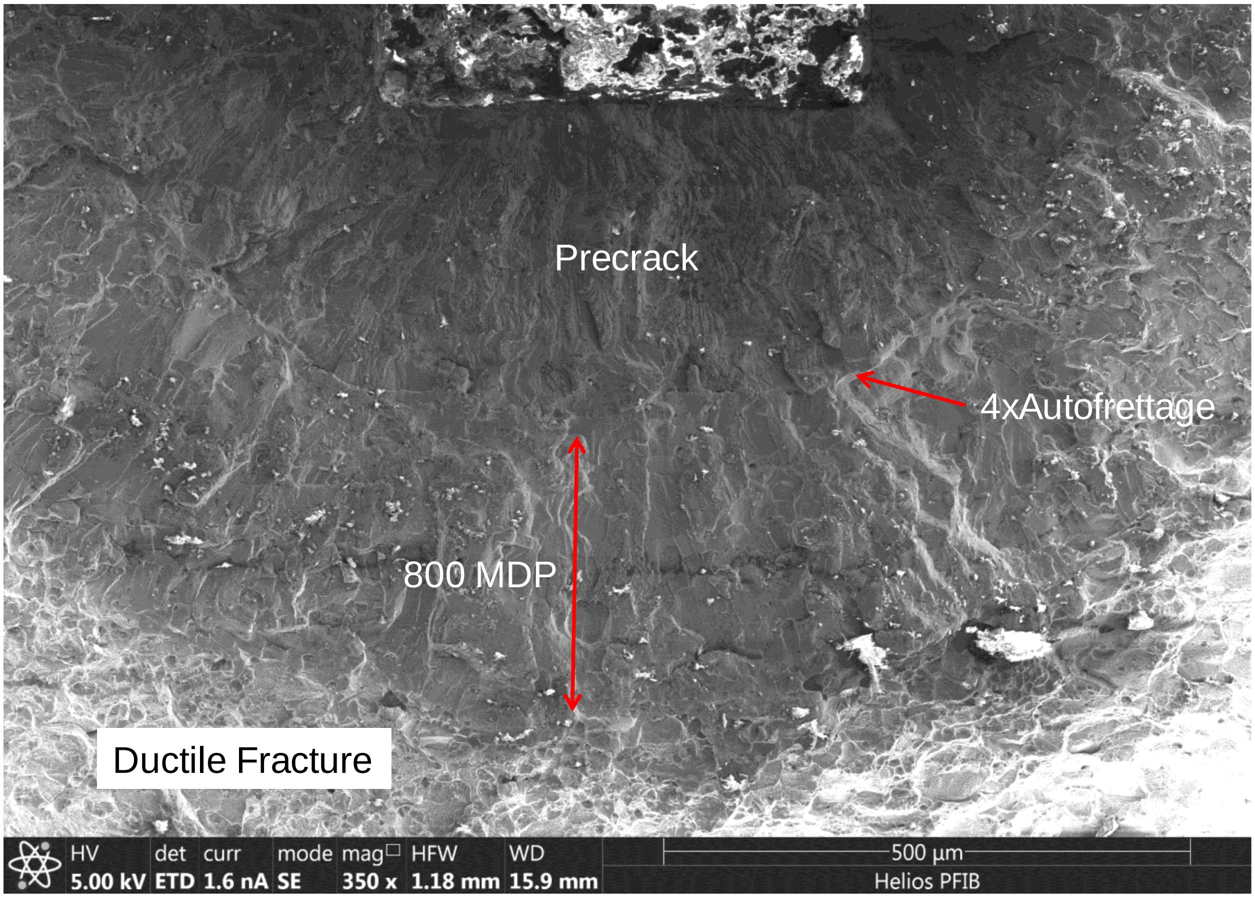

Figure N.4. Higher magnification of the fracture surface for crack N2 of COPV 18099.

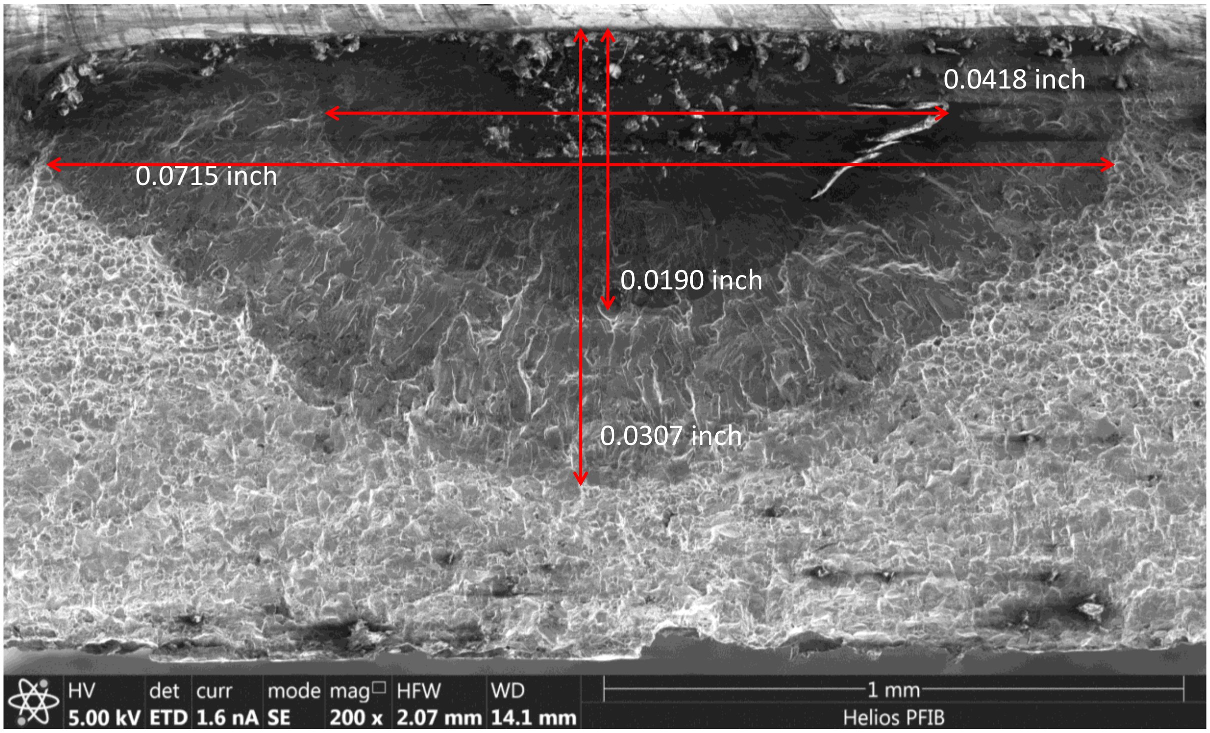

Figure N.5. Fracture surface and crack sizes for crack N3 of COPV 18099.

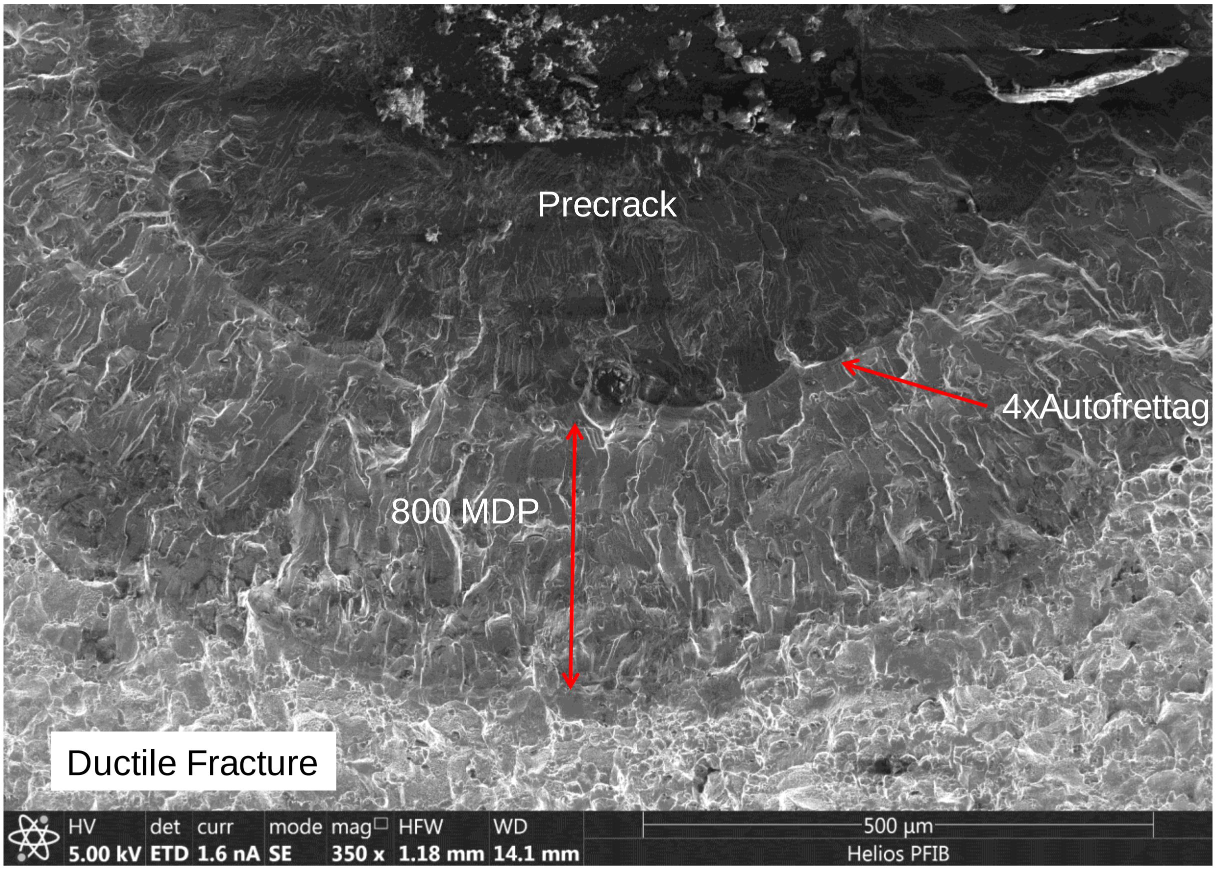

Figure N.6. Higher magnification of the fracture surface for crack N3 of COPV 18099.

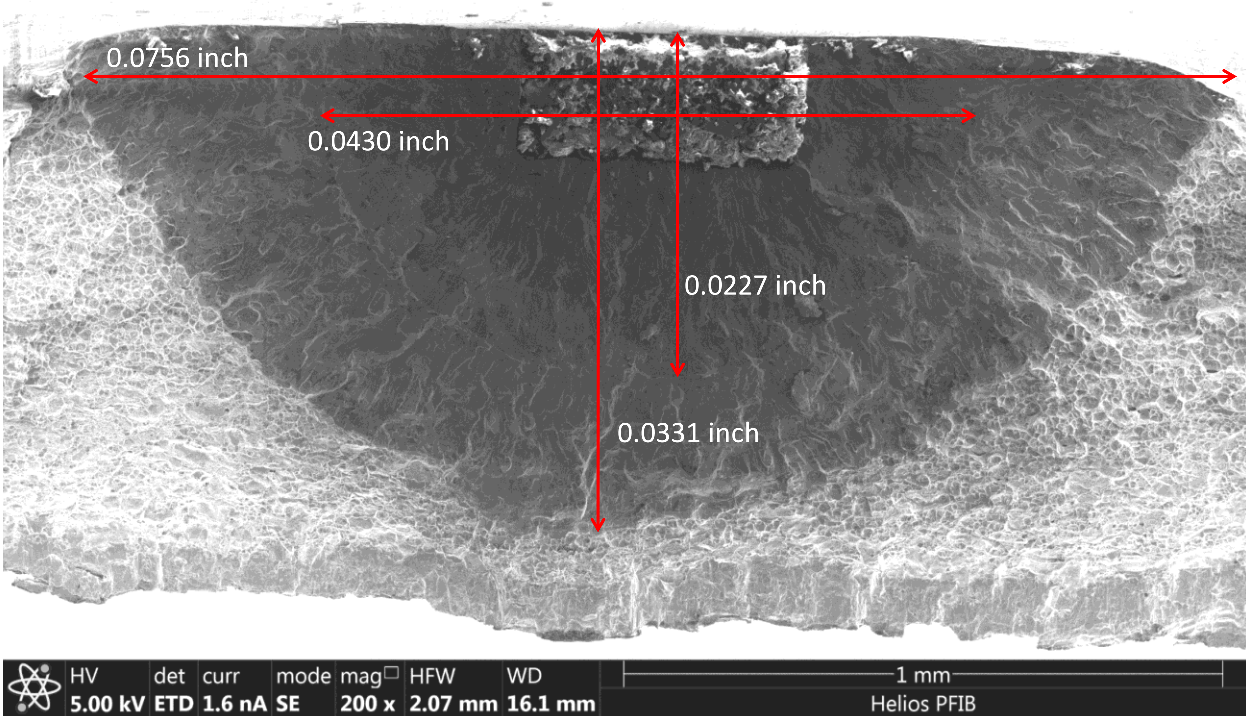

Figure N.7. Fracture surface and crack sizes for crack N4 of COPV 18099.

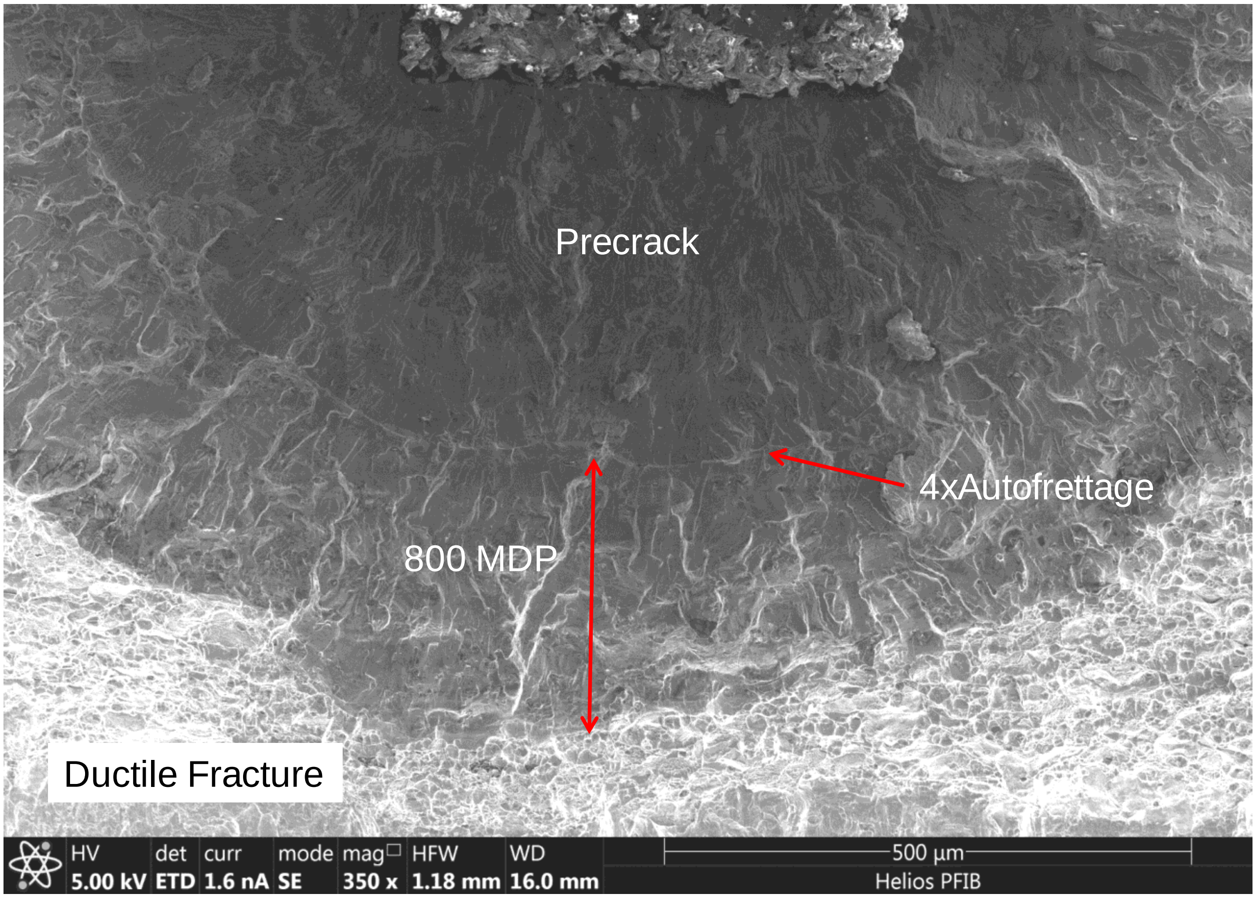

Figure N.8. Higher magnification of the fracture surface for crack N4 of COPV 18099.

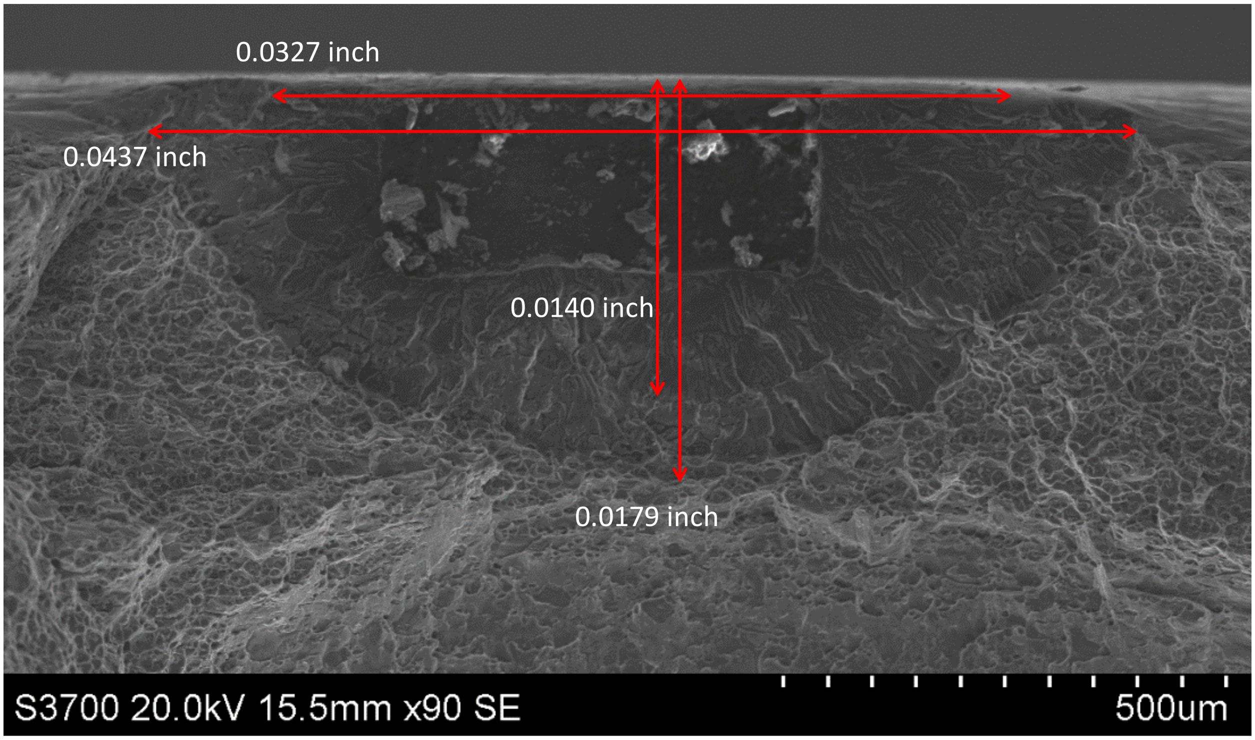

Figure N.9. Fracture surface and crack sizes for crack N5 of COPV 18099.

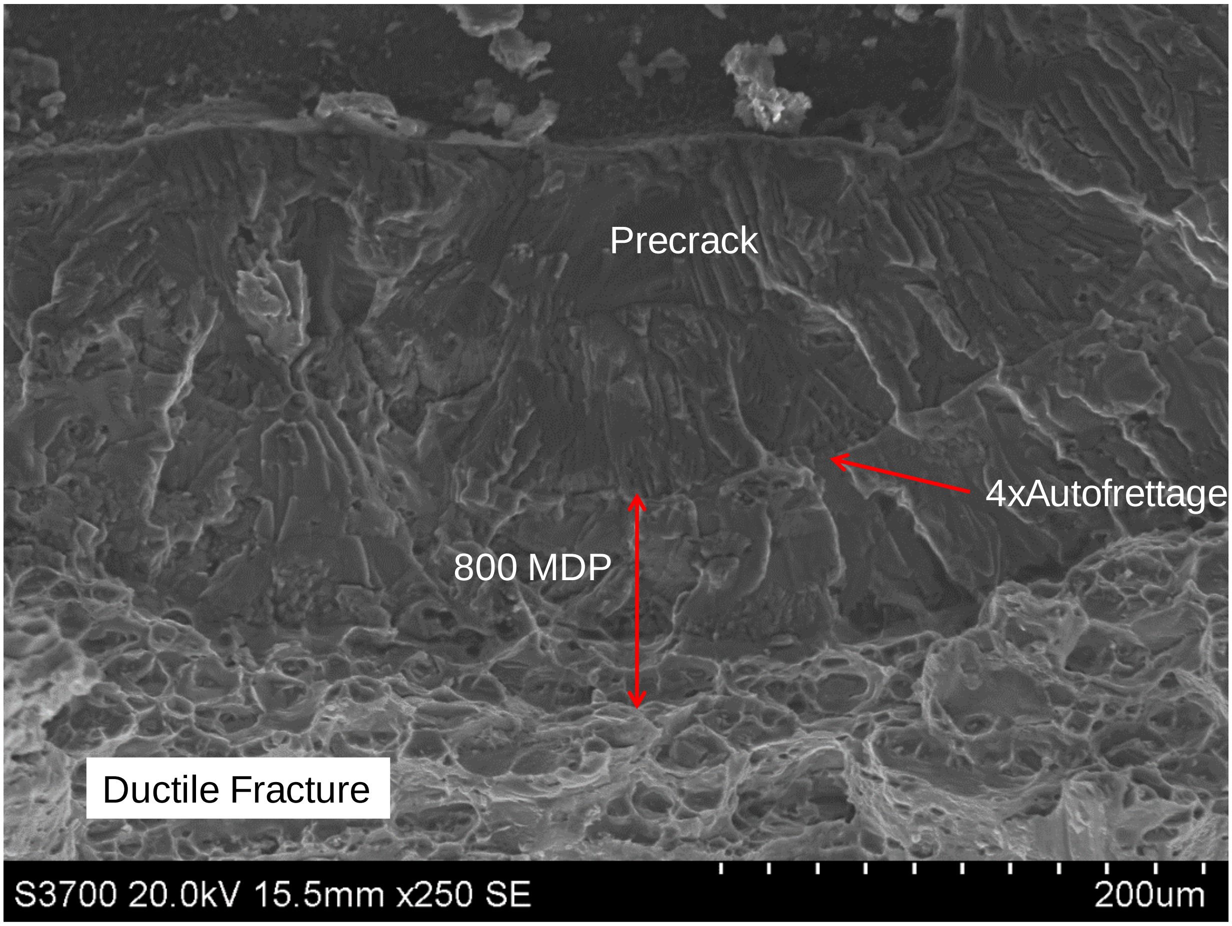

Figure N.10. Higher magnification of the fracture surface for crack N5 of COPV 18099.

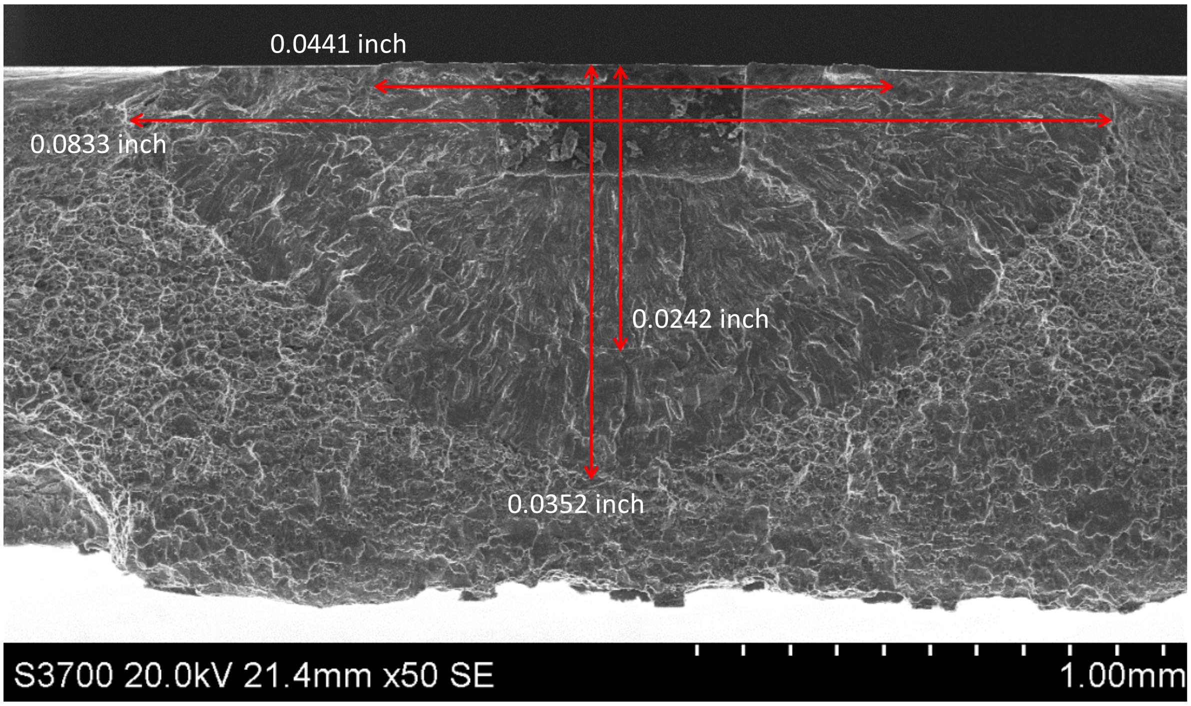

Figure N.11. Fracture surface and crack sizes for crack N6 of COPV 18099.

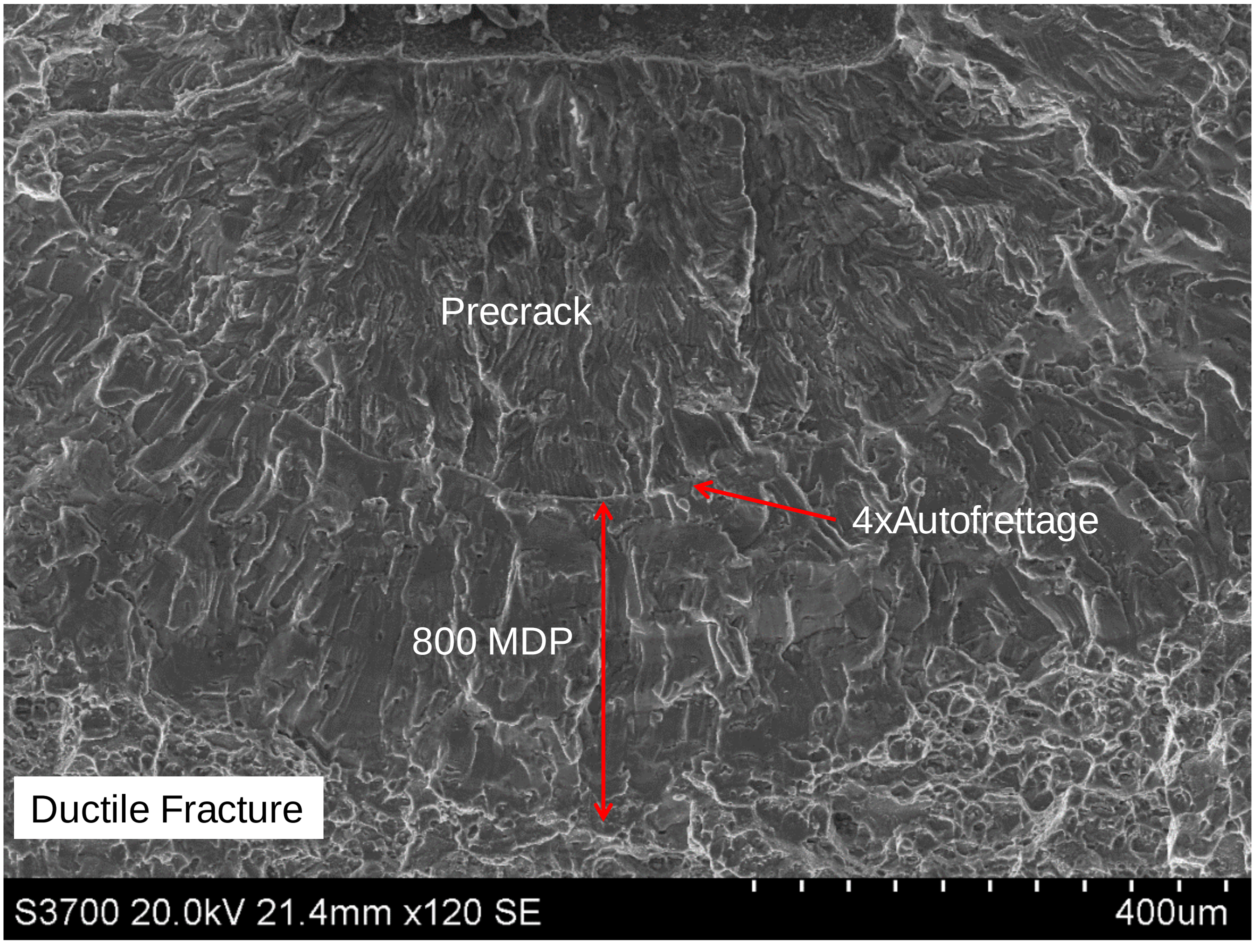

Figure N.12. Higher magnification of the fracture surface for crack N6 of COPV 18099.

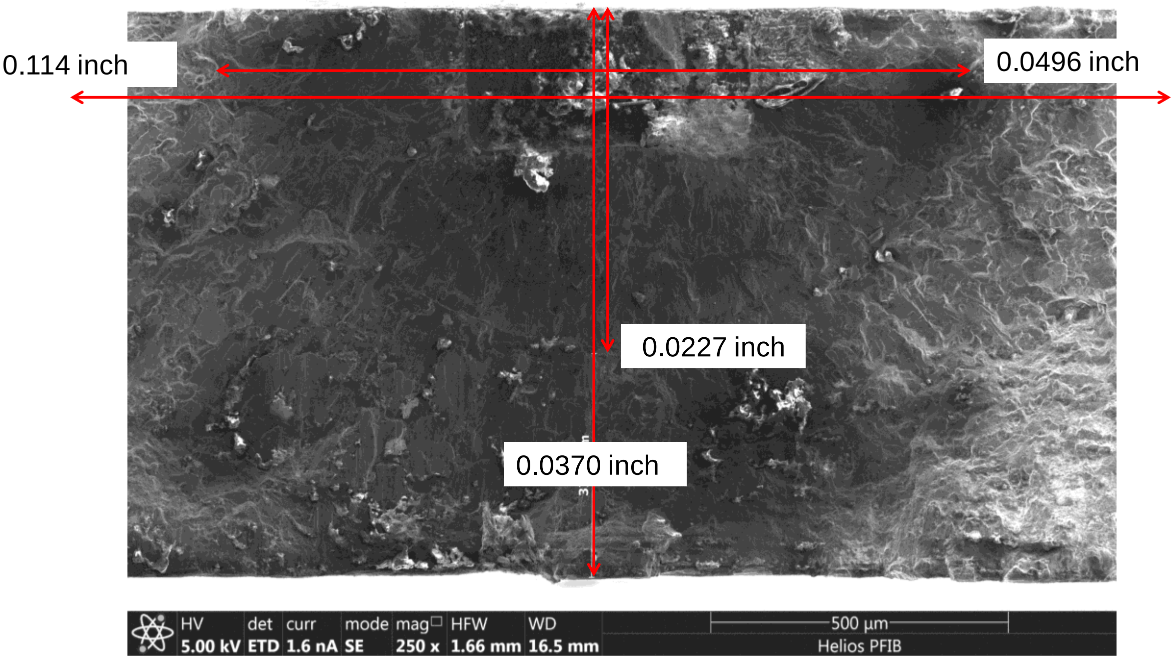

Figure N.13. Fracture surface and crack sizes for crack N7 of COPV 18099.

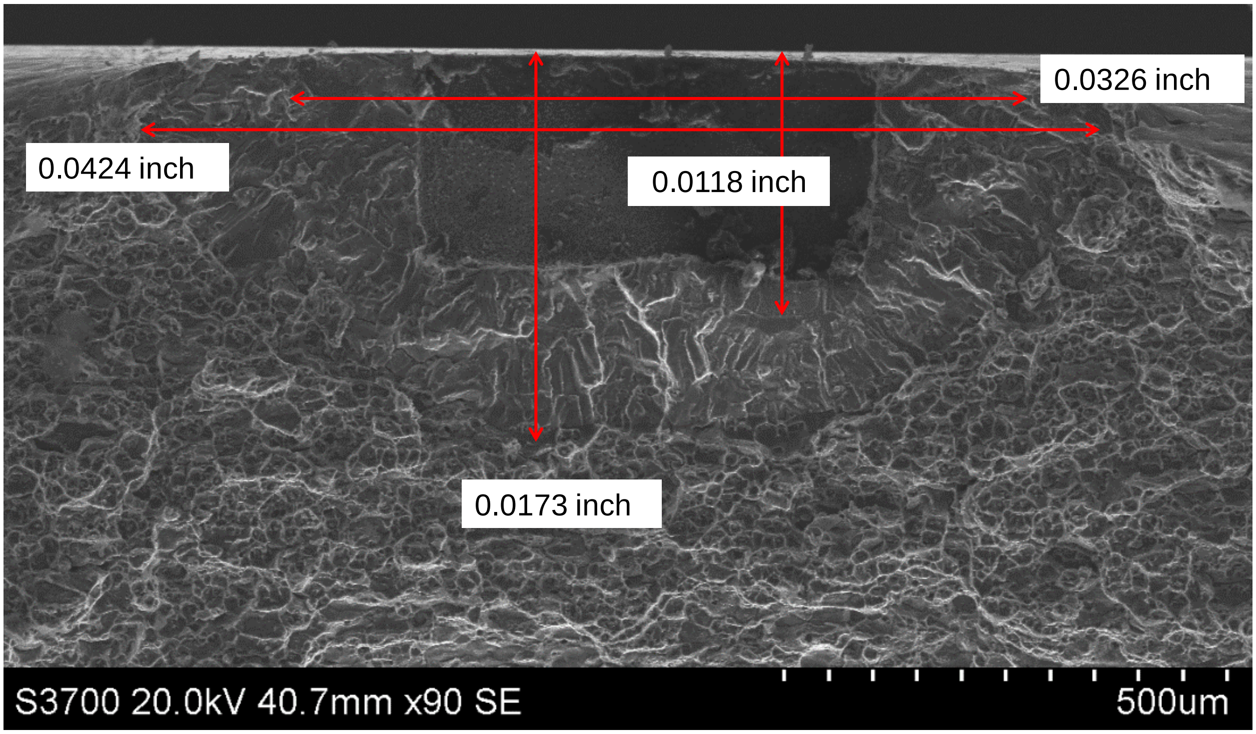

Figure N.14. Fracture surface and crack sizes for crack N8 of COPV 18099.

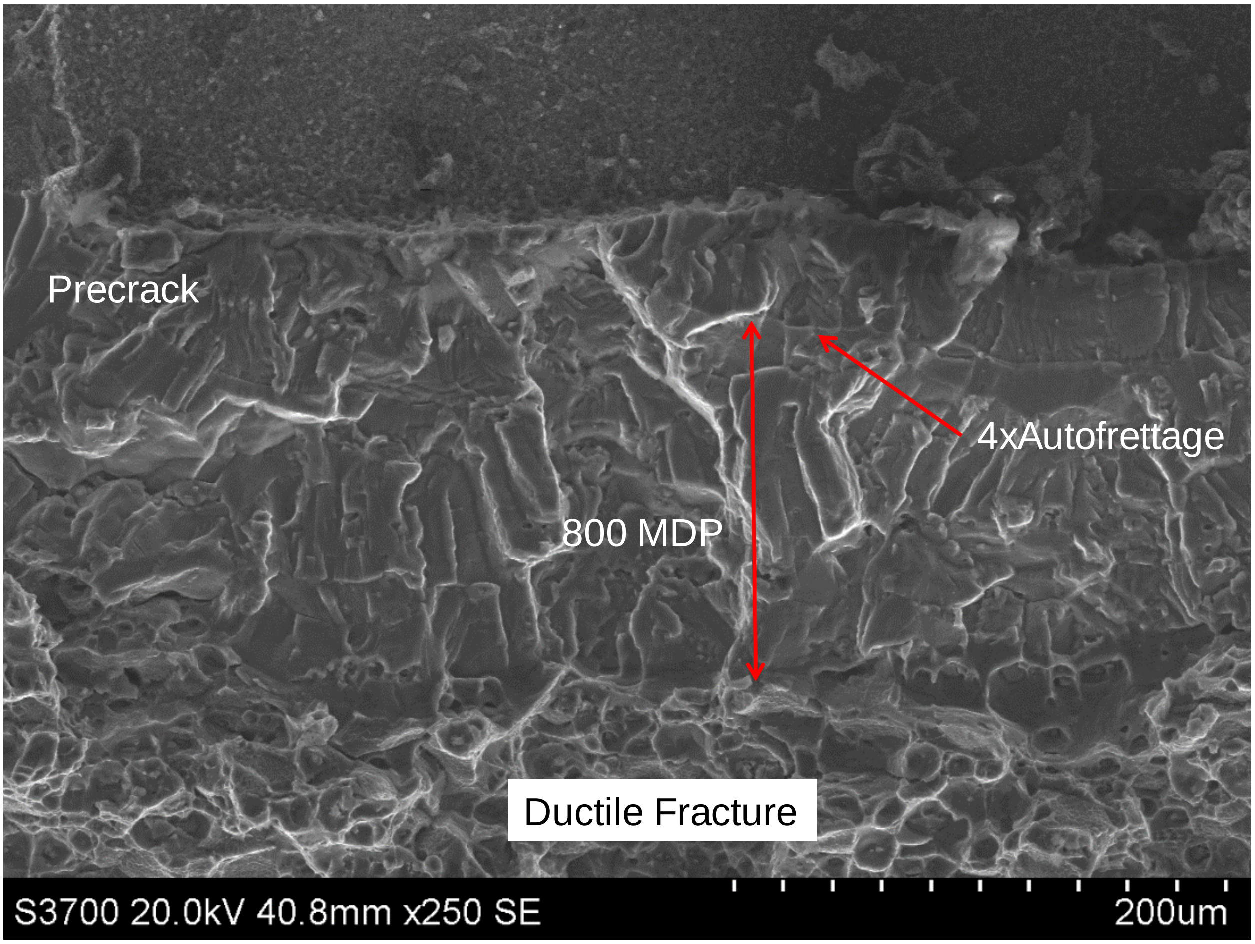

Figure N.15. Higher magnification of the fracture surface for crack N8 of COPV 18099.

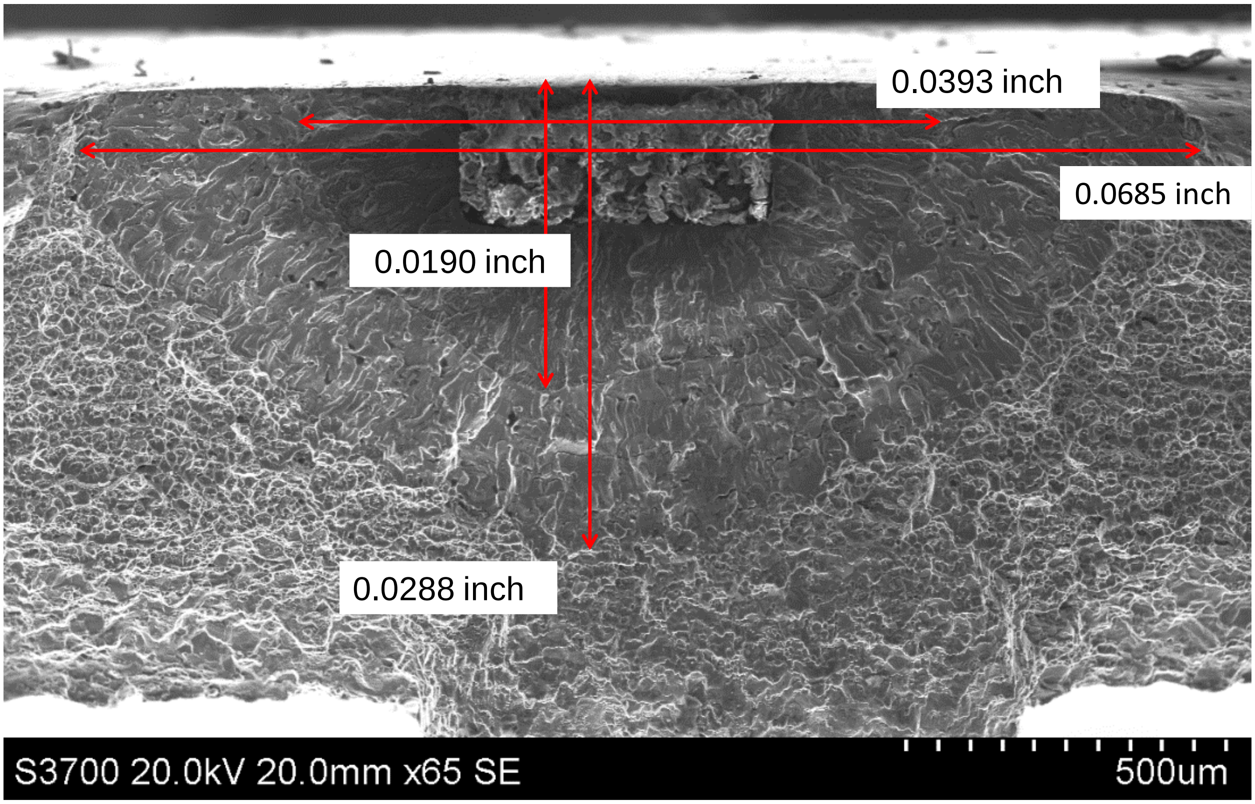

Figure N.16. Fracture surface and crack sizes for crack N9 of COPV 18099.

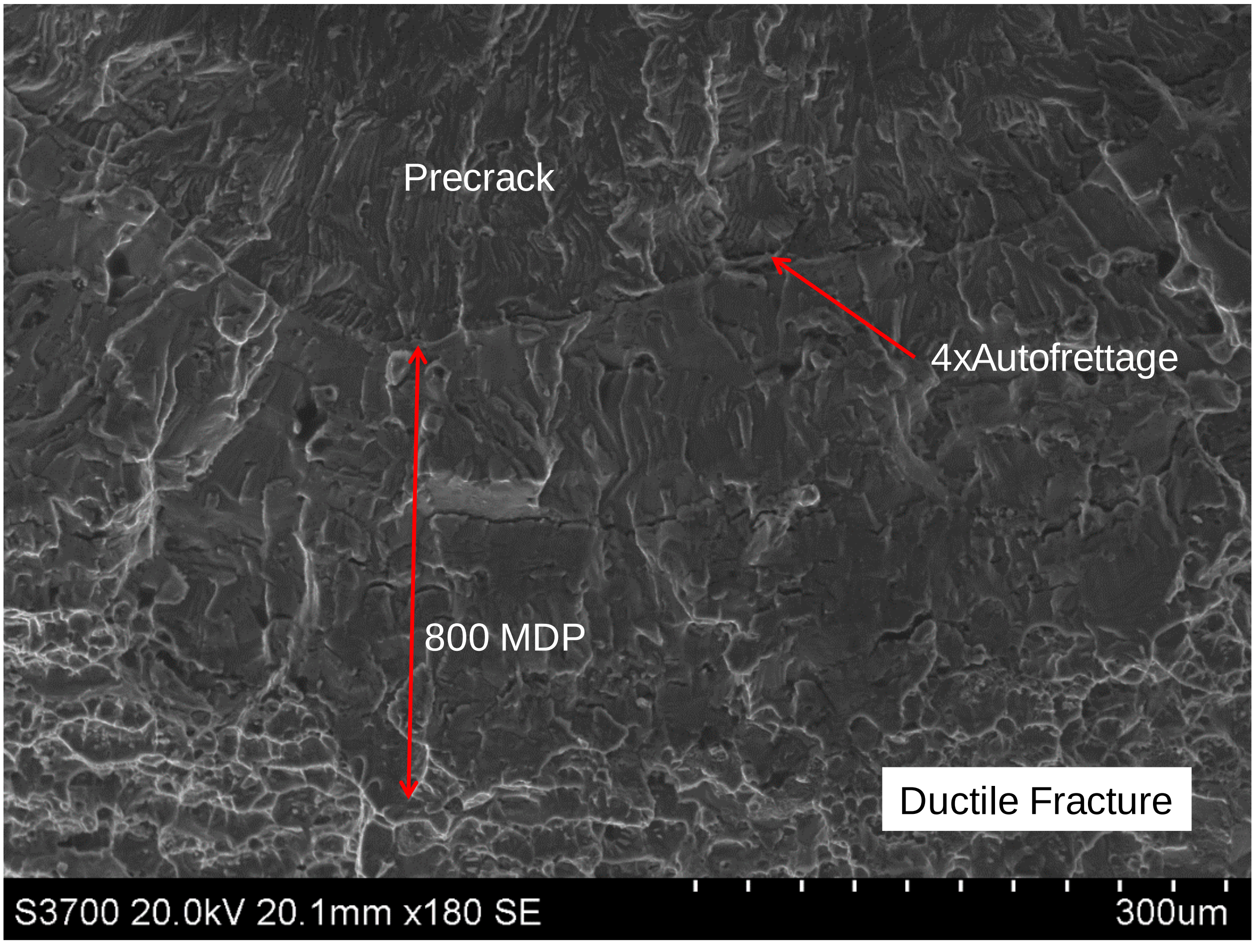

Figure N.17. Higher magnification of the fracture surface for crack N9 of COPV 18099.

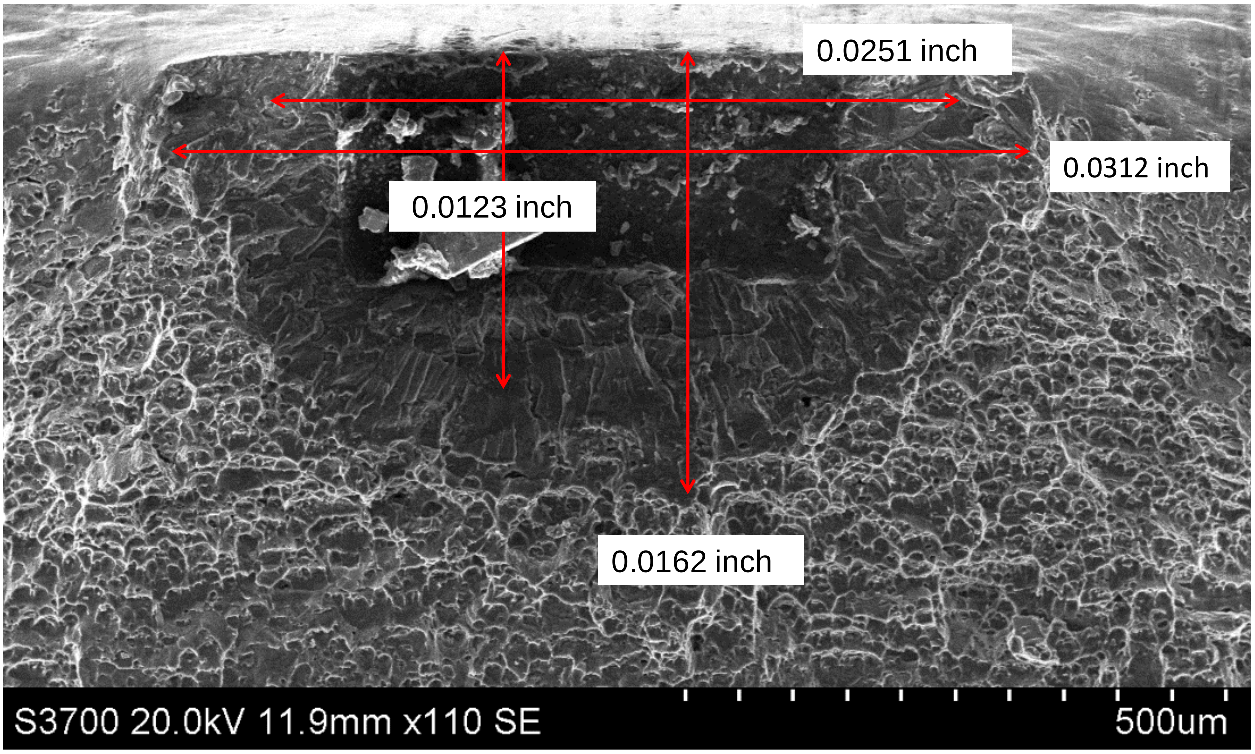

Figure N.18. Fracture surface and crack sizes for crack C2 of COPV 18074.

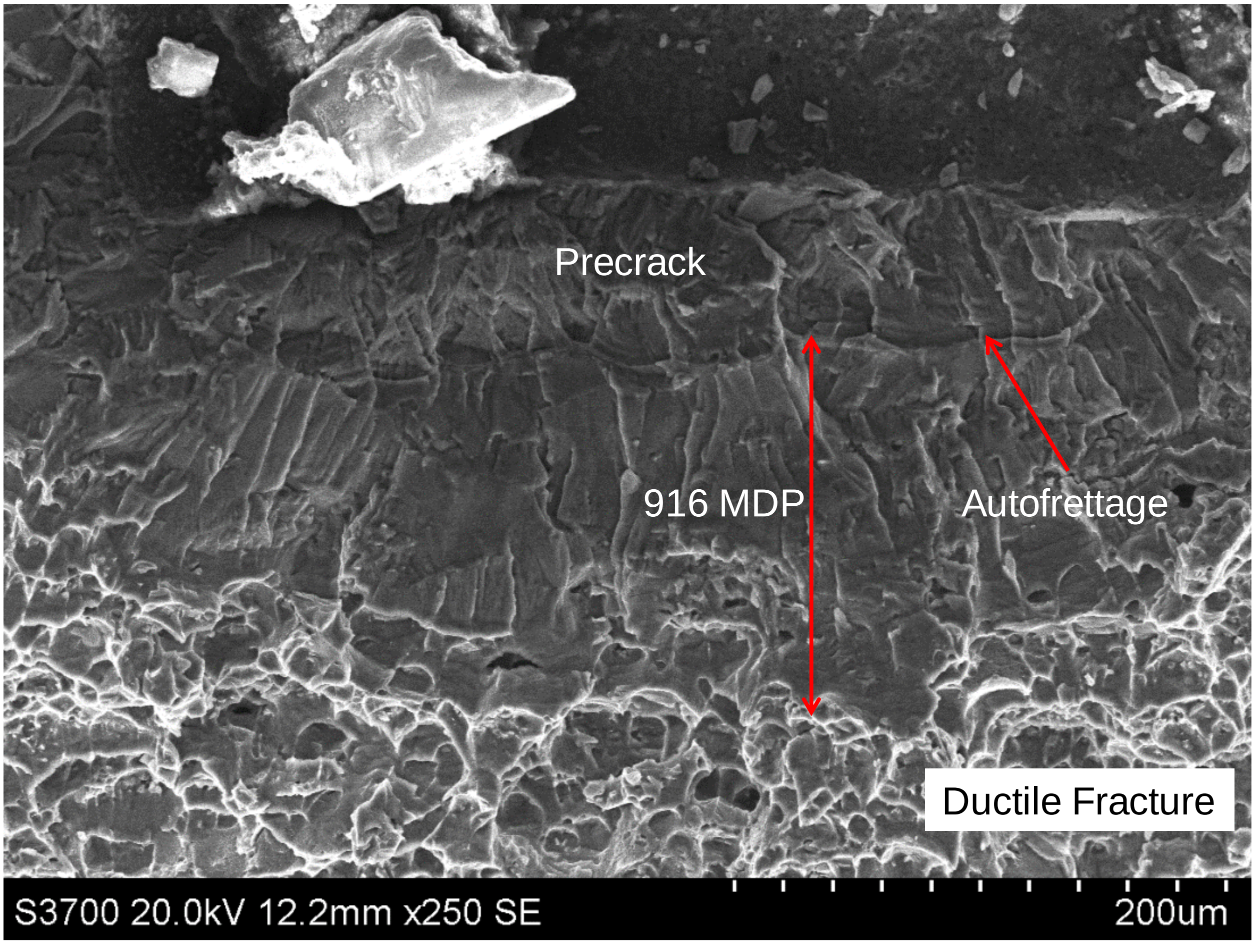

Figure N.19. Higher magnification of the fracture surface for crack C2 of COPV 18074.

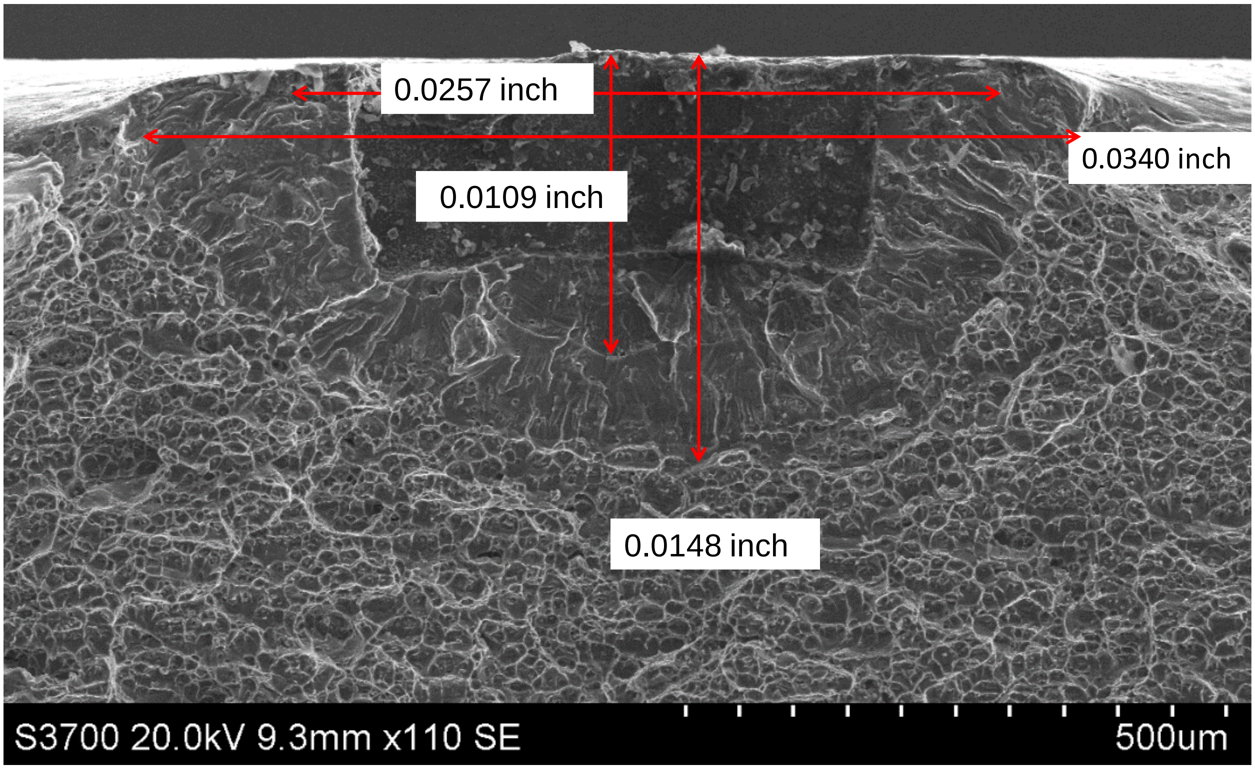

Figure N.20. Fracture surface and crack sizes for crack C3 of COPV 18074.

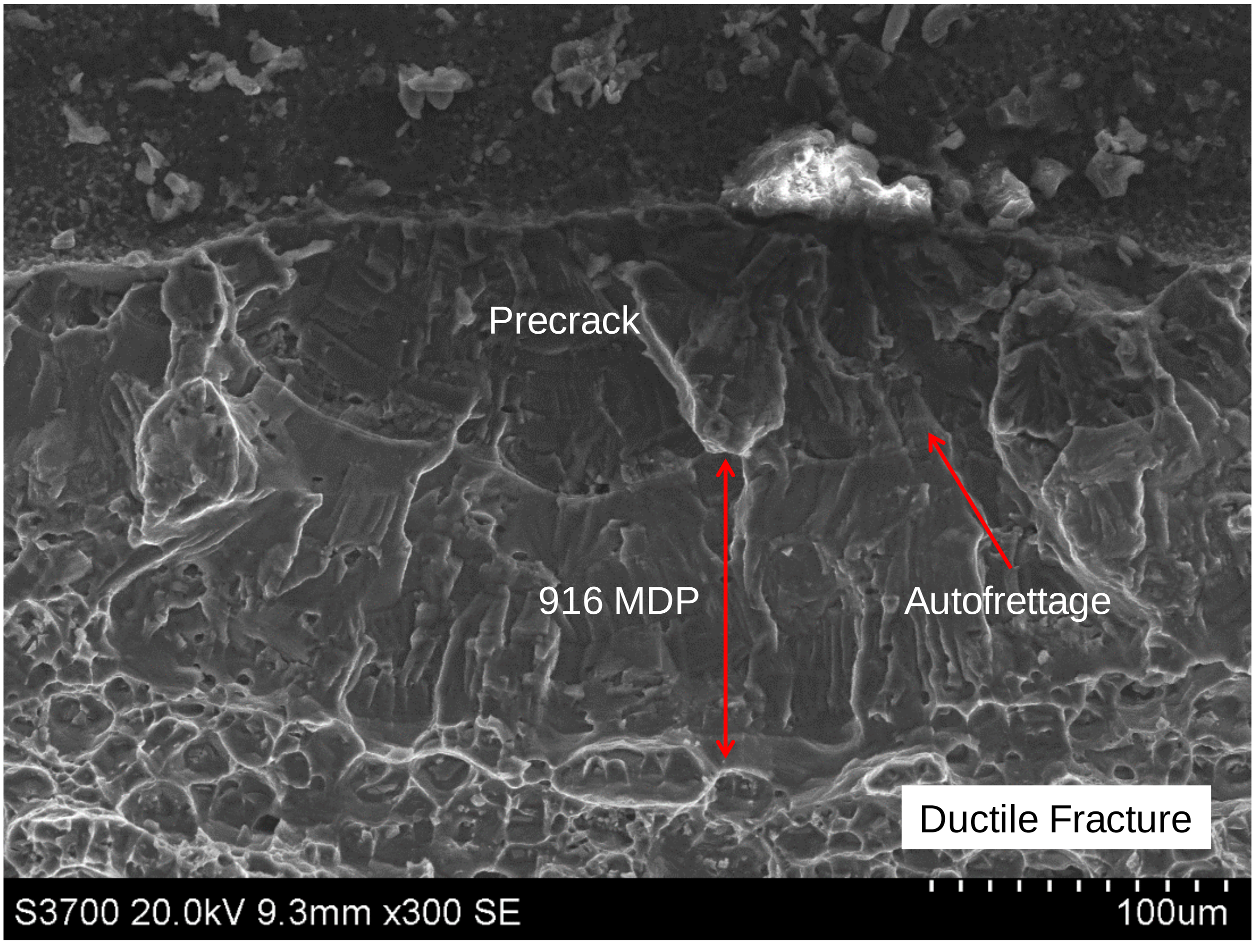

Figure N.21. Higher magnification of the fracture surface for crack C3 of COPV 18074.

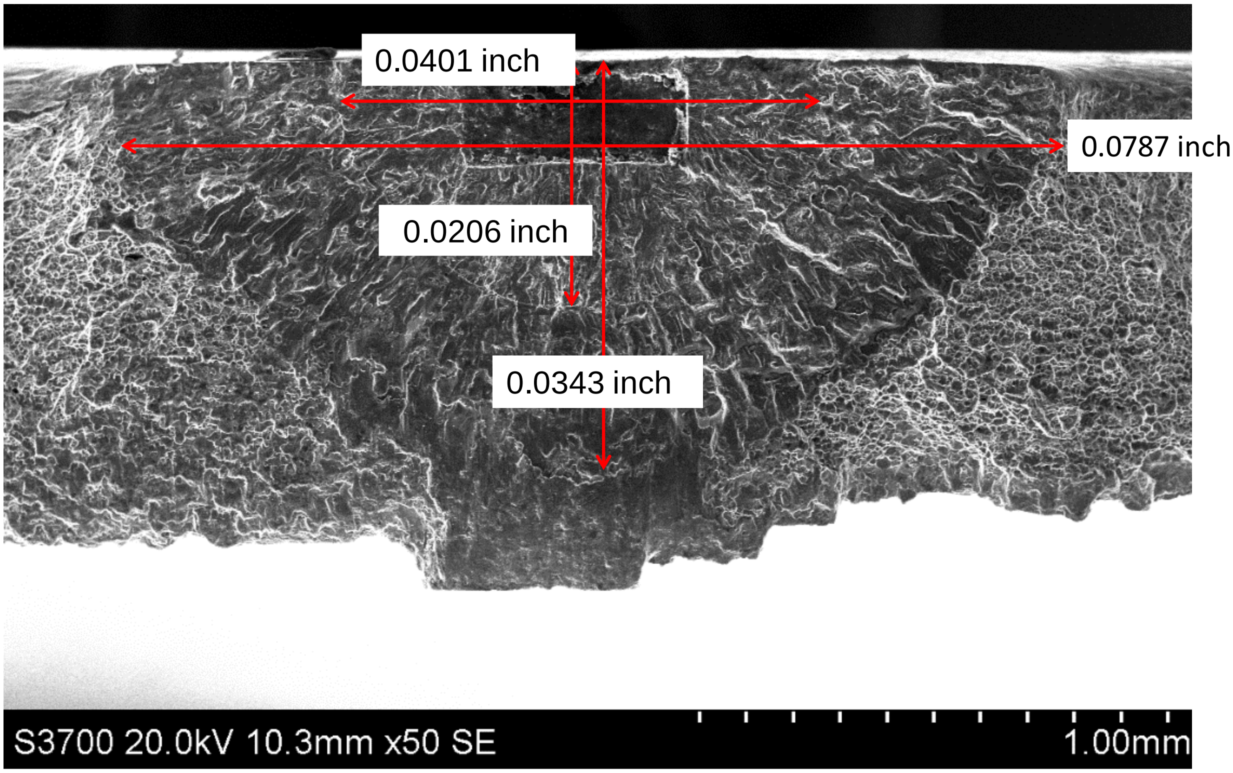

Figure N.22. Fracture surface and crack sizes for crack C4 of COPV 18074.

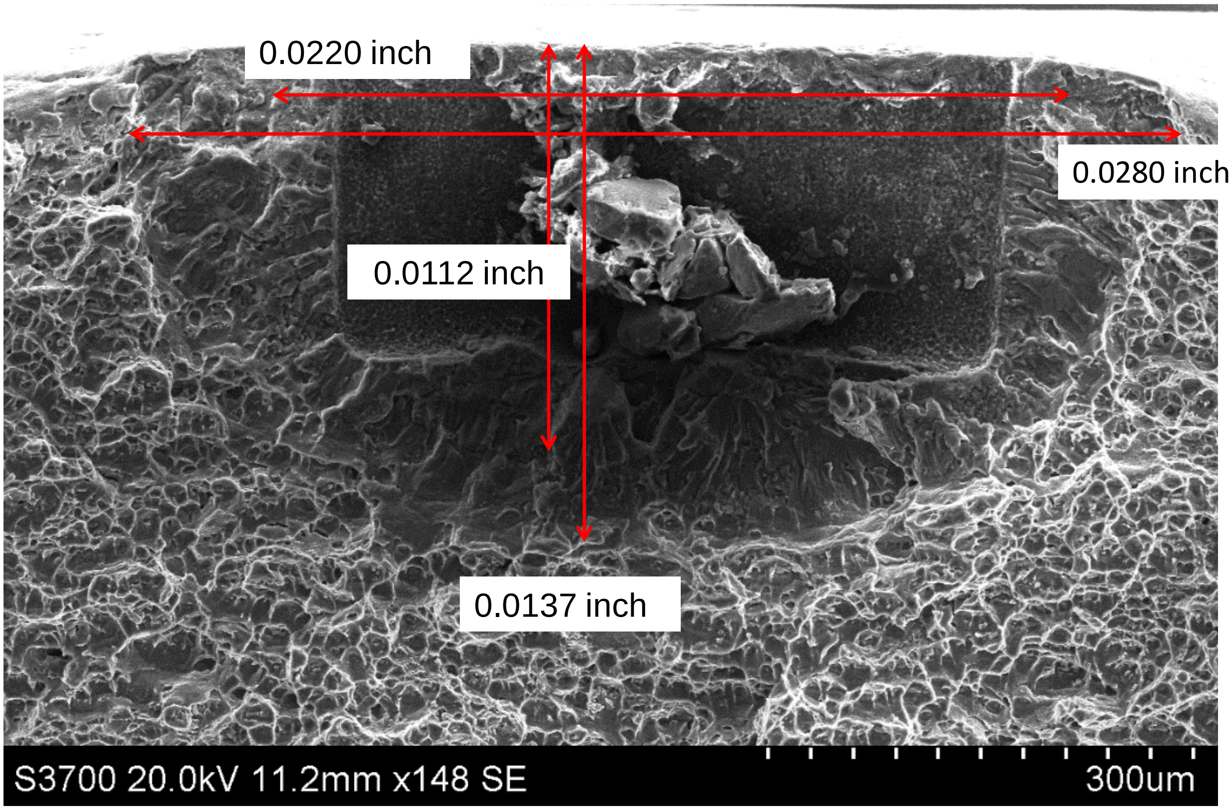

Figure N.23. Fracture surface and crack sizes for crack C5 of COPV 18074.

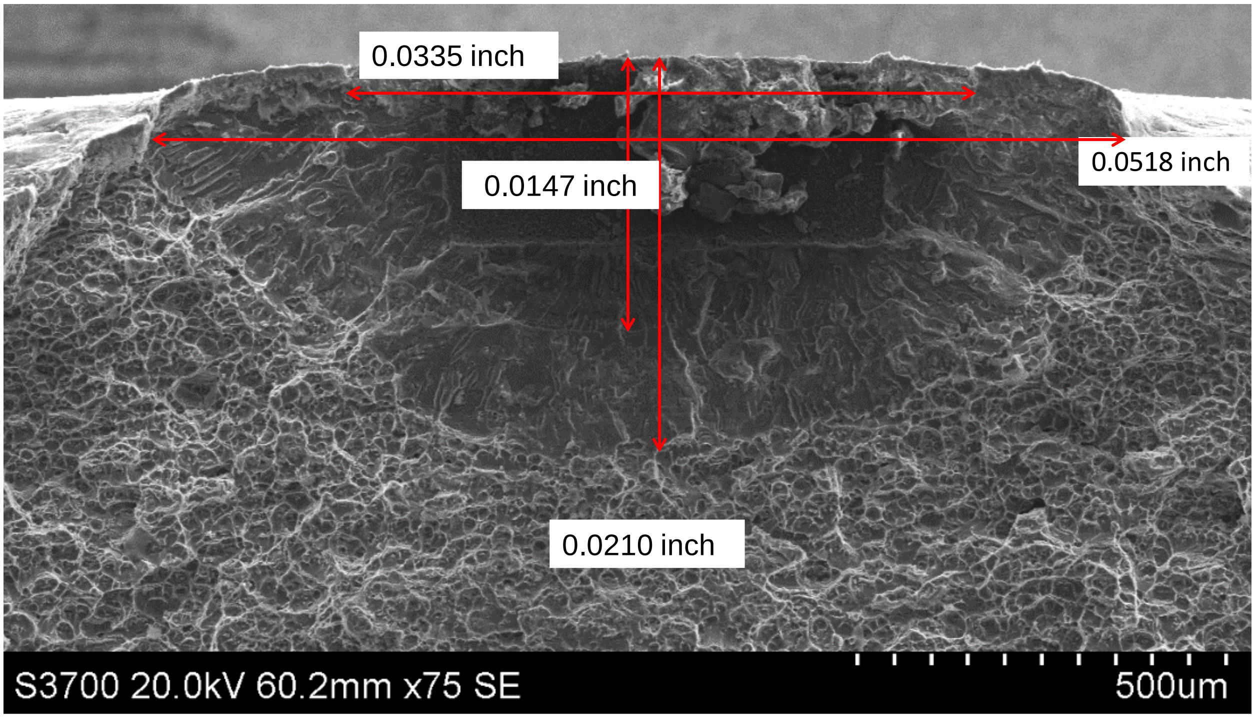

Figure N.24. Fracture surface and crack sizes for crack C7 of COPV 18074.

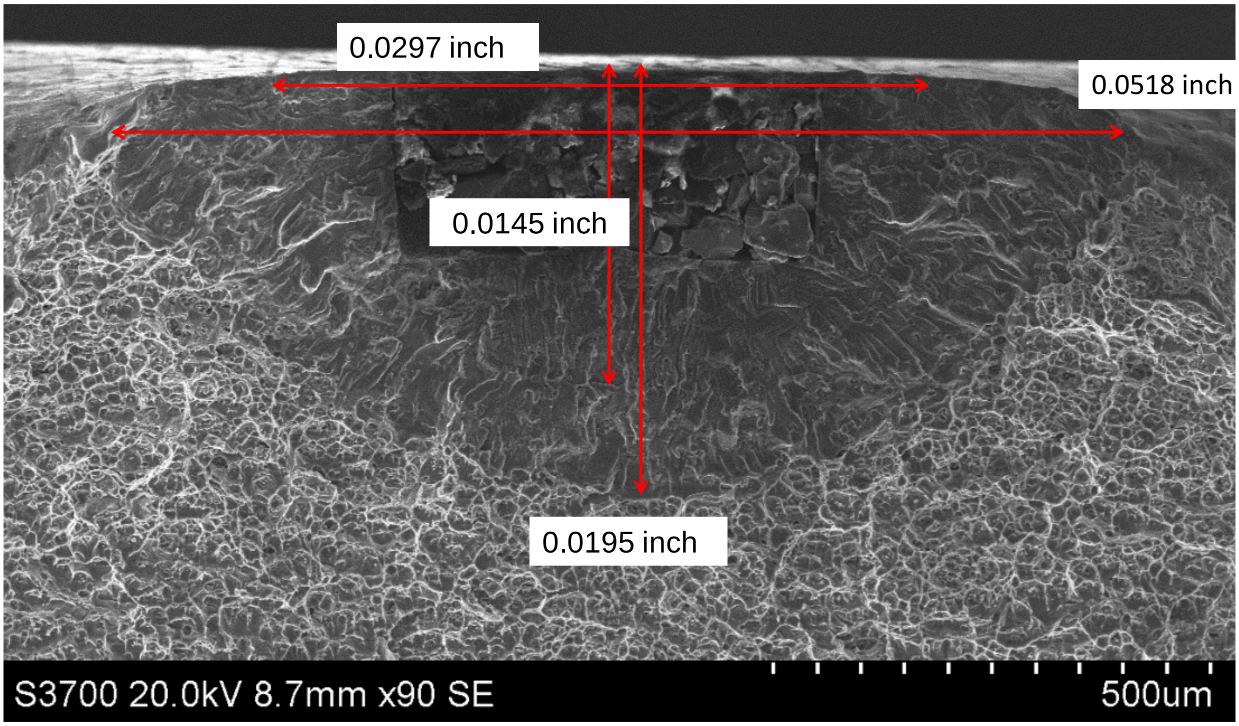

Figure N.25. Fracture surface and crack sizes for crack C8 of COPV 18074.

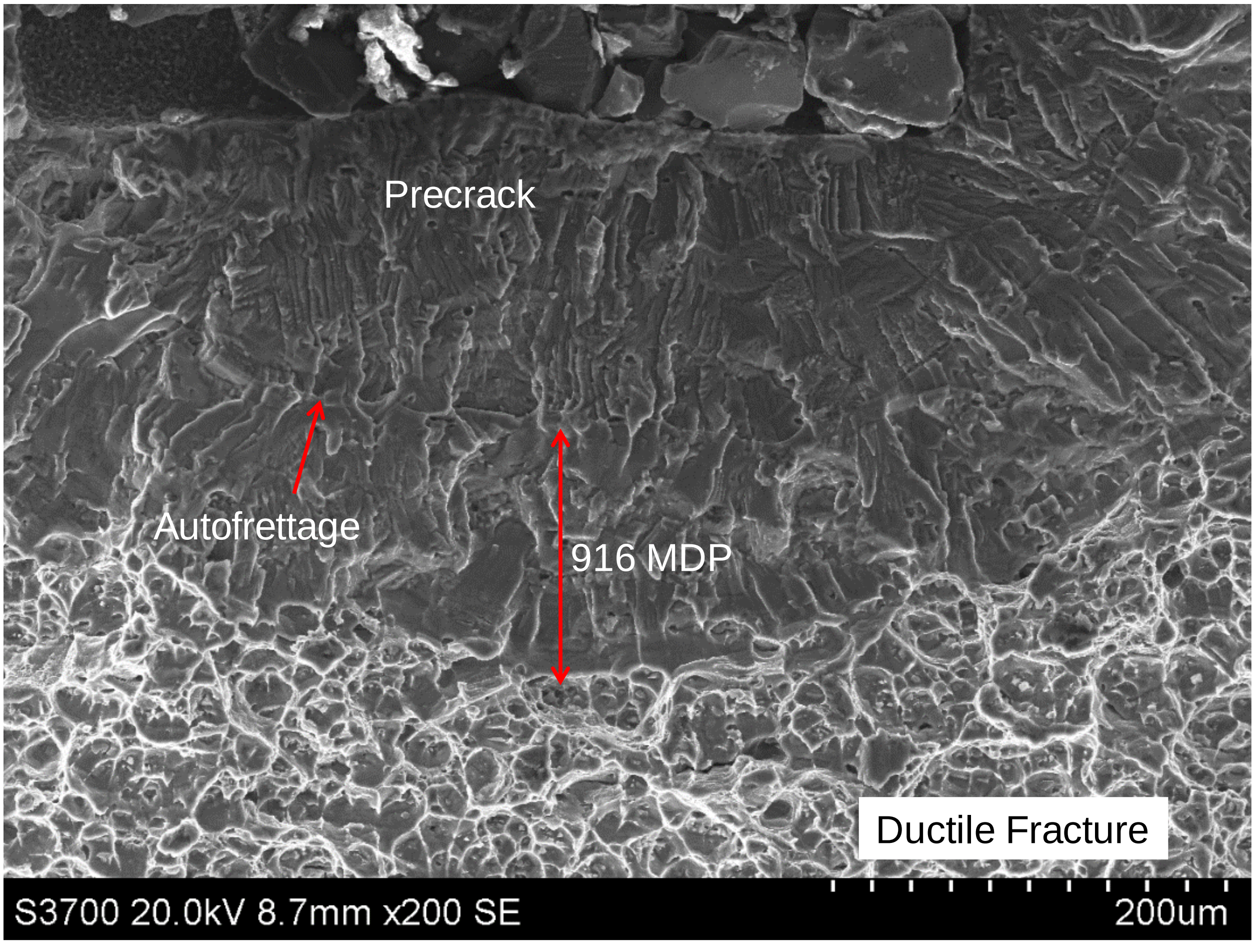

Figure N.26. Higher magnification of the fracture surface for crack C8 of COPV 18074.

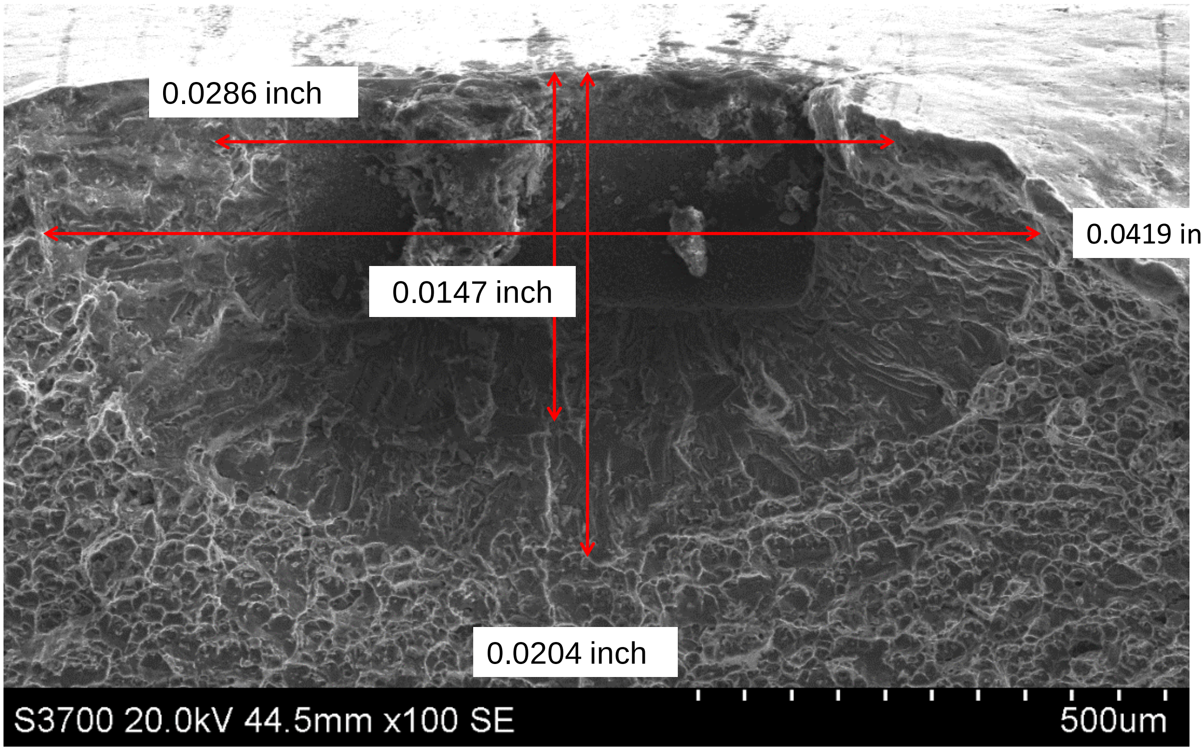

Figure N.27. Fracture surface and crack sizes for crack C9 of COPV 18074.

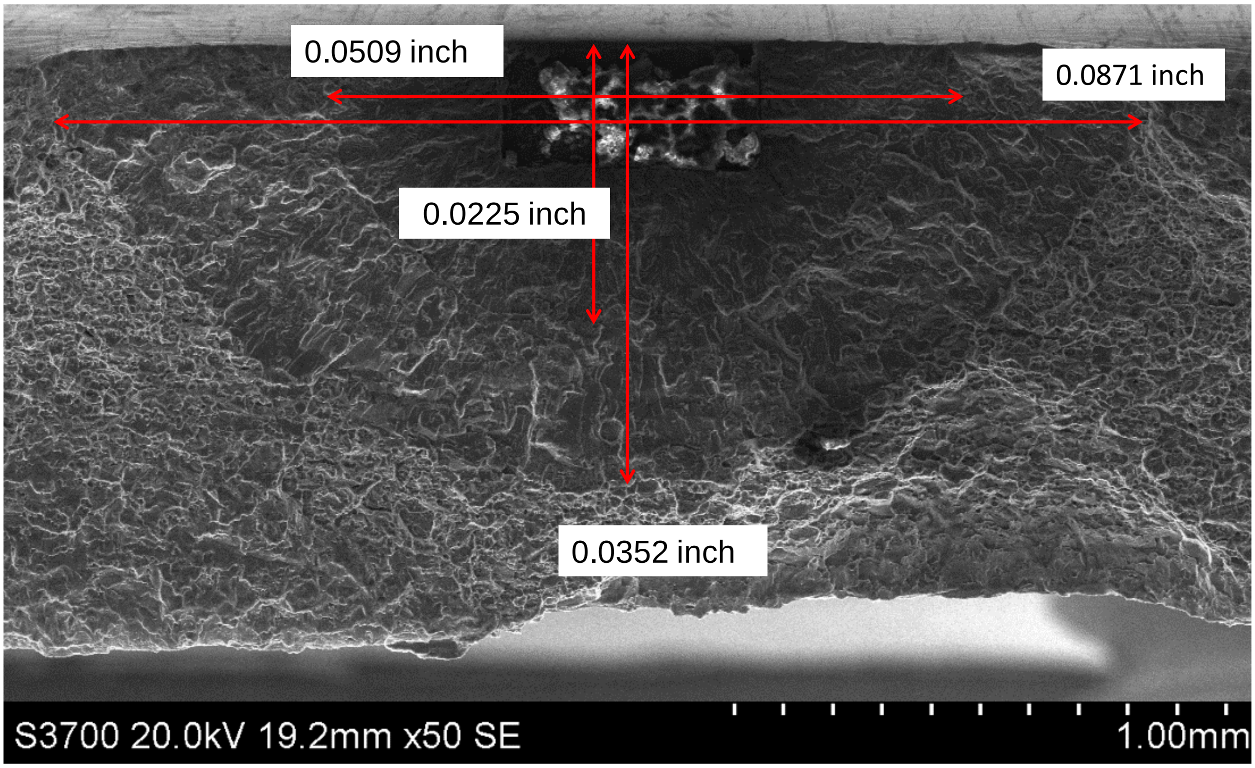

Figure N.28. Fracture surface and crack sizes for crack N2 of COPV 18074.

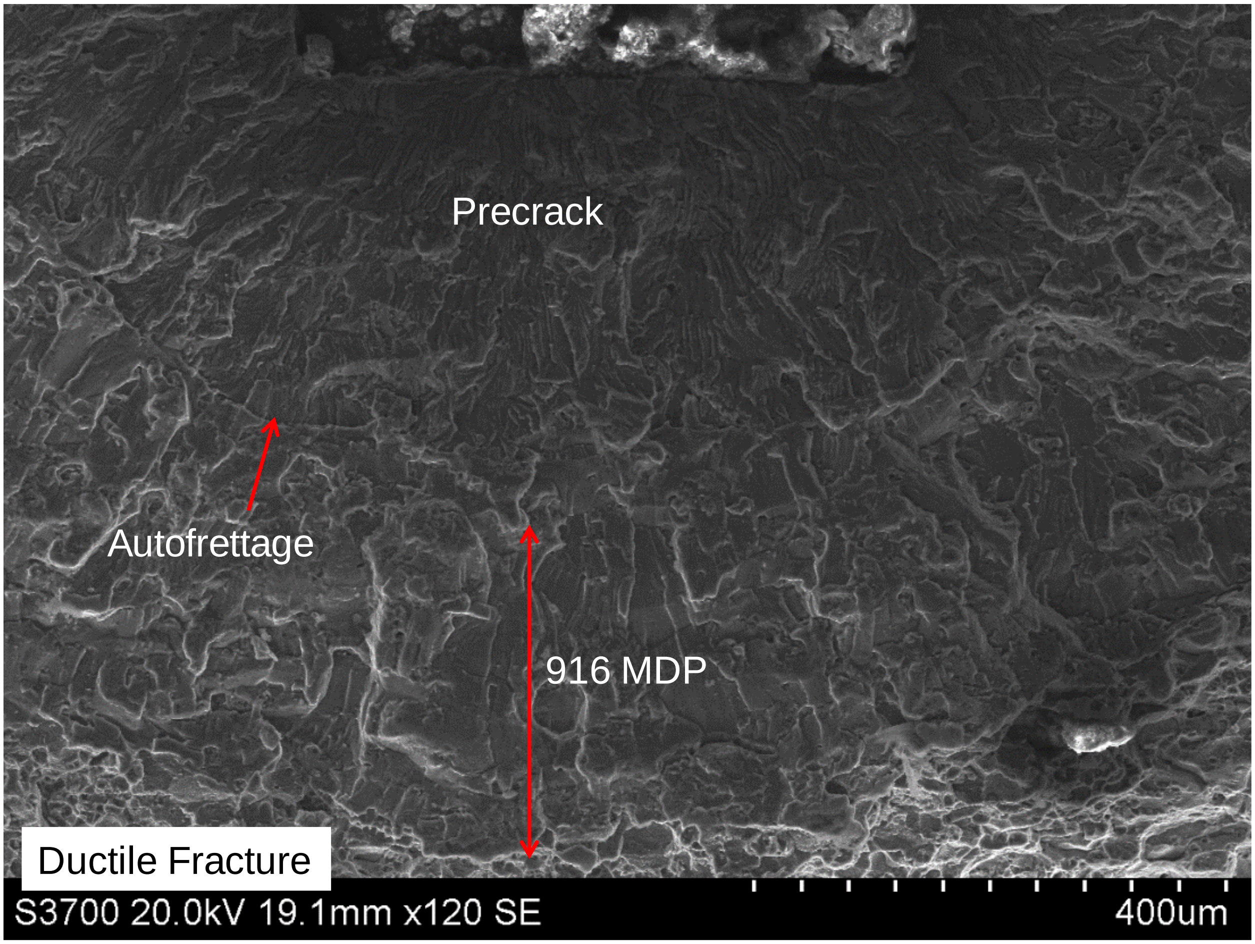

Figure N.29. Higher magnification of the fracture surface for crack N2 of COPV 18074.

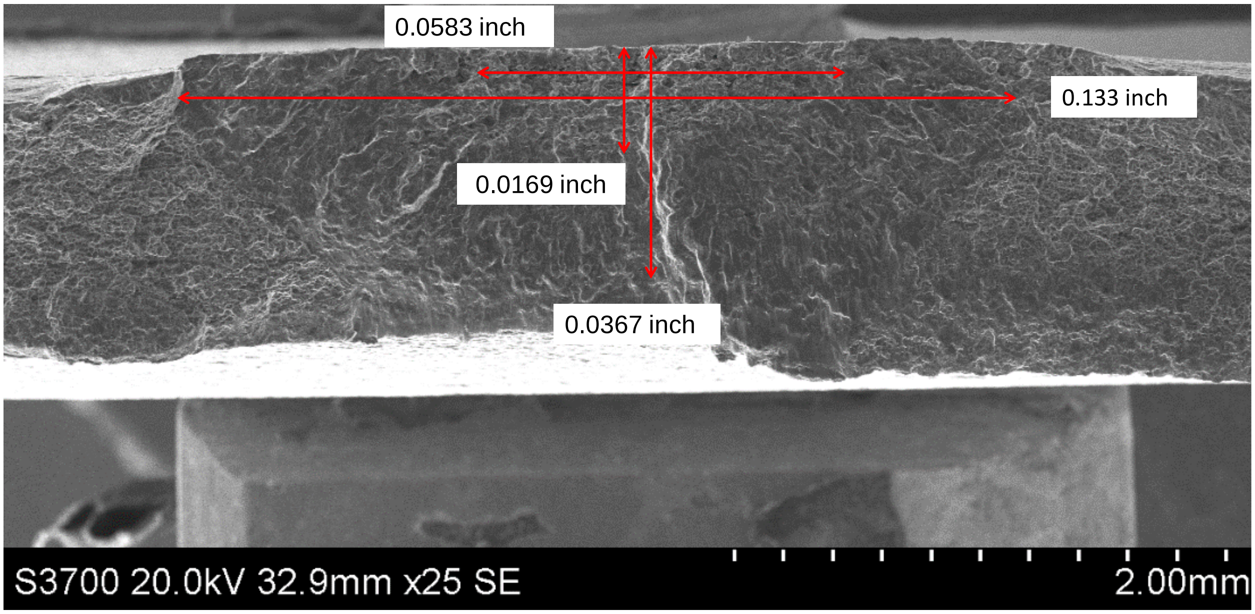

Figure N.30. Fracture surface and crack sizes for crack ID34 of COPV 18074.

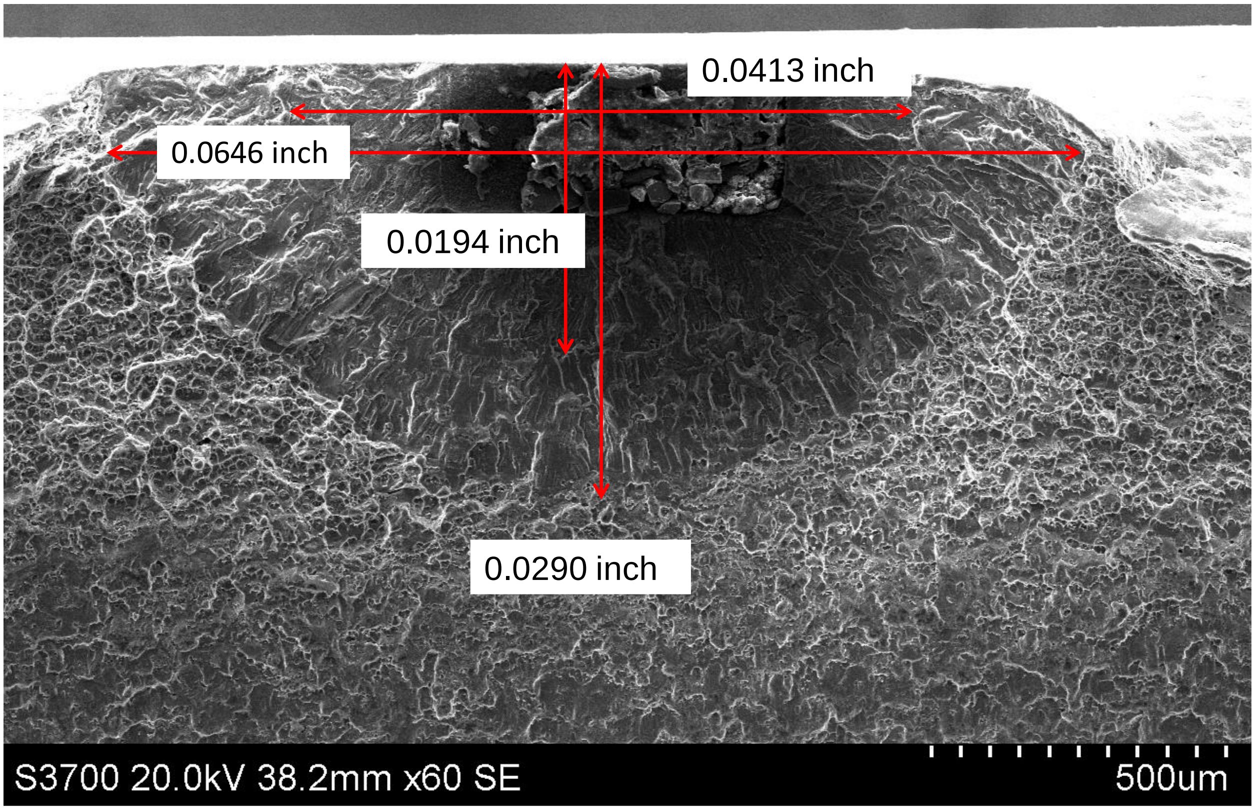

Figure N.31. Fracture surface and crack sizes for crack C1 of COPV 18072.

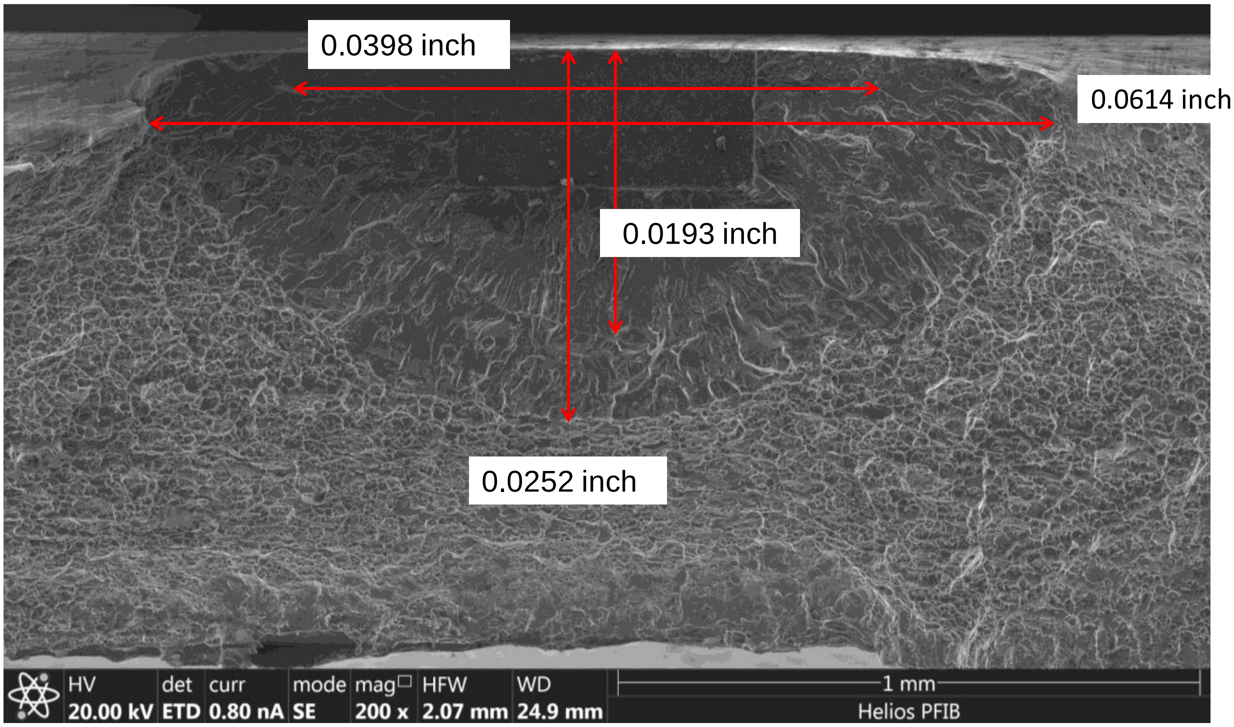

Figure N.32. Fracture surface and crack sizes for crack C2 of COPV 18072.

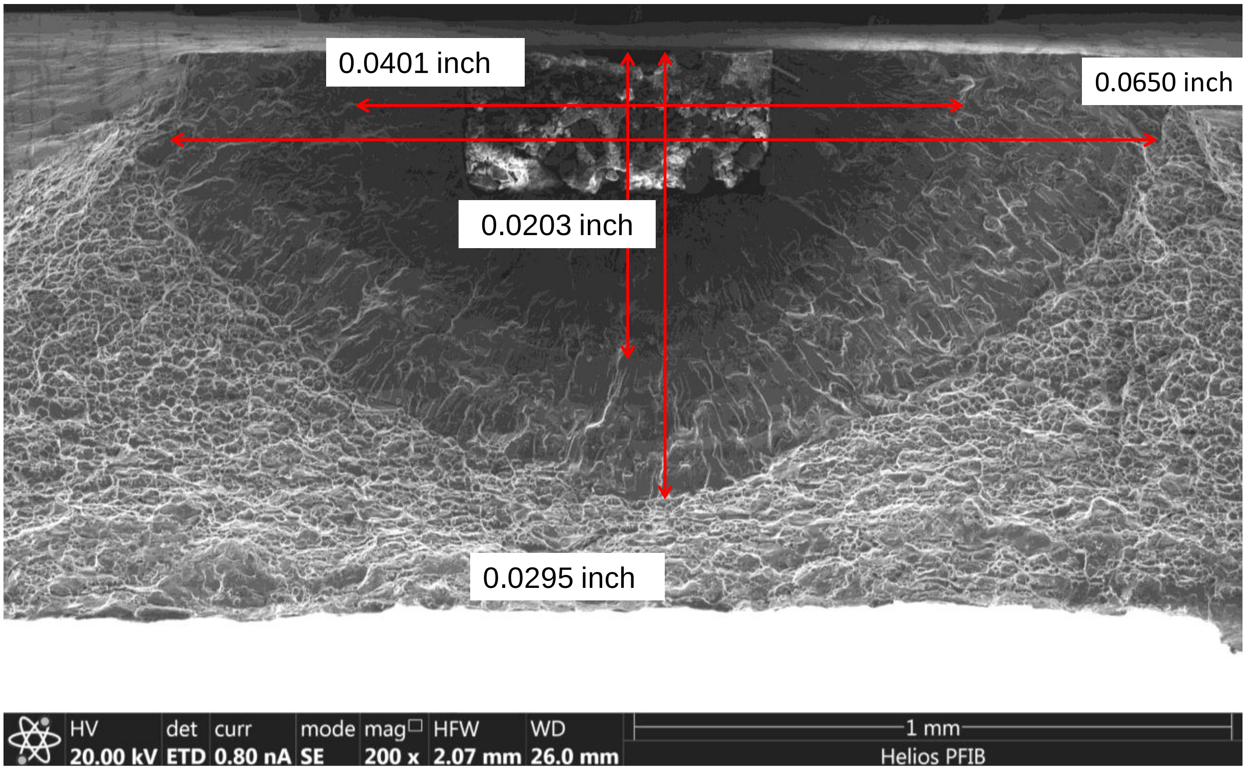

Figure N.33. Fracture surface and crack sizes for crack C4 of COPV 18072.

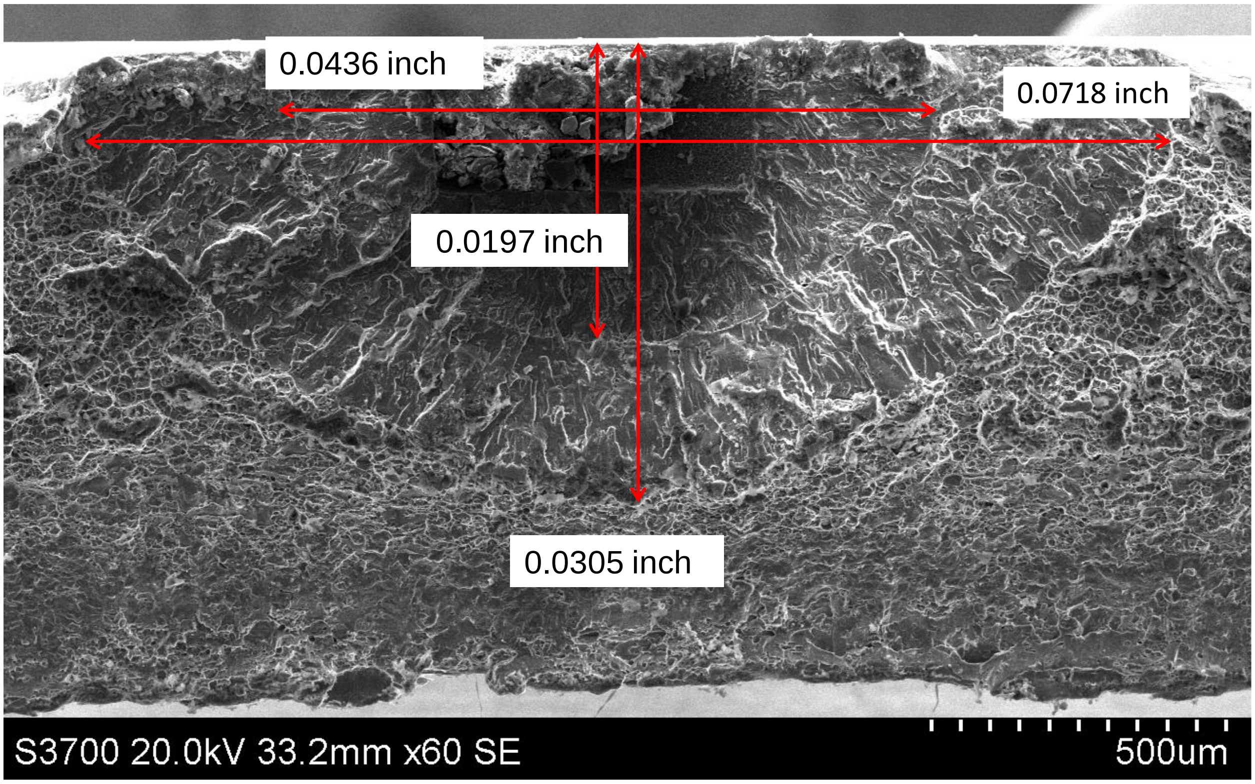

Figure N.34. Fracture surface and crack sizes for crack C5 of COPV 18072.

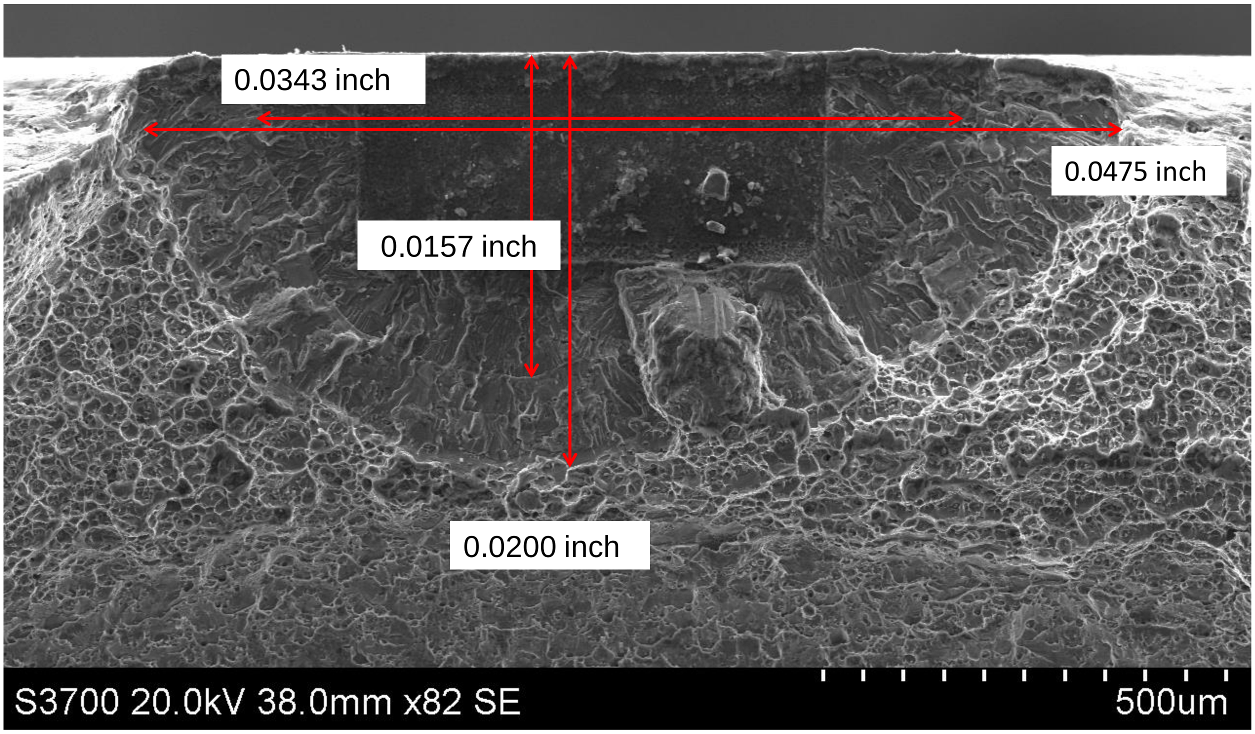

Figure N.35. Fracture surface and crack sizes for crack C6 of COPV 18072.

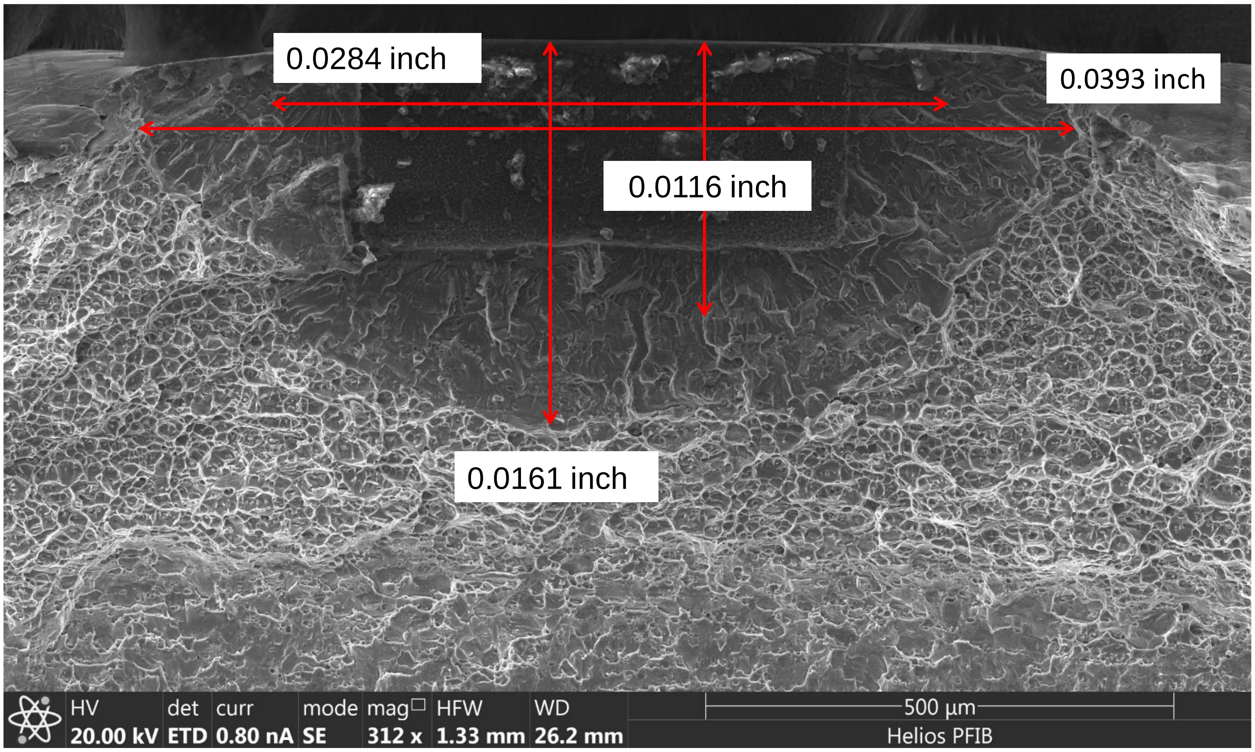

Figure N.36. Fracture surface and crack sizes for crack C7 of COPV 18072.

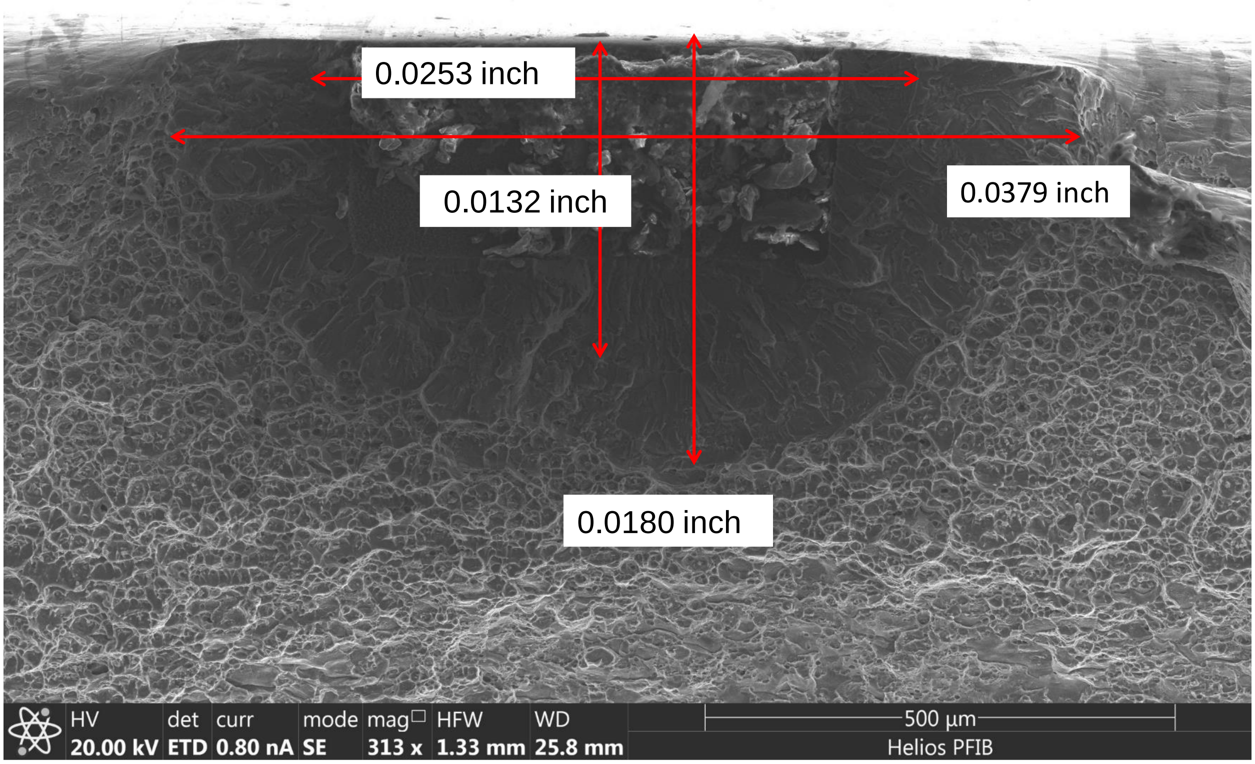

Figure N.37. Fracture surface and crack sizes for crack C8 of COPV 18072.

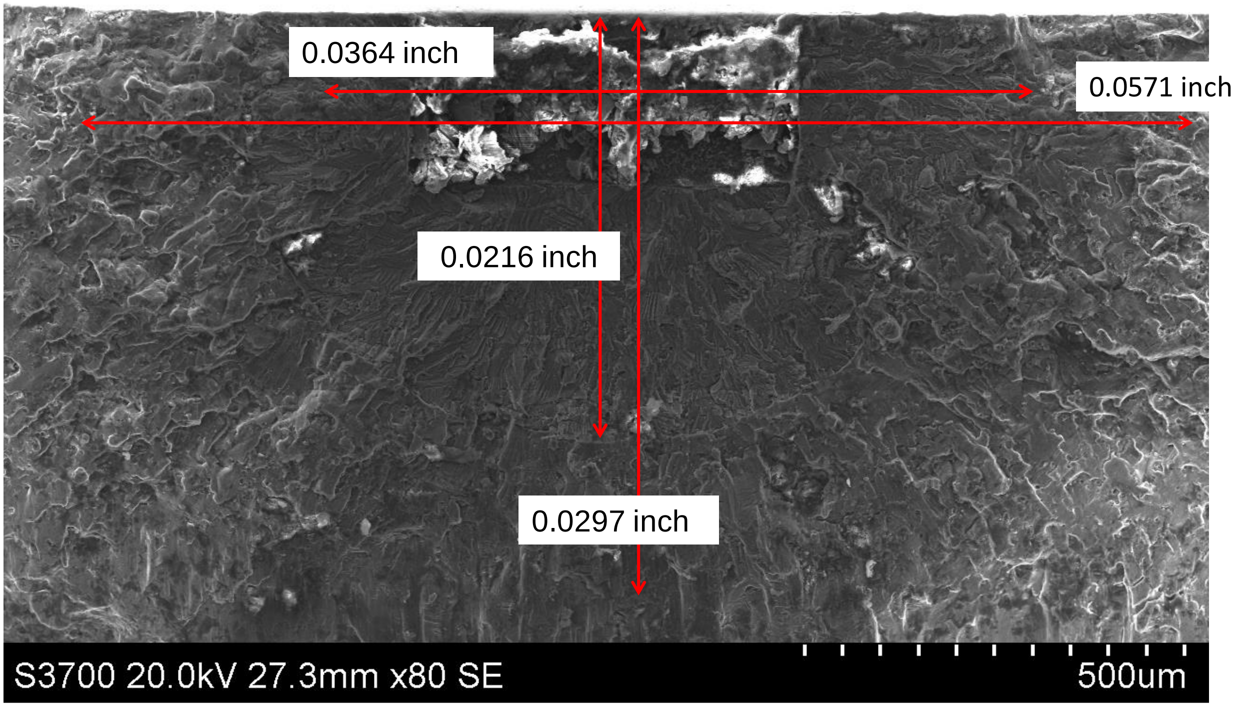

Figure N.38. Fracture surface and crack sizes for crack C9 of COPV 18072.

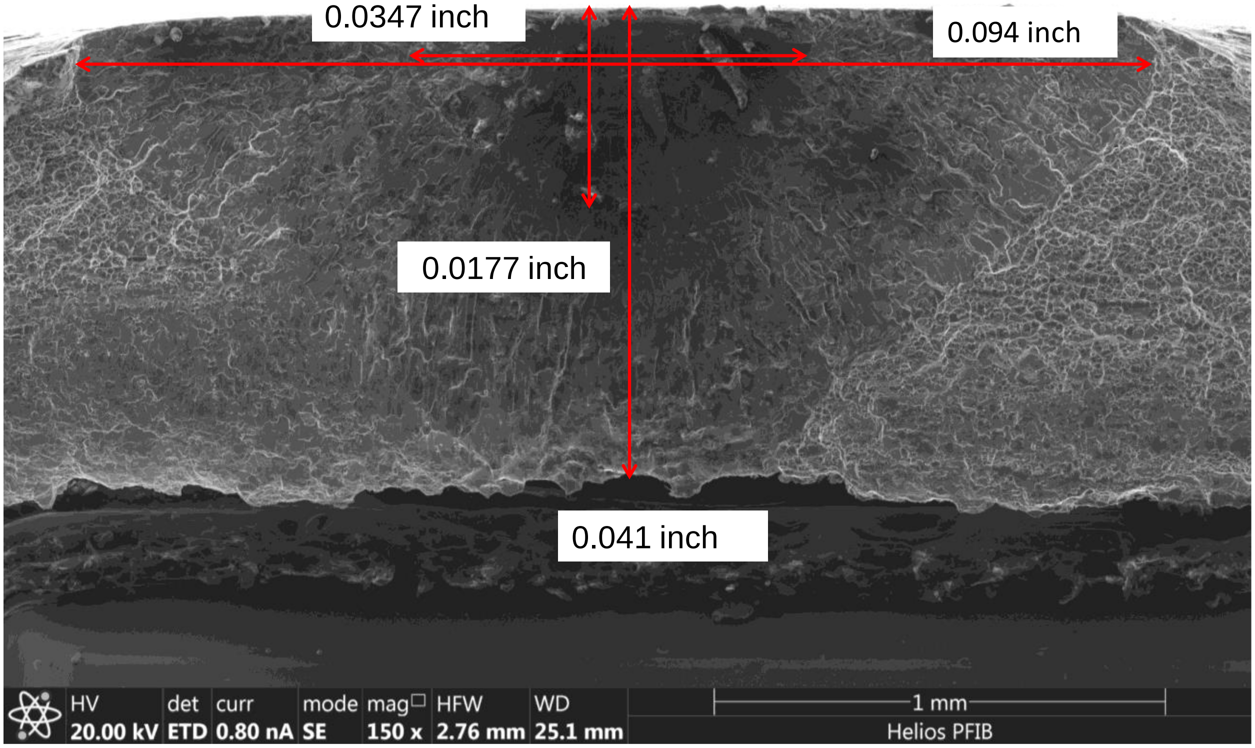

Figure N.39. Fracture surface and crack sizes for crack ID12 of COPV 18072.

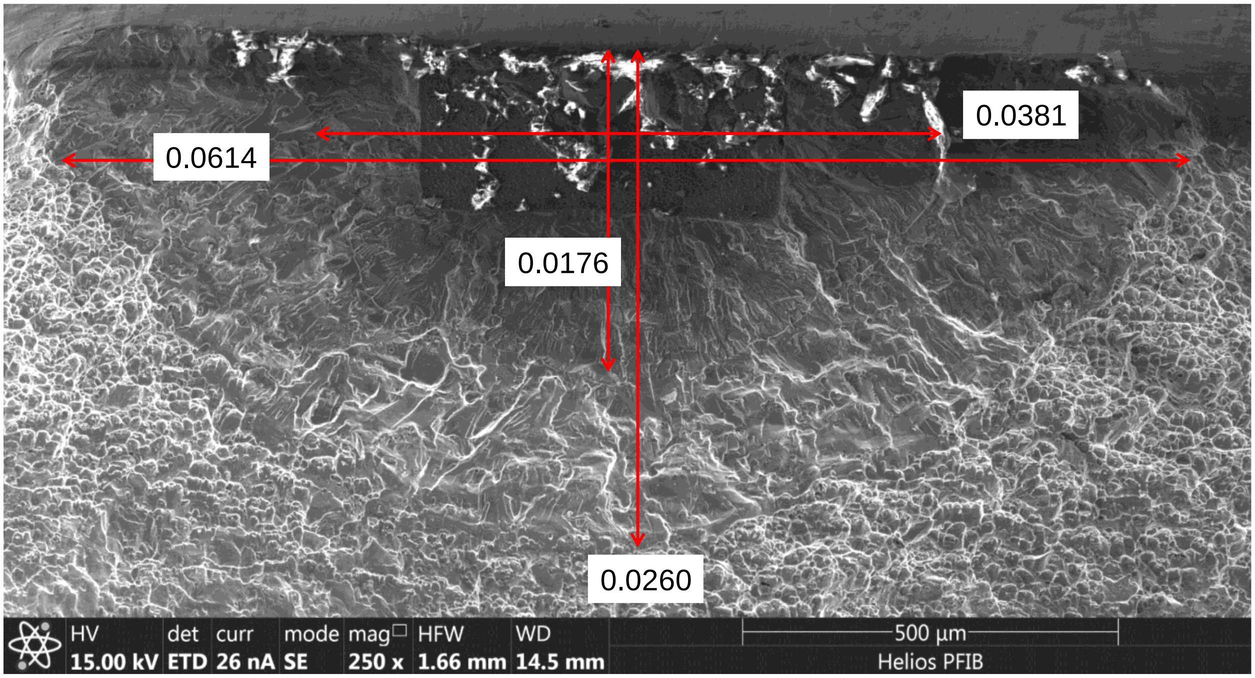

Figure N.40. Fracture surface and crack sizes for crack C1 of COPV 18092.

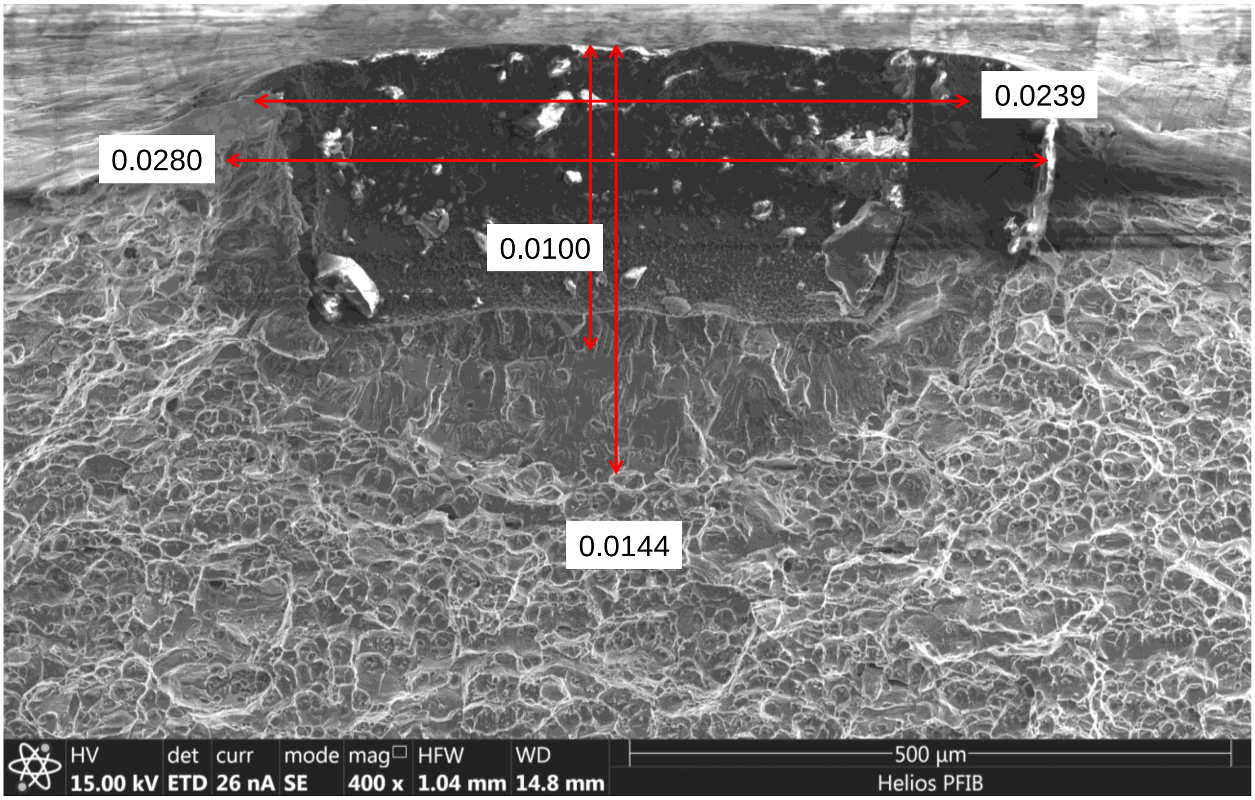

Figure N.41. Fracture surface and crack sizes for crack C2 of COPV 18092.

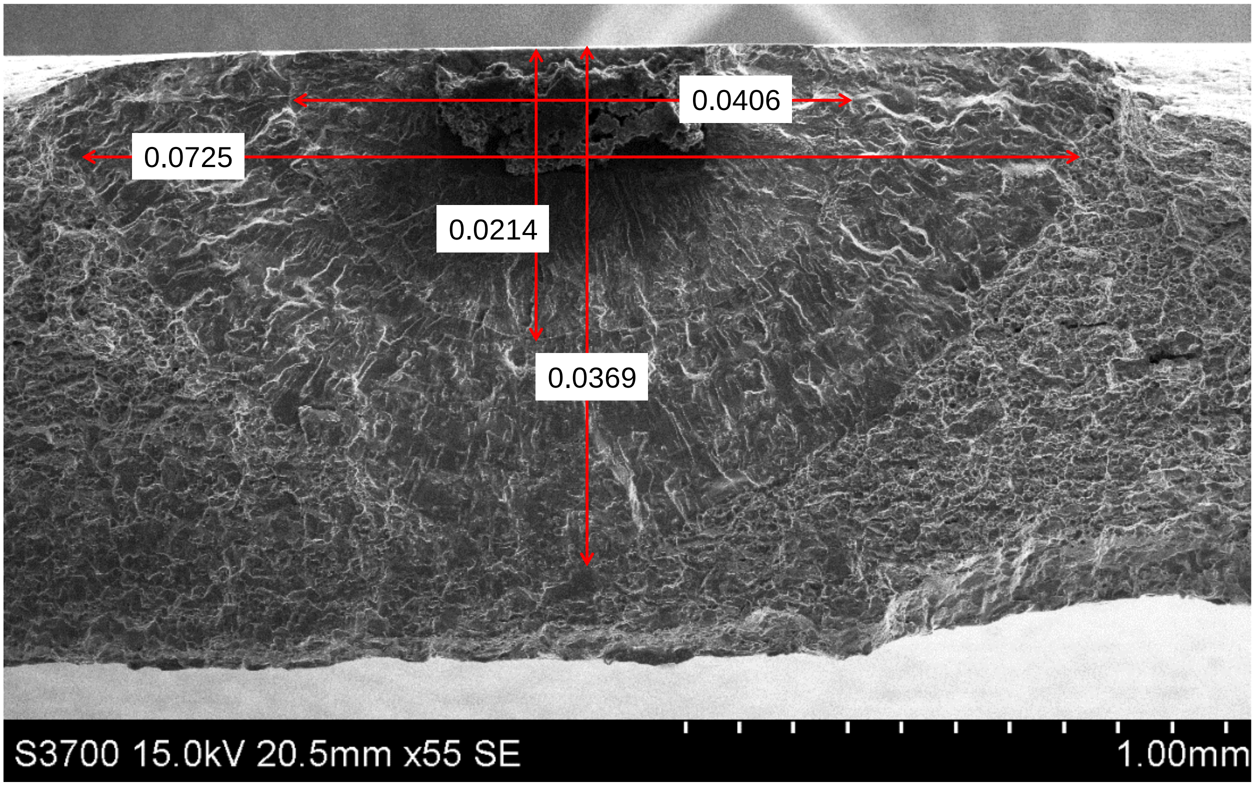

Figure N.42. Fracture surface and crack sizes for crack C3 of COPV 18092.

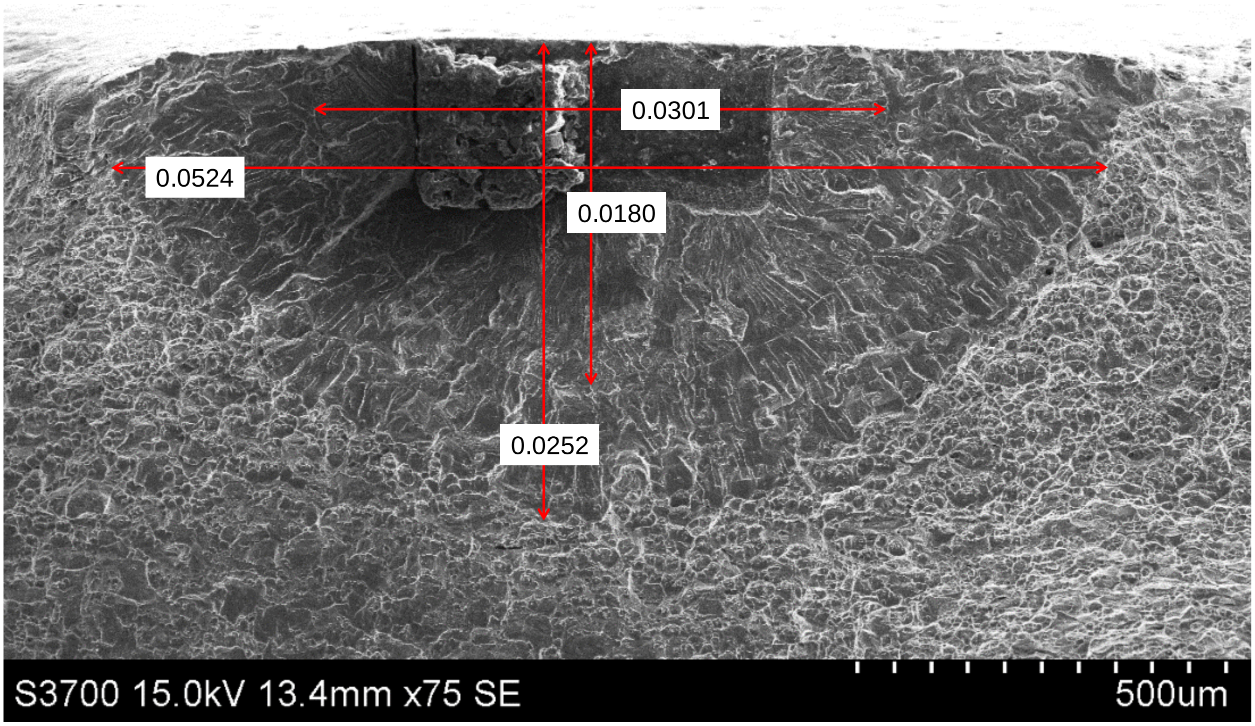

Figure N.43. Fracture surface and crack sizes for crack C4 of COPV 18092.

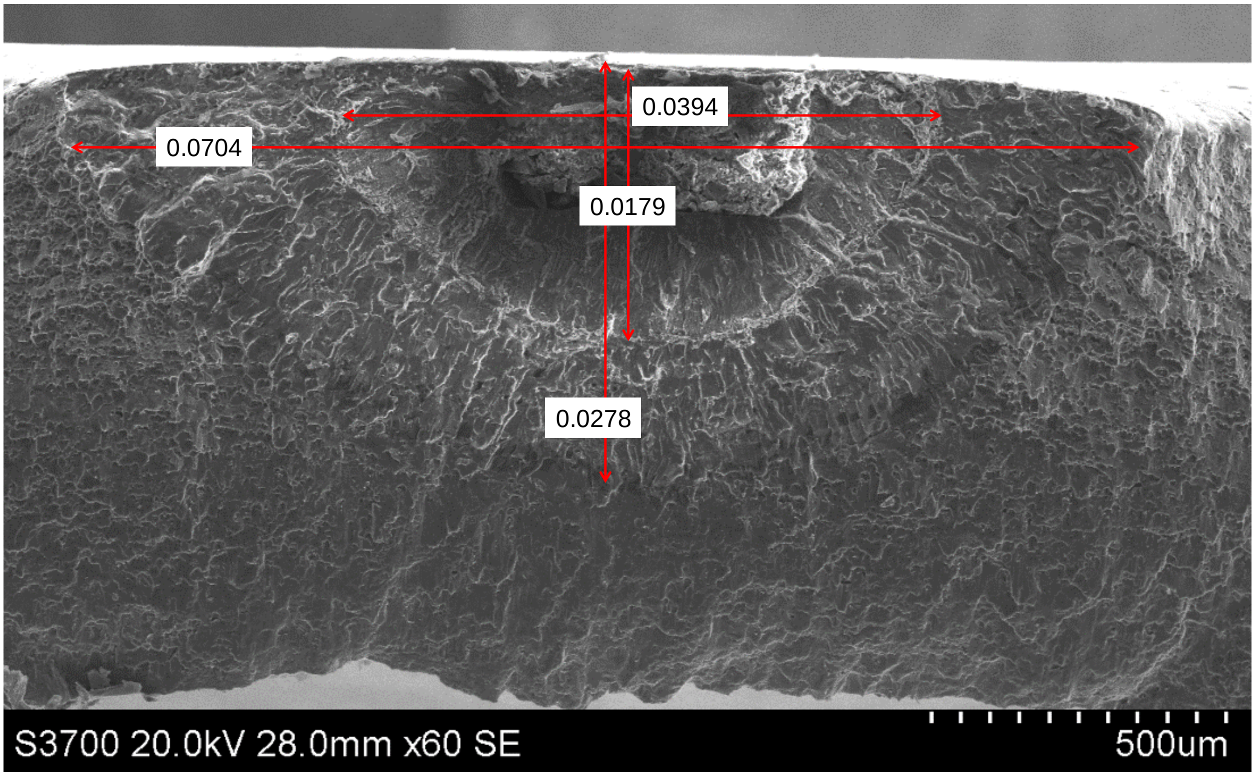

Figure N.44. Fracture surface and crack sizes for crack C5 of COPV 18092.

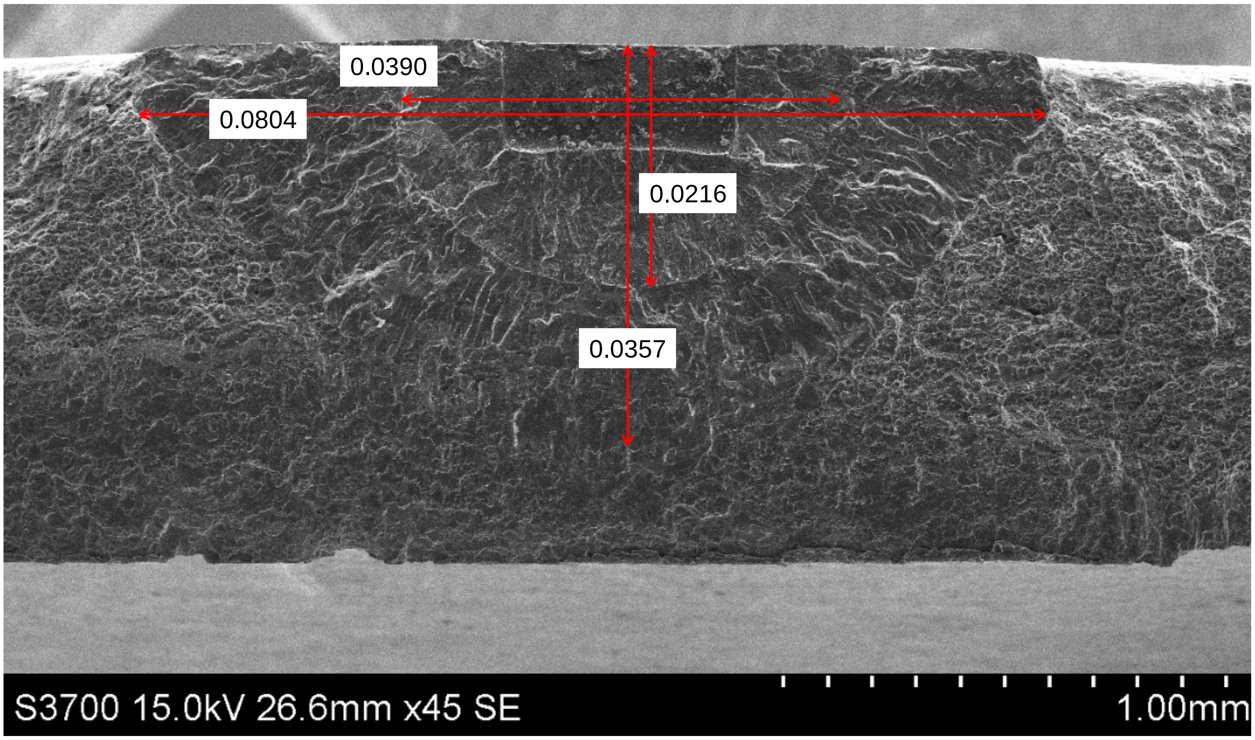

Figure N.45. Fracture surface and crack sizes for crack C6 of COPV 18092.

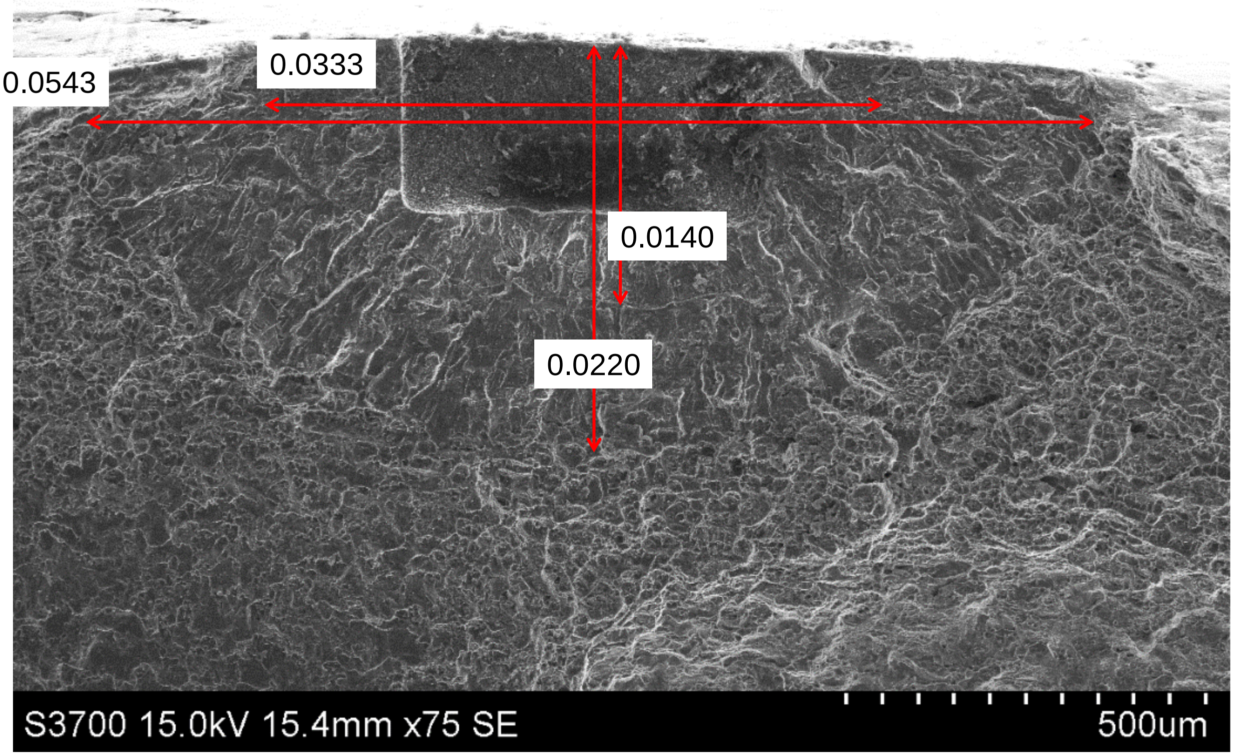

Figure N.46. Fracture surface and crack sizes for crack C7 of COPV 18092.

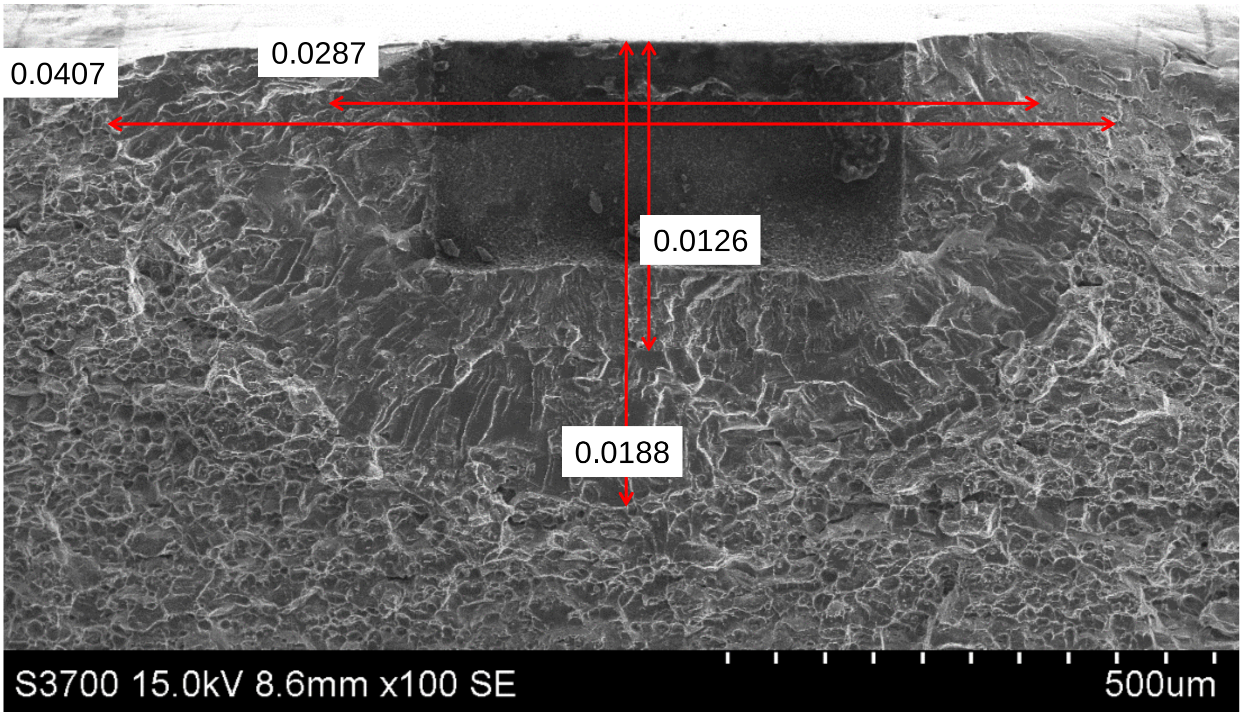

Figure N.47. Fracture surface and crack sizes for crack C8 of COPV 18092.

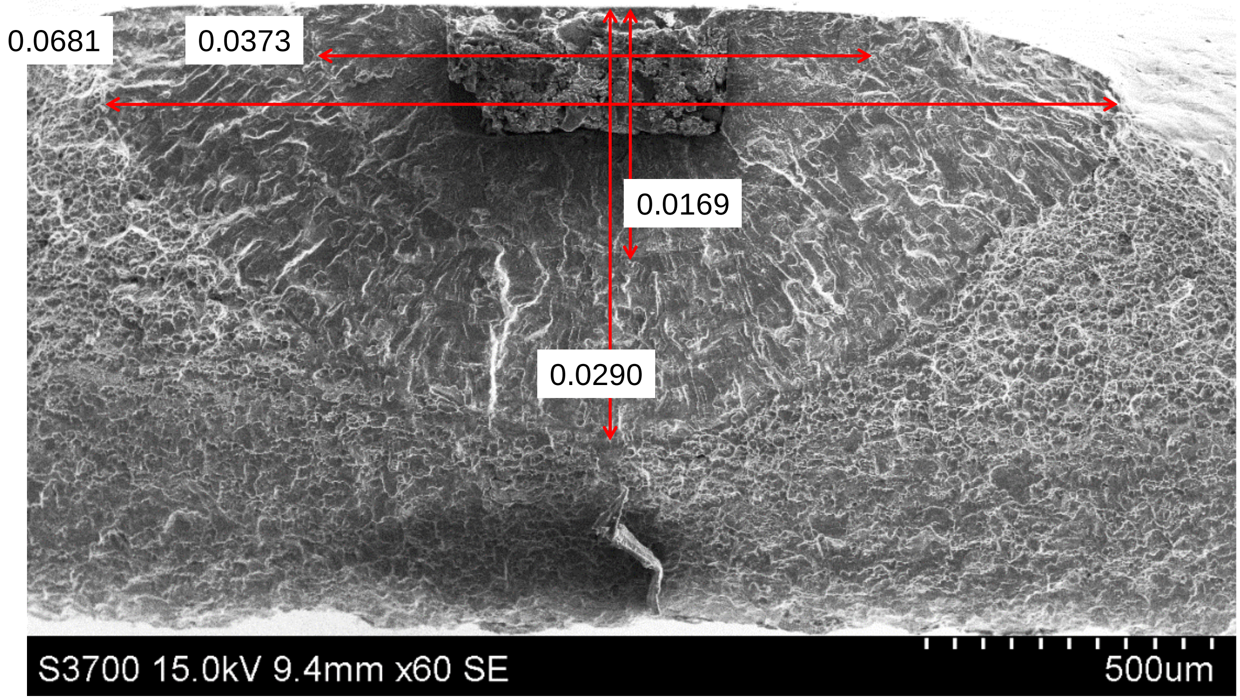

Figure N.48. Fracture surface and crack sizes for crack C9 of COPV 18092.

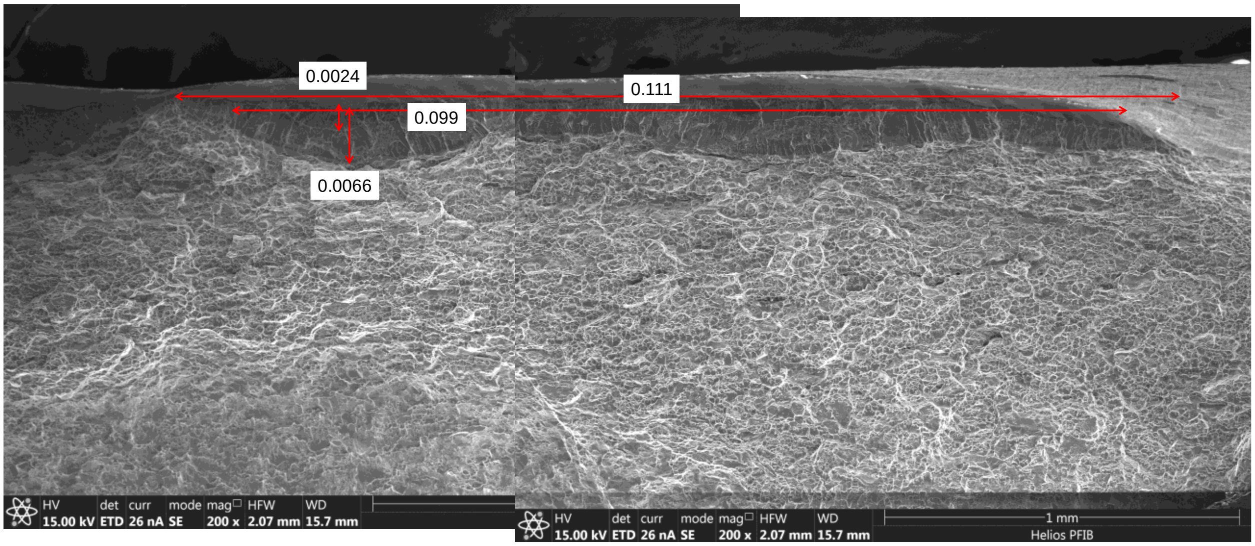

Figure N.49. Fracture surface and crack sizes for crack ID1 of COPV 18092.

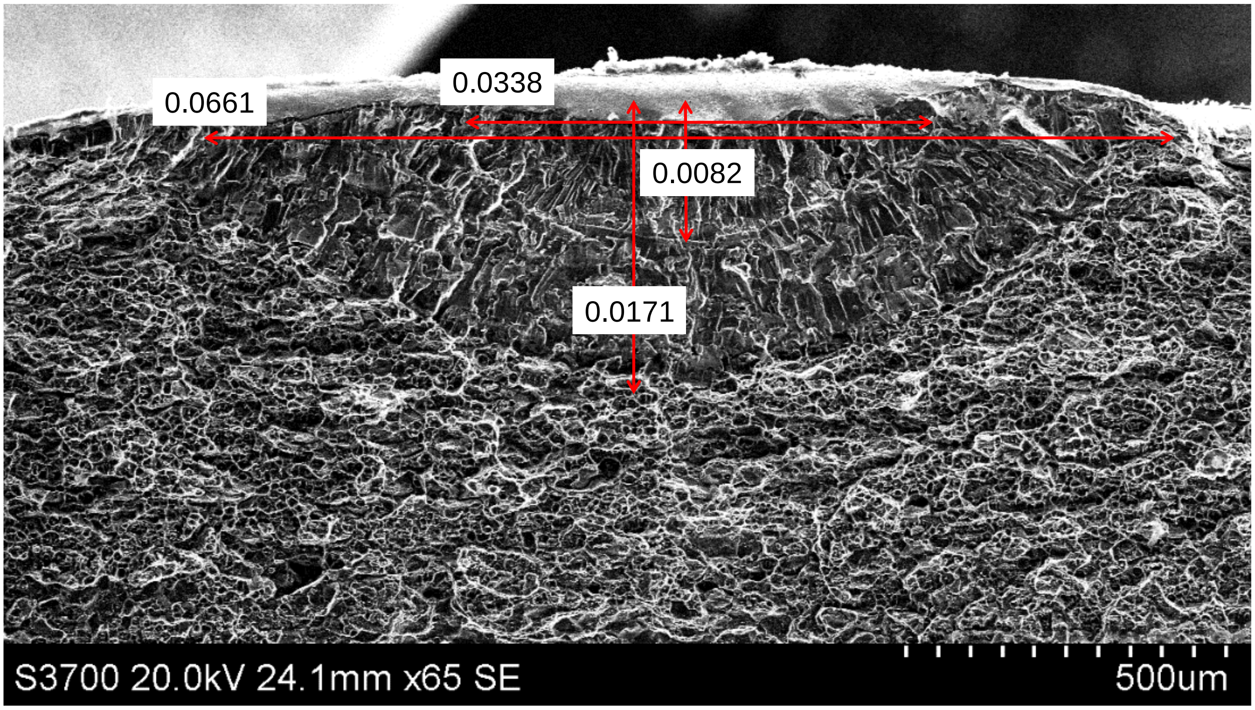

Figure N.50. Fracture surface and crack sizes for crack ID4 of COPV 18092.

Appendix O. Uniaxial Coupons for Damage Tolerance Life Testing

O.1 Overview

Although COPV liners are inherently characterized by a biaxial stress state, AIAA S-081B allows for the use of uniaxial coupons for damage tolerance testing [ref. 2]. Figure O-1 shows the results of a FEM analyzing the biaxial stress state of an AA6061-T6 COPV liner during the autofrettage cycle and subsequent MDP loading. This appendix analyzes the applicability of uniaxial coupons to the biaxial problem of a crack growing in a COPV liner. The crack tip states of a surface crack in a thin walled flat plate are compared for a uniaxial and biaxial stress states using an elastic-plastic FEM. The autofrettage peak load is examined to determine the suitability of using a uniaxial coupon to test for the crack growth obtained during the autofrettage cycle. Then an analysis technique is proposed to add conservatism to a uniaxial autofrettage coupon test.

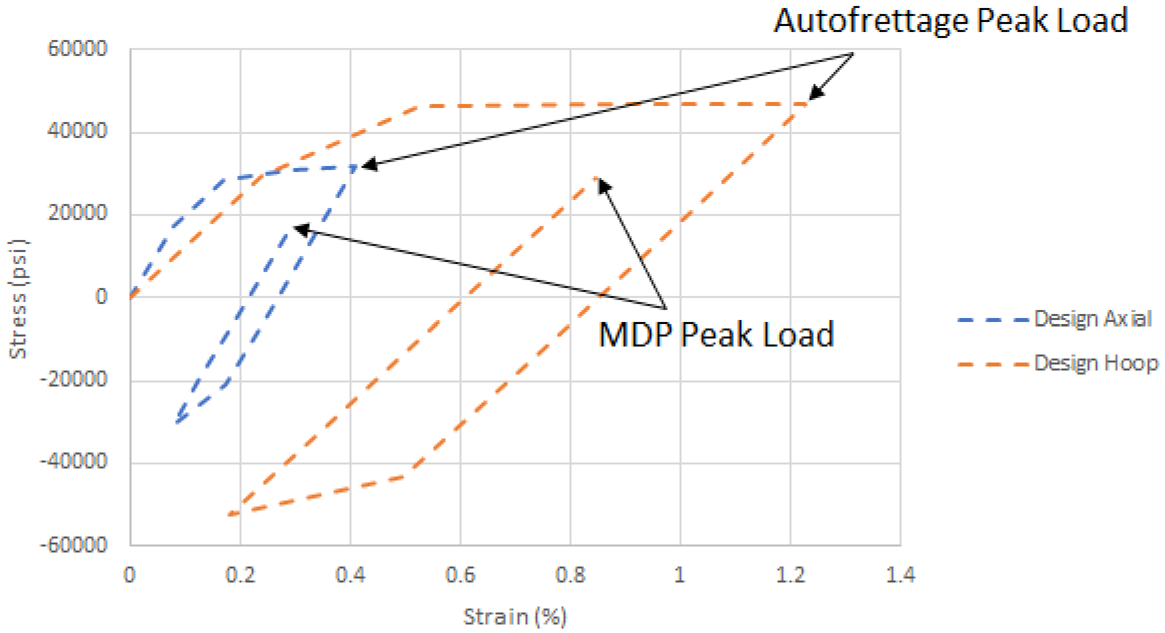

Figure O-1. Stress-strain response of a COPV liner autofrettage and subsequent MDP cycle.

O.2 Autofrettage

A surface crack was modeled in a flat plate and loaded with applied displacement boundary conditions to induce a biaxial far-field strain equivalent to the peak autofrettage strains taken from the analysis shown in Figure O-1. The hoop strain was applied perpendicular to the crack face and the axial strain was applied in the transverse direction. A uniaxial model was also run with the hoop strain applied perpendicular to the crack face and the axial strain neglected. The model configuration is shown in Figure O-2. The stress-strain response from FEA compared to the tank analysis is shown in Figure O-3. The flat plate biaxial model shows good agreement with the tank analysis in both the axial and hoop directions while the uniaxial model matches the hoop strain, but not the stress states. Figure O-3 shows the comparison of crack mouth opening displacement (CMOD) between the crack in the biaxial model and the uniaxial model. The CMOD in the uniaxial case is lower than the biaxial case indicating that the crack tip conditions may be unconservative. The J-integral was also calculated for both cases. The J-integral calculation is not technically valid in this case because all of the material in the model is deforming plastically (i.e. non-proportional loading). In this case, the calculation of J is no longer path-independent [ref. 1]. However, the mesh around the crack tip is identical in both models and the J-integral is calculated along the same path in both cases. This allows the results to be used for a qualitative comparison between the two cases. Figure O-4 shows J as a function of the location along crack font, ϕ, for the biaxial and uniaxial model. As implied by the CMOD results, the uniaxial model underpredicts J along the crack front as compared to the biaxial model. This shows that a crack under a biaxial stress state is likely to begin stable tearing earlier than the same crack loaded uniaxially, indicating that for autofrettage testing, uniaxial coupons are likely unconservative.

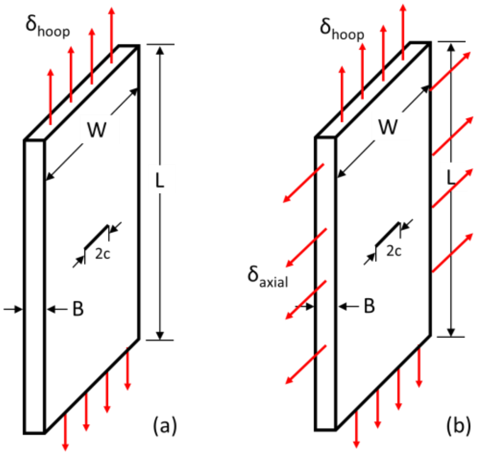

Figure O-2. Model configurations and applied boundary conditions for (a) uniaxial case and (b) biaxial case. δ_{hoop} and δ_{axial} are applied displacements to induce a far-field strain equivalent to the hoop and axial strain, respectively, for the tank analysis.

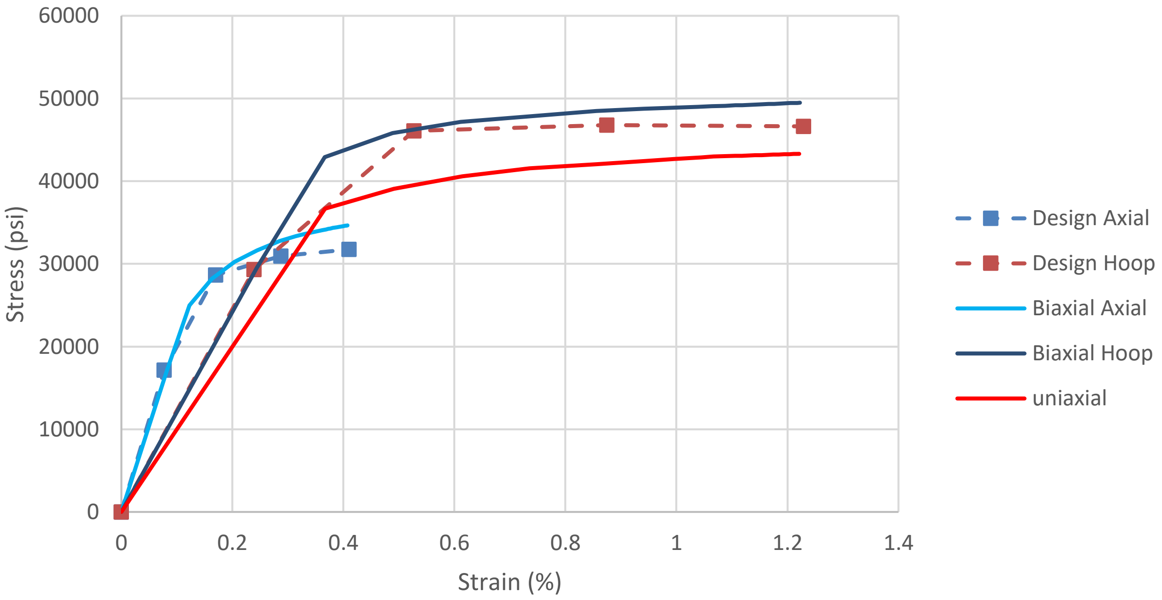

Figure O-3. Stress-strain response for uniaxial and biaxial model as compared to tank analysis up to the peak autofrettage strain.

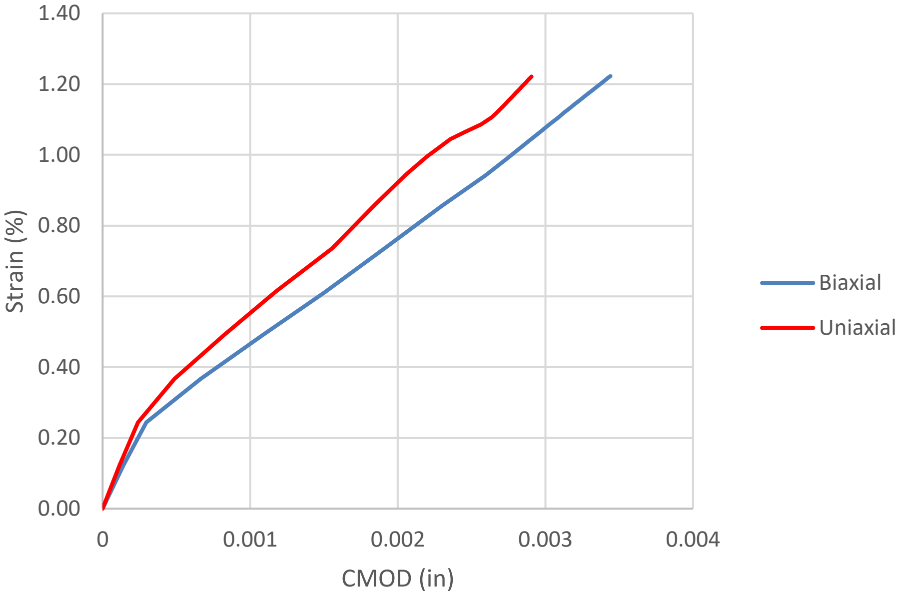

Figure O-4. Far-field strain vs CMOD for biaxial and uniaxial model. The uniaxial model underpredicts CMOD as compared to the biaxial model.

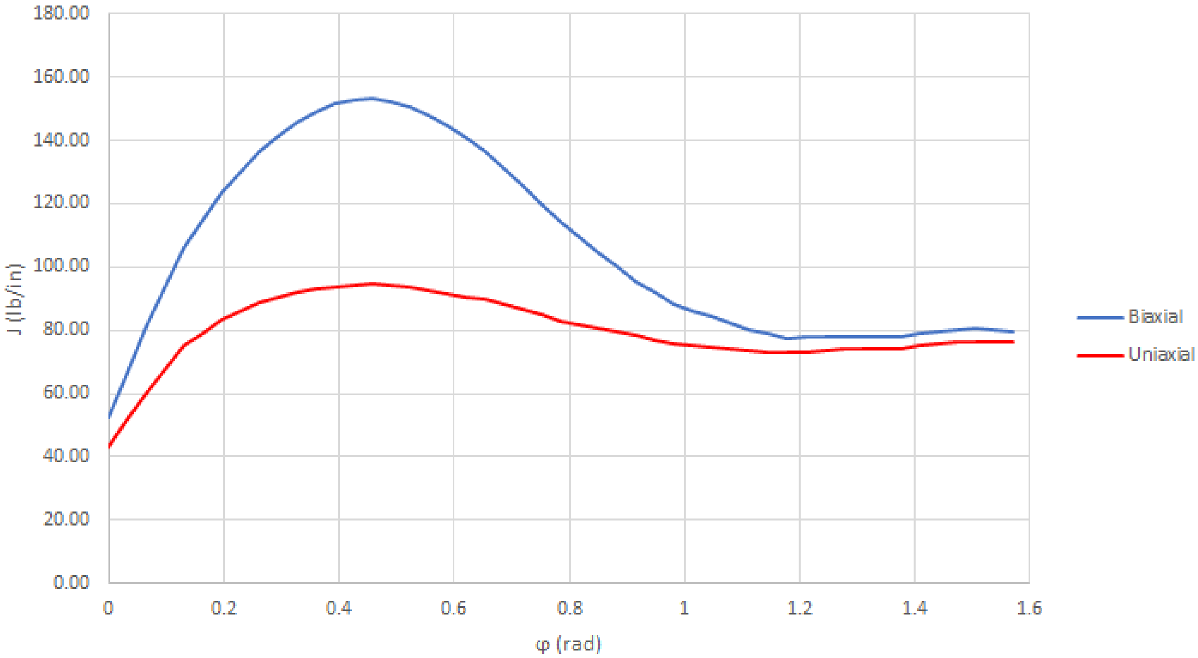

Figure O-5. J vs ϕ for the biaxial and uniaxial models. $\phi = 0$ corresponds to the point at which the crack front intersects the surface of the plate and $\phi = 1.57$ corresponds to the maximum crack depth. The uniaxial model underpredicts J along the crack front.

O.3 Biaxial Correction for Uniaxial Data

Initial analysis has shown that uniaxial coupons may be unconservative for the testing of autofrettage crack growth. Additionally, there are limited options for determining autofrettage crack growth with analysis and biaxial testing may be too complicated to be feasible in many cases. In lieu of testing with biaxial coupons, an analysis approach to add conservatism to uniaxial test data due to the biaxial stress state is proposed here:

(1) Perform elastic-plastic FEA on the uniaxial coupon and biaxial liner for the crack size/shape and strain levels required in the damage tolerance life qualification.

(2) Select a crack tip driving force parameter (e.g., J-integral) and evaluate the parameter along the crack front in the biaxial liner analysis.

(3) Increase the strain level in the uniaxial analysis until the value of the crack tip driving force parameter is equal to that in the biaxial analysis.

(4) Conduct the uniaxial tests at the increased strain level.

O.3.1 Example: 0.082-inch Thick Ti 6Al-4V

Uniaxial autofrettage tests were conducted on coupons extracted from a Ti 6Al-4V liner at a peak strain of 2.65 The NDE crack size for this case was a = 0.025 with a/c = 2.65 (See Section 7.2.2 for full details). Applying the procedure listed above, the J-integral was calculated for the NDE crack with a biaxial FEM and a series of uniaxial models with an increasing autofrettage strain level. The J-integral along the crack front for each case are shown in Figure O-6. At the prescribed autofrettage strain of 2.65%, the uniaxial model underpredicts J as compared to the biaxial model. Increasing the autofrettage strain brings J for the uniaxial case above that predicted in the biaxial model. Figure O-7 shows the initiation values of J, J_{init}, for the uniaxial analysis vs autofrettage strain. This is the value of J at the angle of initiation, indicating the position along the crack front where ductile fracture is expected to begin, as calculated according to ASTM E2899-15 [ref. 4]. The threshold representing J_{init} for the biaxial model is shown with an orange dashed line. The strain required to reach this value of J_{init} is interpolated. In this example, the uniaxial coupon could be tested at a simulated autofrettage strain of 3.8% to achieve the target J of the biaxial condition.

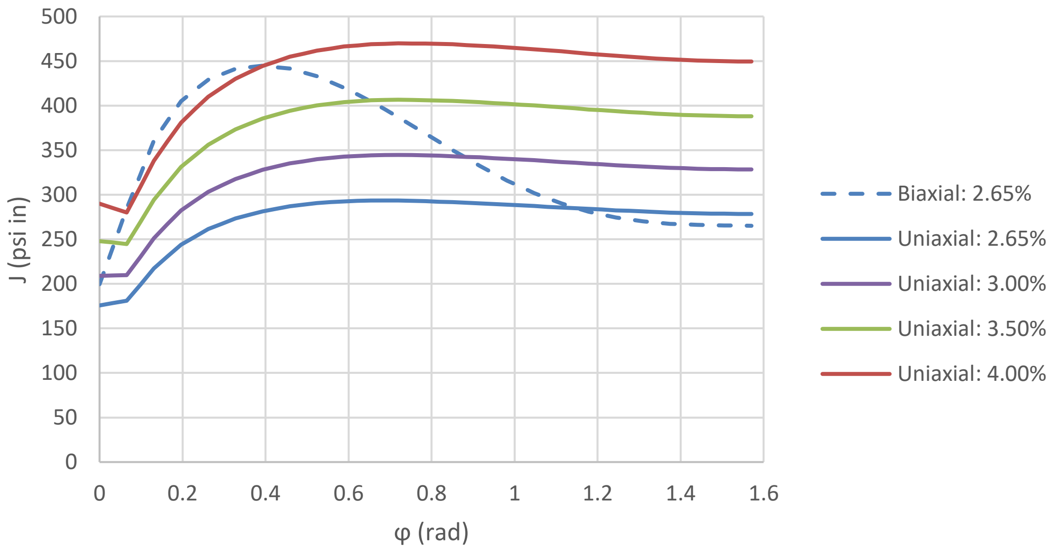

Figure O-6. J along the crack front for the biaxial model, (blue dashed line) representing the expected crack front conditions at the prescribed autofrettage strain, and the uniaxial model with increasing strain levels.

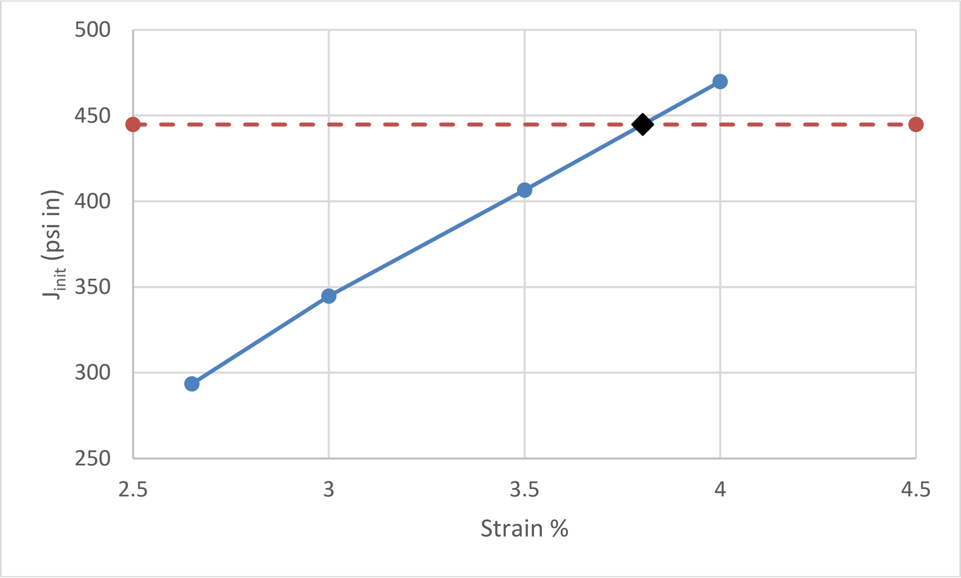

Figure O-7. J_{init} vs. autofrettage strain for the uniaxial model. The black triangle represents the point at which J_{init} in the uniaxial model matches J_{init} calculated from the biaxial model.

O.3.2 Example: 0.060-inch Thick Ti 6Al-4V

Uniaxial autofrettage tests were conducted on coupons extracted from a Ti 6Al-4V liner at a peak strain of 1.0%. The NDE crack size for this case was a = 0.025 with a/c = 1.0 (See Section 7.2.2 for full details). Applying the procedure listed above, the J-integral was calculated for the NDE crack with a biaxial FEM and a series of uniaxial models with an increasing autofrettage strain level. The J-integral along the crack front for each case are shown in Figure O-8. At the prescribed autofrettage strain of 1%, the uniaxial model underpredicts J as compared to the biaxial model. Increasing the autofrettage strain brings J for the uniaxial case above that predicted in the biaxial model. Figure O-9 shows J_{init}, for the uniaxial analysis vs autofrettage strain. The threshold representing J_{init} for the biaxial model is shown with an orange dashed line. The strain required to reach this value of J_{init} is interpolated. In this example, the uniaxial coupon could be tested at a simulated autofrettage strain of 1.3% to achieve the target J of the biaxial condition.

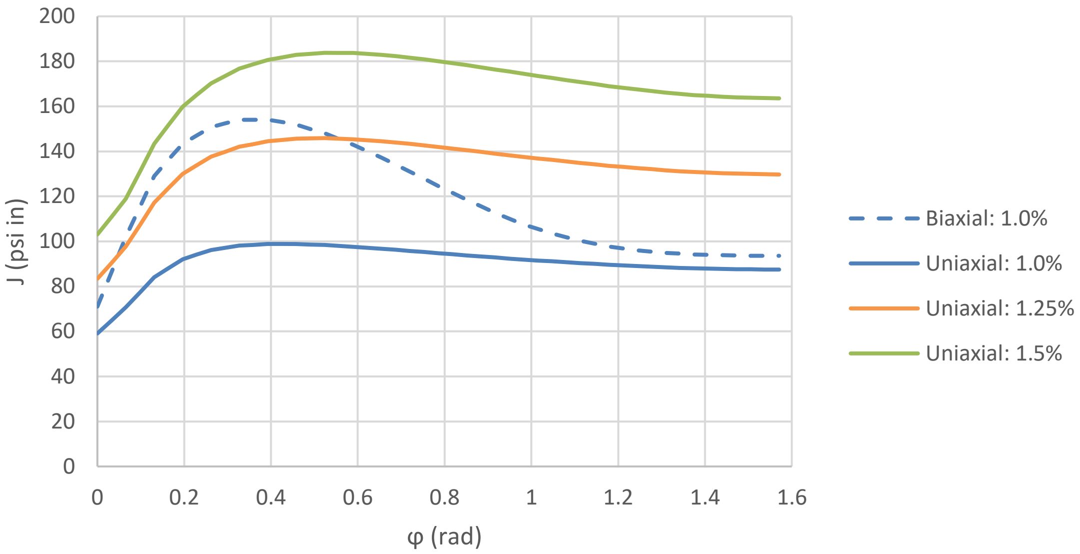

Figure O-8. J along the crack front for the biaxial model, (blue dashed line) representing the expected crack front conditions at the prescribed autofrettage strain, and the uniaxial model with increasing strain levels

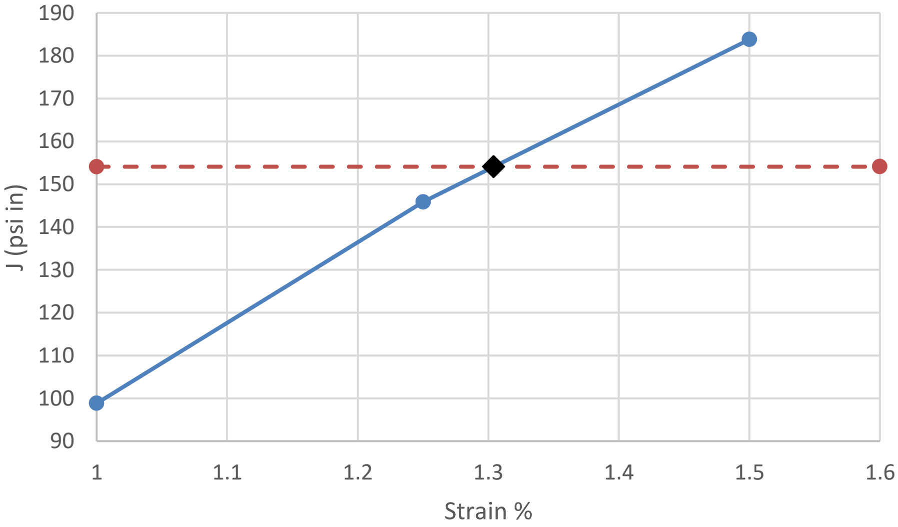

Figure O-9. J_{init} vs. autofrettage strain for the uniaxial model. The black triangle represents the point at which J_{init} in the uniaxial model matches J_{init} calculated from the biaxial model.

References

1. J. R. Rice, "A Path Independent Integral and the Approximate Analysis of Strain Concentration by Notches and Cracks", Journal of Applied Mechanics, 35, 1968, pp. 379–386.
2. ANSI AIAA S-081B.

REPORT DOCUMENTATION PAGE

Form Approved
OMB No. 0704-0188

1. REPORT DATE *(DD-MM-YYYY)*
08/25/2020

2. REPORT TYPE
Technical Memorandum

3. DATES COVERED *(From - To)*

4. TITLE AND SUBTITLE
Composite Overwrapped Pressure Vessel (COPV) Damage Tolerance Life Analysis Methodology and Test Best Practices

Appendices

5a. CONTRACT NUMBER

5b. GRANT NUMBER

5c. PROGRAM ELEMENT NUMBER

6. AUTHOR(S)
Hickman, Heather K.; Russell, Richard W.; Dawicke, David S.;
Leser, William; Leser, Patrick E.; Wincheski, Russell A.;
Hochhalter, Jacob D.; Grimes Ledesma, Lorie R.; Imtiaz, Kauser S.

5d. PROJECT NUMBER

5e. TASK NUMBER

5f. WORK UNIT NUMBER
869021.05.07.02.16

7. PERFORMING ORGANIZATION NAME(S) AND ADDRESS(ES)
NASA Langley Research Center
Hampton, VA 23681-2199

8. PERFORMING ORGANIZATION REPORT NUMBER
NESC-RP-16-01183

9. SPONSORING/MONITORING AGENCY NAME(S) AND ADDRESS(ES)
National Aeronautics and Space Administration
Washington, DC 20546-0001

10. SPONSOR/MONITOR'S ACRONYM(S)
NASA

11. SPONSOR/MONITOR'S REPORT NUMBER(S)
NASA/TM-2020-5006765/Volume II

12. DISTRIBUTION/AVAILABILITY STATEMENT
Unclassified - Unlimited
Subject Category Space Transportation and Safety
Availability: NASA STI Program (757) 864-9658

13. SUPPLEMENTARY NOTES

14. ABSTRACT

The NASA Engineering and Safety Center (NESC) Deputy Director requested an independent assessment to develop data to understand the limitations of linear elastic fracture mechanics (LEFM) computational methods used to predict fatigue crack growth rate (da/dN) behavior of small detectable cracks in thin metal liners for composite overwrapped pressure vessels (COPVs). The NESC assessment team was also requested to demonstrate a test-based methodology for validating damage tolerance requirements for COPVs with elastically responding metal liners where LEFM methods are not appropriate. This document contains the appendices to the main report.

15. SUBJECT TERMS
Composite Overwrapped Pressure Vessels; Linear Elastic Fracture Mechanics; Damage Tolerance; NASA Engineering and Safety Center

16. SECURITY CLASSIFICATION OF:			**17. LIMITATION OF ABSTRACT**	**18. NUMBER OF PAGES**	**19a. NAME OF RESPONSIBLE PERSON**
a. REPORT	**b. ABSTRACT**	**c. THIS PAGE**			STI Help Desk (email: help@sti.nasa.gov)
					19b. TELEPHONE NUMBER *(Include area code)*
U	U	U	UU	210	(443) 757-5802

Standard Form 298 (Rev. 8/98)
Prescribed by ANSI Std. Z39.18